Development of Novel Hyperpolarized Magnetic Resonance Techniques and Compounds for Perfused Organs



Daniel Ball

Department of Physiology, Anatomy and Genetics

University of Oxford

A thesis submitted for the degree of

Doctor of Philosophy

Trinity 2012

Abstract

Hyperpolarization via the Dynamic Nuclear Polarization (DNP) technique has revolutionized our ability to study metabolic changes in real time. The aim of this thesis was to build upon previous work centered around the use of DNP within the isolated perfused rat heart, a well established model system for the study of cardiac metabolism, to enhance the information that can be obtained through the combination of DNP with perfused organs. Initially this was done by using the widely studied DNP probe, [1-^{13}C]pyruvate, to generate images of metabolism within the isolated perfused rat heart. The developed technique was then successfully demonstrated in two models of myocardial infarction. The thesis then proceeds to develop an understanding of how the supra-physiological concentrations of [1-^{13}C]pyruvate commonly used in DNP experiments can affect metabolism in the isolated perfused rat heart, and the way in which the myocardium responds to those changes if it is not adequately supplied with substrates ordinarily present *in vivo*, namely fatty acids. New methods of providing the heart with these required substrates were developed, without significant interference to the biochemical information acquired from DNP experiments. As [1-^{13}C]pyruvate only provides information on a small subset of carbohydrate metabolism, the next chapter develops new compounds to be used with DNP, which would allow the exploration of short chain fatty acid metabolism (butyrate) as well as ketone body metabolism (β-hydroxybutyrate and acetoacetate), and other aspects of carbohydrate metabolism (lactate and alanine). These compounds were developed and then tested for their potential usefulness in the isolated perfused heart. Finally, as the isolated perfused rat heart lacks the diversity of genetic disease models available in the mouse, the final chapter expanded the use of DNP to the isolated perfused mouse heart with all the size challenges that this entails, and makes the transition from the heart to the liver, in order to provide an alternative metabolic viewpoint on the biochemistry of disease models. This thesis thereby permits studies involving isolated perfused organs to be carried out whilst exploiting all the tools that DNP has to offer and consequentially, allows for a vast array of physiologically derived information to help us better understand metabolic diseases.

Abbreviations

ALT: Alanine Transaminase
ATP: Adenosine Triphosphate
CSI: Chemical Shift Imaging
CT: Computed Tomography
DCA: Dichloroacetic Acid
DMSO: Dimethyl Sulphoxide
DNP: Dynamic Nuclear Polarization
ESR: Electron Spin Resonance
ETC: Electron Transport Chain
FDG: Fluorodeoxy Glucose
GLUT: Glucose Transporter
LDH: Lactate Dehydrogenase
LPL: Lipoprotein Lipase
MPT: Mitochondrial Pyruvate Transporter
MRI: Magnetic Resonance Imaging
NEFA: Non-esterified Fatty Acids
NMR: Nuclear Magnetic Resonance
PHIP: Para Hydrogen Induced Polarization
PDH: Pyruvate Dehydrogenase
PDK: Pyruvate Dehydrogenase Kinase
PET: Positron Emission Tomography
RF: Radiofrequency
SABRE: Signal Amplification by Reversible Exchange
SCFA: Short Chain Fatty Acids
SNR: Signal to Noise Ratio
STZ: Streptozotocin
TCA: Tricarboxylic Acid Cycle

Contents

1 Introduction **1**

1.1 Overview 1

1.2 Aims 3

2 Theory **6**

2.1 Aims 6

2.2 NMR physics 6

2.2.1 Dynamic Nuclear Polarization (DNP) 11

2.2.2 Dissolution DNP 16

2.2.3 Tracer requirements 21

2.3 Metabolism 23

2.3.1 Digestion 23

2.3.2 Carbohydrates 26

2.3.3 Fats 29

2.3.4 Amino acids 31

2.3.5 TCA cycle and the ETC 32

3 Metabolic Imaging **34**

3.1 Introduction 34

3.2 Materials and methods 36

3.3 Results 41

3.3.1 CSI protocol optimization 41

3.3.2 Acute infarct model 43

3.3.3 Chronic infarct model 45

3.4 Discussion 50

4 Pyruvate Optimization **55**

4.1 Pyruvate concentration 57

4.1.1 Introduction 57

4.1.2 Materials and methods . . . 59
4.1.3 Results . . . 62
4.1.3.1 [1-^{13}C]pyruvate . . . 62
4.1.3.2 Dichloroacetic acid . . . 69
4.1.3.3 [2-^{13}C]pyruvate . . . 69
4.1.4 Discussion . . . 73
4.2 Fatty acid supply to the heart . . . 76
4.2.1 Introduction . . . 76
4.2.2 Materials and methods . . . 78
4.2.3 Results . . . 81
4.2.4 Discussion . . . 87

5 Hyperpolarized Probe Development 92
5.1 Introduction . . . 92
5.2 General methods . . . 99
5.3 Butyrate . . . 103
5.3.1 Glassing . . . 104
5.3.2 Radical and Gd addition . . . 105
5.3.3 Final formulation . . . 106
5.3.4 Testing . . . 106
5.3.5 Trial perfusion study . . . 113
5.3.5.1 Methods . . . 113
5.3.5.2 Results . . . 115
5.3.5.3 Discussion . . . 116
5.3.6 Trial *in vivo* study . . . 116
5.3.6.1 Methods . . . 116
5.3.6.2 Results . . . 117
5.3.6.3 Discussion . . . 118
5.3.7 Application: diabetic study . . . 120
5.3.7.1 Methods . . . 121
5.3.7.2 Results . . . 122
5.3.7.3 Discussion . . . 124
5.4 Alanine . . . 124
5.5 Lactate . . . 126
5.5.0.4 Methods . . . 127
5.5.0.5 Results . . . 129

5.5.0.6 Discussion 130
5.6 β-hydroxybutyrate and acetoacetate 131
5.7 Discussion 135

6 Assessment of Alternative Organs **139**
6.1 Introduction 139
6.2 Rig design 141
6.2.1 Methods of perfusion 141
6.2.1.1 Cardiac perfusion 141
6.2.1.2 Hepatic perfusion 145
6.2.1.3 General perfusion requirements 145
6.2.1.4 Rig specifications 149
6.3 Perfusion setup testing 157
6.3.1 Mouse heart 157
6.3.1.1 Materials and methods 157
6.3.1.2 Results 159
6.3.1.3 Discussion 167
6.3.2 Liver perfusion 170
6.3.2.1 Materials and methods 170
6.3.2.2 Results 173
6.3.2.3 Discussion 181
6.3.2.4 Conclusion 184

7 General Discussion and Future Directions **186**

References **190**

Chapter 1

Introduction

1.1 Overview

Extensive developments into the understanding of the human body and its functioning at the biochemical level have been made over the last century. "Underground maps" of metabolic pathways now exist [1], and over time, new techniques have emerged to further our understanding of the way in which these metabolic pathways fit together. These techniques can be roughly grouped into those that provide information about the identity of the different species within a pathway and those that predominantly provide kinetic information, and therefore require prior knowledge of the pathway. Radiolabelling and positron emission tomography (PET) are examples of two techniques which provide kinetic information. In radiolabelling, a metabolite of interest, such as glucose, is labelled with ^{3}H or ^{14}C, injected into the tissue of interest, and a known product is collected [2]. In this example, either labelled water or carbon dioxide is measured, and gives information on the rate of production, as well as an absolute value of how much glucose was metabolised, which can be compared in control and disease groups.

PET systems rely on decay by positron emission, and therefore isotopes such as

Isotope	Half life
^{15}O	2 mins
^{11}C	20 mins
^{68}Ga	68 mins
^{18}F	110 mins
^{64}Cu	9 hours
^{124}I	4 days

Table 1.1: This table gives the half-lives of some commonly used PET isotopes. The most useful of these clinically, ^{18}F has a long enough half-life that compounds based on it can be synthesized away from the site of the scanner.

^{11}C, ^{18}F, ^{15}O are required, which leads to the need for a cyclotron to produce these isotopes. Often these isotopes have very short half-lives (Table 1.1), and thus need to be generated close to the PET system (with the exception of ^{18}F, an extensively used probe which can be made off site). In addition, time is required to synthesize relevant probes from the isotope. PET does, however, provide images of acceptable resolution (around 1 – 2 mm), with no depth limit, and a temporal resolution from 10's of seconds to minutes. The sensitivity of tracers is exceptionally good, with detection limits around the pico-mol range (nano grams of the PET probe are sufficient for clinical use [3]). Fluorodeoxyglucose (^{18}FDG) is a good example of a glucose analogue which is used for detecting highly glycolytic tumours in oncology [4, 5]. It is also possible to design probes capable of interrogating metabolic kinetics, as well as antibody binding sites [6], peptides [7] and hormones [8], using the PET isotopes listed in Table 1.1.

Examples of systems providing identification of the particular species in a metabolic pathway include nuclear magnetic resonance (NMR) and mass spectrometry (and its many variants [9]). NMR is developing into a particularly useful tool in clinical research [10–12]; and in the same way that radiolabelling can be used to measure oxidation rates, so too can NMR with the infusion of a stable, NMR visible isotope (^{13}C being the most common for metabolic studies) [13]. Additionally, following substrate perfusion into tissue, blood samples can be taken and submitted for NMR analysis [14]. This gives a snap shot of all the metabolites present at that moment

in time, and their ratios. NMR, however, has a low sensitivity for the ^{13}C nucleus, which results in long scan times for metabolic studies (on the order of several hours for the metabolic analysis of a rat heart).

Mass spectrometry, especially when combined with liquid and gas chromatography, is a useful tool in metabolic analysis [15] in that it provides additional information to aid with the elucidation of unknown metabolites in NMR. It also has the advantage that it provides a quantitative measure of metabolite levels. NMR is not typically used for this purpose, rather it is generally used to provide ratiometric information, although some NMR methods do aim to provide absolute quantification [16].

Lacking from the methods described so far is a technique that allows identification of the metabolites of interest at the same time as providing real-time kinetic data. Dynamic Nuclear Polarization (DNP) is a form of NMR that allows metabolic probes to be traced in real time with a high signal to noise ratio (SNR) thus providing kinetic information and uptake parameters, as well as the identity of the intermediate metabolites in the pathway. A disadvantage however, is that the high level of signal from the metabolite being traced typically lasts less than 60 seconds. To compound this, although there are a large range of potential probes for metabolic assessment, few are likely to yield high enough signal to noise ratios to be useful in perfused organs or *in vivo*, or to provide information on a useful metabolic pathway.

1.2 Aims

This thesis aims to address some of the issues associated with the DNP technique by making improvements to its methodology and application, thereby allowing it to be used routinely in elucidating metabolic changes and pathways in biological systems with a specific focus on isolated perfused organ systems.

Chapter 2 provides some background on the fundamental theory of NMR and DNP, along with a general discussion on the metabolic pathways relevant to the material

in this thesis. Chapter 3 looks at extracting further information from pyruvate, the most routinely used DNP probe due to its ease of use and ability to provide relevant metabolic information on carbohydrate metabolism. By developing a method of imaging (and thereby localizing) metabolism in the isolated perfused heart, the aim was to provide a spatial assessment of metabolism in the diseased heart. Current approaches rely on techniques such as MRI, ultrasound and computed tomography (CT) to examine the diseased heart. Unfortunately, these do not reveal information about the metabolic changes that are occurring – and whether underlying changes in metabolism could predict the observed physiological changes. To do so, molecular imaging techniques need to be employed, and PET could potentially be used for this purpose [17]. However, in the study of cardiac ischemia in a rat model, it is used essentially as a contrast agent as there is difficulty in distinguishing between reduced uptake of FDG due to changes in metabolism or the presence of non-perfusing necrotic tissue. DNP, when combined with novel imaging techniques, will aim to provide this distinction, and to provide further information on metabolic changes.

In order to be truly useful, it should be possible to use the DNP technique without making any compromise to the physiological requirements of the biological system under examination. Currently, supra-physiological concentrations of pyruvate are being used in order to obtain a greater SNR. Isolated heart preparations are also frequently being perfused without the presence of fatty acids (which would ordinarily account for around 70% of their fuel *in vivo* [18]). This is due to the need for albumin to solubilize the fatty acids, which has previously been shown to eliminate the enhanced pyruvate signal [19]. As such, Chapter 4 aims to investigate both these issues. Firstly, to investigate the applied pyruvate concentration, the metabolic effects of using such high concentrations will be explored to determine whether lower pyruvate concentrations could be used while maintaining sufficient signal to noise ratio (SNR). Secondly, methods will be developed to allow the use of fatty acids in the perfusion buffer for

DNP experiments to achieve the ideal physiological preparation.

The next critical step in making the use of DNP more widespread is to increase the availability of different metabolites to survey alternative metabolic pathways. Chapter 5 aims to do this by developing probes that allow the exploration of the major metabolic fuel types, i.e. the fatty acids, the ketone bodies, and the products of glycolysis, alanine and lactate. This development involves appropriate formulation to allow the high signal to noise ratio of the chosen probe to be created during the DNP process. It is also important to minimize adverse effects from the non-physiological compounds sometimes needed in order to create suitable probes. Within Chapter 5, these probes will be characterized with respect to their physical properties and metabolic activity. They will then be further evaluated for potential use in isolated perfused organ systems.

Whilst DNP has so far been evaluated in the isolated perfused rat heart, it remains unexplored in the mouse heart (to date, no literature exists on the process). This is due to the difficulty of achieving a good signal to noise ratio with DNP probes in a system a fraction the size of the rat heart. Yet in avoiding the mouse, a vast array of easily available and clinically relevant transgenic and mutant mouse models are left untouched by a technique that could reveal information on metabolic processes in these animals. Chapter 6 aims to develop the ability to use DNP in the perfused organs of mice. The technical challenges of mouse heart perfusion include the delivery of the hyperpolarized probe within a suitable time frame to an organ which has 1/10th the buffer flow of the perfused rat heart. Chapter 6 then proceeds to develop the use of the isolated perfused mouse liver with DNP, a natural choice following the mouse heart, due to the central role that it plays in the metabolic alterations occurring within the body during changes in substrate supply and disease. An understanding of the changes that occur in the liver, as well as the adaptations in the heart, would better lend itself to a whole body understanding of metabolism.

Chapter 2

Theory

2.1 Aims

This chapter aims to introduce the basic theory of nuclear magnetic resonance (NMR), which underpins all the work carried out in this thesis. The physical basis behind the technique of hyperpolarization via dynamic nuclear polarization (DNP) which allows the signal from low concentration metabolites to be amplified, and the way in which this technique is practically applied will then be explained. Finally, an overview of metabolism will be given, to introduce the pathways that will be probed throughout this thesis using DNP hyperpolarization.

2.2 NMR physics

NMR is an exceptionally useful technique as it allows assignment of a specific signature to a nucleus, thereby helping to identify it through its interaction with the environment, whether that is with another nucleus, an external magnetic field, or radio frequency irradiation. NMR relies on the physical property that nuclei possess, namely a magnetic moment (essentially allowing it to act as a bar magnet), which arises whenever any charged species is spinning. Nuclei without this magnetic mo-

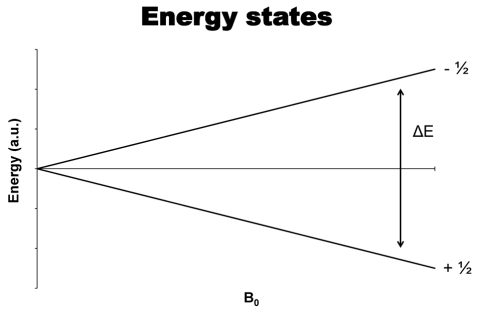


Figure 2.1: Graphical depiction of Equation 2.1 with increasing magnetic field strength, B_0.

ment are NMR invisible, and in practice this is the case where a species has a nuclear spin of 0.

In terms of quantum mechanical theory, the result of placing nuclei with magnetic moments into an external magnetic field is an interaction which creates different energy levels (the Zeeman effect [20]), whereby the gap between energy levels has a defined energy spacing given by Equation 2.1. ΔE denotes the spacing between energy levels, γ is the gyromagnetic ratio (the ratio of the magnetic moment to angular momentum) and B_0 is the external magnetic field experienced by the nucleus. Note the proportionality to γ and B_0, i.e. the higher the external magnetic field, the higher the energy gap between energy levels. This energy spacing is depicted graphically in Figure 2.1.

$$\Delta E = \gamma \hbar B_0 \tag{2.1}$$

Using hydrogen as an example (with a magnetic spin quantum number of S = $\frac{1}{2}$), placement in a magnetic field will generate two magnetic orientations; nuclear spins either aligned with the B_0 field, or opposed to it. The ratio of the populations within the two energy states created is dependent on the Boltzmann distribution (Equation 2.2). From this equation, it can be seen that the population difference is very small, for example, at T = 293 K, k = $1.38*10^{-23}$ (the Boltzmann constant) and B_0 = 11.7 T (the magnetic field of the magnet used in the experiments described in this thesis),

the population difference between the upper (N_{upper}) and lower (N_{lower}) energy states is 512 parts per million (ppm). The difference in population between this upper and lower energy state is known as the polarization, and its low values are the reason for the inherent insensitivity of NMR.

$$N_{upper}/N_{lower} = e^{-\Delta E/kT} \tag{2.2}$$

This difference in populations, or polarization, can be exploited in a similar way to other types of spectroscopy (e.g. infrared or ultraviolet); energy is absorbed by a small proportion of the population, altering their energy state. This energy (ΔE) is supplied to the system by emitting radiation from a coil located around the sample. For the magnetic field strengths used in NMR, the frequency of this energy corresponds to the radiofrequency (RF) range, and is related to the energy needed to change from the lower to the upper energy state by Equation 2.5.

These changes from the lower to the upper energy state will occur as long as they are not forbidden by the rules of quantum mechanics (forbidden transitions can be forced in both NMR and DNP, briefly discussed later in this chapter). The energy, and therefore the frequency of the radiowaves required to induce transitions between energy levels will change depending on the local environment of the nucleus, meaning that it is possible to distinguish different nuclei in a molecule. This is known as chemical shift, and occurs in part because elements have differing electronegativities. Oxygen for example is able to pull more electrons toward itself than Carbon and this decreased electron density around Carbon gives it a higher chemical shift. Upon relaxation, the absorbed energy is released and observed by a detector tuned to the correct frequency.

In terms of classical theory, the NMR experiment can be visualized as the magnetic dipole of nuclear spins pointing toward the Z axis (the direction of the external magnetic field) in their thermal equilibrium position, with magnetization M_0. The mag-

$$\Delta E = hf \tag{2.3}$$

After substitution of Equation 2.3 into Equation 2.1:

$$\gamma\hbar B_0 = hf \tag{2.4}$$

Rearrangement of 2.4 gives Equation 2.5:

$$f = \gamma B_0/2\pi \tag{2.5}$$



Figure 2.2: Pane A depicts the two populations of spins (aligned with the magnetic field, or against it) precessing around the Z axis, at a frequency proportional to B_0. Pane B depicts the net magnetization of the system. Image adapted from http://www.process-nmr.com/.

netic dipoles are in fact precessing around the Z axis, with a frequency proportional to B_0, called the Larmor frequency. This frequency is equivalent to that required in the quantum mechanical description of NMR to induce energy level transitions. At equilibrium, there is no significant contribution to magnetization in either the X or Y planes, as the dipoles are randomly distributed around the Z axis, with vanishingly small probability of significantly strong magnetization in any one given direction (Figure 2.2). In order to detect these nuclear generated magnetic dipoles, it is necessary to force a sizeable magnetization component into the transverse plane, either X or Y, which will in turn induce an electromagnetic field perpendicular to the external magnetic field B_0. This is done by generating an RF field in the transverse plane, thereby creating an additional magnetic field (B_1), which now forces the magnetic dipoles (Figure 2.3) to be coherent, thus producing a non-zero magnetic field in a given direction. Information here is extracted in different ways. Each of these spins may be in different chemical environments, and therefore precess at slightly different Larmor frequencies (exposure to different chemical environments alters the B_0 field

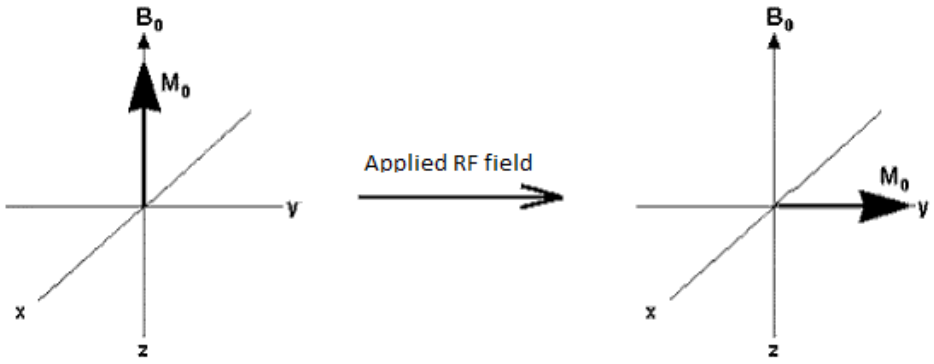


Figure 2.3: This figure shows the change in bulk magnetization from the z axis to the transverse plane (x-y) when an RF field is applied.

experienced). This magnetization recovers back to the Z axis (its thermal equilibrium) after a time (T_1). In addition, the spins begin to become non-cohesive after a specific time (T_2). The detected signal measured by an RF coil is separated into sine and cosine components using a Fourier transform, to obtain a spectrum made up of all the frequencies detected within the sample being excited. From here, the components of the sample (whether living tissue, or a test tube containing a compound) can be identified.

T_1 relaxation can occur via different mechanisms, the most relevant of which are dipolar interactions, paramagnetic relaxation and chemical shift anisotropy (CSA). Dipolar coupling arises from the distance and angle between two nuclei, and is an effect particularly relevant to molecules with protons. This means that generally, ^{13}C nuclei with protons attached relax more quickly than those without. This can be demonstrated by replacing protons with deuterium (spin = 1), and observing the longer T_1 seen. The distance and angle between two nuclei varies rapidly over time due to the natural motion of nuclei in a liquid (known as tumbling), and has the effect of inducing small changing magnetic fields. If a portion of these small changes happen at the NMR frequency of the nucleus, relaxation can happen, allowing nuclei to flip between their different spin states. Paramagnetic relaxation is commonly seen when

metals are present, due to the number of unpaired spins present. In the case of DNP, this is the case, in addition to the organic radical also used which will contribute to paramagnetic relaxation. It works in a similar manner to dipolar coupling, except that it is now an unpaired electron which is generating a small and variable magnetic field, which allows relaxation of the nucleus it is interacting with. CSA is another important relaxation mechanism, and adds another aspect to the dipolar coupling discussed above. In perfect theory, a nucleus and its electron distribution would be spherical. In practise, it is anisotropic (i.e. the electrons are not evenly distributed around the nucleus at any given time), and interacts in a certain way with the main magnetic field to alter the relaxation of the nucleus. In liquids, given the rapid motion of the nuclei, this effect does not play a significant role since all these interactions average out over time, unless discussing solid state NMR, where each of the nuclei would be held in fixed positions.

2.2.1 Dynamic Nuclear Polarization (DNP)

The concept of hyperpolarization dates back to the 1950s, when it was hypothesized that electronic and nuclear transition states could be coupled together in different ways to allow high levels of nuclear polarization and therefore higher signal levels in NMR [21–29]. These techniques were applied in the solid and gaseous states over the next few years [30–33], to achieve higher than thermal equilibrium polarizations. By using microwave irradiation, or other types of radiation of appropriate frequencies to excite typically forbidden transitions, spin exchange between nuclear and electronic spin states can be achieved. From the foundations of this research, the methods used to hyperpolarize nuclei diverged considerably, using different principles and techniques. Those with the potential to be used for metabolic experiments will be described here.

Para hydrogen induced polarization (PHIP) induces polarization by using a singlet species of hydrogen (parahydrogen, default is orthohydrogen, a triplet, both species

existing in a 1:3 ratio at room temperature), and transferring that polarization to a nuclei of interest [34]. Typically, this has relied on the generation of parahydrogen, done by taking advantage of the fact that it is the more stable species at very low temperatures, and is dominant at around 20 K. Thus when hydrogen is cooled to very low temperatures, with the help of a paramagnetic catalyst, parahydrogen is produced, which can be warmed to room temperature. Its decay back to an equilibrium state with orthohydrogen is very slow, and the sample is relatively stable for several hours. When required, the parahydrogen can be added to a species capable of an addition reaction (typically alkene and alkyne species), creating a molecule with polarized protons that can be detected in very small concentrations by an NMR spectrometer. Any subsequent reactions of this species can also be tracked, by looking at the resonance changes to the polarized protons. It is also possible to transfer this very high polarization to other nuclei with lower gyromagnetic ratios (and thus less sensitive species such as carbon) [35]. The technique is problematic due to the limited number of metabolically relevant species that can undertake hydrogenation reactions in this manner. To look at a compound of interest, a precursor with the appropriate unsaturated functional group has to be synthesized (rather than being commercially available), thereby reducing the widespread usefulness of the technique. A clever improvement to PHIP has recently been developed [36], which allows para-hydrogen polarization to be transferred to a much wider variety of compounds using a metal complex centre (signal amplification by reversible exchange, SABRE).

Another technique with good potential is the use of optical pumping to achieve hyperpolarization of gases with a spin of $\frac{1}{2}$. These include ^{129}Xe and ^{3}He which have been widely used in MRI to image the air cavity within the lungs [37], and have been shown to have potential in the diagnosis of pulmonary diseases in the clinic [38–40]. Xenon tracers have a more interesting application, in that they can be bound to biomarkers and tracked [41], or can be used to image perfusion within the brain for

example [42], either by inhalation or by administration as an aerosol injection. Both nuclei have the advantage that no background signal exists within the human body. Concerning ^{3}He, while it has the potential to be useful in the clinic, its development will likely be hindered by the prohibitive cost caused by a low natural availability of the isotope [43].

Finally, there is dynamic nuclear polarization (DNP), which is the technique used in this thesis. Different physical methods exist for achieving this type of hyperpolarization, and can be grouped into thermal mixing, the solid effect, the Overhauser effect and the cross effect [44,45]. These methods all rely on the much higher gyromagnetic ratio that electrons possess when compared to nuclear spins and their considerably shorter longitudinal relaxation time (T_1), which means that electrons are easily polarisable (near complete polarization is achieved at liquid helium temperatures, as predicted using the Boltzmann distribution [46]). This high potential for polarization is exploited with DNP, using microwave irradiation to drive transitions between forbidden states, thereby allowing transfer of the high electronic polarization to nuclei. DNP was made truly useful when it became possible to transfer the high solid state polarization achieved through hyperpolarization to the liquid state at room temperature [47]. This technique, known as dissolution DNP, is the basis of all the experiments discussed in this thesis.

Dissolution DNP can make use of the cross effect, solid effect and thermal mixing mechanisms for polarization transfer. The Overhauser effect mechanism is a specialized case of the solid effect and is reserved for polarization in the liquid state or of metals. The Overhauser effect has demonstrated some interesting applications, including hyperpolarized water [48], as well as having made an extensive impact in NMR allowing 2D correlation spectroscopy, but is not applicable to the dissolution DNP technique used in this thesis. Both the Overhauser effect and the solid effect work by irradiating at the difference between electron (ω_e) and nuclear Larmor fre-

quencies (ω_n), to induce zero and double quantum transitions (which are normally forbidden for the solid effect, and thus the process requires large amounts of energy) to produce a population distribution which falls off at frequencies that differ from $\omega_e \pm \omega_n$, as shown by looking at the effect of microwave frequency against polarization (microwave sweep) (Figure 2.4).

In Figure 2.4, pane (a), the pure solid effect is seen, which reveals clear separation between the positive and negative phases. Unlike in the Overhauser effect, the paramagnetic electrons are static, the electron spin resonance (ESR) band is considerably narrower, and the greatest enhancement can be obtained by irradiating at $\omega_e \pm \omega_n$. Progressing further down the diagram in pane (b), a pseudo solid effect is seen, which occurs when nuclei with lower gyromagnetic ratios are used, or at lower magnetic fields [49]. Of note is the less efficient polarization, largely due to microwave irradiation driving transitions of opposing signs, resulting in a partial cancelling of polarization. As the concentration of the electrons is increased, the ω_e term becomes dominant, and so the microwave irradiation frequency can be approximated by $\omega = \omega_e \pm \omega_{e(1/2)}$ (where $\omega_{e(1/2)}$ is the electron paramagnetic resonance (EPR) linewidth of the electron source, in this case, a chemical molecule known as a radical). As a consequence, cross effect and thermal mixing mechanisms start to dominate (panes (c) and (d) respectively). Cross effect and thermal mixing are difficult to distinguish from each other, and even the comparison between thermal mixing and the pseudo-solid effect can be difficult to judge solely by looking at the microwave sweep. Both thermal mixing and the cross effect work on a three body system (two or more electrons and a nucleus). The transitions here, however, are no longer forbidden, and each double quantum transition is replaced with sequential, single allowed transitions. The ability to predict which of thermal mixing or cross effect will occur depends on the EPR spectrum of the radical being used; for a symmetric EPR lineshape, theory would predict thermal mixing being dominant, for an asymmetric EPR, the cross

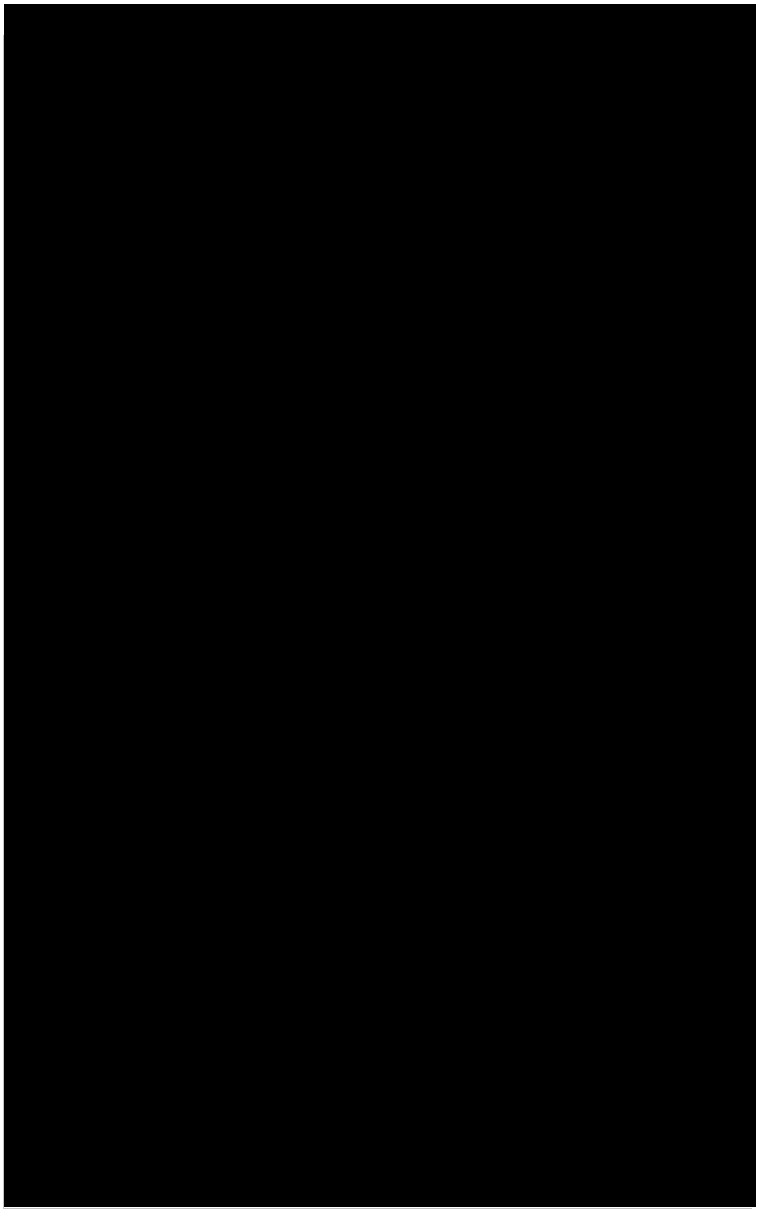


Figure 2.4: Pane (a) shows a well resolved solid effect, where the peaks are clearly separated. (b) shows a pseudo solid effect, where merging begins as a result of using low gyromagnetic ratio (γ) nuclei, or weak magnetic fields. Panes (c) and (d) show the cross effect and thermal effect respectively, which occur via non-forbidden spin transitions. Figure taken from [44].

effect is likely the dominant mechanism. The OX063 radical typically employed for dissolution DNP (and exclusively used in this thesis) induces polarization via thermal mixing, whilst certain biradical forms of the TEMPO radical have asymmetric EPR lineshapes and cause a cross effect mechanism to be employed.

2.2.2 Dissolution DNP

The equipment required to perform dissolution DNP for use with animals has been extensively described previously [50], and will be briefly described here to detail the two dissolution DNP systems used in this work, with particular focus on the way in which they integrate to their respective MRI / NMR systems to allow both *in vivo* and *ex vivo* experiments. The general experiment is as follows. A sample cup, containing a sample to be hyperpolarized is inserted into the polarizer, cooled to 1.4 K, and irradiated with microwave irradiation for about an hour. Once the sample is polarized (has undergone the DNP process, to achieve a high polarization), the dissolution process can begin. To provide a means of extracting the frozen, hyperpolarized sample from the centre of the cavity, melt it, and deliver it outside the system, a dissolution stick was created (Figure 2.5).

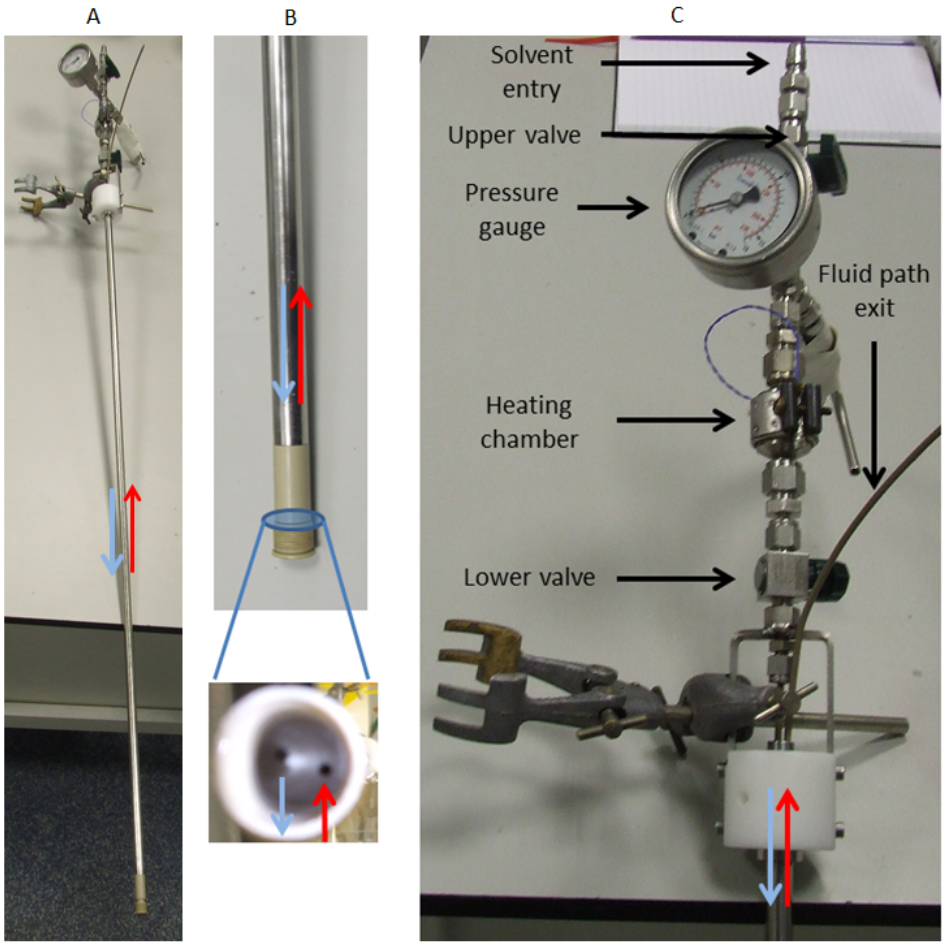


Figure 2.5: An image of the dissolution stick, used with the "alpha system" hyperpolarizer. The system is largely the same in the HyperSense hyperpolarizer, with the exception that the insertion of the dissolution stick is done mechanically, and the valves are all automatically controlled.

It is a long stick (pane A), with the upper portion, shown on the right (pane C), and the lower portion comprising of a tube, the end portion of which is shown on the left (pane B). With the lower valve closed, the cold solvent (usually a water based NaOH buffer) is injected into the top port, and is stored in the heating chamber. The air space is then pressurized with gaseous helium, and the upper valve closed. The heating process begins, and when a temperature of 160°C and a pressure of 10 bar are reached, the dissolution stick is rapidly inserted into the center of the polarizer magnet, where it docks with the sample cup containing the sample being polarized. With the sample cup attached, as in pane B of the figure, the lower valve is then

opened, to allow the hot solvent to proceed down the dissolution stick, along one of two fluid paths, as shown by the blue arrows. The solvent then enters the docked, hollow sample cup, containing the frozen hyperpolarized sample, melting the sample, before the hyperpolarized liquid proceeds up the second fluid path, marked by the red arrows, and out of the fluid path exit, to be injected *in vivo* or into an isolated perfused organ. The high polarization of the sample is retained in the liquid state at room temperature for a short period of time determined by sample T_1, following a decay curve as shown in Figure 2.6. The specific systems that have been used in this thesis to polarize samples will now be discussed.



Figure 2.6: This figure shows the nature of the decay of hyperpolarized samples, after they are ejected from the polarizer. The top pane shows a series of spectra, each representing about a second, taken over two minutes. The small peaks represent metabolites that result from the injection of hyperpolarized [1-^{13}C]pyruvate (largest peak) into a rat heart. The lower pane quantifies this, by showing the decay of hyperpolarized pyruvate, and its metabolites in the rat heart, lactate, alanine and bicarbonate over time. Image adapted from [51].

The primary system, the so called "alpha system", is a prototype dissolution DNP system (Figure 2.7) that is used mainly for *in vivo* work, and is coupled to a Varian INOVA spectrometer for monitoring the build up of the solid state polarization throughout the DNP process.



Figure 2.7: The prototype "alpha system", used for *in vivo* hyperpolarization experiments.

It is adjacent to a horizontal bore 7 T MRI system (Varian Inc, Oxford, UK) system, where injections of the hyperpolarized solutions generated are carried out into the animal, and spectroscopic monitoring occurs. The second system is a commercial "HyperSense" (Abingdon, Oxfordshire, UK) dissolution DNP system (Figure 2.8), based on the alpha system, where the dissolution process and other events involved in starting the hyperpolarization process have been largely automated.



Figure 2.8: The HyperSense, a largely automated version of the alpha system, used primarily for *ex vivo* work, such as that using the isolated perfused heart.

It is placed adjacent to a vertical bore 11.7 T MRI system (Bruker, Inc), and the setup is generally used for *ex vivo* metabolic experiments in perfused organ systems. Both systems are based on a magnet operating at 3.35 T, this magnetic field being specifically chosen because it causes nuclear and electronic Larmor frequencies to be such that polarization can be induced by a small, commercially available microwave source at approximately 94 GHz. Higher magnetic fields can be used, requiring higher microwave frequencies (up to 460 GHz as of 2011), but yielding higher polarizations [52–55]. The problem is that the microwave sources are considerably larger, and more technically involved to maintain and run. Nevertheless, current research is ongoing into the potential of these systems, particularly for samples without isotopi-

cally enriched nuclei (i.e. without ^{13}C labelling), such as proteins for example [56]. Within the polarizing magnet of both systems is an accessible bore (cavity), with a valve at the bottom to allow the entry of liquid helium from the outer to the inner cryostat. The cavity is fitted with an insert (Figure 2.9), which contains:

- A microwave guide: to guide microwaves from source to the sample cup
- An RF coil: to allow sample polarization monitoring
- Low temperature resistors: to determine the level of liquid helium, to ensure it covers the sample [57] (the HyperSense uses a capacitance measurement for this purpose)

The cavity is also linked to a vacuum pump, which pumps on the cavity to lower the pressure to less than 1 mbar ($<$ 3 mbar for the HyperSense), reducing the temperature inside to less than 1.4 K. The polarization achieved is inversely proportional to temperature [58], thus having larger pumps is beneficial to the system, but more costly.

2.2.3 Tracer requirements

The metabolic tracer, comprised of a low molecular weight metabolite, in order to ensure that the signal decay time (T_1) is not too short, is mixed with a radical to provide a source of electrons for the DNP process. The commercially available radical, OX063 (Oxford Instruments, Abingdon, UK) has been shown to provide the best polarization for dissolution DNP, in part because it has a narrow ESR linewidth in comparison to TEMPO. A small amount of a Gadolinium (Gd) based contrast agent is added, to facilitate coupling between the nuclear and electron spin systems. The



Figure 2.9: This figure shows a schematic representation of the alpha system, though the principles are applicable to the HyperSense. 1. the polarizer itself, 2. the vacuum pumps connected to the insert, 3. the insert, which contains the sample to be polarized, and where the dissolution stick is inserted to dissolve the sample, 4. the microwave source, 5. the pressure transducer, to measure the vacuum generated, 6. the microwave guide, which directs the radiation to the sample, 7. the container for the sample, 8. the outer guide for both sample insertion and the dissolution stick, 9. the sample cup, 10. the dissolution stick in the process of being inserted into the insert, to dissolve the sample. Figure taken from [50].

radical and Gd must dissolve in a solvent or solution, which can be the metabolite itself. In cases where the metabolite is a solid (or sometimes even when it is a liquid), a neutral solvent is required to achieve this solubility. In addition, this neutral solvent should allow the entire sample to form a glass (vitrify) upon freezing, which allows maximal transmission of microwave irradiation, necessary for the DNP hyperpolarization process. The formulation process required for specific molecules will be discussed in further detail in Chapter 5.

2.3 Metabolism

In order to provide a general background to the applications described in this thesis, particularly with regards to the development of suitable metabolic probes for use in dissolution DNP, a description of both the underlying physiology and metabolism will be provided below. The pathways described will discuss the origin of each of the metabolites investigated in this thesis, as well as their transformation, and the way in which they relate to the overall working of human biochemistry.

2.3.1 Digestion

The cephalic phase marks the beginning of digestion, the initial neural response to the thought, sight, smell and taste of food, which elicits the release of saliva, insulin stimulation [59], as well as gastric secretions via parasympathetic action. The bolus of food, after having been macerated and briefly acted upon by α-amylase, makes its way down the oesophagus into the stomach. It is further churned for several hours, and acted upon by hydrochloric acid, and various enzymes, including gastric lipase, to break down the fat components, and pepsin, which acts to decompose protein. Chyme, the mechanically, chemically and enzymatically processed food bolus, is secreted via the pyloric sphincter into the duodenum, where its acidity is neutralized by discharge from the common bile duct.

In the small intestine (both the duodenum and the jejunum), most carbohydrates, protein and fats will be broken down to allow absorption. The inner lining of the small intestine is made up of many villi, small protruding folds from the wall, each in turn coated with a brush border, the aim of both components being to increase the available surface area for absorption by several orders of magnitude.

Carbohydrates are broken down by the amylase family of enzymes, where the small

units produced, such as glucose, are then taken up into the blood stream via active transport using the sodium – glucose linked transporters (SGLT-1) [60]. The purpose of this active transport, which requires energy, instead of a passive transport system such as the GLUT family of glucose transporting enzymes, is that complete carbohydrate extraction from the gut into the blood stream is required and a system which relies on passive transport will only ever take up carbohydrates such that the concentration of the blood stream glucose is equal to that of the gut. The blood stream supplying the gut now makes its way to the portal vein, usually at a concentration of glucose many times higher than that of the systemic circulation.

Proteins, having been previously denatured by the acid in the stomach, are now further broken down by trypsin, and several other enzymes each designed to target a different functional group within the protein in order to obtain either the free amino acid, or di and tri peptides (though amino acids are typically found in much higher concentrations within di and tri-peptides, rather than in the free form [61]). Uptake of these amino acids is broken up into several transporter families, which very broadly speaking, can be characterized into small, neutral amino acid transport (system A), those which are basic or acidic (system B) and those that have branched chains or large aliphatic or aromatic side chains (system L). System A is responsible for transporting serine, glycine and **alanine** (a metabolic probe discussed in Chapter 5). It is worth noting that these transporters do not appear to be particularly specific, and there is a large amount of overlap.

Fats are emulsified in the gut with the aid of bile salts, and enzymes secreted by the gall bladder and pancreas via the common bile duct. Pancreatic lipase (lipoprotein lipase, LPL) breaks down fat bound to glycerol backbones into the free constituents, and emulsification is done to a small enough size so as to enable fats to cross the intestinal membrane via various different mechanisms. One such system is the FAT / CD36 transport system, found in varying concentrations along different segments

of the gut [62], and allowing for the uptake of long chain fatty acids (LCFA) into the blood stream. There is uncertainty however over the extent to which fat transport is facilitated [63] or passive [64]. The longer chain fatty acids are packaged into protein based chylomicrons, which feed into the lacteal system, bypassing the portal vein (where most nutrients would first be expected to pass) and into the major branches of the circulatory system above the heart. Short chain fatty acids (SCFA) are not packaged in this way; they are instead released into the blood stream as non-esterified fatty acids (NEFA) bound to albumin, which then progress into the portal vein blood stream, and on into the liver. **Butyrate**, one of the metabolic probes formulated in this thesis, is only present in small quantities via this method, a major source is discussed below. Fats of special importance such as cholesterol and plant sterols, have their own transporters regulated in different ways [65].

The remaining material, after absorption of the bulk of nutrients make their way into the large intestine (the ileum), and it is here that butyrate is produced in significant quantities by intestinal microflora [66]. Any material for fermentation by these microflora would have to be substances that were not digested or absorbed at an earlier stage in the gut, and therefore mostly comprise insoluble plant matter. In addition to butyrate, other SCFAs are produced, namely propionate and acetate. These SCFAs have an important role in the health of the gut, and butyrate in particular is the primary fuel source of the colonocytes [67]. Butyrate, in addition, has many other roles and effects in these cells, as well as being a fuel substrate [68]. The remaining butyrate (after being taken up by colonocytes [69]) and SCFAs pass through the portal vein into the liver, where the majority is metabolized via the end stage of the β-oxidation pathway. Small quantities of butyrate pass through into the peripheral circulation [70], where it can be metabolized by various tissues in the body, including the heart [71].

The metabolism of the three major nutrient groups will now be discussed generally,

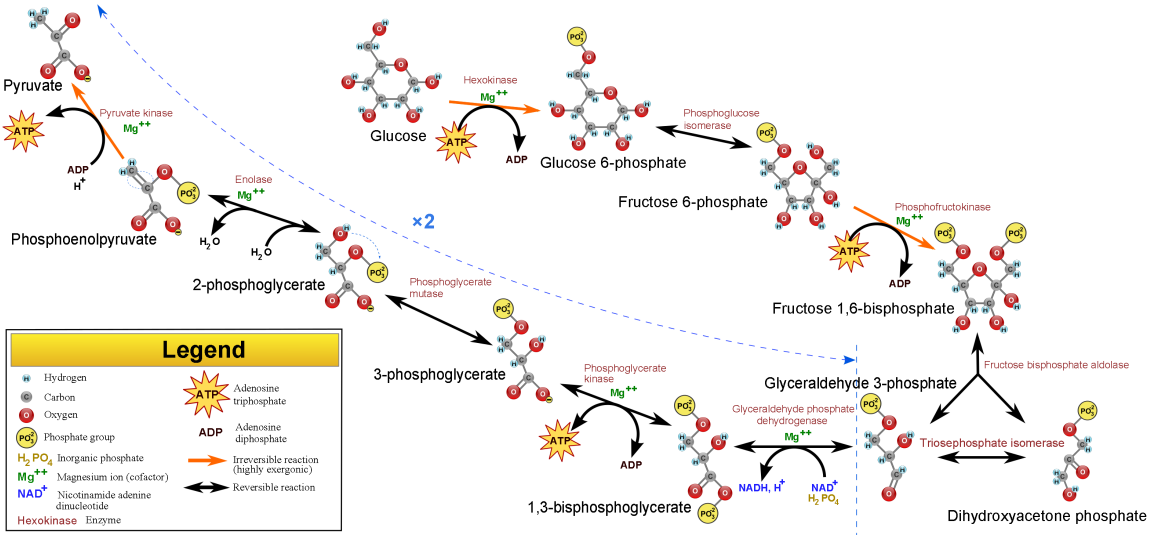


Figure 2.10: The pathway of glycolysis, with the key end product, pyruvate. Image courtesy of the Wikimedia Commons.

as it broadly applies to all tissues. Where there are differences, these will be specified and limited to the hepatic and cardiac systems.

2.3.2 Carbohydrates

Glucose, as the principle carbohydrate, will be the focus of this discussion. It is taken up in the liver in a concentration dependant manner via GLUT 2, and in the heart principally via GLUT 1 and the insulin mediated GLUT 4. From here, it is phosphorylated either by hexokinase (heart) or glucokinase (liver), the difference between each enzyme reflecting the function of the liver as a glucose buffer, and the heart as a regulated consumer. Within the cytosol, it proceeds via various different intermediates within the glycolytic pathway generating ATP and NADH, before arriving at the first of the relevant endpoints, **pyruvate** (a probe discussed later) (Figure 2.10). In the heart, the fate of pyruvate will depend on the metabolic status of the heart, namely whether it is working aerobically or anaerobically. In anaerobic conditions, the predominant pathway is conversion of pyruvate to **lactate** via the lac-

tate dehydrogenase (LDH) enzyme, which exists as a tetramer, made up of different ratios of the m-form (muscle) and the h-form (heart). The purpose of this lactate production is the oxidization of NADH in order to regenerate NAD^+, to allow the glycolytic pathway to continue. The lactate produced is either exported to the liver as part of the Cori cycle for gluconeogenesis, or it can be later oxidized by the heart as a fuel under different conditions. Pyruvate metabolism can also proceed via the alanine transaminase enzyme (ALT) to produce **alanine**, which is then exported to the liver for gluconeogenesis [72] or used for energy generation and protein synthesis. Two main isoforms of ALT exist [73], and each isoform predominantly favors either the formation of pyruvate for gluconeogenesis in the liver, or the formation of alanine for amino acid synthesis for example.

Aerobically, pryuvate is transported into the mitochondria from the cytosol using the mitochondrial pyruvate transporter (MPT). The main pathway from here is the oxidative decarboxylation of pyruvate via the pyruvate dehydrogenase (PDH) enzyme, to CO_2 (which is then subsequently converted into bicarbonate by the carbonic anhydrase enzyme) and acetyl CoA. Acetyl CoA then proceeds via the TCA cycle (Figure 2.11) and electron transport chain (ETC) (Figure 2.13) as described below.

The pathway for pyruvate metabolism in the liver is slightly different; the focus here is on generating precursor materials for biosynthesis. While there is some flux through PDH, the majority of pyruvate metabolism occurs via pyruvate carboxylase, which produces oxaloacetate (OAA) which then proceeds via the TCA cycle to produce various intermediates, including citrate, malate and others shown in Figure 2.11. PDH is indirectly regulated by many factors including PDH kinase (PDK), which phosphorylates and inactivates PDH, and PDH phosphatase (PDP), which dephosphorylates and activates PDH. PDK expression and activity is upregulated by acetyl CoA levels, produced as a result of fatty acid oxidation (FAO), amino acid metabolism, and pyruvate oxidation, and generally signals an abundance of fuel, and therefore a signal

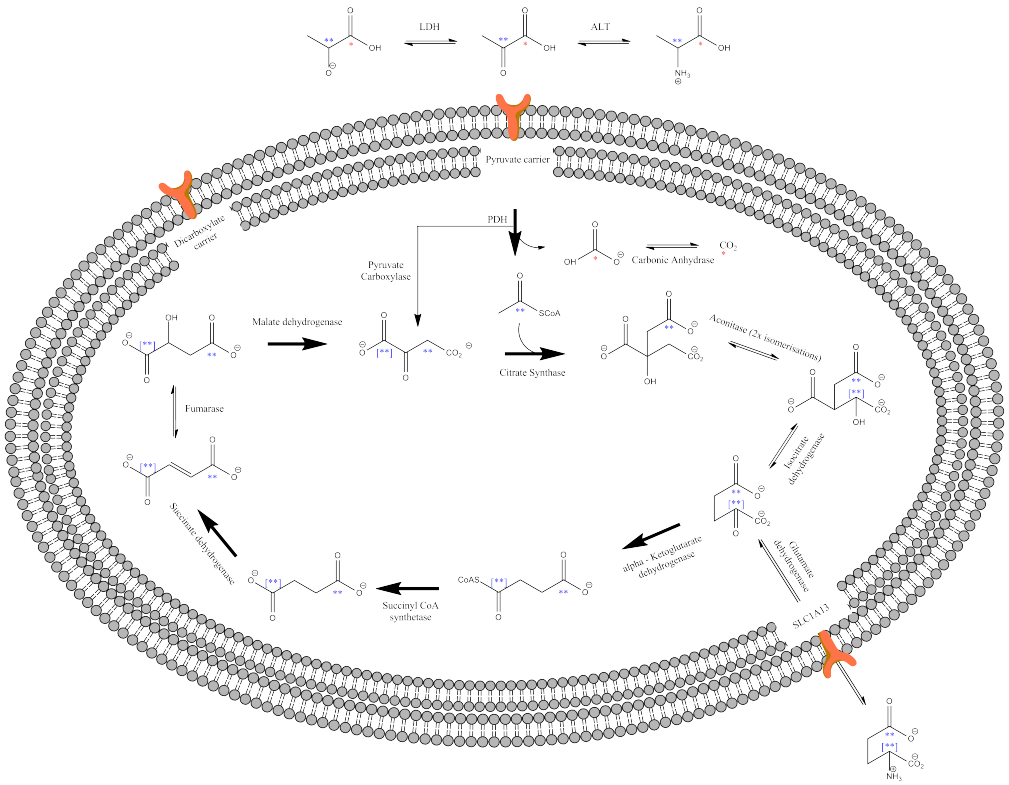


Figure 2.11: A figure depicting cytosolic and mitochondrial metabolism. * indicates the ^{13}C label incorporation if 1-[^{13}C]pyruvate is used as a DNP tracer, ** indicates label incorporation if 2-[^{13}C]pyruvate is used. These are provided as examples of common DNP probes used, and to highlight the relevance of the metabolic understanding needed in designing suitable tracers.

to stop the wastage of glucose. The glucose can then be shuttled into glycogen or fat storage mechanisms. Downregulation of the PDK mediated phosphorylation mechanism occurs in the presence of excess pyruvate. PDK has 4 main isoenzymes [74, 75], with the PDK1, 2, and 4 isoforms being substancially expressed in heart and PDK2 being predominant in the liver. PDP is upregulated by Ca^{2+} (produced by hormonal signaling pathways, as well as local muscle contraction). In liver, it is also upregulated by insulin, which signals high circulating glucose concentrations, and therefore a need to store any excess pyruvate via the fatty acid synthesis pathway.

2.3.3 Fats

Only SCFAs will be considered here as these are most relevant for hyperpolarized work (the reasons for this are discussed in Chapter 5). Fatty acids bound to albumin are released and taken up into the heart and liver, where acetyl CoA is produced via the cyclic process of β-oxidation (fatty acid oxidation). SCFAs enter toward the end of this cyclic process, where they are fully metabolized (Figure 2.12). The end result is two molecules of acetyl CoA which may now enter several different pathways. The two most relevant are the TCA cycle (described below) via condensation with oxaloacetate to produce citrate, or the synthesis of ketone bodies (liver only). In ketone body synthesis, two molecules of acetyl CoA condense to eventually form acetoacetate, the production of which is in part regulated by the intermediary enzyme HMG CoA synthase, almost exclusively found in the liver [76]. Acetoacetate may now spontaneously decarboxylate to acetone, losing CO_2 in the process, making this an irreversible reaction. It can also be exported as is, or converted to β-hydroxy butyrate (3-BHB) in an NADH concentration dependent manner, whereby it can also be exported. The ratio of acetoacetate and 3-BHB therefore gives an indication of the NAD^+ / NADH ratio inside the mitochondrion. However, whilst the liver can produce ketone bodies, it is unable to oxidize them as a metabolic fuel, due to the lack

of the 3-ketoacyl CoA transferase enzyme required to activate acetoacetate. Previous literature [71], and indeed work in this thesis, has shown that the heart actually can produce ketone bodies via the oxidation of butyrate. However, this discrepancy can be explained by the unique structure of butyrate, and the fact that its conversion does not simply follow the FAO, or indeed the ketogenic pathway.

Butyrate is first activated to produce butyryl CoA (a butyrate CoA ester), which is then converted into crotonyl CoA via a dehydrogenase enzyme, to produce a double bond. The purpose of this reaction is to then allow subsequent nucleophilic addition of water to produce an activated 3-BHB-CoA intermediate, which marks the first similarity to the ketone bodies. Where ordinarily in the liver, this product might be metabolised via the HMG CoA synthase enzyme, in other tissues, it can be directly oxidized via acetoacetyl CoA thiolase (ACAT1) to produce acetyl CoA, which then proceeds into the TCA cycle. It can in addition, re-equilibrate with acetoacetate in an NADH coupled manner, first via conversion of acetoacetyl-CoA to acetoacetate via the SCOT1 enzyme, and then via BDH1 (β-hydroxybutyrate dehydrogenase-1) to give 3-BHB (Figure 2.12).

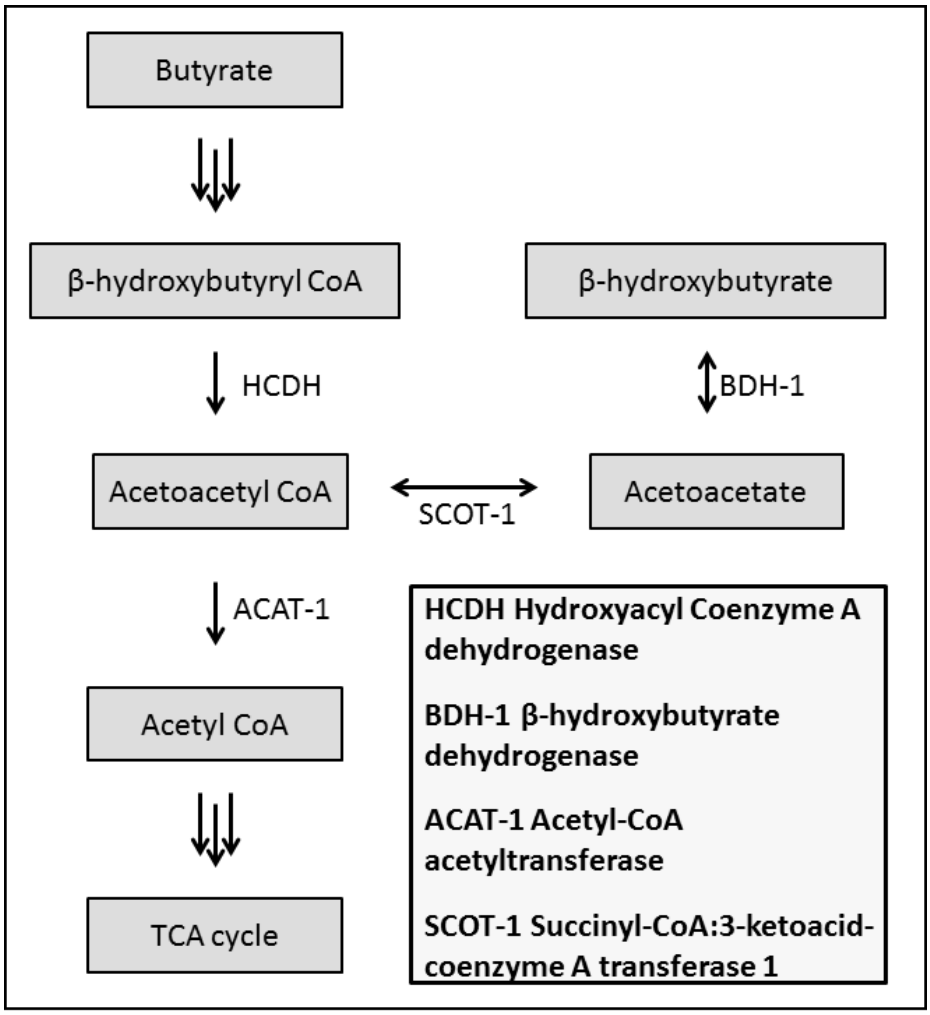


Figure 2.12: The metabolism of butyrate, via the key ketone body enzymes.

2.3.4 Amino acids

Using alanine as a primary focus, its metabolic fate depends on the tissue under study. In liver, its main purpose is to be used as a substrate for gluconeogenesis. This occurs via ALT mediated conversion to pyruvate, which is then converted to OAA via the pyruvate carboxylase enzyme. This allows conversion to malate, which has a transporter available to cross the mitochondrial membrane into the cytosol, where glucose production occurs. Where alanine is oxidized, e.g. in the heart, it again does so using ALT, to produce pyruvate, where it is then decarboxylated producing acetyl CoA and CO_2.

2.3.5 TCA cycle and the ETC

The resultant products of the metabolites described above usually enter the TCA cycle (Figure 2.11), a linked series of chemical reactions, whose overall purpose is to generate reducing potential in the form of NADH and $FADH_2$ to feed into the ETC. The TCA cycle, however, can also provide precursors for other products, such as amino acids, fatty acids and glucose synthesis. The ETC (Figure 2.13) is made up of four complexes, each of which are intricately linked to generate a proton gradient across the inner mitochondrial membrane. The end result is the reduction of oxygen to water, and a driving force for oxidative phosphorylation via ATP (adenosine triphosphate) synthase, to produce ATP from ADP (adenosine diphosphate) and Pi (inorganic phosphate) which can then be used as a direct energy source. Oxidative phosphorylation requires aerobic conditions, however, in anaerobic conditions during a sudden demand for energy, creatine kinase may phosphorylate ADP anaerobically from a pool of phosphocreatine (PCr). These substrates form the basis of the energetic measurements used in this thesis.

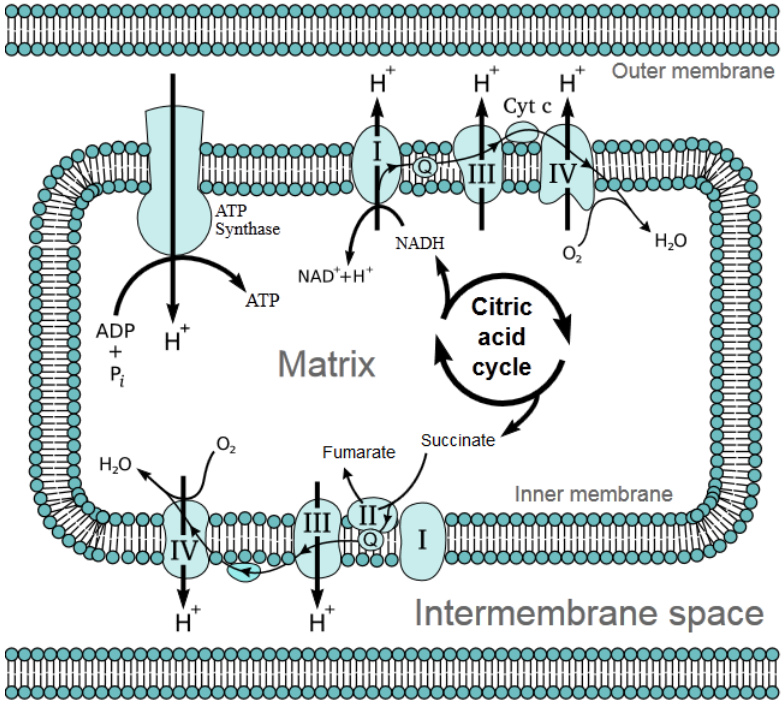


Figure 2.13: A diagram of the electron transport chain (ETC), showing the four major electron transport complexes, which power the ATP synthase enzyme to produce ATP.

Chapter 3

Metabolic Imaging

3.1 Introduction

With the recent advances in the MR sensitivity of the ^{13}C nucleus using Dynamic Nuclear Polarization (DNP) [47], it is now possible to complement structural data using MRI with global metabolic information in the myocardium [77–79]. In addition, work with several *in vivo* animal models has combined DNP with different imaging techniques [80–82], including Chemical Shift Imaging (CSI) [83], to obtain metabolic maps of the heart using hyperpolarized [1-^{13}C]pyruvate [84–86]. However, these studies have focussed on large animals (i.e. pigs) and, to date, there have been only limited studies performed in the *in vivo* rat heart [81]. This is primarily due to the small size and high heart rate of the rat heart [87]. There have also been no metabolic images generated of the perfused rodent heart, despite the wide range of rodent models of heart disease available for study [78, 88, 89].

The isolated perfused rat heart [90] is ideal for the assessment of both physiological and pathological metabolism. It can be studied independent of hormonal and neuronal influences present *in vivo*, making causal changes in disease easier to determine. In addition, as the isolated perfused rat heart is devoid of surrounding tissues,

metabolite signal contaminations from adjacent tissues such as the liver and chest wall are removed. Also, rapid metabolic changes can be assessed after cardiac ischemic interventions more quickly than is possible with *in vivo* models [77]. Higher signal-to-noise ratios (SNR) and improved signal homogeneity can be obtained due to the use of RF coils with a birdcage design, which allow closer placement of the RF coil to the heart. Better spectral separation and narrower linewidths are also possible due to the higher field strengths and narrower bore magnets generally used with the isolated perfused rat heart.

The aim of the work described in this chapter was therefore to develop a combined DNP and CSI protocol for application in the isolated perfused rat heart to generate metabolic images of hyperpolarized [1-^{13}C]pyruvate and its downstream metabolites. As shown in Figure 2.11, following infusion, [1-^{13}C]pyruvate is converted into [1-^{13}C]lactate, via lactate dehydrogenase, [1-^{13}C]alanine, via alanine transaminase and [^{13}C]bicarbonate, via pyruvate dehydrogenase [51]. It should therefore be possible to generate maps of these metabolites in the isolated perfused rat heart and to use the metabolic images of [1-^{13}C]pyruvate as a marker of tissue perfusion, [1-^{13}C]lactate as a marker of anaerobic metabolism and [^{13}C]bicarbonate as a marker of aerobic metabolism.

To demonstrate the utility of the developed DNP-CSI protocol, two different models of myocardial infarction were studied. An acute model, where imaging was performed immediately before and following *ex vivo* occlusion of the left anterior descending (LAD) coronary artery, and a chronic model, where LAD occlusion was performed *in vivo* and the heart perfused and imaged four weeks later. To date, the only known hyperpolarized study of an ischemic model has been performed in pigs [91], and while this study revealed changes in bicarbonate metabolism, it was not easy to separate the effect of the nutritional state of the animal from the effects of ischemia on bicarbonate production [51]. Studying the heart in isolation avoids this problem, and

will allow more confident assessment of metabolic changes. In all infarcted hearts, DNP-CSI data was used to generate cross-sectional maps of pyruvate, lactate and bicarbonate, which were compared to those from control perfused hearts. In addition, MR images acquired during the first passage of a gadolinium contrast agent were used to assess myocardial perfusion, and phosphorus-31 (^{31}P) magnetic resonance spectroscopy was used to examine myocardial energetics. Histological assessment was performed following imaging in the chronically infarcted hearts to confirm the presence of scar in the region of infarction.

3.2 Materials and methods

The [1-^{13}C]pyruvic acid and all unlabelled compounds were obtained from Sigma Aldrich (Gillingham, UK) and the trityl radical, OX063, was obtained from Oxford Instruments (Abingdon, UK). All investigations conformed to Home Office Guidance on the Operation of the Animals (Scientific Procedures) Act, 1986 (HMSO) and to institutional guidelines.

Software and equipment: For all studies, a vertical 11.7 T wide-bore MR imaging system (Magnex, Oxfordshire, UK) was used in combination with a Bruker Avance console (Bruker Medical, Ettlingen, Germany) running Paravision 2.1.1 and XWin-NMR 2.6. Protocols using ^{13}C nuclei were acquired with a single channel, home built, 20 mm birdcage volume RF coil. Those using ^{1}H or ^{31}P nuclei were acquired using a 20 mm, dual channel, RF probe (Rapid Biomedical GmbH, Germany). Spectra and images were processed using jMRUI 2.2, Matlab 2011b (Mathworks, MA, USA) and ImageJ (W. Rasband, NIH, USA) as detailed below.

Perfusion protocol: Male Wistar rats were anaesthetized with a 1.3 ml / kg intraperitoneal injection of pentobarbital sodium (200 mg / ml Euthatal), and after loss of pedal reflexes, a thoracotomy was performed and the heart excised and placed into ice-cold Krebs Henseleit (KH) buffer. The aorta was then cannulated and the

heart perfused in the Langendorff mode initially under 65 mmHg perfusion pressure and maintained at 37 °C. A drain was inserted into the left ventricle (to alleviate intraventricular pressure from Thebesian flow) along with a polyethylene balloon to measure heart rate and contractile function. The rate pressure product (RPP) was used as an index of cardiac function derived from the multiplication of the heart rate (HR) and the developed pressure (DP). A 20 mm NMR tube was placed over the heart and inserted into the bore of the 11.7 T magnet, whereby the heart was then subjected to 85 mmHg perfusion pressure. After a 5 minute stabilization period, a constant flow pump was set to deliver KH buffer at a flow rate of 15 ml / min. The KH buffer contained 118 mM NaCl, 4.7 mM KCl, 1.2 mM $MgSO_4.7H_2O$, 1.75 mM $CaCl_2.2H_2O$, 0.5 mM Na_2EDTA, 11 mM glucose, 25 mM $NaHCO_3$ and 2.5 mM sodium pyruvate.

Hyperpolarized sample preparation and dissolution: Aliquots (30 µl) of [1-^{13}C]pyruvic acid were mixed with the trityl radical (OX063, 15 mM), 3 µl of 0.1 M solution of Dotarem (Guerbet, France) and placed in a HyperSense hyperpolarizer [77] (Oxford Instruments, Abingdon, UK). The samples were polarized at 94.128 GHz for one hour and, following polarization, the frozen [1-^{13}C]pyruvic acid was dissolved with 6 ml of hot NaOH (60 mM)/EDTA (0.2 mM)/Tris buffer (40 mM) to neutralise the pH. Following dissolution, the hyperpolarized sodium pyruvate solution was added to 178 ml of Krebs-Henseleit buffer (without pyruvate) to yield a 2.5 mM hyperpolarized sodium [1-^{13}C]pyruvate solution. This solution was then delivered to the heart as a bolus over 120 seconds, and the CSI protocol (detailed below) applied.

Parameter optimization: Prior to commencement of the myocardial infarction studies, a B_1 field map was constructed using the ^{13}C RF coil to ensure that the sensitive region of the coil was homogenous. To ascertain the ideal flow rate to the heart the maximum hyperpolarized [1-^{13}C]pyruvate signal amplitude was investigated using a simple pulse-acquire acquisition at flow rates of 5, 10, 15 and 20 mls / min. Follow-

ing this, several parameters relevant to the CSI acquisition protocol were optimized. The effect of variation in the acquisition flip angle (n = 3; 22.5°, 45°, 67.5° and 90°) and repetition time (TR; n = 3; 200, 400, 600, 800, 1000 and 1200 ms) on the maximum signal amplitude of [1-^{13}C]pyruvate, [1-^{13}C]lactate and [^{13}C]bicarbonate were then investigated. These acquisitions were performed using the CSI protocol but with the gradient amplitudes set to zero, thus allowing the temporal variation in signal amplitude to be explored.

Infarct studies: Two groups of isolated hearts were investigated, one in which hearts were isolated and a myocardial infarction induced during perfusion (n = 9) to investigate acute metabolic changes, and a second group that was surgically infarcted *in vivo* (n = 4) then isolated and perfused 4 weeks after infarction to investigate chronic metabolic changes. For the acute study group, hearts from healthy male Wistar rats (BW ~ 300 g) were assessed as described below. These same hearts were then infarcted by occlusion of the LAD and the assessment repeated. All hearts recovered contractile function. To generate the *in vivo* infarcts, animals were anaesthetized with isoflurane, intubated and connected to a ventilator (Harvard Apparatus, MA, USA). A lateral incision was made along the sternum, and clamps inserted between the 3rd and 4th intercostal space on the left side of the rib cage to reveal the heart. The LAD coronary artery was identified and ligated to create a myocardial infarction. Dr Carolyn Carr from the Cardiac Metabolism Research Group at the University of Oxford kindly performed all *in vivo* myocardial infarction surgery. The rats were then left for 4 weeks and, on the day before metabolic assessment, *in vivo* CINE MRI scans [87] were performed on the rats to characterize the severity of the infarct (slice thickness = 1.5 mm, slices = 10, matrix size = 256 x 256, ECG triggered and respiratory gated). For metabolic assessment, the hearts were subsequently excised, perfused in the Langendorff mode, and subjected to the assessment protocol described below.

Assessment protocol: An initial localizer scan was performed to ensure that the heart was placed within the most sensitive region of the RF coil and shimming performed to give a proton linewidth of approximately 50 Hz. A high-resolution axial scan (TR = 100 ms, TE = 1.28 ms, slice thickness = 1 mm, FOV = 24 x 24 mm, matrix = 128 x 128, averages = 8) allowed orientation of the heart with subsequently acquired data. Following polarization and dissolution, the hyperpolarized [1-^{13}C]pyruvate solution was infused into the heart and a CSI acquisition performed. The CSI protocol consisted of an in-house developed elliptical CSI acquisition with parameters: TR = 0.5 s, FA = 45°, slice thickness = 5 mm, FOV = 24 x 24 mm, matrix = 8 x 8, averages = 2, lasting approximately 30 seconds. This provided a metabolic distribution map of [1-^{13}C]pyruvate and its metabolites, lactate and bicarbonate. Subsequently, a first-pass gadolinium contrast agent scan was performed to quantify the degree of myocardial perfusion and, where relevant, to confirm the presence and location of the infarcted region. The gadolinium protocol, derived from previous work [88], comprised a fast gradient echo (FGRE) sequence to acquire an image every 128 ms with an in-plane spatial resolution of 78 µm (TR = 2 ms, slice thickness = 1 mm, FOV = 20 x 20 mm). Six seconds after the start of this sequence, 25 µl of Gadoteric acid DTPA complex (0.5 mM Omniscan, GE Healthcare) was administered via a prefilled drug line. A total of 128 images were acquired giving a total imaging time of 22 seconds. Following this scan, global cardiac energetic status was measured using a fully relaxed ^{31}P spectrum (TR = 15 s, flip angle 90°, 40 averages, bandwidth = 49.39 ppm, number of points = 2048). Upon completion of all acquisitions, chronically infarcted hearts were frozen in a water based glycol mixture (OCT) for later histological analysis to determine the extent of cell necrosis. Slices were stained with Hematoxylin and Eosin (H&E), as well as Picrosirius Red [92, 93].

Data analysis: The high-resolution axial slice was used for heart orientation when analyzing gadolinium and CSI data. For both sets of data, four square regions of

interest were created, one over the infarct region, two in the peri infarct zones, and one in the remote inferior region of the left ventricle. The two peri-infarct zones were averaged for analysis. An outline of the heart from the epicardial border of the high resolution axial proton scan was overlaid onto the gadolinium and CSI images to further aid orientation. The larger circular dashed segment of this outline corresponds to the left ventricle, the smaller crescent shaped segment is the right ventricle.

The data acquired using the CSI protocol were zero filled to match the resolution of the proton images and Fourier transformed using software written in-house in Matlab R2011b (Mathworks, MA, USA). Following Fourier transformation, the frequencies of the pyruvate, lactate and bicarbonate resonances were selected and the area under each resonance calculated on a pixel-by-pixel basis to allow the generation of metabolic images. The mean signal intensity within the four selected regions of interest was then calculated for each metabolic image. The gadolinium contrast agent scans were initially processed in ImageJ (W. Rasband, NIH, USA) where the mean signal intensity in the four regions of interest was recorded for each of the 128 frames of the acquisition. The time-course data produced was subsequently fit to a sigmoidal function to allow calculation of the signal increase observed upon addition of gadolinium.

Statistical analysis: Data are reported as mean±SEM and all statistical analysis was performed using GraphPad Prism (Graphpad, CA, USA). Statistical significance between the pre-occlusion and post-occlusion data for each selected region of interest in the acute infarct model was assessed using a paired Student's t-test. Statistical significance between the different regions of interest in the chronic infarct model was performed using a one-way ANOVA and a post-hoc Bonferroni multiple comparison test. Statistical significance was considered at the $p<0.05$ level.

3.3 Results

3.3.1 CSI protocol optimization

Variation of the buffer flow rate (Figure 3.1 , Panel A) showed that a higher flow rate led to earlier arrival of the hyperpolarized [1-^{13}C]pyruvate at the heart, resulting in a higher pyruvate signal amplitude due to the shorter hyperpolarization decay time. Based on these results, and previous measurements of flow in the Langendorff perfused heart, a flow rate of 15 mls / min was chosen as a suitable compromise between enhanced signal and an appropriate workload for the isolated perfused heart. Variation of the applied flip angle (Figure 3.1, Panel B) demonstrated no significant relationship between pyruvate, bicarbonate or lactate signal amplitudes and the applied flip angle. There did appear to be a trend toward higher hyperpolarized pyruvate signal amplitude and lower metabolite signal amplitudes with increasing flip angle. This may be expected, as higher flip angles would lead to increased signal intensity from the in-flowing pyruvate but would destroy the enhanced polarization therefore limiting the signal from downstream metabolites. As a result, 45^{o} was chosen as the flip angle for this study, providing the best compromise between pyruvate and metabolite signal intensities. A range of repetition time (TR) values between 200 and 1200 ms were subsequently investigated (Figure 3.1, Panel C) and a significant increase in both pyruvate and downstream metabolite maximum signal intensities was observed at longer repitition times. Again, this would be expected, as an increased TR would allow more time for in-flow of new hyperpolarized pyruvate and subsequent conversion into lactate and bicarbonate. However, increased repetition times also lead to an increase in the total CSI imaging time and therefore increased decay of the hyperpolarized signal in the later stages of the image acquisition. As a result, a repetition time of 500 ms was chosen to maintain imaging times at approximately one minute whilst allowing the acquisition of two signal averages and an 8 x 8 acquisition ma-

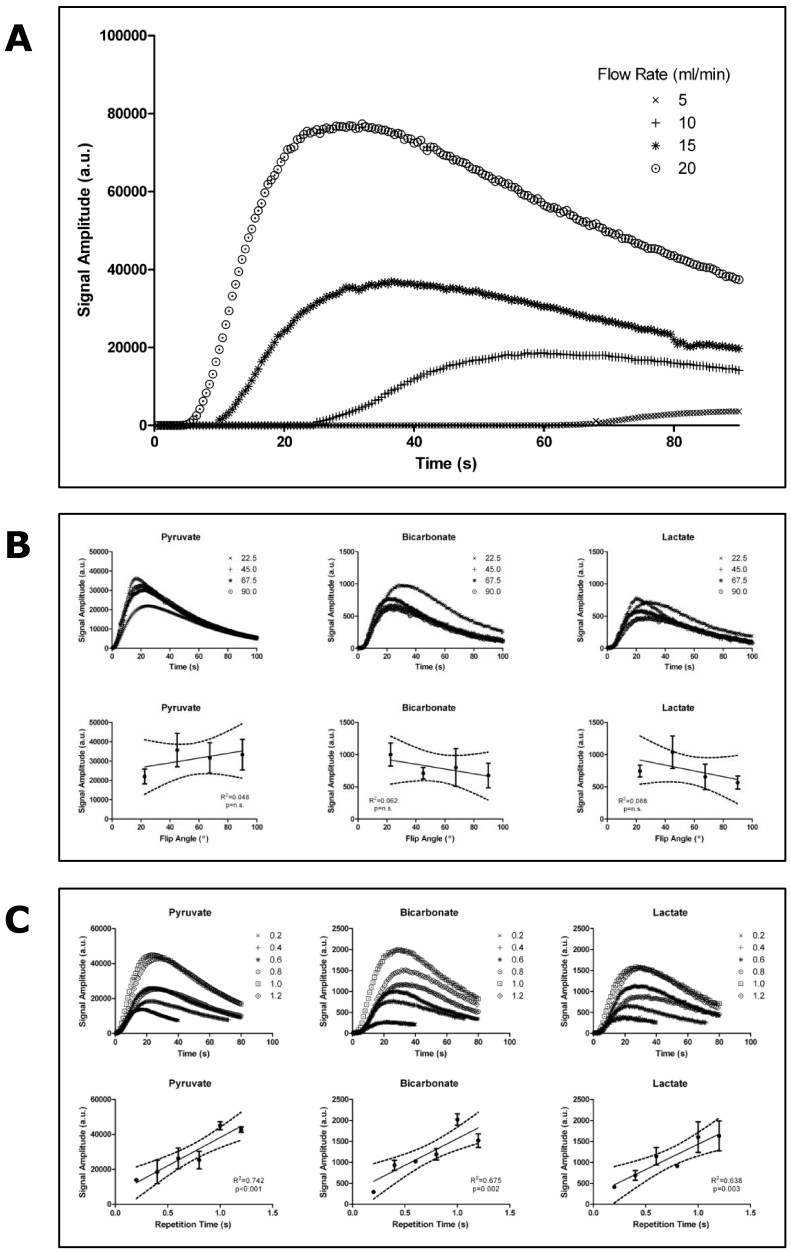


Figure 3.1: Panel A shows the variation in signal amplitude of hyperpolarized [1-^{13}C]pyruvate with respect to flow rate from the cannula into the perfused heart. There is a direct correlation between flow rate and maximum signal amplitude. Panel B shows the variation in signal amplitude with respect to flip angle for both pyruvate and its metabolites. No significant correlation was observed and a flip angle of 45° was chosen given the trend for increasing pyruvate and decreasing metabolite signals. Panel C demonstrates the correlation between TR and signal amplitude for each of the metabolite signals, as expected a positive correlation was obtained in each case.

trix, thereby maintaining relatively high signal amplitudes from the hyperpolarized pyruvate and its metabolites.

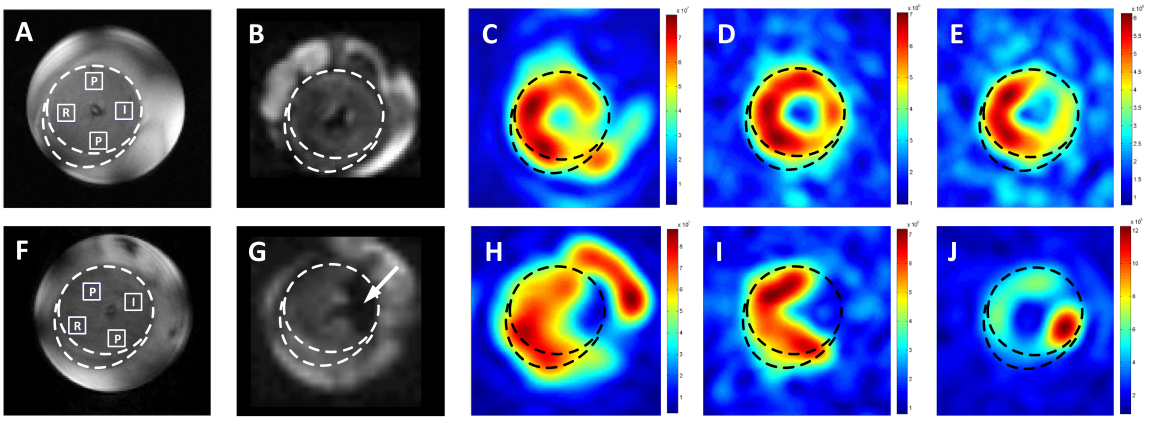


Figure 3.2: Example gadolinium contrast perfusion and DNP-CSI images from the acute infarct model. Panels A-E shown the images acquired before occlusion of the LAD and Panels F-J shows the images acquired immediately after LAD occlusion. Panels A/F detail high resolution axial scans used to allow better correlation between the gadolinium contrast perfusion and DNP-CSI scans. The 4 boxes shown represent the infarcted (I), peri-infarcted (P) and remote (R) regions of interest used for subsequent data analysis. Panels B/G show the final frame of the gadolinium contrast agent scans, with the white arrow indicating an area of decreased perfusion following infarct. The large circular segment in dashed lines is the left ventricle, the crescent shaped segment is the right ventricle. Example metabolite images for pyruvate (Panels C/H), bicarbonate (Panels D/I) and lactate (Panels E/J) are also shown.

3.3.2 Acute infarct model

Figure 3.2 shows example images acquired before (Panels A-E) and after (Panels F-J) occlusion of the LAD in the Langendorff perfused rat heart. Panels A and F represent the high-resolution axial images and demonstrate the regions of interest selected as infarct (I), peri-infarct (P) and remote (R) tissue for subsequent analysis. Panels B and G show single timeframe acquisitions from the end of the gadolinium contrast agent scans. There is a clear area of low signal intensity in the region of the heart supplied by the occluded LAD, as shown by the white arrow. Panels C-E and H-J

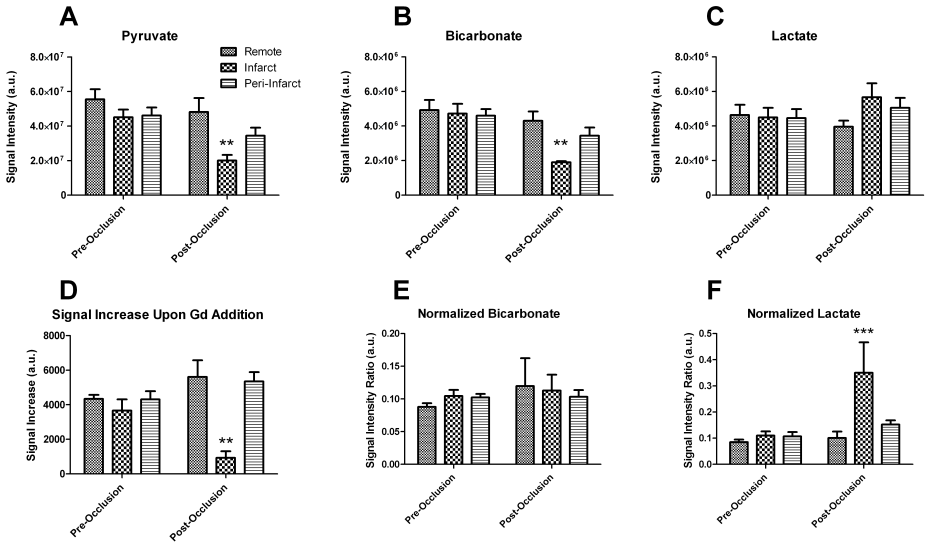


Figure 3.3: Quantitative analysis of the metabolic images and gadolinium contrast agent scans generated in the acute infarct model. Panels A-C show the mean signal intensities of pyruvate, bicarbonate and lactate respectively in the remote, infarct and peri-infarct regions before and after occlusion of the LAD. Panel D shows the signal increase observed upon addition of the gadolinium contrast agent, whilst panels E and F show the normalized bicarbonate and lactate signal intensities respectively in the same regions. (** $p<0.01$, *** $p<0.001$)

show metabolite maps of pyruvate, bicarbonate and lactate from before and after the LAD occlusion respectively. In the images generated before the LAD occlusion, there is a reasonable level of signal homogeneity around the circumference of the left ventricle, although there is a slight elevation in signal intensity in the septal wall, potentially caused by contamination from the right ventricular cavity/myocardium. In the post occlusion images, there is a clear area of reduced signal in the pyruvate and bicarbonate images, which corresponds to the infarct area, as demonstrated by the low signal intensity in the gadolinium contrast image. Conversely, the post occlusion lactate image shows an elevated signal intensity, which correlates with the infarct area. Quantitative analysis of the gadolinium and CSI images for all hearts is shown in Figure 3.3. A significant reduction in pyruvate signal intensity in the infarct region was observed (Panel A) which corresponded with a significant reduc-

tion in gadolinium induced signal increase (Panel D), indicating a reduction in buffer perfusion to the infarct region. No difference in perfusion to the peri-infarct or remote regions was observed in either the pyruvate images or the gadolinium contrast agent scans. A significant reduction in bicarbonate signal intensity (Panel B) was observed in the infarct region but not in the peri-infarct or remote regions. To account for the reduced perfusion of the hyperpolarized pyruvate to the infarct region, the bicarbonate signal intensity was normalized to that of the pyruvate. No significant change in the normalised bicarbonate signal was seen in any region, before or after occlusion of the LAD (Panel E). No significant differences in the lactate signal intensity were observed for any region of interest, before and after occlusion. However, following normalization to the pyruvate signal intensity to account for the reduced perfusion to the infarct region, a significant increase in lactate signal intensity was observed in the infarct region (Panel F). To provide an index of the relative balance between anaerobic and aerobic metabolism within the different regions, Figure 3.4 shows the ratio of the lactate to bicarbonate signal intensities for the different regions of interest. A highly significant elevation in the ratio was seen in the infarct region, indicating an increased reliance on anaerobic metabolism in the area of tissue no longer perfused via the LAD. Following occlusion of the LAD, there was a significant reduction in the RPP (Table 3.1, $27\pm6\text{x}10^3$ vs. $18\pm3\text{x}10^3$ mmHg / min, $p<0.05$) but no significant change in the PCr / ATP ratio (Table 3.1, 2.0 ± 0.1 vs. 2.3 ± 0.1, $p=0.2$), indicating reduced cardiac function but maintenance of normal global cardiac energetics in the acutely infarcted perfused rat heart.

3.3.3 Chronic infarct model

The CINE protocol used for *in vivo* infarct verification showed a significantly reduced ejection fraction in the infarcted hearts as compared to control scans taken 1 week prior to surgery (n=4, $56\pm4\%$ vs $78\pm3\%$, $p<0.05$). When perfused, the hearts showed

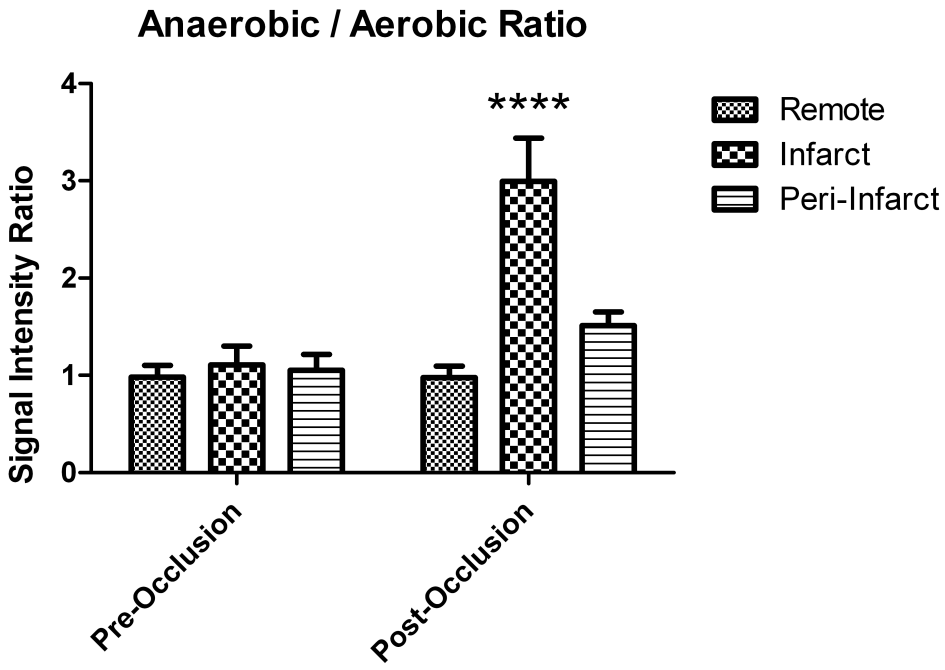


Figure 3.4: The ratio of lactate and bicarbonate signal intensities in the remote, infarct and peri-infarct regions before and after occlusion of the LAD. The ratio represents an index of the balance between anaerobic and aerobic metabolism in the different regions. A significant increase was seen in the infarct region following occlusion of the LAD. (**** $p<0.0001$)

	PCr / ATP	Heart Rate (bpm)	RPP (x10^3 mmHg / min)
Control (pre-occlusion)	2.0±0.1	290±30	27±6
Acute infarct (post occlusion)	2.3±0.1	310±40	18±3*
Chronic infarct (*in vivo* occlusion)	1.6±0.1*	300±30	16±7*

Table 3.1: Cardiac energetic and functional status. The table shows a significant decrease in the PCr / ATP ratio when comparing controls to chronic infarcts and a significant decrease in RPP when comparing controls to both infarct groups (*$p<0.05$).

a significantly reduced RPP (Table 3.1, 27±6 x10^3 vs 16±7x10^3 mmHg / min, $p<0.05$) and PCr / ATP ratio (Table 3.1, 2.0±0.1 vs 1.6±0.1, $p<0.05$) when compared to the acutely infarcted hearts pre-occlusion. Taken together, these data demonstrated a significant functional and energetic impairment in the chronically infarcted hearts. Figure 3.5 shows example images (Panels A-E) and quantitative analysis (Panels F-J) of the chronically infarcted Langendorff perfused rat heart. Panel A shows the high-resolution axial scan and indicates the selected regions of interest for this example heart. The gadolinium contrast agent scan in panel B highlights the reduction in gadolinium induced signal increase seen in the infarcted region, which is quantified in panel G, confirming a reduction in perfusion to the infarcted area when compared to the remote and peri-infarct regions. Panels C-E show example pyruvate, bicarbonate and lactate images from this heart. There is an obvious reduction in signal amplitude for both pyruvate and its downstream metabolites in the infarct region. This is confirmed by the quantitative analysis shown in Panels H-J, which indicate reductions in pyruvate, bicarbonate and lactate signal intensities in the infarct region when compared with the remote and peri-infarct regions. This would imply a significant reduction in perfusion and as a consequence, reduced metabolism in the infarcted region of the heart. The anaerobic / aerobic ratio, as measured for the acute heart, revealed no significant differences in the chronic model (Figure 3.6). H&E histology staining revealed necrosis in the chronically infarcted hearts (Figure 3.7) via visualization of delocalized nuclei and a reduced tissue mass in the infarcted area when compared to controls. In addition, a large number of collagen deposits in the infarct region could be seen as visualized with Picrosirius Red staining.

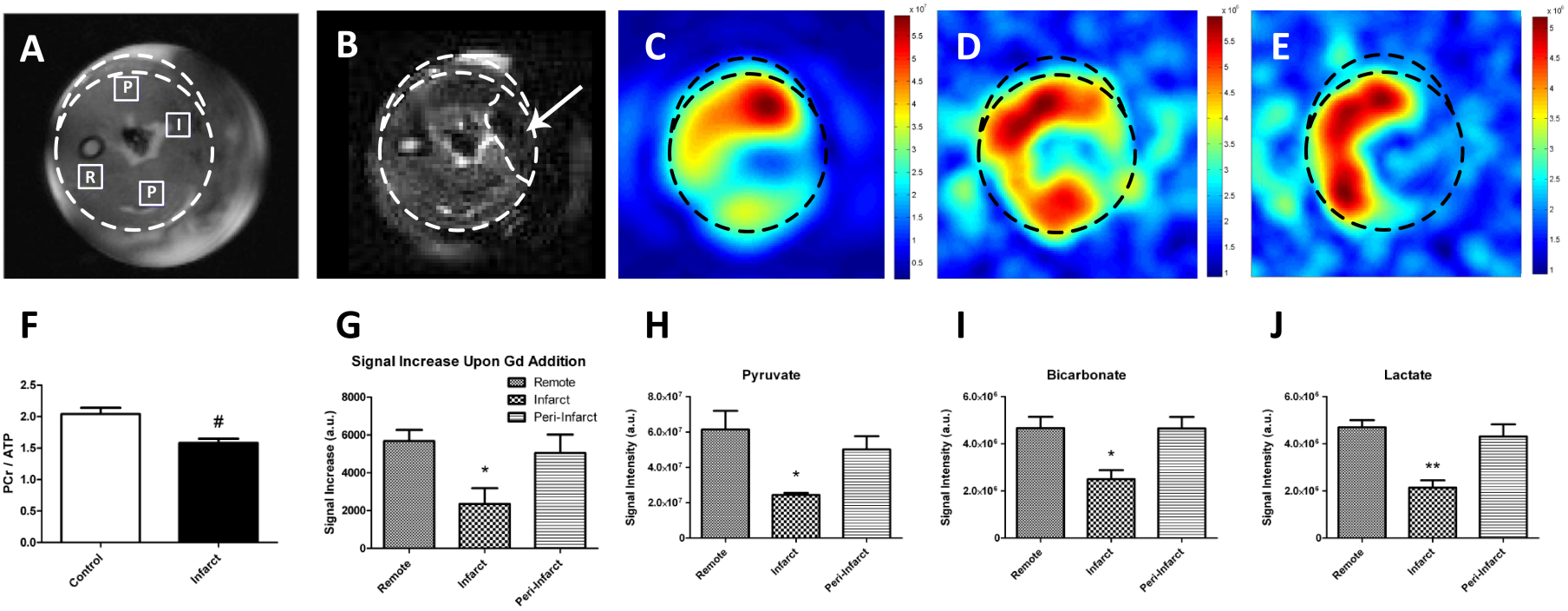


Figure 3.5: Example images and quantitative analysis in the chronically infarcted hearts. Panel A shows a high-resolution axial scan, whilst panels B-E show the gadolinium perfusion, pyruvate, bicarbonate and lactate images respectively. A significant reduction in PCr / ATP (Panel F) is seen alongside a significant reduction in perfusion as assessed by both gadolinium contrast (Panel G) and pyruvate signal intensity (Panel H). Absolute bicarbonate (Panel I) and absolute lactate (Panel J) shows a significant decrease in the infarct area when compared to the remote region. (* $p<0.05$, ** $p<0.01$, # $p<0.05$ vs control, n = 4)

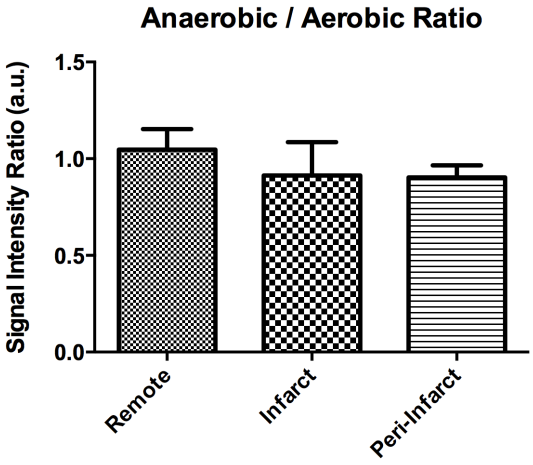


Figure 3.6: The ratio of lactate to bicarbonate (the anaerobic to aerobic index) in the chronic infarct model, shows no significant differences across any region of the myocardium.

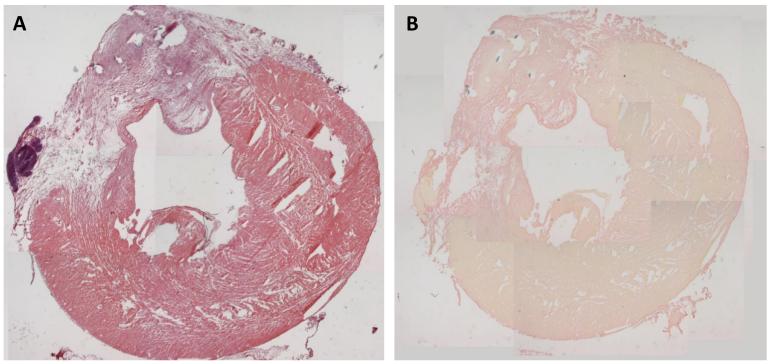


Figure 3.7: An example histological section from the chronically infarcted heart. Panel A shows H&E staining revealing in blue the nuclei that have been delocalised from the membrane (top left of Panel A). Panel B shows the collagen that is stained in red using Picrosirius red (top left of Panel B). Anatomically, the top left region corresponds to the area of the heart supplied by the left anterior descending coronary artery (the septum and part of the left ventricle) which was ligated to create an infarct. The images are 10X magnification, 15 mm wide.

3.4 Discussion

In this study, an optimized DNP-CSI protocol has been developed for the perfused rat heart. The ability to visualize metabolic distribution and map it to the anatomical layout of the heart has been demonstrated using two different infarct models. Clear differences in the metabolic response within the acutely and chronically infarcted heart were observed and were correlated with alterations in perfusion, function and energetics.

Images with a higher spatial resolution, and thinner slice thickness than have been previously demonstrated *in vivo* were produced in this study. This was particularly relevant for a rodent infarct model, where it may be difficult to distinguish healthy myocardium from ischemic tissue in a thick slice, given the small size of the rat heart. Further, this study allowed the same heart to be studied before and after an intervention, allowing the acquisition of control and 'disease' data within the same heart. Changes in metabolism induced minutes after an ischemic intervention were assessed; looking at metabolic changes of the heart minutes after infarct generation would be exceptionally difficult in an *in vivo* model. The DNP-CSI protocol generated here can be easily incorporated into standard perfused heart protocols and the examples presented demonstrate the ease with which the DNP-CSI acquisition can be combined with other acquisitions (such as late gadolinium perfusion and ^{31}P spectroscopy) to generate a comprehensive assessment of the perfused heart.

Several different metabolic acquisition sequences have recently been developed, broadly categorised into spectroscopic and spectral-spatial sequences. A spectroscopic sequence is used here, and has the advantage that no prior knowledge of which metabolic peaks are expected was needed. Conservatively rated gradient amplifiers can also be used. The disadvantage, however, is that acquisitions require a long period of time when compared to the hyperpolarized T_1 of the sample, resulting in a lack of temporal information from the imaging. An elliptical CSI sequence was employed here, as

tends to be used generally in imaging sequences so as to acquire the centre of k-space as quickly as possible whilst the hyperpolarized signal is still high, before acquiring the finer detail on the outer edge of k-space. A variable delay sequence, that allocates more acquisition time to the centre of k-space, and less to the outer edge could improve this technique further. Spectral-spatial acquisition methods allow for very good temporal resolution due to the very short acquisition times [85], however, the expected metabolites must be known [94]. In addition, high performance gradients are needed to image the area of interest rapidly. Based on these short acquisition techniques, three dimensional methods were made possible [95–97], and would certainly find good use in cardiac imaging.

The work developed here made use of a spectroscopic elliptical-CSI sequence, and before acquiring data in the infarcted heart, it was first necessary to optimize the DNP-CSI protocol for small volume imaging in the perfused heart system. While previous studies [86, 98] have performed DNP-CSI *in vivo*, the acquisition of data from the perfused heart is different in several ways:

1. The *in vivo* situation is complicated by in flow and multiple pass effects. Generally, there is a single bolus injection and, therefore, a single source of hyperpolarized [1-^{13}C]pyruvate, whose decay can be predicted in a straightforward manner with respect to both T_1 and RF pulse considerations. In comparison, the perfused heart has a constant influx of hyperpolarized pyruvate throughout the acquisition. This fresh influx of hyperpolarized pyruvate allows for much larger flip angles to be used for the RF excitation and results in subsequently higher metabolite signal levels. In the *in vivo* experiments, more complex RF pulse sequences are required to avoid destroying the hyperpolarized pyruvate signal too quickly [82].

2. Frequently, when imaging *in vivo*, surface RF coils have been utilized. This generally results in a drop-off in sensitivity with distance from the coil and

requires correction for the inhomogeneous flip angle experienced [99]. In the isolated perfused heart, the heart can be located inside a birdcage RF coil, therefore ensuring that the entire heart is within the homogenous region of the coil. Even with the use of volume coils *in vivo*, the chest wall can contaminate the signal, and the close proximity of air spaces within the lungs can increase spectral linewidths.

Following optimization, the DNP-CSI protocol allowed the generation of high signal-to-noise ratio (SNR) metabolic images, which clearly delineate the structure of the left ventricle (Figure 3.2). However, this was only possible for metabolites into which the ^{13}C label was significantly incorporated. In our experiments, [1-^{13}C]alanine did not fit this criterion, generating low SNR images, which were therefore excluded from our subsequent analysis. In light of *in vivo* studies which have either demonstrated the presence of alanine [81, 84] or have chosen not to process it [85, 91] in the cardiac region, the low SNR warrants comment. Studies carried out in pigs [84] tend to show low levels of alanine in comparison to lactate and bicarbonate, yet recent work in the *in vivo* rat heart appears to show alanine levels comparable to those of bicarbonate. It is interesting that relative to the myocardium, a large contribution of alanine appears to come from the chest wall. This chest wall contribution cannot be the case in the isolated perfused heart, providing one possible reason for the low alanine signal seen in this study. In addition, the thick slices needed with current and future rodent *in vivo* studies are likely to acquire some contamination from the liver, despite respiratory motion compensation. Even with the acquisition of high SNR images provided by pyruvate, bicarbonate and lactate in the perfused heart, there was still a residual level of inhomogeneity in the images generated in this study. This may be due to inherent regional differences in perfusion within the different territories of the myocardium.

To demonstrate the utility of the developed protocol in the study of the diseased heart, two different models of myocardial infarction were investigated. In both mod-

els, LAD occlusion was used to reduce perfusion to the anterolateral region of the heart, thereby creating an infarct. The reduction in flow to the LAD territory was clearly visible using a first-pass gadolinium perfusion acquisition and resulted in a significant reduction in the gadolinium-induced signal increase in both infarct models. This reduced perfusion was also apparent in the corresponding [1-^{13}C]pyruvate images demonstrating the utility of hyperpolarized pyruvate as an index of myocardial perfusion.

In the acute infarct model, LAD occlusion led to a significant decrease in cardiac function (Table 3.1) but no alteration in the PCr / ATP ratio, implying that despite the reduced tissue perfusion, global cardiac energetic status was able to be maintained, at least for a limited time period. In the acutely ischemic environment of this model, there should be a reduction in oxidative metabolism and a concomitant increase in anaerobic metabolism [100]. A decrease in the bicarbonate signal, due to a drop in PDH flux, and an increase in lactate signal in the infarct region would therefore be expected. In support of this, a significant decrease in the absolute bicarbonate signal in the acutely infarcted region was observed. However, whilst there was a trend for the absolute lactate signal to increase, this was not significant ($p=0.2$). Interpretation of this data is complicated by the change in perfusion to the infarcted area and the subsequently reduced supply of [1-^{13}C]pyruvate. The simplest ways to account for this are to either eliminate the effect of perfusion by calculating the ratio of lactate and bicarbonate signal intensities or to normalize the metabolite data with respect to the hyperpolarized pyruvate. The ratio of lactate and bicarbonate signal intensities provides an index of the balance between anaerobic and aerobic metabolism and, as would be expected, this ratio was significantly increased in the acutely infarcted heart. The normalized lactate signal was also seen to be significantly increased demonstrating an increased anaerobic metabolism. However, the underlying mechanism may not be as simple as an increased flux through lactate dehydrogenase. Experimental

evidence has shown that in the presence of a large amount of isotopically unlabelled lactate, as would be the case in infarcted glycolytic cardiac cells, an infusion of hyperpolarized [1-^{13}C]pyruvate will result in a greater than expected hyperpolarized lactate signal [101]. This implies that the lactate seen is essentially a reflection of the lactate already present in the myocardium. The normalized bicarbonate data, however, does not reveal a significant decrease as might be expected, suggesting that the reduction in aerobic metabolism in the infarct region is proportional to the reduction in pyruvate delivery to the area.

In the chronic infarct model, there was a significant reduction in both cardiac function and energetics, resulting from significant structural remodelling of the heart. This was seen in combination with a significant reduction in perfusion to the infarct region (as assessed by both gadolinium contrast and pyruvate signal intensity) and reductions in the signal intensity of both bicarbonate and lactate. The absolute decrease in metabolite levels can be explained by the decrease in pyruvate flow to the area and a decrease in the number of cells in the infarct area that are capable of pyruvate metabolism (Figure 3.5). Normalizing this data to the pyruvate signal showed no change, which leads to two possibilities. Either there are cells remaining in the necrotic infarct area that are metabolizing as expected or, due to the slice thickness of the DNP-CSI acquisition (5 mm), some healthy tissue was encompassed within the myocardium above and below the infarcted area.

In conclusion, the value of applying the developed DNP-CSI protocol in the perfused rat heart has been demonstrated. Metabolism can be elucidated independent of hormonal influences, revealing the true contribution of ischemia to PDH flux. Metabolic contamination both from the ventricular cavity and non-myocardial tissue, problematic *in vivo*, are removed in the isolated perfused heart, to allow for accurate metabolic assessment of the myocardium. DNP-CSI in the isolated heart can therefore be a useful tool for the visualization of metabolic alterations in the diseased heart.

Chapter 4

Pyruvate Optimization

The tracer molecule first tested in a liquid state DNP experiment was urea [47]. It was shown to provide a high nuclear polarization, but presented little in the way of a breakthrough application in the biomedical sciences. Urea was initially demonstrated in angiographic applications [102], but DNP needed a different direction. Attention quickly turned towards pyruvic acid [103], which as a starting compound, proved ideal for metabolic assessment. Although unknown at the time, it would become the flagship for dissolution DNP, as demonstrated by its use in the first human clinical trials [104]. Pyruvic acid is self glassing, has the potential for a very high nuclear polarization (few metabolically relevant compounds can rival this), and is a key component in the glycolytic pathway, as previously described in Chapter 2.

Hyperpolarized pyruvic acid (pyruvate) has found application in assessing metabolic pathways, both *in vivo* and *ex vivo* [51, 77, 78, 105, 106] as well as for metabolic imaging [85,107,108]. Whilst technical developments have been rapid and exciting for the field, thought is now needed as to whether the DNP technique is being employed in a way that gives accurate metabolic information about the systems being probed. Two examples of potential areas where further work is required to opimize the use of pyruvic acid will form the focus of this chapter.

The first example is the large concentrations of pyruvate currently being used in isolated perfused organ systems (both cardiac [109] and hepatic [19]), in order to generate high signal to noise ratios. This same problem does exist *in vivo*, but work has been carried out in the rodent model to investigate and address the issue [110,111]. In bringing a new technique such as DNP to the research environment, with the eventual aim that it should be widely used in the clinic, the importance of understanding the information being obtained and the ways it can provide an incorrect result are crucial. In the pyruvate concentration study described in this chapter, a striking example will be shown where this is the case.

The second area covered in this chapter will examine the provision of fatty acids to the perfused heart. To ensure that a perfused heart preparation is as physiological as possible, fatty acids should ideally be provided in the perfusion buffer, given that *in vivo*, hearts would typically derive about 70% of their energy from fatty acid sources [18]. However, previous work [19] has shown that the common method of using bovine serum albumin (BSA) to solubilise long chain fatty acids significantly reduces the observed signal from hyperpolarized pyruvate. This is due to the binding of pyruvate by the albumin, leading to a quenching of the hyperpolarized signal. The aim of the work described here was to find a solution to this problem, and to therefore allow the use of albumin and long chain fatty acids (typically palmitate) in hyperpolarized experiments. In addition, an alternative way of providing the perfused heart with a source of fatty acids, without compromising the hyperpolarized signal intensity in any way needed to be found, particularly in instances where low polarization probes may need to be used. This chapter will go on to describe the metabolic differences seen with and without the provision of fatty acids, and the impact these results may have when planning future studies.

4.1 Pyruvate concentration

4.1.1 Introduction

The aim of this study was to elucidate the impact of pyruvate concentration on the metabolic assessment of the perfused rat heart. Over the last 10 years, the use of DNP has allowed very high signal to noise ratio MR spectra to be generated from suitable metabolic probes. Despite this remarkable development, it can still be difficult to obtain adequate signal from downstream metabolites in biological systems. This is due to a number of factors, including the polarization of the probe itself, its rate of T_1 decay, the rate and steps involved in its enzymatic transformation, and to a small extent, the RF pulses used in order to acquire the data. Of the above factors, enzymatic conversion is arguably the most important. Decay time is a matter of good initial probe selection and not a factor that can currently be altered significantly, although a great deal of work is ongoing in this area [112]. Taking [1-^{13}C]pyruvate as an example, $^{13}CO_2$ will be considered in terms of the problems downstream metabolites can pose with regards to low signal levels. It has a low signal to noise ratio, as compared to the production of lactate or bicarbonate for example. The initial steps involved in [1-^{13}C]pyruvate metabolism are either conversion to [1-^{13}C]alanine, [1-^{13}C]lactate or $^{13}CO_2$. The enzyme with the highest driving force for these transformations will determine which of these metabolites has a higher visible polarization. In turn, each of these metabolites will also have varying T_1 decay times, and therefore lose their polarization at different rates. From here, lactate and alanine can be converted back to pyruvate, further diminishing their polarization. $^{13}CO_2$ in comparison, is irriversibly formed and subsequently converted via the enzyme carbonic anhydrase to [1-^{13}C]bicarbonate in a reversible manner. The balance between bicarbonate and CO_2 is driven by the pH of the local environment and at physiological pH values leads to a 10:1 ratio between bicarbonate and CO_2. This balance means that CO_2 is often

observed at very low levels in cardiac spectra. In addition, a poor initial polarization can often render these low signals too noisy for accurate analysis, or will make them "invisible".

One simple solution to this problem of low downstream signals is to increase the concentration of the original tracer. This greatly improves the acquired signal to noise ratio, allowing acquisition of high temporal resolution spectra, without the need for spectral summing. Unfortunately, little appears to be known about the consequences of such supraphysiological concentrations. While it may intuitively be accepted that enzymes must have a limit as to the number of substrates that can be processed per unit time, it has either been assumed that this limit is high enough not too matter in this case (i.e. enzyme saturation is not an issue) or that through the lack of an alternative choice, larger concentrations had to be used.

The widely used [113], and well polarized [77] [1-^{13}C] and [2-^{13}C]pyruvate were chosen as the basis for this study, and it was the aim of this work to demonstrate not only that saturation effects are evident at the high concentrations typically used in the perfused heart, but that using these high concentrations may lead to incorrect conclusions being drawn from experiments.

To this end, two groups of hearts were studied in the same way, with each group being perfused with KH buffer, using either [1-^{13}C] or [2-^{13}C]pyruvate as the hyperpolarized probe, spanning physiological to vastly supraphysiological concentrations. In all hearts, cardiac energetics were monitored using ^{31}P spectroscopy at each of the pyruvate concentrations. Receiver gain was carefully controlled to achieve the best signal possible with each concentration, and hyperpolarized samples were allowed to buildup until maximal polarizations were achieved.

Finally, in order to demonstrate the utility of the information provided by this concentration study, a method was needed to change the activity of the PDH enzyme, in order to see whether the use of different [1-^{13}C]pyruvate concentrations could reveal

this change in activity. Dichloroacetic acid (DCA), an inhibitor of PDK [114] was used to alter PDH flux. PDK is responsible for the phosphorylation of the PDH enzyme, hence inhibiting it. The outcome of DCA provision is therefore an increase in pyruvate to bicarbonate flux, demonstrated in previous radiolabelled studies [115]. Therefore, in order to demonstrate the importance of this study, two further groups of hearts were perfused with standard KH initially, before being switched to a KH buffer containing 1 mM DCA. Each group was probed using either 0.625 mM or 2.5 mM pyruvate. At all times, the concentration of pyruvate in the KH buffer was equal to that of the probe being investigated.

4.1.2 Materials and methods

Perfusion protocol: For both [1-^{13}C]pyruvate (n = 5) and [2-^{13}C]pyruvate (n = 5) studies, male Wistar rats were anaesthetized with a 1.3 ml / kg intraperitoneal injection of pentobarbital sodium (200 mg / ml Euthatal), and after loss of pedal reflexes, a thoracotomy was performed and the heart excised and placed into ice-cold Krebs Henseleit (KH) buffer. The aorta was then cannulated and the heart perfused in the Langendorff mode initially under 65 mmHg perfusion pressure and maintained at 37 ^{o}C. A 20 mm NMR tube was placed over the heart and inserted into the bore of the 11.7 T magnet, whereby the heart was then subjected to 85 mmHg perfusion pressure. After a 5 minute stabilization period, a constant flow pump was set to deliver KH buffer at a flow rate matching that of the coronary flow of the heart. The perfusion buffer contained 118 mM NaCl, 4.7 mM KCl, 1.2 mM $MgSO_4.7H_2O$, 1.75 mM $CaCl_2.2H_2O$, 0.5 mM Na_2EDTA, 11 mM glucose, 25 mM $NaHCO_3$ and concentrations of sodium pyruvate as follows: 0.15 mM, 0.3 mM, 0.625 mM, 1.25 mM or 2.5 mM. Following polarization of the frozen [1-^{13}C] or [2-^{13}C]pyruvic acid, the sample was dissolved with 6 ml of hot NaOH/EDTA/Tris buffer to neutralise the pH. Following dissolution, different hyperpolarized pyruvate concentrations were achieved

by dilution of the output from the polarizer in different volumes of KH buffer (Table 4.1). This solution was then delivered to the heart as a bolus over 120 seconds, with the hyerpolarized pyruvate concentration reaching the heart being equal to that in the perfusion buffer.

Concentration (mM)	Sample size (μl)	KH buffer volume (ml)
0.15	3.75	328
0.3	7.5	328
0.625	7.5	164
1.25	30	328
2.5	30	164

Table 4.1: This table shows the different pyruvic acid sample sizes and buffer volumes used to generate different hyperpolarized [1-^{13}C] and [2-^{13}C]pyruvate concentrations. The KH buffer volume does not include the 6 ml of dissolution buffer injected into the HyperSense to melt the pyruvic acid sample.

Spectroscopy: A ^{13}C pulse-acquire experiment was started immediately after the dissolution of the hyperpolarized tracer (TR = 1 s, FA = 30^{o}, BW = 180 ppm, 4096 pts), and the sum of 60 spectra were taken beginning with the first spectrum showing hyperpolarized pyruvate. The ratio of the bicarbonate and CO_2 signals to that of the pyruvate was used as a measure of flux through the pyruvate dehydrogenase (PDH) enzyme. All other metabolites were similarly normalized. pH was obtained using the ratio of bicarbonate and CO_2 in the Henderson-Hasselbalch equation, with a pKa = 6.15, as previously reported [116].

Immediately following the acquisition of the ^{13}C spectra, a series of rapid 30 second ^{31}P scans (as described in Section 3.2) was performed using a dual tuned 10 mm ^{1}H / ^{31}P probe, over a period of 25 mins. Fully relaxed ^{31}P scans were not performed in order to reduce the length of the protocol, and thus the absolute PCr / ATP ratios reported here may appear low due to partial saturation effects on the PCr and ATP resonances. Ten minutes into the rapid ^{31}P scans, the perfusion buffer delivered to the hearts was changed from the initial KH buffer with pyruvate, to

KH buffer with a different, randomized concentration of pyruvate. The phosphorous and hyperpolarized ^{13}C scans were repeated, and another buffer change carried out. A final hyperpolarized pyruvate scan was then performed. Figure 4.1 shows this diagrammatically. The experiment as designed resulted in four hyperpolarized scans being performed per pyruvate concentration. pH using ^{31}P data was calculated by using the change in chemical shifts between PCr and Pi automatically within the jMRUI processing software.

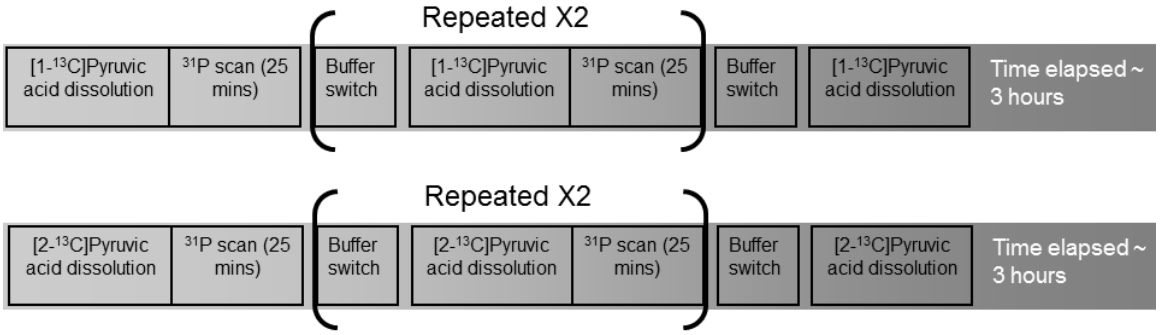


Figure 4.1: The protocol used in the concentration study experiment is shown here digrammatically.

Dichloroacetic acid: The protocol described above was repeated with the initial buffer containing either 0.625 (n = 6) or 2.5 mM (n = 4) pyruvate, and being switched to the same buffer but also containing 1 mM DCA.

Software and equipment: For all studies, a vertical bore 11.7 T wide-bore MR imaging system (Magnex, Oxfordshire, UK) was used in combination with a Bruker Avance console (Bruker Medical, Ettlingen, Germany) running Paravision 2.1.1 and XWinNMR 2.6. Protocols using ^{13}C nuclei were acquired with a dual channel 20 mm RF coil (M2M, Cleveland, USA). Those using ^{1}H or ^{31}P nuclei were acquired using a 20 mm, dual channel, RF probe (Rapid Biomedical GmbH, Germany). Spectra were processed using jMRUI 2.2 and Matlab 2011b (Mathworks, MA, USA).

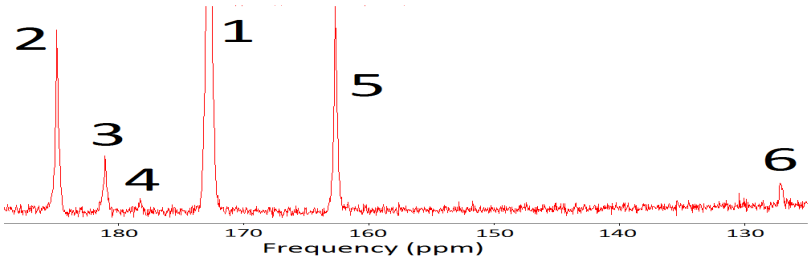
Data analysis: All statistical tests were carried out at the $p<0.05$ significance level. Units are a.u., unless otherwise specified. Correlations between data sets were per-

formed using a Pearson's correlation coefficient (CC) analysis. Data are expressed as mean±standard deviation. Following processing, all ^{13}C metabolite signal amplitudes were corrected for pyruvic acid sample size, receiver gain on the NMR system, and the polarizations achieved on the HyperSense. Metabolite data were fitted against hyperpolarized [1-^{13}C] and [2-^{13}C]pyruvate concentrations using a linear or a Michaelis-Menten fit, with linear regression (R^2 value) used to determine the most appropriate fit.

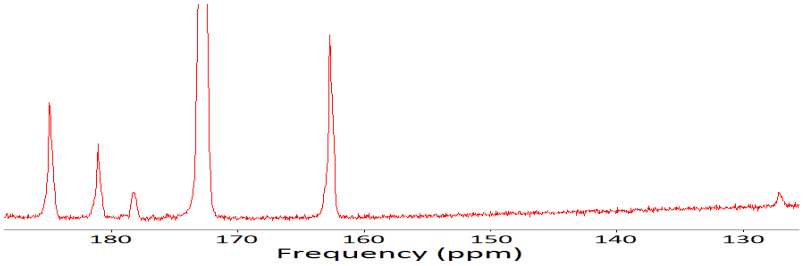
4.1.3 Results

4.1.3.1 [1-^{13}C]pyruvate

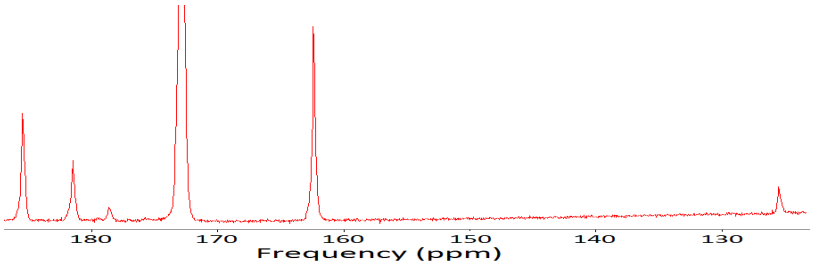
Sample spectra at each concentration are shown in Figure 4.2.



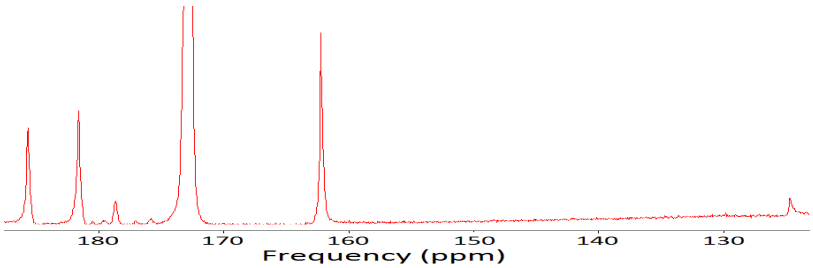
(a) 0.15 mM



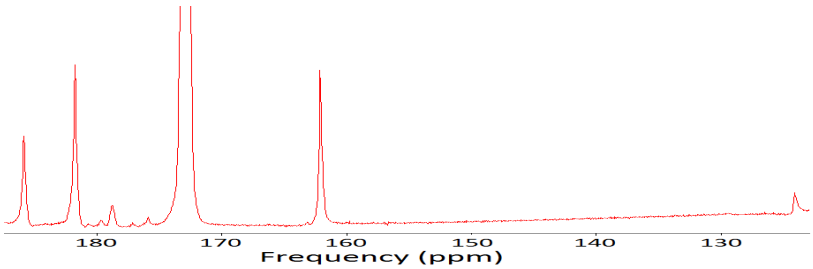
(b) 0.3 mM



(c) 0.625 mM



(d) 1.25 mM



(e) 2.5 mM

Figure 4.2: Representative spectra are shown from each concentration used. Peak (1) is pyruvate, (2) lactate, (3) pyruvate hydrate, (4) alanine, (5) bicarbonate, (6) CO_2.

The SNR with increasing [1-^{13}C]pyruvate concentration demonstrated a positive correlation (CC = 0.93), and is shown in Figure 4.3.

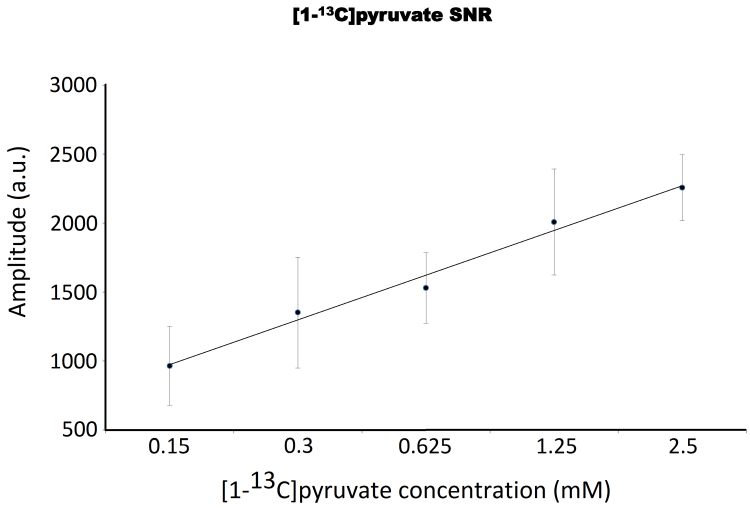


Figure 4.3: This figure shows the increasing SNR as [1-^{13}C]pyruvate concentration increases. n = 5

Looking at the downstream metabolites of [1-^{13}C]pyruvate, alanine and lactate also had linear relationships (R^2 = 0.9889, and 0.9790 respectively) with [1-^{13}C]pyruvate concentration, while bicarbonate and CO_2 showed strong saturation kinetics at the higher infused pyruvate concentrations, and both were best fitted with Michaelis-Menten functions (R^2 = 0.9561 and 0.9931 respectively). The plots and fits of these metabolites are shown in Figure 4.4 and Table 4.2.

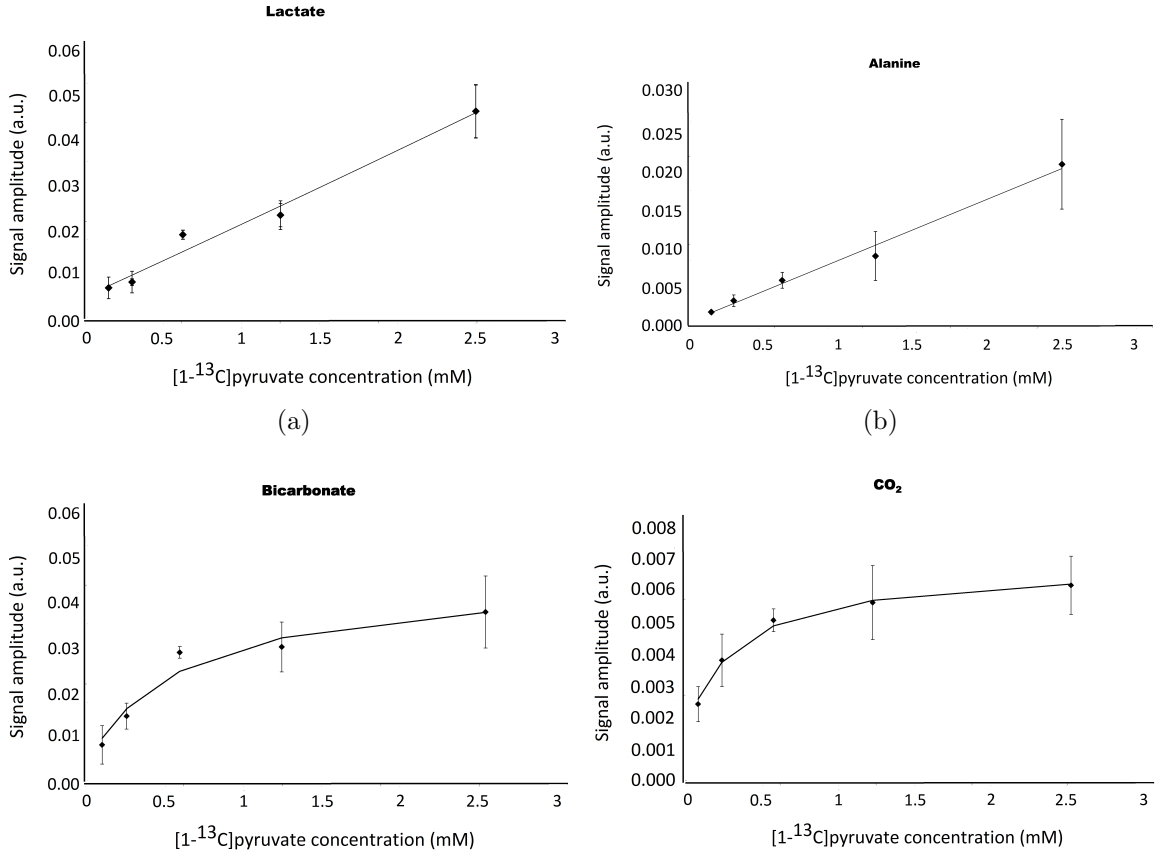


Figure 4.4: These plots show the change in metabolites with respect to [1-^{13}C]pyruvate concentration. n = 5

Metabolites	Linear	Michaelis-Menten
Lacate	**0.9790**	N/A
Alanine	**0.9889**	0.9739
Bicarbonate	0.7593	**0.9561**
CO_2	0.7046	**0.9931**

Table 4.2: Linear regression (R^2) value using different fitting functions for [1-^{13}C]pyruvate metabolite data. Michaelis-Menten fitting was not possible for lactate.

There was a positive correlation between PCr / ATP ratios and pyruvate concentrations, although this did not reach significance (CC = 0.85, p = 0.07, Figure 4.5).

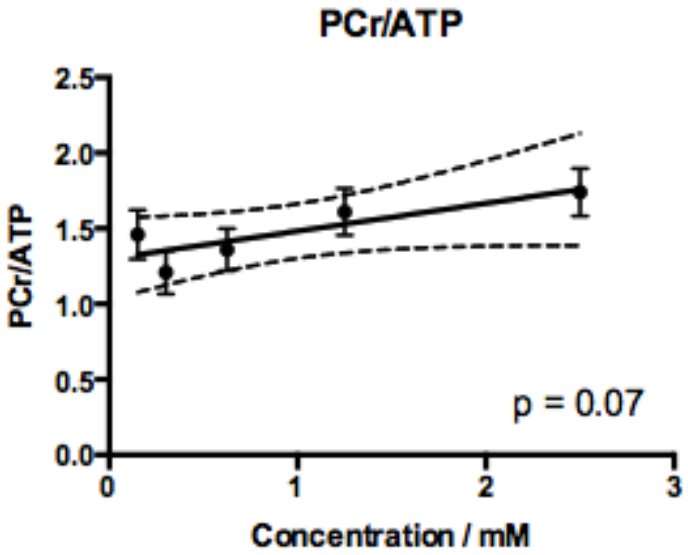


Figure 4.5: The figure shows the correlation of [1-^{13}C]pyruvate concentration with PCr / ATP ratio as measured by ^{31}P MRS. The correlation is not significant (p = 0.07), n = 5.

pH, as measured with ^{31}P spectroscopy at the different [1-^{13}C]pyruvate concentrations showed no correlation with [1-^{13}C]pyruvate concentration (CC = -0.08, Figure 4.6).

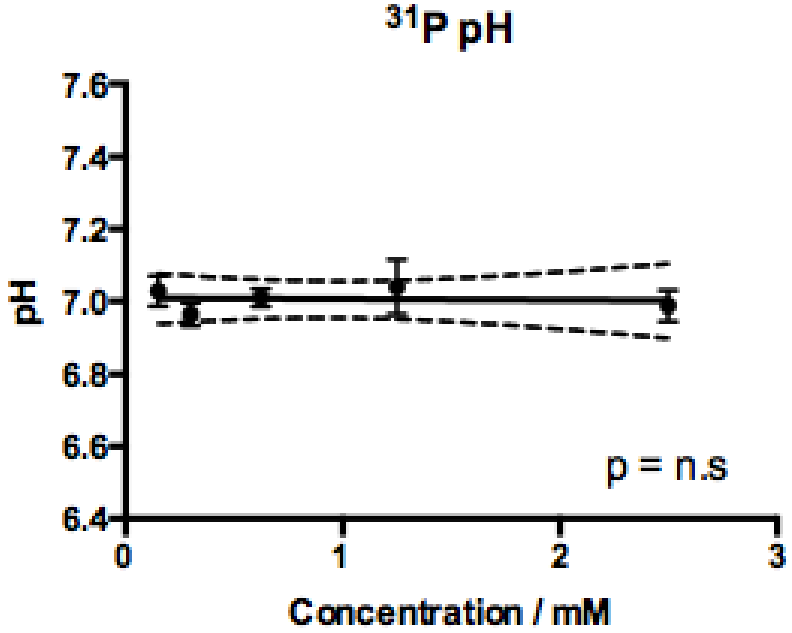
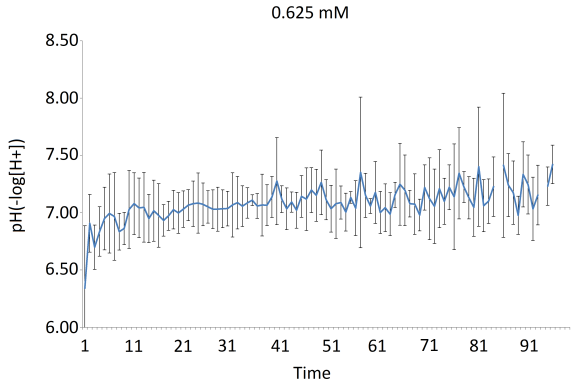
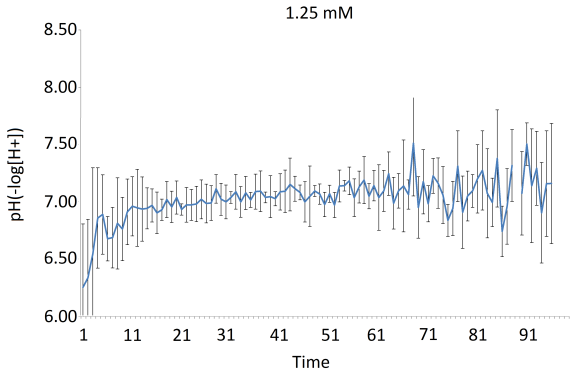


Figure 4.6: pH, as measured by ^{31}P MRS shows no correlation with [1-^{13}C]pyruvate concentration.

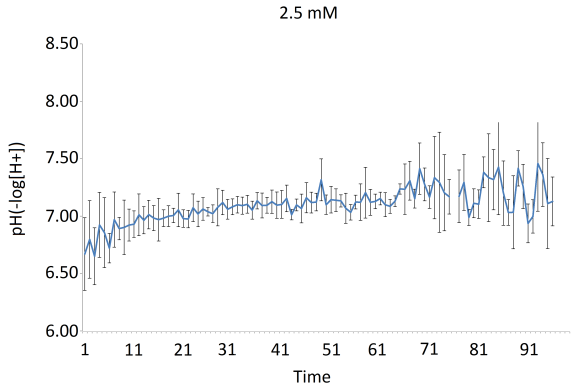
pH, as measured by the bicarbonate and CO_2 ratio, is plotted over time in Figure 4.7. This was done because, in order to obtain an accurate pH, it was not sufficient to use the summed ^{13}C bicarbonate and CO_2 data. This is due to the fact that a period of time is needed for the two metabolites to reach an equilibrium, thus giving a more accurate reflection of pH. It was not possible to obtain pH from the lower [1-^{13}C]pyruvate concentrations due to the low signal to noise ratio of the CO_2 peak.



(a) 7.11±0.10



(b) 7.11±0.07



(c) 7.12±0.05

Figure 4.7: Cardiac pH, as measured by bicarbonate and CO_2 ratio derived from hyperpolarized [1-^{13}C]pyruvate (n = 3). The establishment of a steady state pH takes approximately 50 seconds from the first appearance of signal. In each of the plots, the pH was calculated from the 10 seconds following establishment of a steady state.

4.1.3.2 Dichloroacetic acid

No significant change in PDH flux (bicarbonate and CO_2) was seen between the control 2.5 mM [1-^{13}C]pyruvate group, and that containing 1 mM DCA ($p = 0.692$), however, a significant increase in PDH flux was seen upon the addition of 1 mM DCA when using 0.625 mM pyruvate ($p<0.05$) (Figure 4.8).

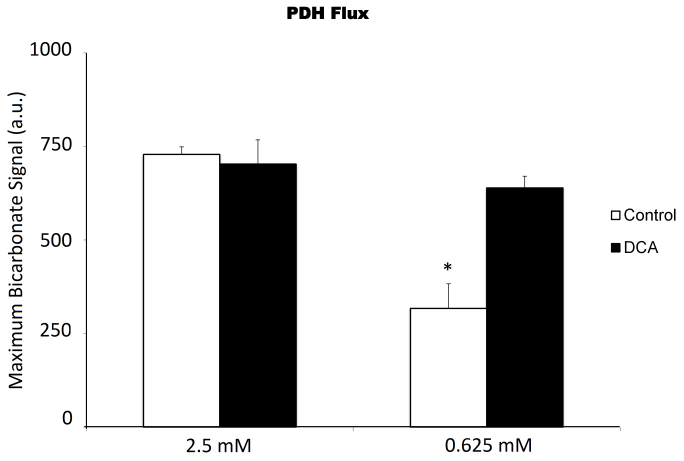
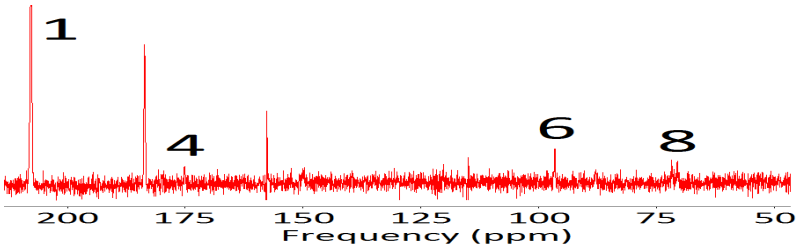


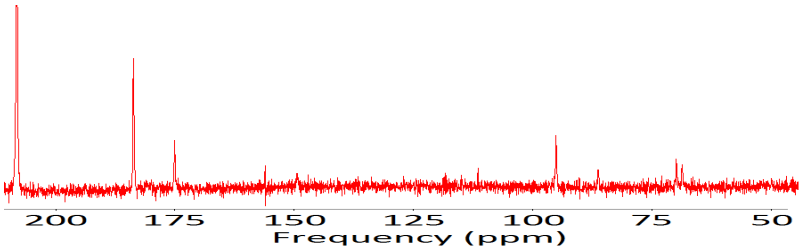
Figure 4.8: This shows the effect of adding 1 mM DCA to the perfusion buffer, using either 0.625 mM or 2.5 mM [1-^{13}]C pyruvate as the hyperpolarized probe. No difference was seen within the 2.5 mM group, but a significant increase in PDH flux was seen when DCA was added to the system probed with 0.625 mM hyperpolarized pyruvate (* $p < 0.05$), $n = 10$.

4.1.3.3 [2-^{13}C]pyruvate

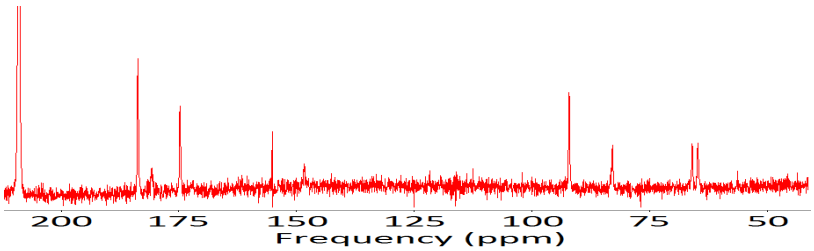
Sample spectra at each concentration are shown in Figure 4.9.



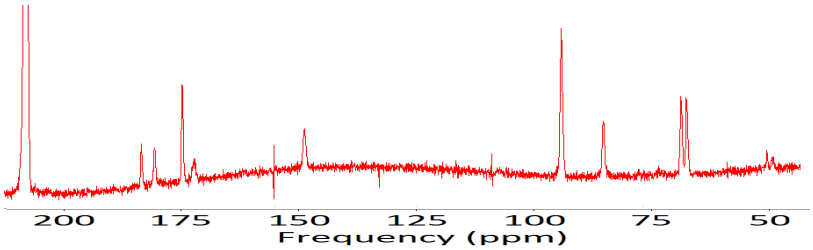
(a) 0.15 mM



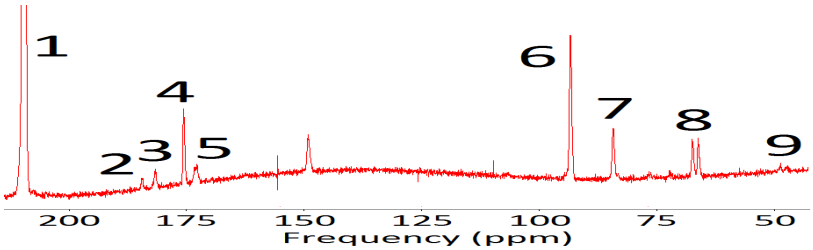
(b) 0.3 mM



(c) 0.625 mM



(d) 1.25 mM



(e) 2.5 mM

Figure 4.9: Representative spectra are shown from each concentration used. Peak (1) pyruvate, (2) C5-glutamate, (3) citrate, (4) acetyl carnitine, (5) C1-pyruvate, (6) pyruvate hydrate, (7) impurity, (8) C2-lactate, (9) C2-alanine. Not all peaks are visible by eye at the lower pyruvate concentrations. Small unidentified peaks are impurities, present in the injected sample.

The SNR with increasing [2-^{13}C]pyruvate concentration demonstrated a positive correlation (CC = 0.89), and is shown in Figure 4.10.

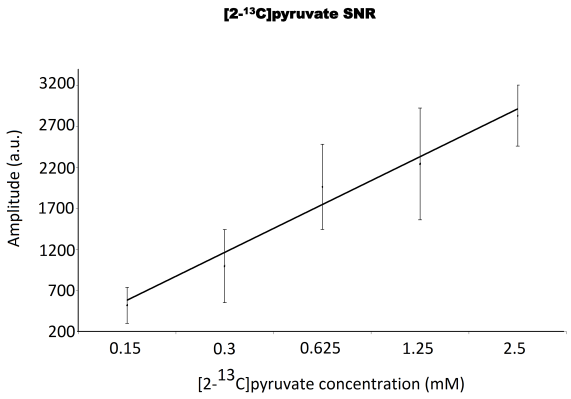


Figure 4.10: This figure shows the increasing SNR as [2-^{13}C]pyruvate concentration increases. n = 5

Lactate and alanine were not considered in this study, as they were better dealt with using [1-^{13}C]pyruvate, as previously discussed. Acetyl carnitine and citrate were best fit with a Michaelis-Menten function (R^2 = 0.9702, 0.9749 respectively), whereas glutamate showed no evidence of variation with concentration and could not be fitted with a simple function, as shown in Figure 4.11.

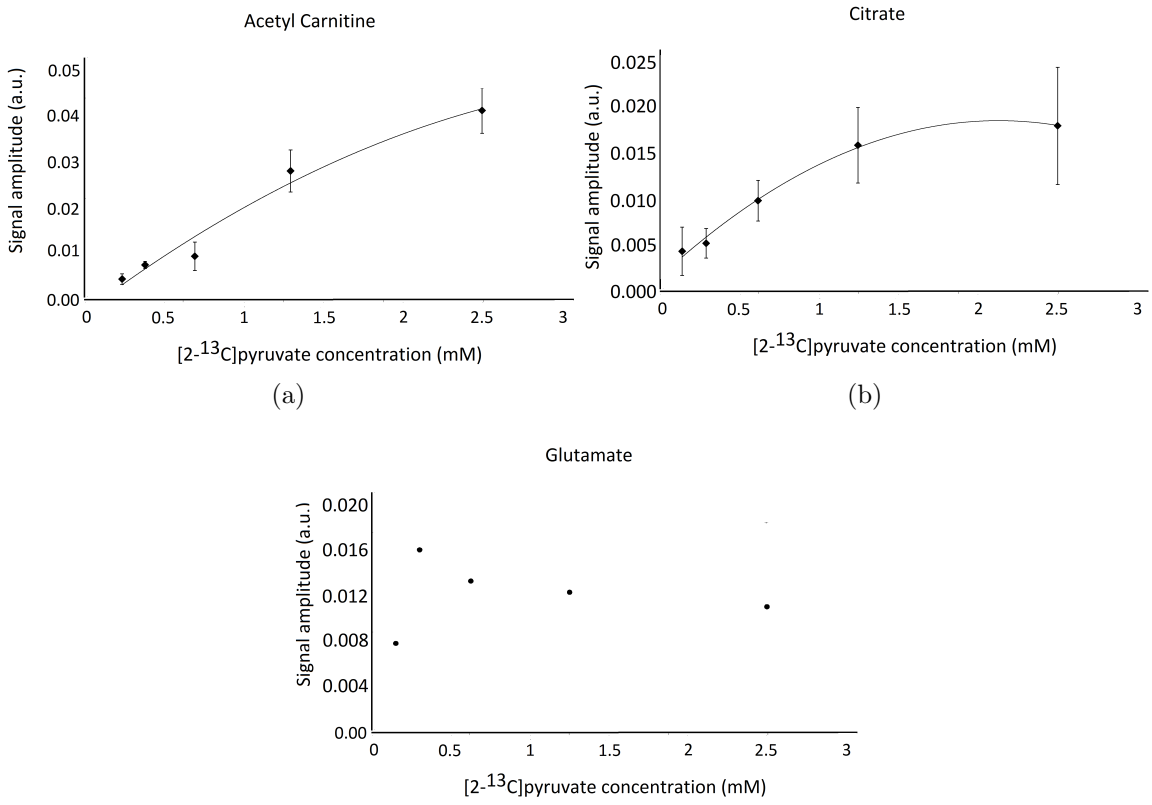


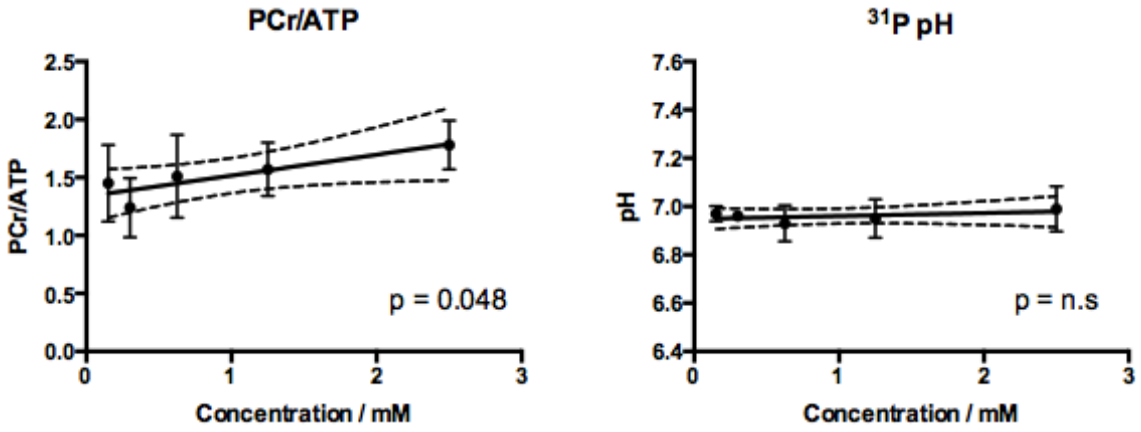
Figure 4.11: These plots show the change in metabolites with respect to [2-^{13}C]pyruvate concentration. No suitable fit was possible for glutamate. n = 5

The fits of these metabolites are shown in Table 4.3.

Metabolites	Linear	Michaelis-Menten
Acetyl Carnitine	0.9588	**0.9702**
Citrate	0.8577	**0.9749**
Glutamate	0.0093	**0.1590**

Table 4.3: Linear regression (R^2) value using different fitting functions for [2-^{13}C] pyruvate metabolite data.

Following the trend seen with [1-^{13}C]pyruvate, a significant positive correlation between PCr / ATP ratio (CC = 0.87) and [2-^{13}C]pyruvate concentration was observed, but none with pH (CC = 0.51) as assessed by ^{31}P spectroscopy (Figure 4.12).



(a) (b)

Figure 4.12: Plots of the change in PCr / ATP ratio and pH as a function of [2-^{13}C]pyruvate concentration. n = 5

4.1.4 Discussion

The [1-^{13}C]pyruvate concentration study showed a linear relationship between initial pyruvate concentration and signal intensity for alanine and lactate, but the appearance of saturation kinetics for bicarbonate and CO_2. This would suggest that the alanine transaminase (ALT) and the lactate dehydrogenase (LDH) enzyme pathways are not being saturated and also that pyruvate uptake into the cell is not limiting at the concentrations studied. At the highest concentrations investigated, pyruvate dehydrogenase (PDH) flux had clearly reached near complete saturation, as observed from the bicarbonate and CO_2 signals seen. This may have significant implications in studies where the experiment may cause PDH flux to increase, as the full extent of such changes may not be revealed using such high concentrations of pyruvate. This was successfully demonstrated here with the DCA experiments, which only revealed a significantly increased PDH flux at the lower [1-^{13}C]pyruvate concentration. The converse is also true, an agent (either pharmacological or physiological, such as ketone bodies [117]) expected to decrease PDH flux may not reveal significant changes at higher pyruvate concentrations, in the saturation region. In addition, aspects of

metabolic control such as end product inhibition would also likely be affected [77].

The DCA data provides the most satisfactory result from this study, a demonstration that the choice of pyruvate probe concentration when assessing metabolism can be the difference between rejecting or accepting the null hypothesis (by a very large margin in this case, where h_0 = DCA increases PDH flux in the isolated perfused heart). This experiment should provide thought for all hyperpolarized experiments carried out, whether *ex vivo* or *in vivo*. With the development of new probes, especially those with plans to move into the clinic (such as pyruvate and fumarate), the concentration of DNP hyperpolarized probes used will become a very important area for investigation.

The [2-^{13}C]pyruvate concentration study showed no linear relationships between initial pyruvate concentrations and the downstream metabolites, glutamate, acetyl carnitine and citrate. Acetyl carnitine was beginning to show some evidence of saturation at the higher pyruvate concentrations. When large quantities of acetyl-CoA (resulting from a TCA cycle unable to use it rapidly enough [118]) are produced, acetyl carnitine is formed via the carnitine acetyl transferase (CAT) enzyme [119]. The CAT enzyme provides a mechanism by which acetyl CoA may be stored for later use. This would however imply an excessive level of substrate being provided, and the global physiological response in such situations would be hepatic fatty acid synthesis. The saturation seen in the citrate graph would seem to support the argument that the TCA cycle is being saturated with acetyl CoA, as a result of too high a concentration of pyruvate, and the resultant shuttling of excess energy to the CAT system. As for glutamate, spectral quality at the lower concentrations was poor, and thus establishing a pattern with respect to [2-^{13}C]pyruvate was not possible.

A brief comment on PCr / ATP ratio for both [1-^{13}C] and [2-^{13}C]pyruvate. Whilst in the former case not quite significant, and in the latter, only just significant, both appear to show a trend for increasing PCr / ATP concentrations with increasing fuel supply. This is perhaps not unexpected, given the role of PCr as an energy buffering

compound, for use in times when a sudden energy demand is required.

Based on this study data, while 2.5 mM offers spectra with the highest signal to noise ratio, 0.625 mM offers a very acceptable compromise, with each metabolite clearly distinguishable and the time course still quantifiable with good results. Below this optimal concentration, bicarbonate and CO_2 became difficult to reliably quantify. The lower concentration is particularly suitable in light of the saturation effects seen with both [1-^{13}C] and [2-^{13}C]pyruvate probes, and as further demonstrated with the DCA data. The very low concentrations can mean losing the per-second resolution quantification that is possible with high signal to noise, as spectral summing becomes necessary (0.15 mM certainly, and sometimes 0.325 mM, but never 0.625 mM and above). Some information is lost as a result of summing, for example accurate determination of the arrival times of different metabolites with respect to pyruvate, although the importance of this data is not yet fully understood. However, judgment on which concentration to use will need to be made on the basis of the expected metabolic change in any given study, and the importance of measuring the absolute value of a change in say PDH flux, or merely any change, however small. It should be noted that it is possible to overcome some of the effects of the low signal to noise ratio for the lower concentrations, by using smaller pyruvic acid sample sizes (which generate higher polarizations than larger samples), and smaller KH buffer volumes to generate lower concentrations.

An interesting technique recently developed [120], useful to the study of probe concentration, would allow for individual enzyme kinetics to be measured using hyperpolariztion. By embedding the enzyme to be looked at (LDH was used in this example) in a large alginate matrix and perfusing it with hyperpolarized [1-^{13}C]pyruvate, the rate and kinetic parameters of the transformation could be determined under any conditions desired. Using this technique would allow verification of the saturation effects seen in this concentration study, and to separate out the influence of cellular

uptake, cofactors and product feedback inhibition for example.

In conclusion, a better understanding of the relationship between pyruvate concentration and metabolic effects has been established in perfused rat hearts, and will alter the way in which future experiments are performed. This development will, where possible, also be applied carefully to the study of new compounds, in deciding a suitable concentration to use. This study marks a further step taken in being able to incorporate DNP as a truly physiological method of assessing metabolic function, and brings us closer to using more relevant perfusion buffers for the isolated perfused rat heart.

4.2 Fatty acid supply to the heart

4.2.1 Introduction

This section aims to discuss the supply of fatty acids to the perfused rat heart during hyperpolarized experiments. The *in vivo* heart, under healthy conditions, derives most of its energy supply from fatty acids [18]. In order to derive accurate metabolic information from the isolated perfused heart, attempts should therefore be made to ensure that it too is supplied with fatty acids. Supplying these insoluble fatty acids, however, requires a large carrier molecule, albumin, in order to solubilize the fatty acids in aqueous solutions (such as blood and KH buffer). As previously reported [19], the use of albumin also binds other molecules, including pyruvate. Thus, when perfusing the heart with hyperpolarized [1-^{13}C]pyruvate, it is bound reversibly to albumin, thus considerably reducing the observable hyperpolarized signal. One solution to this might be to increase the concentration of pyruvate used, as performed in previous work [19], but in that study [1-^{13}C]pyruvate concentrations of 20 mM were needed to achieve a sufficient SNR. However, using such a pyruvate concentration would negate the benefit of preparing a physiological, fatty acid perfused isolated heart as demon-

strated previously in this chapter. This study has therefore examined alternative methods enabling the provision of fatty acids to the isolated perfused heart. A reduced concentration of albumin (0.5%) bound to palmitate (0.4 mM), was attempted, thus allowing the supply of a long chain fatty acid, with the intention being that the supply of a physiological quantity of fatty acid was more important than achieving physiological levels of albumin in solution (around 4% in blood). To supplement this study, a method that did not involve the use of albumin and which should not have any deliterious effect on hyperpolarized [1-^{13}C]pyruvate signal was also attempted. Intralipid, a triglyceride emulsion containing largely linoleate, palmitate and oleate, was therefore considered. Intralipid is a non-physiological triglyceride extensively used in the clinic [121–123] for fatty acid provision (as well as other applications). It is a soybean oil emulsion, commercially prepared and easily available and is primarily composed of linoeic (40%), oleic (20%) and palmitic (10%) acids, with the balance being other fatty acids and phospholipids [124]. Intralipid is known to be taken up by the heart [125] as verified by radiolabelled experiments, and thus makes a good potential candidate for FA supply in the form of triacylglycerols (TAG). Intralipid lacks, however, the sophisticated protein based delivery system of chylomicrons and VLDL in combination with the VLDL receptor and lipoprotein lipase (LPL), or the mechanism of FFA transfer from albumin to FABPpm or FAT/CD36 [126, 127]. It is likely that breakdown of Intralipid first occurs via LPL, before being transported via FABP [128–131]. Intralipid in this study was used in two concentrations, 0.4 mM and 4 mM.

In this study, both of these fatty acid sources were assessed with regard to their ability to induce the expected decrease in PDH activity, which should occur upon supply of fatty acids to the heart (the Randle cycle). In addition, their effect on the signal from hyperpolarized pyruvate was also considered. To further investigate the mechanism by which signal loss occurs when albumin was used in the presence of hyperpolarized

solutions, both hyperpolarized and thermal T_1 studies on [1-^{13}C]pyruvate were also carried out in the presence of different buffer compositions.

4.2.2 Materials and methods

Albumin / palmitate buffer preparation: Palmitic acid (10 mmoles) was added to 2 ml of ethanol and heated in a water bath at 70 °C until melted. Potassium carbonate (anhydrous, 10 mmoles) was dissolved in a minimum amount of water, and added dropwise to the molten palmitic acid solution to create a white salt. This was then heated in a water bath until dry (approx. 5 hours). The powder was then dissolved in saline solution (154 mM), made up to 100 ml and stored in the fridge. Dialysis tubing was prepared as follows: 50 cm of dialysis tubing was cut, and placed into 3 L of double distilled water at 80 °C, containing 60 g of sodium carbonate and 1.116 g Na_2EDTA, and left for 30 mins. The tubing was then rinsed with ddH_2O, and stored in water to avoid cracking. The albumin KH buffer was prepared by adding 10 g albumin (0.5 % final) to 200 ml KH buffer (without glucose, 1.45 mM $CaCl_2$, and containing 4.3 mM KCl, due to the potassium salt in the palmitate preparation) in a glass beaker, heated to 37 °C and slowly stirred until completely dissolved, in order to avoid foam formation. The previously prepared palmitate salt (100 mM) was heated in a water bath to 70 °C, and once molten, was transferred carefully in 1 ml aliquots to the KH-albumin solution, using a preheated pipette tip to achieve a final palmitate content of 0.8 mmoles. The KH-albumin-palmitate solution was then diluted with 1800 ml KH, and ion concentrations adjusted as required (particularly calcium and potassium). The solution was then transferred to two portions of dialysis tubing, tied off at one end. The other end was tied off, and left overnight in a cold room to dialyse in KH. The following day, the KH solution was discarded, and the ionic concentration of the albumin-palmitate solution was readjusted. Glucose (11 mM) was then added to the buffer. This produced a KH solution containing 0.5 %

albumin bound with 0.4 mM palmitate.

Perfusion: Hearts from 13 male Wistar rats (Harlan, UK) in three groups (Intralipid (0.4 mM) n = 4, Intralipid (4 mM) n = 5, albumin (0.5 %) bound to palmitate (0.4 mM) (alb/palm) n = 4 were perfused in the Langendorff mode as previously described (Section 4.1.2).

Spectroscopy: The hearts were initially perfused with KH buffer containing only 11 mM glucose and 0.625 mM pyruvate. A small drain was inserted into the left ventricle, followed by a polyethylene balloon and the EDP adjusted to achieve a pressure of approximately 4 – 5 mmHg once in the magnet. This balloon was set to continually monitor heart rate and developed pressure throughout experiments as a measure of cardiac function. RPP (the rate pressure product) was derived from multiplying heart rate by developed pressure, and was assessed 10 minutes either side of any change in buffer composition.

After locating the heart in the centre of the magnet and shimming to reduce the proton linewidth to around 50 Hz, a hyperpolarized pyruvate study was performed as previously described in Section 4.1.2. Briefly, a 0.625 mM hyperpolarized [1-^{13}C]pyruvate solution was delivered to the heart as a bolus over 120 seconds under a gravity fed system, and a ^{13}C pulse-acquire experiment commenced (TR = 1 s, FA = 30 ^{o}, BW = 180 ppm, 4096 pts). Following acquisition, the sum of 50 spectra were taken, beginning with the first spectrum which showed the appearance of hyperpolarized pyruvate, and the ratio of the bicarbonate and the CO_2 signals to the pyruvate signal was used as a measure of flux through the pyruvate dehydrogenase (PDH) enzyme. All other metabolites were similarly normalized. A fully relaxed, ^{31}P acquisition was performed, followed by a series of rapid, high temporal resolution ^{31}P acquisitions, as previously described in Section 3.2. The KH buffer was subsequently switched to one containing pyruvate (0.625 mM) and either Intralipid (0.4 mM or 4 mM) or palmitate (0.4 mM) bound to albumin (0.5 %) and following a period of stabilization (around

30 minutes) a repeat hyperpolarized pyruvate dissolution was carried out.

T_1 measurements: Hyperpolarized T_1 measurements were carried out by dissolving 2.9 ml of a 20 mM hyperpolarized [1-^{13}C]pyruvate solution into 2.9 ml of either KH, KH with albumin, or KH with albumin bound palmitate, to yield a final pyruvate concentration of 10 mM, with a 16% albumin solution in a 1:3 ratio with palmitate. These values were scaled up from the 0.625 mM pyruvate, 0.5% albumin and 0.4 mM palmitate used above, in order to yield a high enough signal to noise ratio for the thermal T_1 experiments to be performed, so that both hyperpolarized and thermal datasets could be directly compared. Hyperpolarized T_1 was measured by using a multiple flip angle acquisition in order to correct for the effects of RF pulses, and subsequently fitted to an exponential decay function, of the form e^{-t/T_1}. Thermal T_1 measurements were performed on a Bruker Avance 300 MHz system, using a 500 µl volume of the combinations previously stated, with the addition of 10% D_2O for frequency locking. A ^{13}C proton decoupled spectrum was run (zgpg30, n = 128, FA = 30 °, d1 = 2 seconds) in order to determine the frequency of the pyruvate resonance (which was subject to variation with pH and temperature). This value was then used to run an inversion recovery T_1 protocol with power gated decoupling (t1irpg pulse program, with parameters n = 12, d1 = 300, and variable delays of 10 msec, 10, 30, 60, 90, 120, 150 and 180 secs). Thermal T_1 data were processed using TopSpin 1.3 (Bruker BioSpin, Ettlingen, Germany).

Data analysis: Comparisons between two measurements were carried out using a paired t-test. For temporal data with more than two measurements, a 1 way ANOVA with a posthoc Bonferonni-Holm correction was applied. All tests were carried out at the $p<0.05$ significance level. Units are a.u., unless otherwise specified. Data are expressed as mean±standard deviation. Spectra were processed and quantified using jMRUI.

Group	PCr / ATP (a.u.)	Cardiac pH	Heart rate (BPM)	RPP (mmHg / min)
1. KH alone	1.1±0.1	6.9±0.1	310±30	30000±4000
1. Intralipid (0.4 mM)	1.2±0.2	6.9±0.1	310±20	29000±3000
2. KH alone	1.2±0.2	6.9±0.1	290±40	24000±5000
2. Intralipid (4 mM)	1.4±0.1	6.9±0.1	280±20	22000±5000
3. KH alone	1.4±0.1	6.9±0.1	280±20	21000±4000
3. Albumin bound palmitate	1.4±0.2	6.9±0.1	280±20	21000±4000

Table 4.4: Summary of results. Each buffer containing Intralipid (0.4 mM), Intralipid (4 mM) and albumin bound palmitate have their own controls containing KH alone.

4.2.3 Results

Cardiac energetics and function: ^{31}P data and cardiac pH revealed no significant change in PCr / ATP ratio during the change from KH alone to KH with either Intralipid (0.4 mM), Intralipid (4 mM) or albumin bound palmitate (0.4 mM). There were no significant differences in the heart rate or RPP within any of the groups. The data is presented in Table 4.4.

Signal loss: The signal to noise ratio (SNR) of the hyperpolarized [1-^{13}C]pyruvate signal in each of the KH buffers containing 0.5% albumin with 0.4 mM palmitate, 0.4 mM Intralipid or 4 mM Intralipid was measured. There was a significant reduction in SNR upon addition of the albumin / palmitate containing buffer (200±60 to 90±50), but no significant differences in SNR upon addition of 0.4 mM Intralipid (170±50 to 200±70) or 4 mM Intralipid (130±50 to 120±50) were seen. To see if there were changes in the kinetic parameters of the pyruvate signal, an initial analysis was carried out by looking at the time during which hyperpolarized [1-^{13}C]pyruvate maintained signal amplitude above 50% of its maximum during the time course of the hyperpolarized dissolution. Perfusion with hyperpolarized [1-^{13}C]pyruvate in the presence of albumin (0.5%) bound palmitate (0.4 mM) showed a significant increase in the rate of pyruvate signal decay. With perfusions involving 0.4 mM and 4 mM Intralipid,

there was no significant change in the pyruvate signal decay (Figure 4.13).

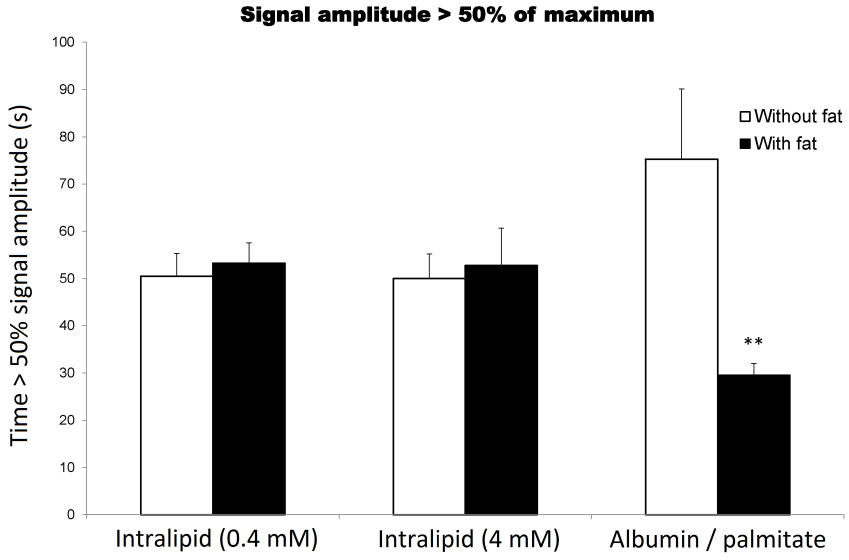


Figure 4.13: The graph shows the time during which the hyperpolarized [1-^{13}C]pyruvate signal remains above 50% of its maximum without and with fats. ** $p<0.01$, n = 13

To try and understand this observed difference further, the hyperpolarized signal data from the perfused heart experiments with and without albumin / palmitate were further considered. In the absence of a suitable kinetic hyperpolarized signal model for the perfused heart (although no shortages exist for *in vivo* models [19, 51, 111, 132–134]), the first portion of the signal (net increase) was approximated by a linear fit, with the second portion, after the maximum signal had been reached (net decay), was fitted to an exponential decay function (Figure 4.14).

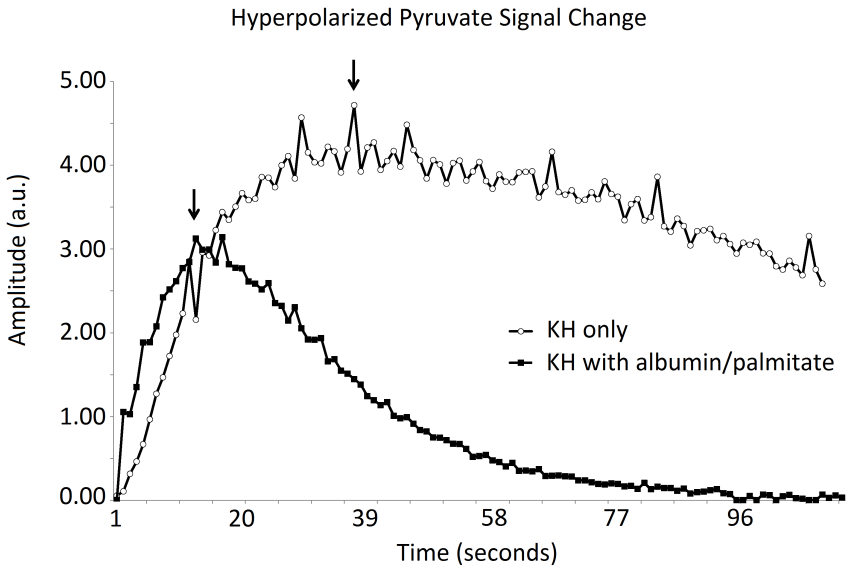
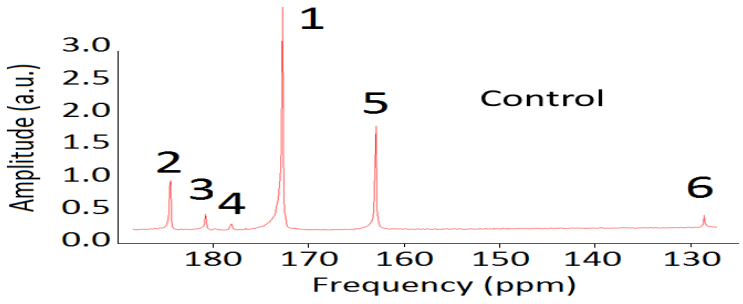


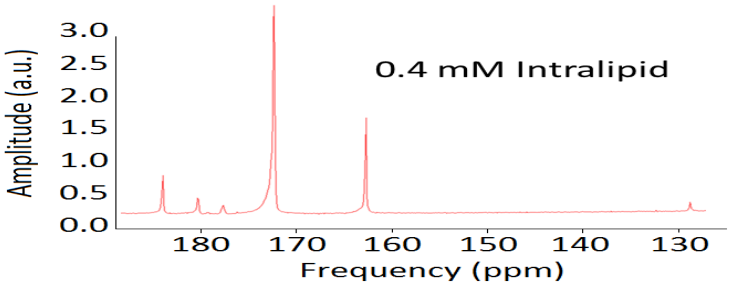
Figure 4.14: Representative hyperpolarized [1-^{13}C]pyruvate signal infusion and decay curves with KH alone or KH with alb/palm. The signal infusion portion begins from the moment signal is seen, up to and including the maximum signal value, indicated by the black arrows. The signal decay portion is everything after the black arrows. The signal amplitudes have been normalized relative to their peak maximum.

Hyperpolarized pyruvate signal infusion and decay were then compared in the absence and presence of albumin / palmitate. In the initial signal increase, the rate of pyruvate (0.032 ± 0.008 vs 0.07 ± 0.03) was significantly increased in the presence of KH and albumin / palmitate, as compared to KH alone. In the signal decay portion, the decay constant of pyruvate (-0.013 ± 0.004 vs -0.052 ± 0.003) was significantly decreased when albumin was present, showing that the rate of decay was significantly increased, as compared to KH alone.

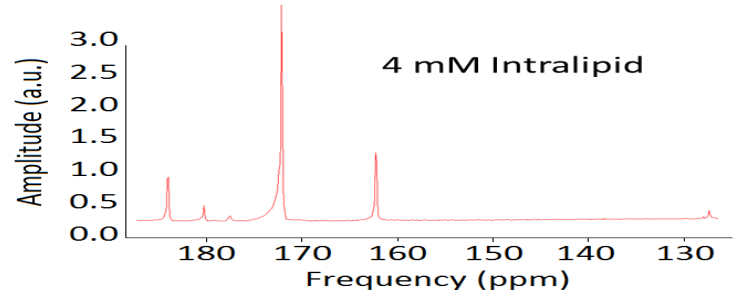
Cardiac metabolism: Example spectra of hyperpolarized [1-^{13}C]pyruvate in the absence and presence of fats are shown in Figure 4.15.



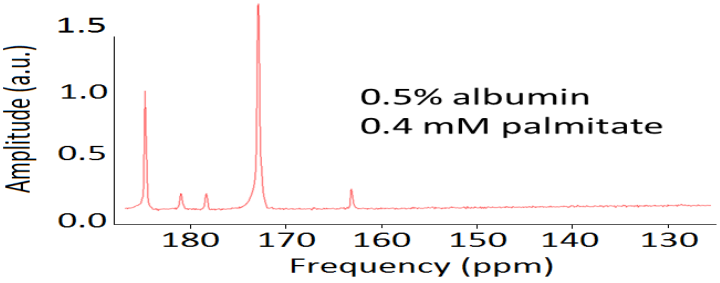
(a)



(b)



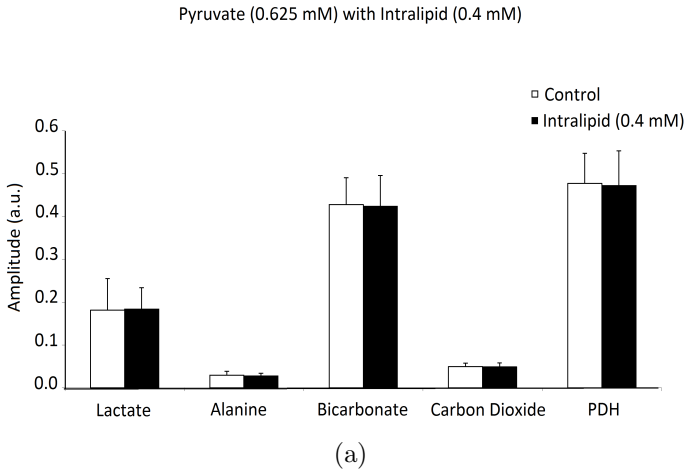
(c)



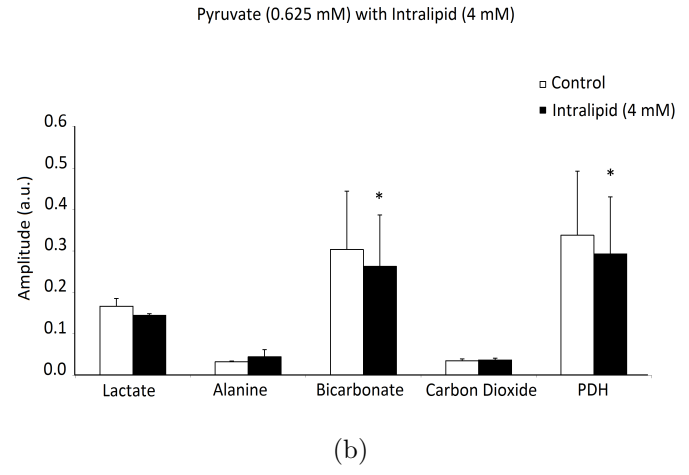
(d)

Figure 4.15: Representative hyperpolarized [1-^{13}C]pyruvate spectra in the absence of fatty acids (control), and in the presence of Intralipid (0.4 mM), Intralipid (4 mM) and 0.5 % albumin / 0.4 mM palmitate. Peaks are (1) pyruvate, (2) lactate, (3) pyruvate hydrate, (4) alanine, (5) bicarbonate, (6) CO_2.

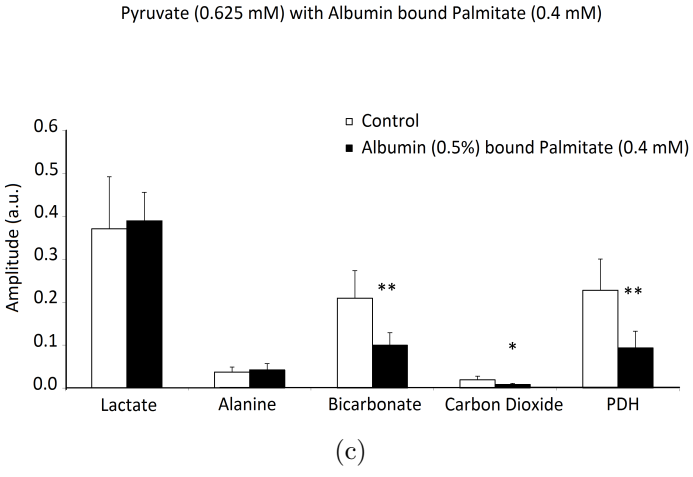
The use of 0.4 mM Intralipid as a source of fatty acid did not elicit any significant change in PDH flux (0.48±0.07 to 0.47±0.08). However, using a higher concentration of Intralipid (4 mM) did reveal a significant decrease in PDH flux (0.34±0.16 to 0.29±0.14). The use of 0.5% albumin in conjunction with 0.4 mM palmitate also proved successful, with a significant decrease in PDH flux seen (0.23±0.07 to 0.09±0.04) (Figure 4.16). There were no significant changes observed for lactate, or alanine.



(a)



(b)



(c)

Figure 4.16: The change in PDH flux, and other [1-^{13}C]pyruvate metabolites, without and with 0.4 mM Intralipid (n = 4), 4 mM Intralipid (n = 5) or Albumin (0.5%) bound palmitate (0.4 mM) (n = 4). *p $<$ 0.05

Hyperpolarized and thermal [1-^{13}C]pyruvate T_1: The T_1 of hyperpolarized

pyruvate in KH buffer was measured to be 27±2 seconds. In the presence of albumin, the hyperpolarized T_1 dropped to 6±1, but partially recovered in the presence of albumin bound palmitate (0.4 mM) to 22±1 seconds. The thermal T_1 of pyruvate in KH alone was 61±5, and with albumin dropped to 29±10 seconds. As with the hyperpolarized T_1 data, this value was recovered in the presence of palmitate to 62±7 seconds. All hyperpolarized T_1s between groups were significantly different. Thermal T_1s between KH alone and albumin were significantly different. The large differences in T_1 values between thermal and hyperpolarized experiments can potentially be explained by an increase in relaxation rate (decrease in T_1) of the ^{13}C nucleus with magnetic field strength, since the experiments were carried out on two different magnets at different field strengths.

4.2.4 Discussion

This study was carried out in order to obtain a method to deliver physiologically appropriate long chain fatty acids to the isolated perfused heart, whilst still being able to use hyperpolarized pyruvate. Previous work [19] concluded that the presence of albumin, even with palmitate, would not allow the use of hyperpolarized pyruvate, unless pyruvate was used in extremely high concentrations (> 20 mM) to achieve a greater signal. This concentration is not desirable for the reasons previously explained in this chapter, nor is it physiologically accurate to provide the perfused heart with a buffer that does not contain fatty acids.

As an example, Boehm et al [135] looked at the effect of palmitate (as would be present *in vivo*) on the isolated rat heart derived from a model of hyperthyroidism, and found a significant drop in cardiac output when fatty acids were supplied. This was associated with decreased myocardial efficiency (caused by increased mitochondrial uncoupling proteins (UCP)). A significant increase in fatty acid oxidation was noted [136], which would be expected to cause a decrease in glycolysis, and therefore a drop

in PDH enzyme activity. This was confirmed in a separate study, where Atherton et al [78], using the same model, carried out a hyperpolarized pyruvate study *in vivo* and found a near 60% drop in PDH flux. Provision of the long chain fatty acid palmitate caused increased uncoupling, by inducing a stressor. By solely providing glucose and pyruvate to the isolated heart, these major effects are likely to be overlooked. For example, had this PDH enzyme activity been measured in the isolated perfused heart, without the use of fatty acids, it could be tentatively predicted that if indeed the primary cause for the PDH reduction was the hyperthyroid mediated increase in FAO, then little or no change would have been seen in PDH flux.

The work described here has successfully demonstrated that it is possible to use albumin and palmitate in combination with sensible, near physiological concentrations of pyruvate, but that there is a reduction in T_1, and therefore a reduction in observed signal. In addition, it has also been shown that an alternative exists, in the form of Intralipid which can be used in cases where a hyperpolarized probe with a low polarization is to be used, and any potential decrease in its T_1 would cause unacceptable signal loss. In terms of mechanism for the hyperpolarized signal loss in the presence of albumin, both the thermal and hyperpolarized T_1 data shows that a decrease in T_1 was responsible for the loss of signal, and that the binding of pyruvate to albumin effectively renders a portion of the hyperpolarized pyruvate pool MR invisible. This happens in a dynamic fashion however, such that there is constant exchange between the albumin – pyruvate pool and the free pyruvate pool. As the magnetization caused by hyperpolarization is non-recoverable, the result is a quenching of the hyperpolarized signal. The significant increase in the gradient of the hyperpolarized pyruvate signal in the presence of albumin is due to the competing effect between the influx of fresh, but constantly decaying hyperpolarized signal, with the rapid signal decay due to albumin binding (Figure 4.14). Looking at this graph, the manner in which the signal decays is different for both. In the KH only situation, it appears that there

is still a continuous influx of hyperpolarized pyruvate, thus giving the decay curve a more convex appearance (of the form $-Ax^2 - Bx$), where contributions from new signal and decay are roughly equal. In the situation with KH and alb/palm, whilst there is at all times during acquisition an influx of pyruvate, it appears that the polarization is lost much sooner, and so the decay portion resembles much more closely an exponential decay function (Ae^{-kx}), as it is dominated by the T_1 decay. Looking at the beginning of the signal (signal infusion), it would seem that in the case where alb/palm is present, the magnetization of the entire hyperpolarized pyruvate pool is reduced considerably (to a third of the KH alone value, as previously shown), which would mean that it takes less buffer flow (containing the hyperpolarized pyruvate) to obtain maximum signal, since the mixing of pyruvate and buffer is not perfect, and there will be a gradient as it reaches the heart. This is further exasperated by the fact that albumin itself is absorbing part of the pyruvate pool (albeit dynamically), which would worsen this effect.

It is possible to reduce the extent to which this loss of magnetization happens however, by binding albumin with palmitate in a high density (3:1 was used here), and indeed this is confirmed in the results with a partial recovery of the T_1 of pyruvate. The albumin / palmitate ratio was chosen as the result of previous work on the kinetics of albumin [137, 138], which demonstrated that there are six high availability sites with strong binding affinity for palmitate and a further six sites with medium binding capability. As the limiting factor for binding is unlikely to be the availability of sites, and much more likely to be due to the negligible solubility of palmitate in any form in aqueous solutions [139], a conservative 3:1 ratio was chosen. It was also shown that the binding of these sites reduces the binding constants for the other secondary and tertiary sites present on albumin (of which there are more than 60), so possibly explaining the reason for the recovered T_1, as pyruvate is less likely to bind to these sites if palmitate binding has induced a conformational change. Other more involved

techniques were explored, including the possibility of acetylating or guanidating BSA, thus removing many of the polar interactions that a small molecule like pyruvate is likely to rely on for binding. This was shown to be successful, in that palmitate could still be bound, but this possibility was not explored further as little is known as to how chemical alteration of BSA may alter FA delivery to the myocardium.

A possible biological alternative to providing the heart with fatty acids (in the form of triacylglycerols), without the possibility of interfering too much with the hyperpolarized signal would be using chylomicron and VLDL preparations. These can be generated *in vivo* by liver perfusion over several hours [140] to produce VLDL in very small quantities. The resultant lipoproteins are successfully taken up by the isolated perfused heart [141]. This method is typically used for radiolabelled experiments, but with a small enough recirculating volume, could be adapted for hyperpolarized experiments.

The results of perfusions with Intralipid unfortunately did not demonstrate a significant PDH reduction at the lower concentrations (0.4 mM), and it required a ten-fold increase in Intralipid (4 mM) before being able to observe a significant change in PDH flux (Figure 4.16). It would seem that the lack of an efficient transfer mechanism for cardiac uptake, as described for VLDL and albumin, is partially responsible for the much larger concentrations of Intralipid required. However, the advantage is that there is no appreciable change in hyperpolarized signal or its decay in the presence of this substrate, which makes it particularly suitable for those hyperpolarized probes with low SNR to begin with. In addition, no significant detrimental alterations to cardiac function or energetics were seen when using the higher concentrations of Intralipid. One caution with Intralipid, particularly during long perfusions is its stability with the high ionic concentration of the buffer used. Flocculation was not observed to occur (this would manifest fairly evidently as the buffer consistency would change from skimmed milk to a yellow, unevenly distributed solution). Nevertheless,

this should be checked carefully.

Other possible experimental methods for fatty acid delivery to the heart without the extent of signal loss seen using high albumin concentrations might include the creation of palmitic acid based micelles [142], or the use of large molecules that can surround palmitate (or other FA molecules), and render them soluble [143, 144]. The referenced works demonstrate this method using β-methyl cyclodextrin, which is able to successfully and efficiently transfer large chain fatty acids to membranes, although done in an uncontrolled manner. This remains to be tested on a larger scale, using whole organ systems.

In conclusion, this work has demonstrated two classes of potential alternatives to the problem facing hyperpolarization with isolated perfused organ models, to successfully provide the perfused heart with a source of fatty acids without affecting the integrity of the hyperpolarized pyruvate experiment. The use of Intralipid in the perfusion buffer would appear to provide a satisfactory source of fatty acids to allow for more physiological experiments when using hyperpolarized pyruvate in the setting of the perfused heart model. However, when using hyperpolarized probes with high polarization, that have a certain binding affinity to albumin, such as pyruvate, the use of albumin and palmitate can still provide the gold standard for heart perfusions.

Chapter 5

Hyperpolarized Probe Development

5.1 Introduction

From the outset of dissolution DNPs' rapid development, one of the major problems has been a lack of variety in the availability of useful metabolic probes. [1-^{13}C]pyruvate has become extremely popular due to its ease of use and very good signal to noise ratio, but allows for only a small subset of metabolism to be explored. Recently however, the development of novel hyperpolarized probes has been expanding rapidly. [2-^{13}]pyruvate has been used to explore cardiac metabolism [77], fumarate to localize and attempt to quantify cell death [145], ascorbic acid to determine the oxidative state of tissue [146], amongst many others [113]. Whilst these probes have shown promising results for their specific applications, there was still a lack of suitable compounds addressing the many pathways of cardiac metabolism (recently, alanine [147] and lactate [148] have, however, been tested *in vivo* in different models). In order to address this issue, the aims of this chapter were to develop and test new metabolites of interest, in particular, those that could act as fuels for the

heart.

In order to complement the information provided by pyruvate, at the end of the glycolytic pathway, hyperpolarized lactate and alanine were characterized. In addition, given the prominence of fatty acids as a fuel for the heart, these needed to be considered. Due to the very short T_1s of long chain fatty acids, which would primarily be used in the heart, the short chain fatty acid butyrate was considered. Following this, its metabolites, the ketone bodies (and cardiac fuels in themselves during fasting) were hyperpolarized and tested. The metabolic pathway for this is described in Chapter 2.

There are a number of factors that make compounds suitable for the DNP hyperpolarization process. For metabolic work, the compound chosen must be metabolically relevant, or at least be a prodrug (and therefore metabolize to a compound that is of use, the conversion of ethyl pyruvate or ethyl acetoacetate to pyruvate and acetoacetate are examples of such conversions). Compounds also need to satisfy the following criteria:

Relaxation time: The T_1, a measure of the length of time the hyperpolarized metabolite will retain its high signal (high polarization), must be sufficiently long for it to be taken up by the biological system of interest and metabolized, whilst considering the delay in getting the hyperpolarized compound from the hyperpolarizer to the isolated perfused organ, or *in vivo* model. In practice, this usually translates to a compound having a molecular mass of around 200 or less, which results in a T_1 of 20 seconds or more. Secondly, only certain functional groups within these compounds typically have such long relaxation times, namely carbonyls, carboxyls or quaternary carbons. It is possible to overcome this limitation, however, by deuterating (replacing a hydrogen with a deuterium atom) a carbon in a metabolite of interest. Several successful compounds with high T_1s and polarizations have been developed in this way [149]. However, such compounds are rarely commercially available and must be

synthesized. Ubiquitously deuterated compounds will tend to improve T_1, irrespective of the carbon of interest, and whilst they are more easily available commercially, are prohibitively expensive. It is also possible to increase the T_1 by using deuterated solvents in either the formulation of the compound (which also increases polarization [150]), and / or the dissolution buffer, but in practice, this serves little purpose as the DNP hyperpolarized compound will spend most of the time within (non-deuterated) physiological KH buffer, or blood. In addition, deuterated compounds are toxic to living tissue in large quantities, due to the altered enzyme kinetics of the deuterium bond.

T_1 can also change with field strength (though not necessarily linearly). Whilst little can be changed in this respect, it is worth noting, as it implies that hyperpolarized compounds which prove successful in the isolated perfused organ model (generally used in conjunction with a high field magnet), may prove less successful *in vivo* (where a lower field magnet is typically used) or vice versa. Another interesting effect is the acidity and basicity of a compound, which is also capable of having an extremely large effect on the observed T_1. Certain small amino acids demonstrate this very well. Under very acidic conditions (i.e. when the amine and carboxylic acid groups are protonated), the T_1 is very high. However, under basic conditions, the T_1 reduces to a fraction of its original value. There is generally a good middle ground at physiological pH. Therefore, care should be taken when choosing the pH of the compound formulation – changing this is sometimes necessary to ensure compound solubility (discussed later), and if basic conditions, which dramatically reduce T_1 for amino acids, are chosen for this, the dissolution must neutralize the hyperpolarized sample rapidly. Failure to do so will remove any hyperpolarized signal very quickly. As a guide for formulation, thermal T_1s of at least 25 seconds or more for compounds can be used as a good indicator of the likelihood of success. For comparison, the very successful [1-^{13}C]pyruvate has a T_1 of ~ 60 seconds.

Glassing: The compound must form a glass (a state of matter with a short range order) in the solid state after freezing. Formation of a crystalline solid is opaque but a glass will be translucent when frozen. Glassing is required so that the interaction between the compound and the microwave irradiation allows polarization of the nuclei. This is as a result of better microwave distribution in the glass, and secondly, the improved ^{13}C-^{13}C spin diffusion that must occur for the hyperpolarization process to be successful. Given that there is generally about 1 paramagnetic center (i.e. the OX063 radical) per 1000 ^{13}C nuclei in the optimum polarization mixture, the importance of spin diffusion becomes evident. In a few cases (notably pyruvic acid), the liquid metabolite of interest glasses without any additional solvents. Typically, however, another solvent is required to allow glassing, for both liquid and solid metabolites. Where metabolites are present in the solid state, these must first be dissolved before they can be used. Typically, as these metabolites are small, as a result of the T_1 requirements, a small amount of water can be sufficient to create a glassing mixture. However, these are exceptions, and in the majority of cases, another solvent (or mixture of solvents) is needed.

Many compounds will glass when dissolved in glycerol, a physiologically occurring alcohol produced from triglyceride metabolism. It is self glassing, and excellent at glassing a wide range of small metabolites. It should arguably be the compound of choice in formulations used in humans, as its metabolism is well understood, and should not cause any undue physiological disturbances *in vivo* since it is used in such small quantities. However, in the research setting, glycerol suffers from several drawbacks. It is extremely viscous, and dissolving solids in it is very difficult and time consuming. The final mixture is difficult to work with, in terms of transferring the prepared sample to a sample cup for hyperpolarization. Finally, glycerol based samples additionally can produce unreliable polarizations. However, where chemistry facilities with adequate equipment allow for the preparation of prepackaged samples

ready for hyperpolarization, glycerol should be used in the clinical setting.

In routine use, DMSO has been the solvent and glassing agent of choice for all sample preparations. It is an excellent glassing agent, very miscible with polar molecules, and not at all viscous. A disadvantage with DMSO is that it is not naturally produced in living systems, but in experiments typically run, less than 1 mM DMSO is used for the isolated perfused heart. Therefore, DMSO should be considered safe in the concentrations used (DMSO is used extensively *in vitro* and *in vivo*, with extensive characterisation [151]), however, DMSO does have one issue which was observed in some hyperpolarized samples. If left for a period of time in formulation, the OX063 radical will tend to come out of solution, and cannot be easily reincorporated. For this reason, in this work, DMSO was always added to the sample immediately prior to insertion into the polarizer. With careful consideration of the order in which all the components of the probe formulation are added, issues such as these can be avoided. In terms of strategies for solubilizing and glassing compounds, there are two further factors to consider. Both the OX063 radical, and the Gd based contrast agent must dissolve in the final mixture. If the compound is a liquid, but does not glass, adding a small amount of DMSO will usually glass the solution. Deciding on the amount to add depends on ensuring that the sample is not diluted too much (discussed later), but it is also important that the sample glasses in a stable and repeatable manner, and thus adding a little more than the minimum required amount of DMSO (or other glassing agent) is recommended. Examples of other glassing agents will be discussed later in considering the formulation of butyrate. It is unsual that solid compounds dissolve well in DMSO – for this reason, solids should be dissolved in a minimum amount of water, with the help of a sonicator. This solution should be fluid, with a little more water added if necessary. This will ensure easy and reliable transfer to the sample cup, where DMSO is then added prior to insertion in the hyperpolarizer. The caution with adding additional fluid to the sample is that more concentrated samples

tend to have shorter build up times, and higher polarization amplitudes [50].

Radical and gadolinium contrast agents: The radical used throughout this thesis (OX063, sometimes referred to by the internal identification at GE Healthcare, AH100136) is a green powder, with a molecular mass of 1426.78. It is light sensitive and highly susceptible to static charge. It is surrounded by many bulky ligands, whose purpose is to prevent interaction between the radical and external molecules. Radicals are highly reactive species, and their protection is key in maintaining their effectiveness for DNP hyperpolarization experiments. OX063 is very soluble in water, glycerol and DMSO, and is supplied in purities ranging from 80% to 99% - a fact which should be taken into account when preparing sample formulations. This is currently the best radical available for wide spread DNP hyperpolarization experiments. Other radicals can be used, though these tend to produce lower hyperpolarization levels. These radicals are structurally similar to OX063, and include Finland (AH110355, MW = 1036.14) and OX063Me (AH111501, MW = 1546). More complex biradicals have been generated, but ultimately have not proved successful enough to justify the increased cost [152].

The gadolinium complex generally used is a commercially available contrast agent (Dotarem, Guerbet, France) with bulky ligands surrounding the gadolinium metal complex. The reason for this is slightly different to that of the OX063 radical – in this case, the bulky ligands serve to prevent electron interaction between the gadolinium itself and the hyperpolarized nuclei. Without these ligands, DNP hyperpolarization would occur as normal inside the hyperpolarizer, but upon dissolution, all enhanced signal would be lost, as free gadolinium acts as a rapid relaxation agent. This is demonstrated with the use of free gadolinium chloride in sample preparations producing excellent polarization amplitudes, but no liquid state polarization. Where gadolinium is used in this text, it is taken to refer to the complexed form. Gadolinium sample addition has the effect of increasing both polarization amplitude and buildup

time until saturation occurs. The role of gadolinium as a facilitator of electronic – nuclear spin diffusion is particularly interesting, as its use appears to become redundant when DNP hyperpolarization occurs at higher magnetic field strengths [153].

Deciding on the amount of radical and gadolinium agent to add to a formulation is largely based on trial and error, but this process can be improved by observing certain trends. Minimization of experimental time in this way is especially important given the high cost of the OX063 radical. Increasing radical concentration increases polarization amplitude to a maximum point, after which it decreases again linearly. Buildup time (the time it takes to reach maximum potential polarization) however decreases exponentially with increasing radical concentration (Figure 5.1).

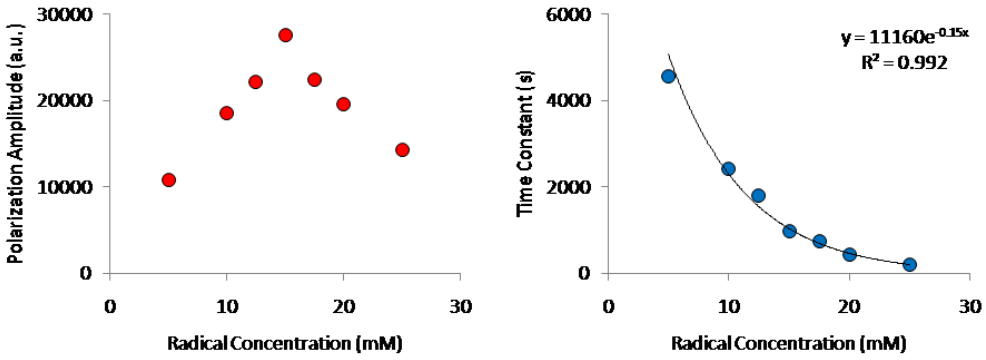


Figure 5.1: A diagram showing the change in buildup amplitude and time with varying OX063 radical concentration using [1-^{13}C]pyruvic acid in the solid state. Reproduced from [58].

By using these properties, a great deal of time can be saved in troubleshooting compound formulations. A good starting point for the radical concentration is 15 mM, as this is the concentration currently used for a wide variety of compounds.

Dissolution considerations: To ensure adequate dissolution of the frozen hyperpolarized compound, 6 mls is typically used as a dissolution volume, though this can range from around 4 mls to 10 mls, in order to better control the concentration at which the hyperpolarized sample leaves the polarizer. Whilst the assumption has

always been that the developed probe needs to be soluble in an aqueous solution, usually the case in metabolic experiments, organic solvents could also be used for the dissolution step in the hyperpolarizer, perhaps for probes that are difficult to solubilize. This may prove useful for specialized experiments.

Taking all of these factors into account, a summary of the steps needed to optimize a sample for DNP hyperpolarization is shown in Figure 5.2. In the light of these steps, the aims of this chapter were to demonstrate a specific example of compound formulation from initial testing to application in a disease model *in vivo*. Hyperpolarized [1-^{13}C]butyrate was chosen as it provided a novel way to assess short chain fatty acid metabolism. In addition, formulations for the other relevant metabolites, lactate, alanine, acetoacetate and β-hydroxybutyrate were developed, characterized, and tested in the isolated perfused rat heart and subsequently described.

5.2 General methods

Compound development: The labelled compounds [1-^{13}C]pyruvic acid, [1,3-^{13}C]β-hydroxybutyrate, [1-^{13}C]lactate (sodium salt) (50:50 w/w solution with water), [1-^{13}C]alanine, [1-^{13}C]ethyl acetoacetate and [1-^{13}C]butyric acid were obtained as high purity samples (> 98%) from Sigma Aldrich (Gillingham, UK).

[1-^{13}C]alanine was converted to the aqueous soluble hydrochloride salt as follows: 142 mg of [1-^{13}C]alanine was added to 200 μl 37.5 % w/w concentrated hydrochloric acid with 600 μl ethanol and vortexed until completely dissolved. This solution was very slowly added to 25 mls of ethyl ether, and spun down for 10 minutes at 1500 rpm. The top ethyl ether layer was removed by pipetting, and the white powder ([1-^{13}C]alanine hydrochloride) was then air dried.

It was not possible to directly obtain free acetoacetic acid or the sodium salt, presumably due to its short half life (2 hours for the acid, several days for the base),

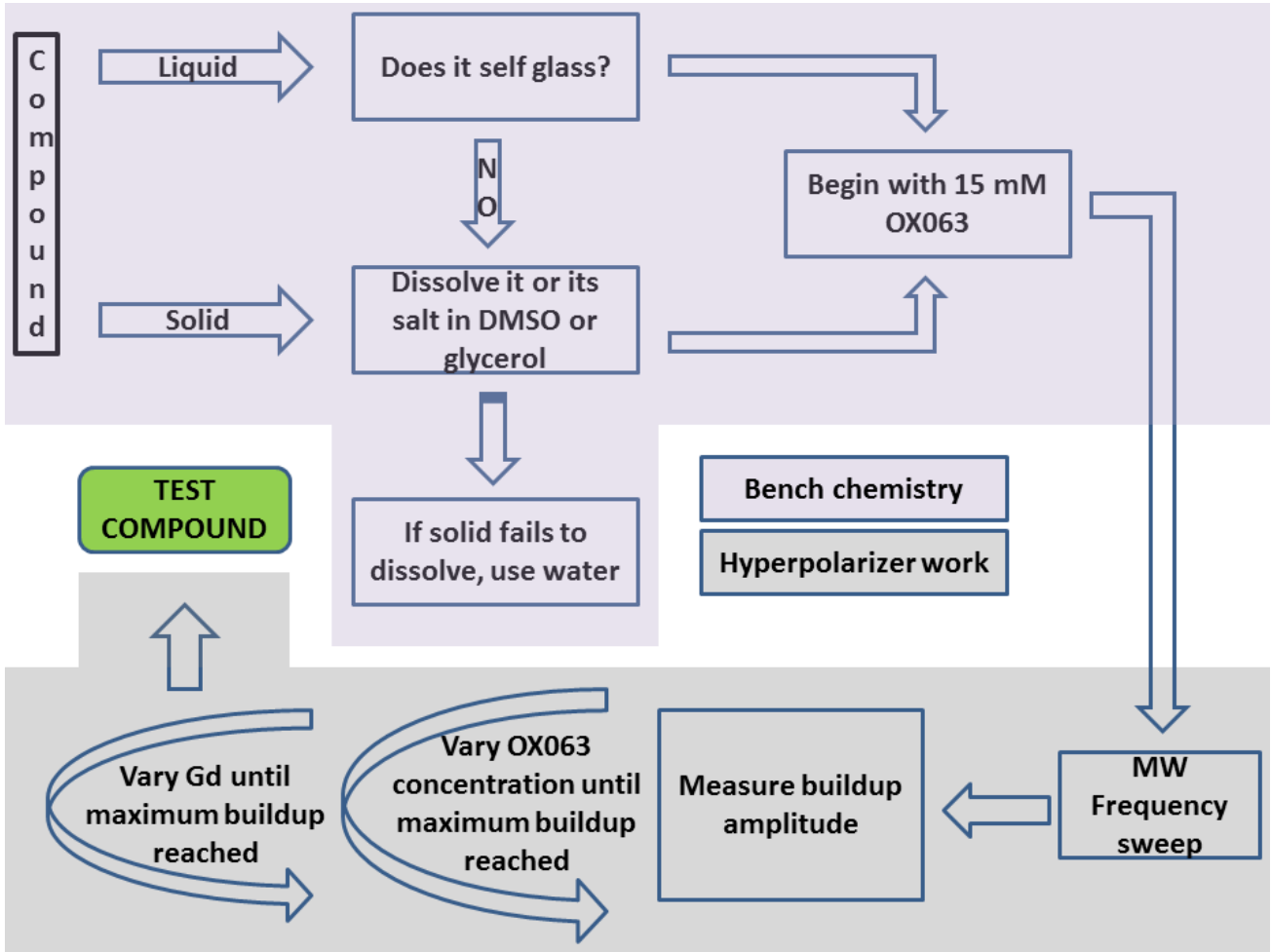


Figure 5.2: A diagram showing the formulation and optimization steps used in this thesis.

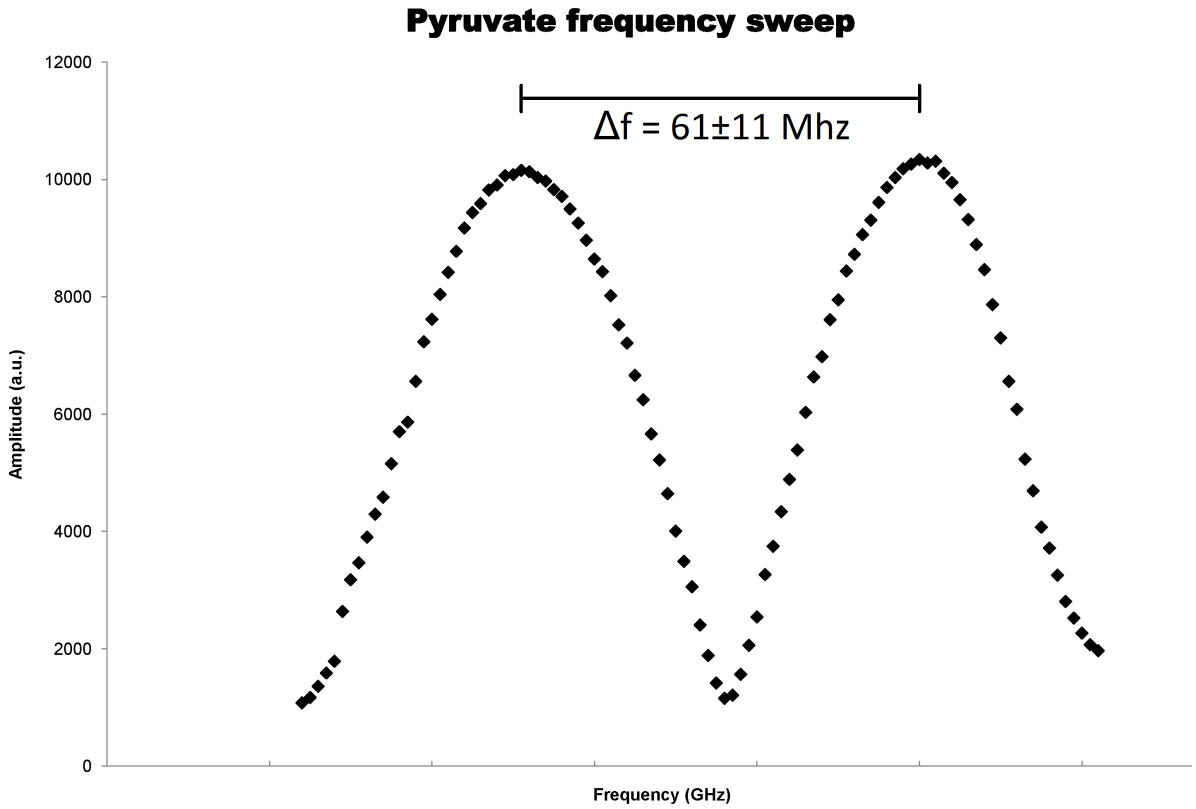


Figure 5.3: An example microwave sweep reflecting the thermal mixing effect of [1-^{13}C]pyruvate hyperpolarization. The difference between the maxima of each of the peaks is shown by Δf. Microwave irradiation time was 300 seconds per 1 MHz step.

whereby decomposition occurs via decarboxylation. [1-^{13}C]Ethyl acetoacetate was therefore converted to sodium acetoacetate as follows: 500 µl [1-^{13}C]ethyl acetoacetate was added to 8 ml of 1M NaOH and stirred for 10 hours at room temperature. The solution was then freeze dried overnight, to create the product, a white powder.

Characterization: Microwave sweeps, i.e. the variation in maximal polarization with microwave frequency, were carried out for all compounds, and show the same profile (a pattern reflecting a likely thermal mixing effect). An example of this is shown with [1-^{13}C]pyruvate in Figure 5.3. Differences in the absolute optimum polarization frequency occur over time due to instability in the microwave source, and therefore the frequency difference between the positive and negative polarizations are

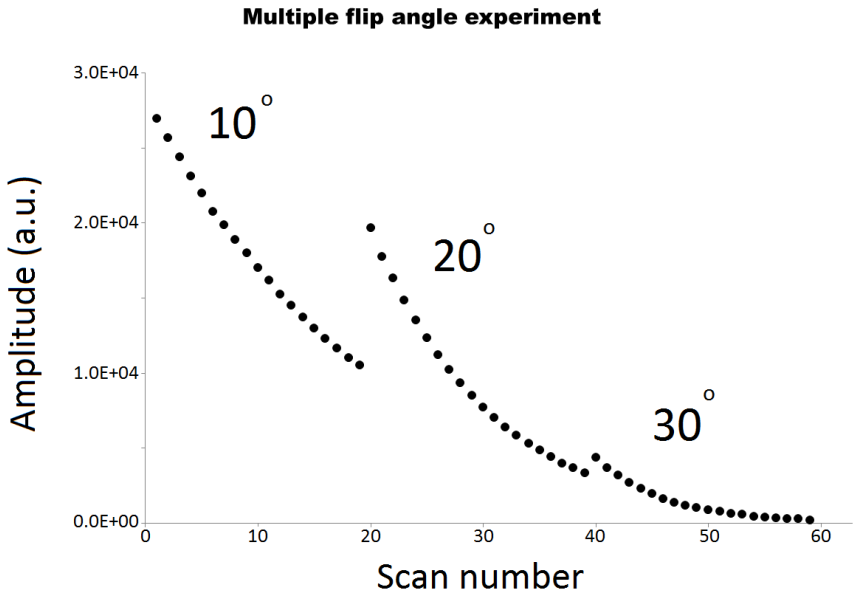


Figure 5.4: A sample plot showing the variation in acquired hyperpolarized signal amplitude over time using three different flip angles (10°, 20° and 30°).

quoted in this thesis. Polarization amplitudes and buildup time constants for each of the compounds were obtained from the HyperSense, following polarization of each compound for 1 hour. Liquid state hyperpolarized T_1 and polarizations were derived by injecting 4 ml of hyperpolarized compound into a pre-shimmed 20 mm NMR tube, and two ^{13}C scans were started. The first was a multiple flip angle experiment (FA = 10°, 20°, 30°, NS = 20 per FA, TD = 4096, SW = 180.693, TR = 1.25 secs) to obtain the T_1 as derived from a modified exponential fit. This protocol was used as it allowed FA variation within the T_1 fitting algorithm, to minimize FA calibration errors. An example of the data acquired is shown in Figure 5.4. The second scan was a thermal equilibrium experiment (NS = 24, TD = 4096, SW = 180.693, TR = 250 secs) of the hyperpolarized sample (after complete loss of hyperpolarization), in order to derive the liquid state polarization relative to the hyperpolarized state. The SNR from the first hyperpolarized spectrum and the thermal scan were used in Equation 5.1 to derive the polarization. For the above characterizations, [1-^{13}C]pyruvate was used as a comparison.

Algorithm 5.1 The equations used to measure the polarization as dervied from the measured signal to noise ratios (SNR). NS = number of scans, FA = flip angle and B_0 = 11.7 T.

$$\text{Polarization} = \left(\frac{SNR_{hyp}}{SNR_{thermal}}\right)\left(tanh\left(\frac{\gamma\hbar\mathbf{B_0}}{2k_bT}\right)\right)$$

$$\text{SNR}_{\text{hyp}} = \frac{SNR_{measured}}{Sin(FA)\sqrt{NS}}$$

$$\text{SNR}_{\text{thermal}} = \frac{SNR_{measured}}{Sin(FA)\sqrt{NS}}$$

Finally, all hypepolarized samples were tested in the isolated perfused rat heart, using methods previously described in Chapter 4. All KH buffers were matched in composition to the concentration of the hyperpolarized probe used. Hyperpolarized [1-^{13}C]alanine, was tested at 2.5 mM, [1-^{13}C]lactate, [1,3-^{13}C]β-hydroxybutyrate, [1-^{13}C]acetoacetate and [1-^{13}C]butyrate were all tested as 4 mM solutions.

5.3 Butyrate

Butyrate, as one of the most promising compounds of those developed in this thesis, was followed through as a case study in order to demonstrate an approach to probe development from start to finish, thus completely evaluating a potentially useful hyperpolarized metabolite. Each of the steps taken will be described below.

5.3.1 Glassing

Compound mixture	Glasses
Butyric acid	Opaque
Butyric acid:glycerol 50:50	Opaque
Butyric acid:ethylene glycol 50:50	Opaque
Butyric acid:EtOH 50:50	Opaque
Butyric acid:$CHCl_3$ 50:50	Opaque
Butyric acid:propan-2-ol 50:50	Transparent
Butyric acid:DMSO 50:50	Transparent

Table 5.1: Glassing experiments

The first step taken was to glass the compound, by cooling it in liquid nitrogen and observing whether it becomes transparent or opaque. The results of this development are shown in Table 5.1. It can be seen that butyric acid itself does not glass, and therefore a variety of solvents, which could act as glassing agents were surveyed. Some of the agents used require comment. All solvents used were miscible with butyric acid. At this stage, the aim was not necessarily to choose glassing agents which were biologically sound, but to obtain an idea of the classes of compounds that could be used for the task. This can be misleading, however, as not all glassing agents work for all compounds. Ethylene glycol for example has previously been used to glass ^{15}N labelled nitrate for hyperpolarization but was not seen to work in this case. Increasing the ratio of glassing agent to compound would not be sensible, as this would reduce the compound concentration, thereby reducing potential buildup amplitude, and therefore the achievable polarization and acquired SNR levels. DMSO appeared to be the better choice here for general compound formulation. In contrast to alcohols, DMSO has a higher dipole moment, and is therefore better able to dissolve small polar molecules (of the kind that make up a large number of small metabolites under consideration for hyperpolarization studies). The OX063 radical did not appear to be stable in the alcohols for any length of time. DMSO is relatively unreactive with respect to the compounds used in this thesis. Given the above properties, and

therefore its ability to glass a far wider range of metabolites, DMSO was chosen as the glassing solvent for all hyperpolarized probes in this thesis.

5.3.2 Radical and Gd addition

A series of different OX063 and Gd concentrations were attempted, with the aim to maximize potential polarization, and minimize buildup time. This is perhaps not as acute an issue with *in vivo* work, where only one hyperpolarized injection per animal tends to occur, or indeed for the newest hyperpolarization system (Spinlab, GE Healthcare), which is capable of multiple sample hyperpolarizations at one time, but for isolated perfused organ work, where more than one hyperpolarized dissolution is carried out per organ, a balance must be made between buildup time, and the total duration of the perfusion experiment. Therefore, a time limit of 1 hour was imposed in order to achieve the best polarization. Table 5.2 summarizes some of the formulations attempted for hyperpolarized [1-^{13}C]butyric acid. Some comments are needed on the formulation table. Increasing the OX063 radical concentration is seen to increase buildup amplitude (until it decreases again), but drops the time constant. Gd increases both buildup amplitude and time constant. Initially, a 50:50 ratio of glassing agent (DMSO) and [1-^{13}C]butyric acid was used, and whilst this produced satisfactory polarizations, it was unlikely to be adequate for experimental use. Therefore, the ratio between the two was changed, and less DMSO was added, and replaced with [1-^{13}C]butyric acid. This would naturally be expected to increase the buildup amplitude, simply by virtue of the fact that there is more labelled probe present. However, if this ratio changes too much in favour of [1-^{13}C]butyric acid, the sample will no longer glass.

Formulation	OX063 (mM)	Gd (mM)	TC (s)	Buildup (a.u.)
Ba:DMSO 50:50	7.5	0	3000	1500
	15	0.2	1500	3000
	15	0.5	1500	6600
	15	1.5	2700	12000
	15	1.7	2600	11000
	22.5	1.0	2000	10000
	22.5	1.5	2100	10800
Ba:DMSO 80:20	15	0.7	3100	17000
	15	1.0	4000	18500
	15	1.4	4200	17000
	20	0.7	2000	12000
	20	1.0	2800	17000
	22	0.7	2000	10000
	22	1.0	2800	15000
	22	1.2	3000	18000

Table 5.2: A table showing some of the formulations attempted for hyperpolarized [1-^{13}C]butyric acid. TC (time constant) is a metric used to indicate the time taken for polarization buildup. Buildup is the measure of hyperpolarization achieved within the polarizer, as a function of the total sample volume. Ba = butyric acid

5.3.3 Final formulation

From this development work, the final formulation of [1-^{13}C]butyric acid was seen to be made up from 20.74 µl butyric acid, 0.54 mg OX063, 5.18 µl DMSO and 3.4 µl 10 mM Dotarem. The liquid state polarization obtained was 7±4%, with a measured hyperpolarized T_1 of 20±1 seconds. A sample microwave sweep is shown in Figure 5.5. An example spectrum of both the thermal and hyperpolarized [1-^{13}C]butyrate are shown in Figure 5.6.

5.3.4 Testing

Following good sample polarizations, hyperpolarized [1-^{13}C]butyric acid was then tested on the isolated perfused rat heart, using a 4 mM concentration of the compound (a sample spectrum is shown in Figure 5.7), which produced a series of metabolite peaks. A compound such as this had never been developed before, and there was little

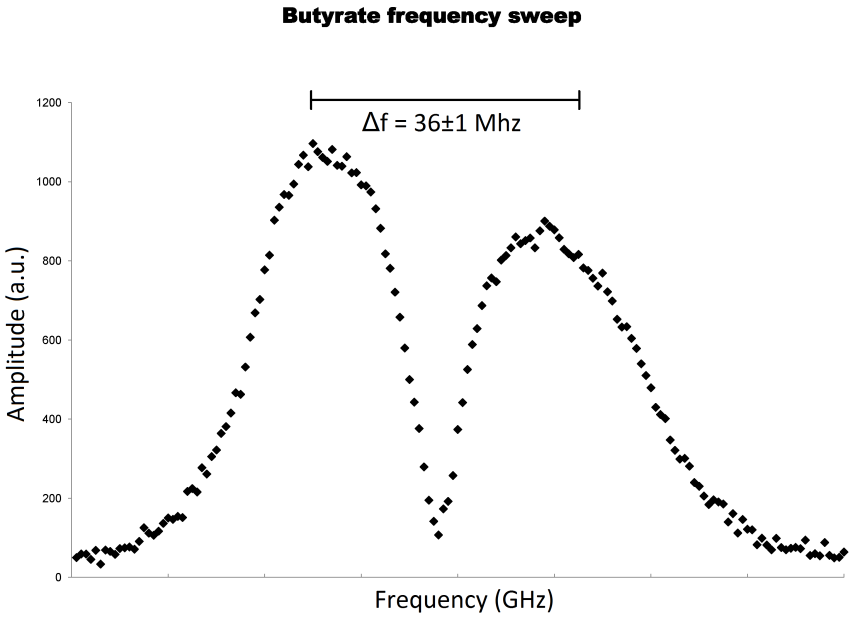
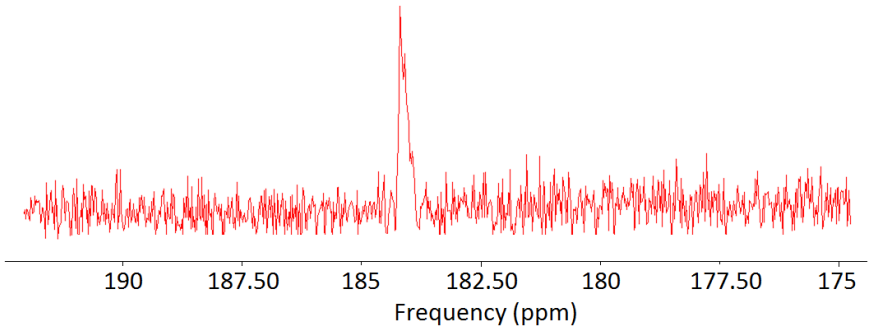
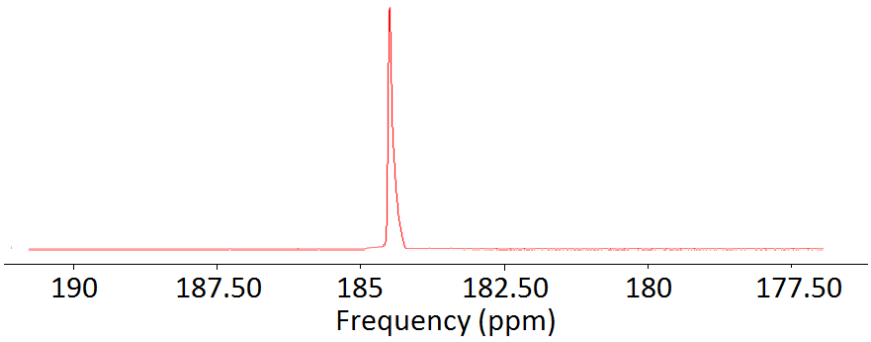


Figure 5.5: A sample microwave frequency sweep of hyperpolarized [1-^{13}C]butyric acid. Δf denotes the frequency separation between the peak maxima.



(a)



(b)

Figure 5.6: Shown are representative [1-^{13}C]butyrate spectra, under thermal conditions (a) and following hyperpolarization (b).

in the way of spectral peak information, as compared to the information available on hyperpolarized pyruvate metabolites. Therefore establishing the identity of the peaks required further work.

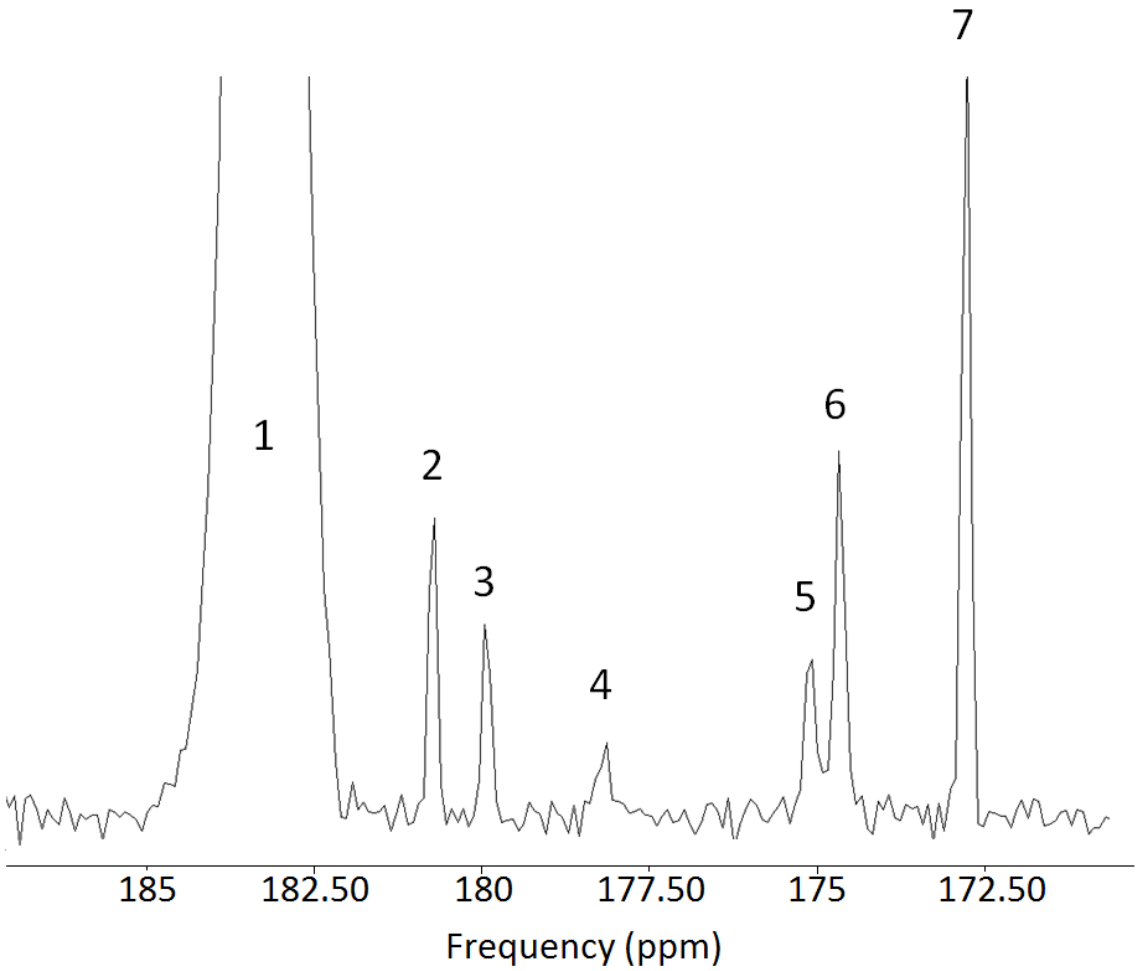


Figure 5.7: A representative hyperpolarized [1-^{13}C]butyrate spectrum from the isolated perfused rat heart. The peaks were positioned at (1) 184 ppm, (2) 181.16 ppm, (3) 181.1 ppm, (4) 178.43 ppm, (5) 175 ppm, (6) 174.6 ppm and (7) 172.6 ppm.

Metabolite identification: A male Wistar rat heart was perfused for 40 min with KH buffer, at a constant flow rate of 15 mls / min, with recirculating buffer, using labelled [1-^{13}C]butyrate at a concentration of 4 mM. After 40 mins, the heart was freeze clamped in liquid nitrogen and kept at -80°C until needed. Metabolite extraction was performed as follows: 200 µl of 2:1 methanol / chloroform was added to half

of a heart (˜ 500 mg) crushed in liquid nitrogen, and sonicated for 15 mins. Following this, 200 µl of water and 200 µl of chloroform were then added, briefly vortexed and centrifuged at 13,500 rpm for 20 minutes. The aqueous layer was then removed and air dried (approximately 2 hours). The dried yellow extract had 400 µl of D_2O in 250 mM sodium phosphate (pH 7.4) added to it, vortexed, put into a 5 mm NMR tube and run on a Bruker Avance 300 MHz system. ^{1}H spectra were acquired using a water suppression pulse sequence (SW = 4789, NS = 1024, points = 16384, ppg = zg60pr), followed by a 2D HMBC acquisition correlating ^{1}H and ^{13}C nuclei across multiple bonds (NS = 256, ppg = hmbcgpndqf, SW = 2635, 16762). ^{13}C spectra were then acquired (SW = 17985, NS = 16384, ppg = zgpg30).

An example ^{1}H spectrum of the metabolites seen in the isolated perfused rat heart upon perfusion of [1-^{13}C]butyric acid is shown in Figure 5.8. It is a complex spectrum, with many overlapping features, and is of little use on its own as a way of identifying possible metabolites in the [1-^{13}C]butyric acid metabolic pathway. Looking at an example 1D ^{13}C spectrum (Figure 5.9) proves to be more useful, but still not conclusive. The reason for this is that many metabolites can be located in a very similar position on a spectrum. Thus, a way was needed of being able to decide which metabolite belongs to which spectral position. This was done by using the now useful ^{1}H information, and physically correlating it to the ^{13}C data. The technique works by exciting only bonds which are nearby to the ^{13}C nucleus of interest, and a sample spectrum is shown in Figure 5.10.

Peak allocations for the acquired data are shown in Table 5.3, using an NMR database (www.smpdb.ca). The peaks were assigned as (1) butyrate, (2) C5-glutamate, (3) β-hydroxybutyrate, (4) citrate, (5) unknown, (6) acetoacetate, (7) acetyl carnitine.

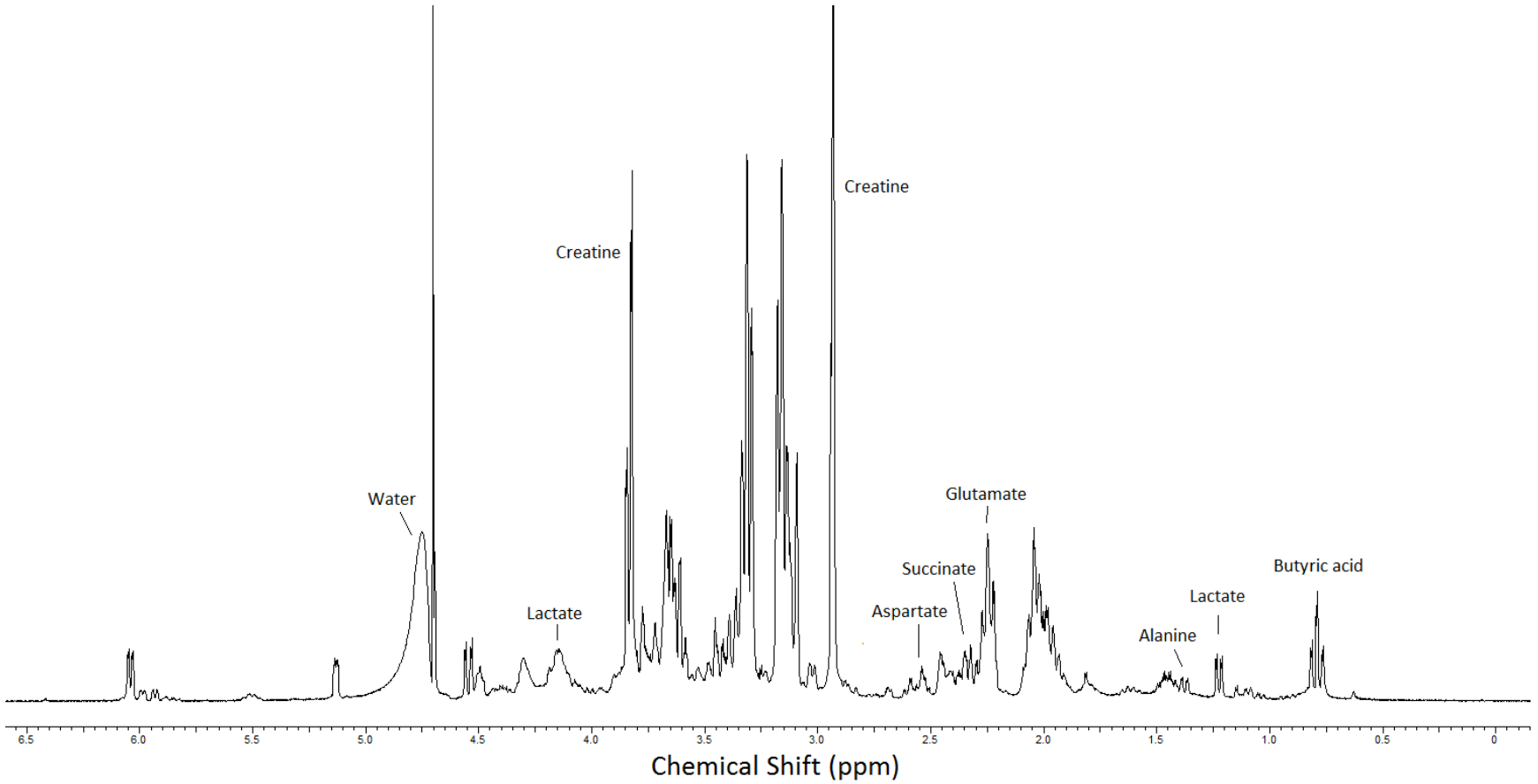


Figure 5.8: A ^{1}H spectrum of metabolites extracted from the isolated rat heart, perfused with [1-^{13}C]butyric acid. Some common and distinctive metabolites have been annotated on the spectrum.

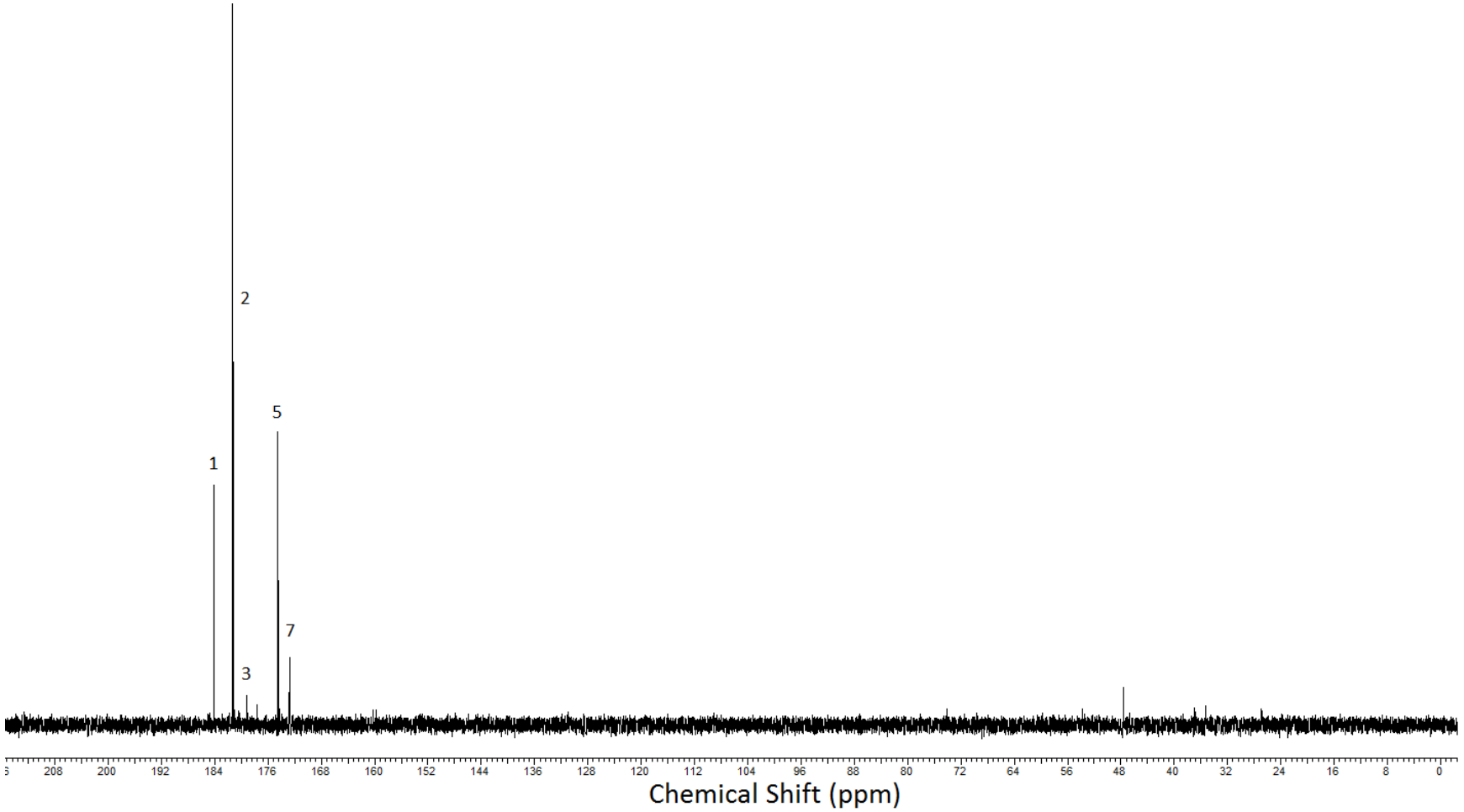


Figure 5.9: A ^{13}C spectrum of metabolites extracted from the isolated rat heart, perfused with [1-^{13}C]butyric acid under steady state conditions. The assigned peaks are detailed in Table 5.3.

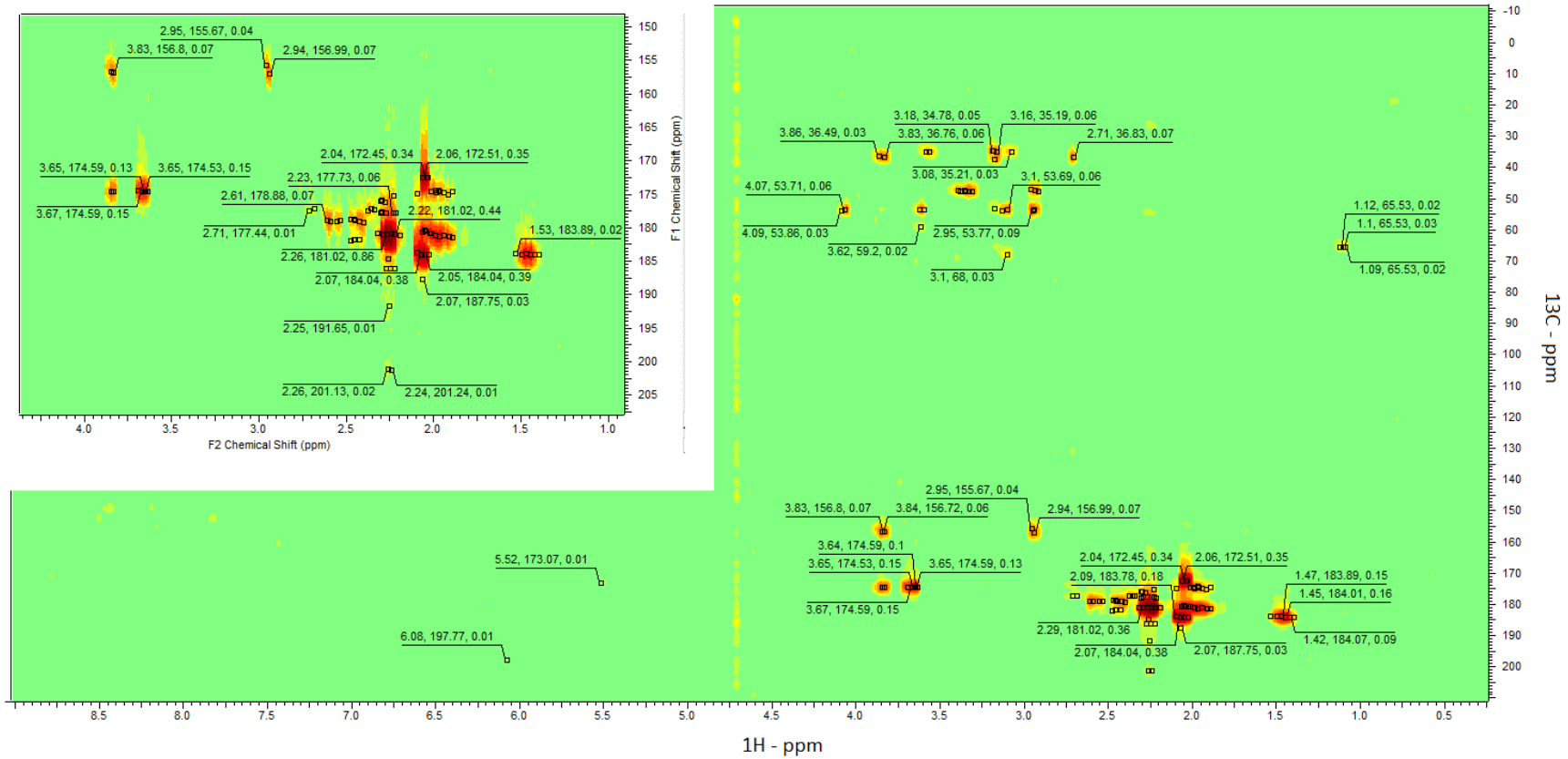


Figure 5.10: An HMBC spectrum, correlating both ^{1}H and ^{13}C data, from metabolites extracted from the isolated perfused rat heart, perfused with [1-^{13}C]butyric acid. Inset is a zoomed in region of dense peaks. Metabolite peak assignments are listed in Table 5.3.

Peak number	Allocated metabolite	^{13}C (ppm)	^{1}H (ppm)
1	Butyrate	184.04	1.45, 2.05
2	C5-glutamate	181.28	1.97, 2.19
3	β-hydroxybutyrate	181.02	2.29, 2.26, 2.32
4	Citrate	177.78	2.47, 2.23
5	Unknown	174.62	1.96, 2.01
6	Acetoacetate	174.53	1.99, 3.84
7	Acetyl Carnitine	172.51	2.03, 2.94

Table 5.3: This table gives the peak allocations for each of ^{13}C and the correlated ^{1}H, as acquired from the 2D HMBC data.

5.3.5 Trial perfusion study

With reasonably confident metabolic peak assignments having been made, an isolated perfused rat heart study was carried out to look at the effects of butyrate on the myocardium, and to assess whether altering the substrate delivered to the heart would have any effect on hyperpolarized [1-^{13}C]butyric acid metabolism.

5.3.5.1 Methods

Perfusion protocol: A 25.9 μl [1-^{13}C]butyric acid sample was polarized for 1 hour. Following polarization of the frozen [1-^{13}C]butyric acid, the sample was dissolved with 6 ml of hot NaOH/EDTA/Tris buffer to neutralise the pH. This was diluted in KH buffer to give a 4 mM butyrate solution. This solution was then delivered to the heart as a bolus over 120 seconds under gravity flow, with the hyerpolarized butyate concentration delivered to the heart being equal to that in the perfusion buffer. The Langendorff perfusion protocol was as previously described in Chapter 4. Male Wistar rats were perfused in groups as follows. Hearts were assigned randomly to be perfused either with KH containing 0 mM glucose and 4 mM butyrate, or 2.5 mM glucose and 4 mM butyrate, or 10 mM glucose and 4 mM butyrate (N = 5).

Spectroscopy: Following localization of the isolated perfused heart and shimming to reduce the proton linewdith to around 60 Hz, a hyperpolarized [1-^{13}C]butyrate

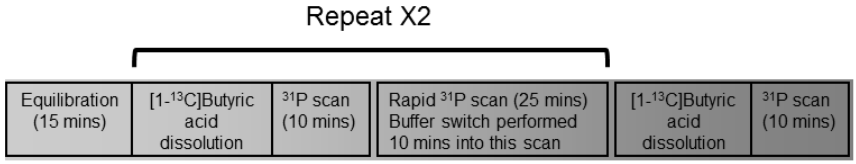


Figure 5.11: A figure showing the protocol for the trial perfusion study.

dissolution was performed. Following acquisition, the sum of 90 spectra were taken, beginning with the first appearance of hyperpolarized butyrate and processed with ACD / NMR. The ratio of the metabolites to the butyrate signal was then calculated. The carbon coil was removed, the phosphorous coil inserted, and a fully relaxed ^{31}P scan was performed as described in Section 3.2. Following this, a series of rapid 30 second ^{31}P scans were acquired for 25 minutes as described in Section 3.2. Ten minutes into this scan, the buffer was switched to another as per the perfusion protocol. A further hyperpolarized [1-^{13}C]butyrate dissolution was carried out, a fully relaxed and rapid ^{31}P scan were started, with a final buffer change. Finally, a hyperpolarized [1-^{13}C]butyrate dissolution was performed, with a final fully relaxed ^{31}P scan. This protocol resulted in four [1-^{13}C]butyric acid dissolutions per group of varied glucose concentrations. Cardiac functional data was obtained from a balloon inserted into the left ventricle as described in Section 3.2. Finally, ^{31}P and functional data from a control group of hearts (N = 7), perfused only with KH containing glucose, with no hyperpolarizations carried out were included in the comparisons made with butyrate perfused hearts, in order to assess the effects of butyrate on myocardial energetics and function. A summary of the protocol is shown in Figure 5.11.

Data analysis: Comparisons between two groups were carried out using a paired t-test. For temporal data with more than two groups, a 1 way ANOVA with a posthoc Bonferonni-Holm correction was applied. All tests were carried out at the $p<0.05$ significance level. Units are a.u., unless otherwise specified. Data are expressed as mean±standard deviation. ^{31}P spectra were processed and quantified using jMRUI.

Glucose concentration	PCr / ATP	Heart rate (BPM)	RPP (mmHg / min)
0 mM	2.8±0.9	340±30	27,000±4,000
2.5 mM	3.0±0.8	320±30	29,000±4,000
10 mM	2.80±0.33	315±40	25,000±4,000
Control	2.3±0.5	320±40	26,000±4,000

Table 5.4: Cardiac energetics using different concentrations of glucose in the presence of 4 mM butyrate. Control data contains only 10 mM glucose with no butyrate. No differences were seen between any of the groups.

^{13}C data was processed in ACD / NMR.

5.3.5.2 Results

Table 5.4 shows the cardiac energetic changes in the presence of different glucose concentrations. There were no significant differences between any of the groups in the hyperpolarized [1-^{13}C]butyric acid metabolites, as shown in Figure 5.12.

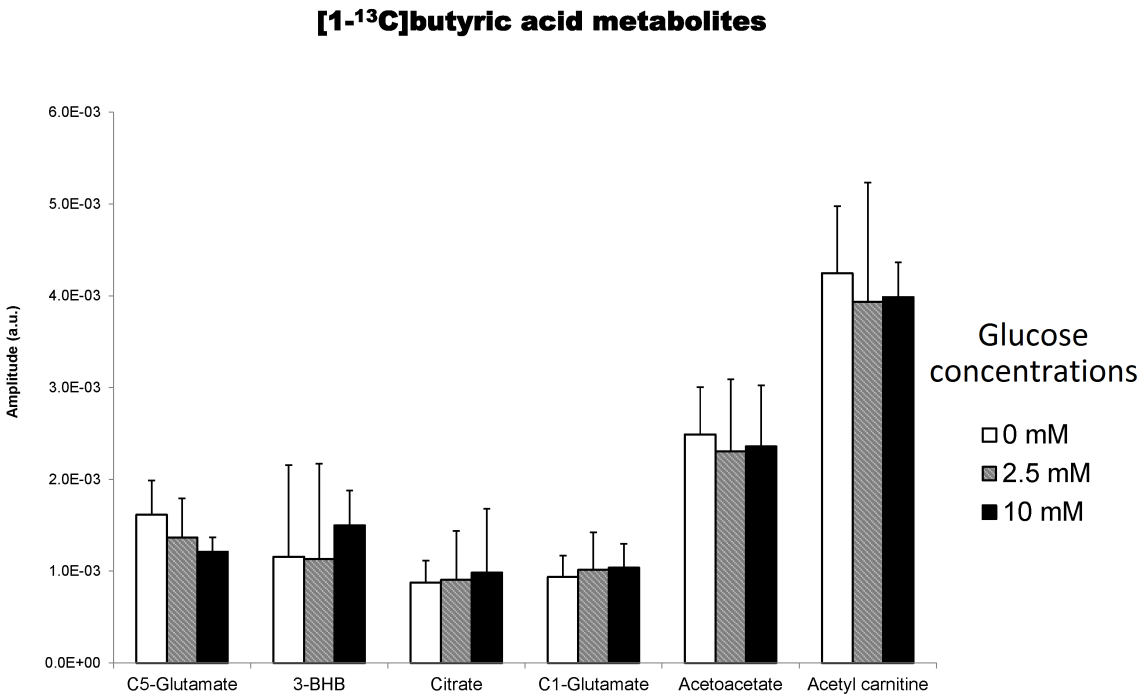


Figure 5.12: This graph shows the normalized metabolites dervied from hyperpolarized [1-^{13}C]butyric acid. There are no significant differences between any of the groups containing either 0 mM glucose, 2.5 mM glucose or 10 mM glucose.

5.3.5.3 Discussion

The data does not appear to show any adverse effects on the heart from the presence of butyrate as a source of fuel in the KH buffer. This was demonstrated with the use of control heart perfusions, which were done in the presence of 10 mM glucose, but no butyrate, and showed no differences using either ^{31}P or contractile function compared to hearts initially perfused with butyrate. The 4 mM concentration of hyperpolarized [1-^{13}C]butyrate was chosen as this was the lowest concentration that provided adequate spectral quality. A higher concentration was not used, as this value is already supraphysiological [154]. In terms of hyperpolarized [1-^{13}C]butyric acid metabolism, no changes were seen in the absence or presence of an alternative source of fuel (glucose). Whilst it is likely that the proportion of butyrate taken up by the heart would change with differing concentrations of glucose and it would be reasonable to expect a change in ketone body and glycolytic metabolites, as suggested by previous work [71], the high concentration of butyrate used in this study may have masked any such changes.

5.3.6 Trial *in vivo* study

With satisfactory evidence that hyperpolarized [1-^{13}C]butyric acid does not appear to detrimentally affect the isolated perfused heart, despite the relatively high 4 mM concentration used, it remained to be seen whether the probe was suitable for use in an *in vivo* rat model, and to carry out a study to assess both safety, and to determine whether hyperpolarized [1-^{13}C]butyric acid would demonstrate any alterations in its metabolism, using a simple fed and fasted model.

5.3.6.1 Methods

A 25.9 μl sample of [1-^{13}C]butyric acid was inserted into the alpha system, and hyperpolarized for an hour. Male Wistar rats (N = 6, BW = 300±10 g) were kept in

a 12 hour light / dark cycle, and were were fasted from 17:00 the evening prior to scanning the following morning, thus inducing the fasting state. The same animals were then scanned a minimum of 48 hours later, with no fasting, generating a fed group. All scanning was completed by 13:00. Male Wistar rats were anaesthetized with 2% isoflurane in oxygen, followed by insertion of a tail vein catheter. They were then placed into a home built cradle, had a rectal thermometer inserted, and were air heated to ensure a core body temperature of 37 °C. ECG leads were attached and a respiration loop fitted, with continous monitoring of heart and respiration rate for the duration of the experiment. The rats were placed such that their chest was located over a small home built ^{13}C 20 mm diameter butterfly coil. The cradle, holding the anaesthetized rat, was placed into the bore of a 7 T horizontal scanner, connected to a Varian INOVA console. Localization of the heart was confirmed by acquisition of a proton axial image (TE = 1.17 ms , TR = 2.33 ms, matrix size = 64X64, FOV = 60X60 mm, slice thickness = 2.5 mm, FA = 15°), and shimming was performed to reduce the proton linewidth to 180±40 Hz. Immediately prior to injection of the hyperpolarized sample into the rat, an ECG gated ^{13}C pulse acquire sequence (TR = 1 sec, FA = 5°, SW = 6,000 Hz, points = 2048, NS = 60) was started, and following dissolution with 6 ml of 30 mM NaOH buffer, 1 ml of a 36.4 mM hyperpolarized [1-^{13}C]butyric acid solution was then injected over 10 seconds into the rat, via the tail vein catheter. The remaining hyperpolarized solution was injected into a homebuilt polarimeter, to measure polarization. ^{13}C data were summed over 30 spectra, and metabolites normalized to the [1-^{13}C]butyrate peak.

5.3.6.2 Results

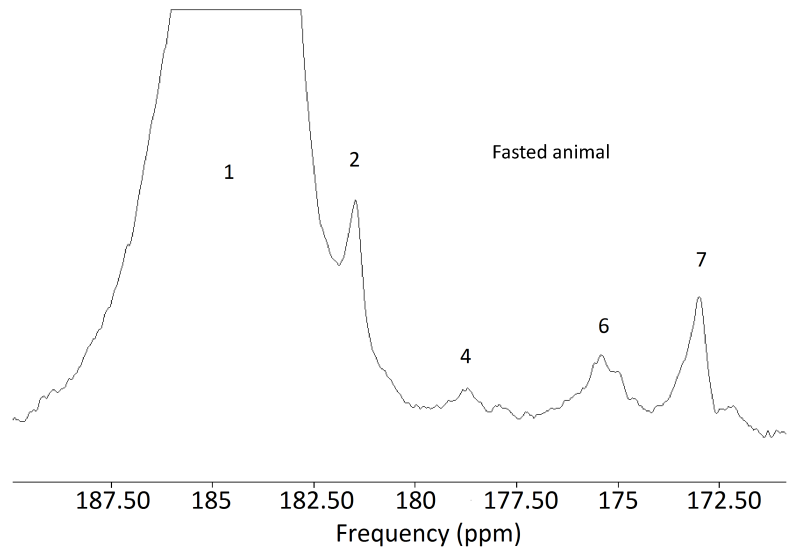
All animals used in this study recovered completely, with no obvious deliterious effects to the animals from the injection of hyperpolarized [1-^{13}C]butyric acid. The average [1-^{13}C]butyric acid polarization, as measured by the polarimeter was 8±3%. Figure

5.13 shows example spectra from both the fed and fasted state animals. No differences in hyperpolarized[1-^{13}C]butyric acid metabolism were seen in the fed and fasted state (Figure 5.14).

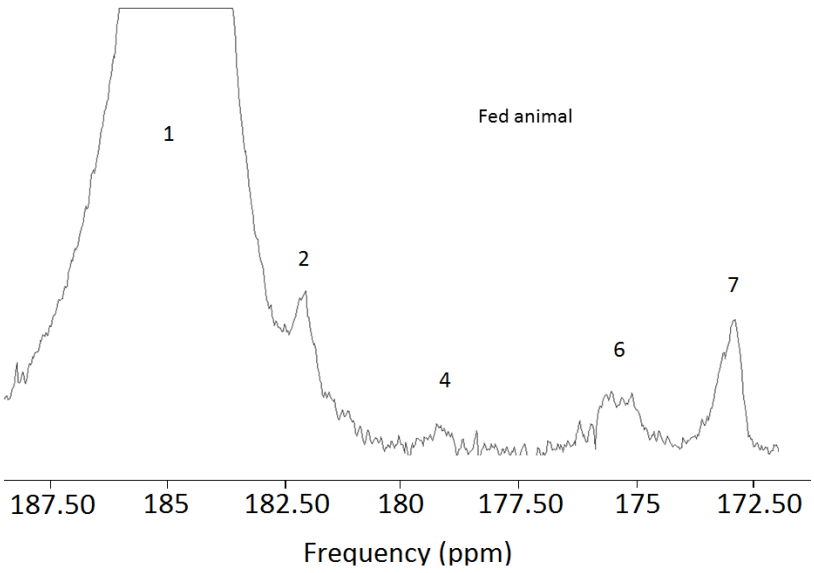
5.3.6.3 Discussion

As compared to the isolated perfused heart, where much narrower linewidths are possible (on the order of 50 Hz), this study suffered from broad linewidths, as a result of respiratory motion and susceptibility as a result of the tissue and air interfaces near the heart. As a result, β-hydroxybutyrate could not be visualized. In addition, the quality of the spectra in the *in vivo* model was considerably worse than that achieved in the isolated perfused heart. For reasons previously discussed, it would be expected that spectral quality in the perfused heart would be better, given the nature of the birdcage RF coil used, and its proximity to the heart, as compared to the large distance *in vivo* between the surface coil and the heart. Therefore, consideration is needed as to what else could be done in order to improve the signal to noise *in vivo*. Increasing the sample concentration is one such method, which should result in better signal to noise. However, the main disadvantage with this study was that it was wasteful of sample. Only 1 ml was used for animal injection, another 1 ml was used for polarimeter and pH measurement, which left around 3 – 4 mls of sample which was discarded. A better alternative might have been to inject more hyperpolarization solution into each animal. Other similar rodent studies using DNP hyperpolarization have done, using up to 3 mls per injection [147]. With an adult rat, this volume would equate to less than 10% of its blood volume. This technique could have further been improved by altering the volume and composition of the dissolution medium.

As compared to the isolated perfused rat heart study, not all metabolite peaks were quantifiable in this case. Of the metabolites that were quantifiable, no differences were seen between the fed and fasted states. It would be reasonable to expect that



(a)



(b)

Figure 5.13: These spectra show representative hyperpolarized [1-^{13}C]butyric acid metabolism in both the fasted (a) and fed (b) state. The peaks are butyrate (1), C5-glutamate (2), citrate (4), acetoacetate (6), acetyl carnitine (7).

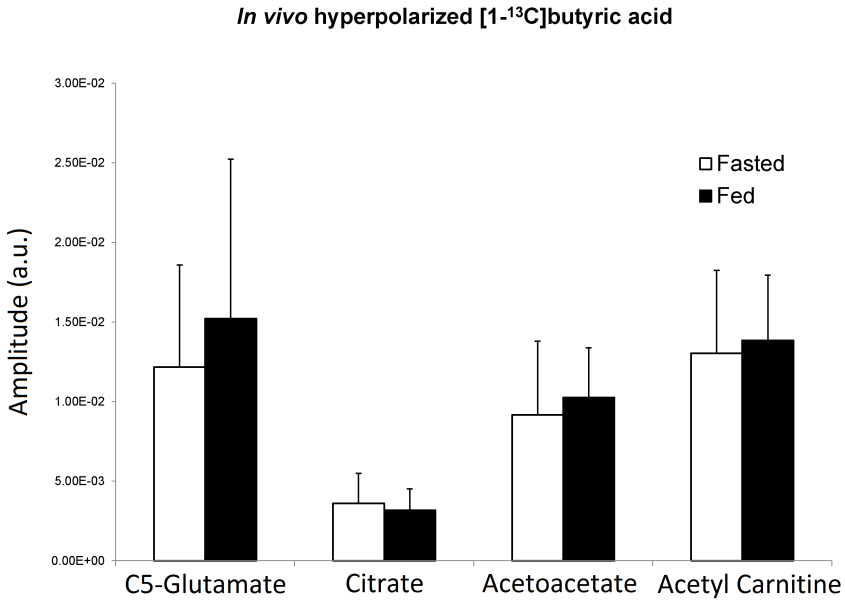


Figure 5.14: Hyperpolarized [1-^{13}C]butyric acid metabolite comparison in both the fed and fasted state. β-hydroxybutyrate could not be adequately quantified in this study. There are no differences across metabolites.

following a period of fasting, the increased uptake and oxidation of fatty acids and ketone bodies would have resulted in increased hyperpolarized [1-^{13}C]butyric acid oxidation, and upregulated ketone body oxidation as previously described [155–157]], but these changes were not seen in this study. Whilst there is research on the effects of long chain fatty acid uptake and metabolism in the fed and fasted conditions, little exists on possible changes that may occur with short chain fatty acids. Therefore, further work is first required to establish the expected changes in short chain fatty acid metabolism, using techniques such as radiolabelling, to determine uptake under different conditions.

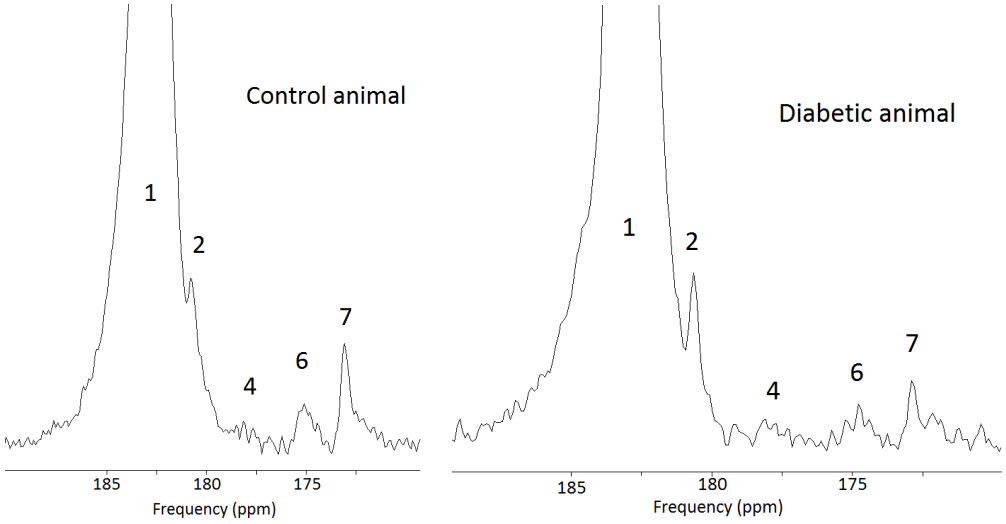
5.3.7 Application: diabetic study

It could be reasonably concluded that there does not appear to be a deliterious effect on animal health, as a result of the dose of hyperpolarized [1-^{13}C]butyric acid injected. Whilst the use of the butyric acid probe appears to be very promising, it would appear

that more severe metabolic alterations are required in order to alter the metabolism of short chain fatty acids. Hyperpolarized [1-^{13}C]pyruvate would be expected to, and indeed does, show significant metabolic changes in the fed and fasted state [51]. In order to attempt to elicit metabolic changes using hyperpolarized[1-^{13}C]butyric acid, relevant to those of short chain fatty acid metabolism, a model of type II diabetes was induced in male Wistar rats. This diabetic model was chosen as it is rapid to induce using a combination of high fat feeding and streptozotocin (STZ), an antibiotic which targets pancreatic beta cells [158]. The combination has been demonstrated to simulate a mild model of type II diabetes [159]. Milder or more severe diabetic models can be induced by altering the dose of STZ administered, as described in the methods.

5.3.7.1 Methods

The diabetic model was induced as follows. Male Wistar rats (diabetic group) (N = 8) were fed a high fat diet for 3 weeks (60% fat, 35% protein, 5% carbohydrate, ID:829197, Special Diet Services, Witham, England), whilst the control group (N = 6) were chow fed for 3 weeks, and age matched to diabetic group animals. After two weeks on the high fat diet, diabetic group animals were fasted overnight and the following morning, were injected with 15 mg / kg bodyweight streptozotocin (STZ) in 300 μl citrate buffer (pH 4.5) prepared 15 minutes prior to injection. Diabetic animals were then fed high fat diet as normal, until the end of the 3rd week, where they were assessed as previously described in Section 5.3.6.1. Diabetic status was assessed by saphenous blood sampling using a portable glucose meter (Abbott Laboratories, Maidenhead, UK), as well as post mortem glucose and insulin measurements, assessed on a Pentra ABL 400 (Horiba Medical, Montpellier, France) and an insulin ELIZA assay (Mercodia, Uppsala, Sweden).



(a) (b)

Figure 5.15: These spectra show hyperpolarized [1-^{13}C]butyric acid metabolism in both the fasted (a) and fed (b) state. The peaks are butyrate (1), C5-glutamate (2), citrate (4), acetoacetate (6), acetyl carnitine (7).

5.3.7.2 Results

Sample spectra from both control and diabetic animals are shown in Figure 5.15. No detrimental effects were seen as a result of hyperpolarized [1-^{13}C]butyrate injection on either control or diabetic group animals. Control and diabetic group animal weights were 315±15 and 314±23 g respectively, and were not significantly different. Insulin levels, as measured post mortem were significantly decreased in the diabetic group (4.6±1.7 vs 1.8±1.3 µg / L). There was a significant increase in blood glucose as measured during anaesthesia via the saphenous vein (9.6±1.9 vs 16.6±4.9 mM), although no significant differences were seen in blood glucose post mortem (15.9±1.4 vs 20.8±6.9 mM, p = 0.12). Significant changes in hyperpolarized[1-^{13}C]butyric acid metabolism were seen when comparing control and diabetic animals (Table 5.5 and Figure 5.16).

Metabolite	Control	Diabetic
C5-glutamate	0.05±0.02	0.018±0.002*
BHB	0.013±0.006	0.004±0.001*
Citrate	0.002±0.001	0.003±0.001
Acetoacetate	0.004±0.001	0.002±0.002
Acetyl Carnitine	0.015±0.006	0.004±0.003*

Table 5.5: The metabolic changes seen with hyperpolarized [1-^{13}]butyrate under control and diabetic conditions are shown in this table. *p<0.05 denotes significant changes with respect to control data.

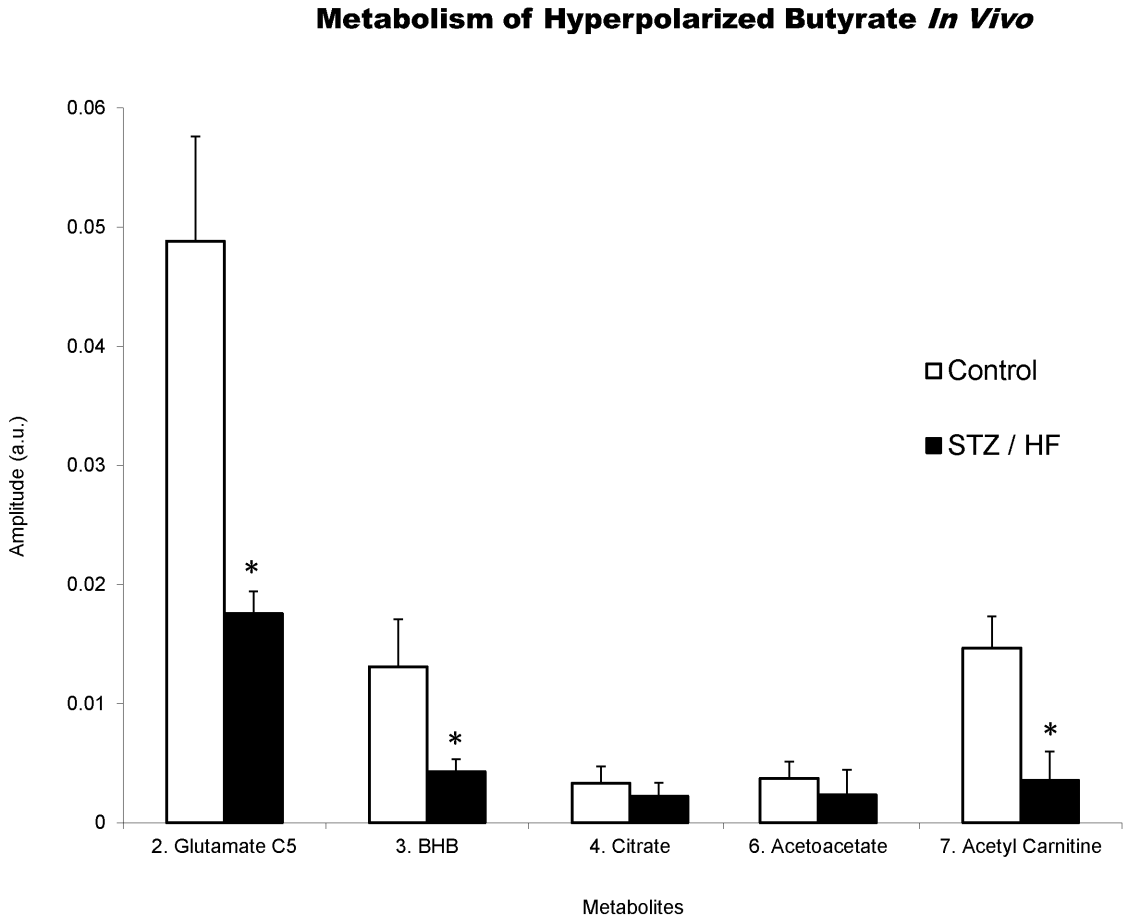


Figure 5.16: This chart shows the differences in hyperpolarized [1-^{13}C]butyrate metabolism in both the control and diabetic (STZ / HF) groups. Significant reductions were seen in acetyl carnitine, C5-glutamate and β-hydroxybutyrate. Whilst the other metabolites did not show significant differences, it does appear that metabolism across all butyrate metabolites was reduced in the diabetic animals. *p<0.05

5.3.7.3 Discussion

The animals were confirmed as being mildy diabetic, although the lack of a significant difference in glucose post mortem may be due to the method of terminal anaesthesia used. Nevertheless, this diabetic model appears to have produced a change in the metabolism of hyperpolarized [1-^{13}C]butyrate. The only information that can be confidently derived from the data is that there is likley a reduction in uptake of hyperpolarized [1-^{13}C]butyrate, by looking at both the significant differences, and the overal trend of the metabolites in the diabetic state. It is believed that MCT1 is responsible for butyrate uptake into cells [160, 161], a transporter also shared by pyruvate, lactate and the ketone bodies amongst other small metabolites. In muscle, MCT1 has been shown to be downregulated in type II diabetes [162], which would go some way to explaining the observed results.

In conclusion, butyrate has been demonstrated to reveal a large number of metabolites, with reasonably good spectral quality, both *ex vivo* and *in vivo*. It had been shown that it is sensitive enough to detect changes in butyrate uptake in the diabetic heart, which may occur due to alterations in the transporter MCT1. However, further work is required to thoroughly investigate the metabolic information that can be obtained in both healthy and diseased states from hyperpolarized butyrate.

5.4 Alanine

The formulation of alanine was made up from from 20 mg [1-^{13}C]alanine.HCl, with 5 µl of 60 mM OX063 dissolved in water, 15 µl DMSO and 2 µl 10 mM Dotarem. It has a hyperpolarized T_1 of 22±1 seconds, and a polarization of 3±1%. An example microwave sweep of hyperpolarized alanine is shown in Figure 5.17. The formulation used for alanine solidifies soon after preparation, and should be transferred quickly to the sample cup. It was however easily miscible initially, and appeared as a light

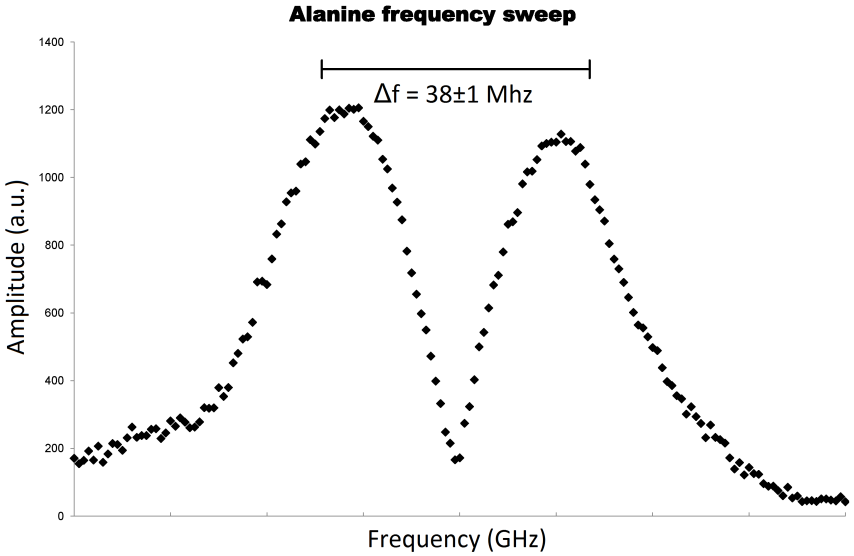


Figure 5.17: An example of a hyperpolarized [1-^{13}C]alanine microwave sweep. Δf represents the difference in microwave frequency between the peak amplitude maxima.

orange coloured sample. Upon testing, spectral quality in the isolated perfused rat heart was dissappointing, presumably as a result of rapid polarization decay (an example spectrum is shown in Figure 5.18). This was in spite of using a very high supraphysiological concentration of the probe. Only pyruvate could be seen as a metabolite, whilst lactate was not visible above the noise floor. Metabolites derived from hyperpolarized [1-^{13}C]alanine would be difficult to quantify for use in a study. Other work has used hyperpolarized alanine *in vivo* [147], and despite the injection of 3 mls of a 6 M hyperpolarized [1-^{13}C]alanine solution into a normal male Sprague Dawley rat, summing of the pyruvate and lactate metabolites was needed across the entire animal (abdomen, kidneys, heart, liver) to obtain sufficient signal to noise, thus rendering the probe as it stands of no particular value. Currently, no recommendation for the use of hyperpolarized [1-^{13}C]alanine can be made for the isolated perfused rat heart, let alone for *in vivo* studies. The only envisaged possibility for its use is in a system where high flow rates are present, thus delivering fresh hyperpolarized substrate quickly, and enabling the use of high flip angle acquisitions. Such an example might be the isolated perfused adult rat liver, where flow rates exceed 40 mls / min.

With such flow rates, it may also be possible to use more reasonable concentrations of hyperpolarized alanine.

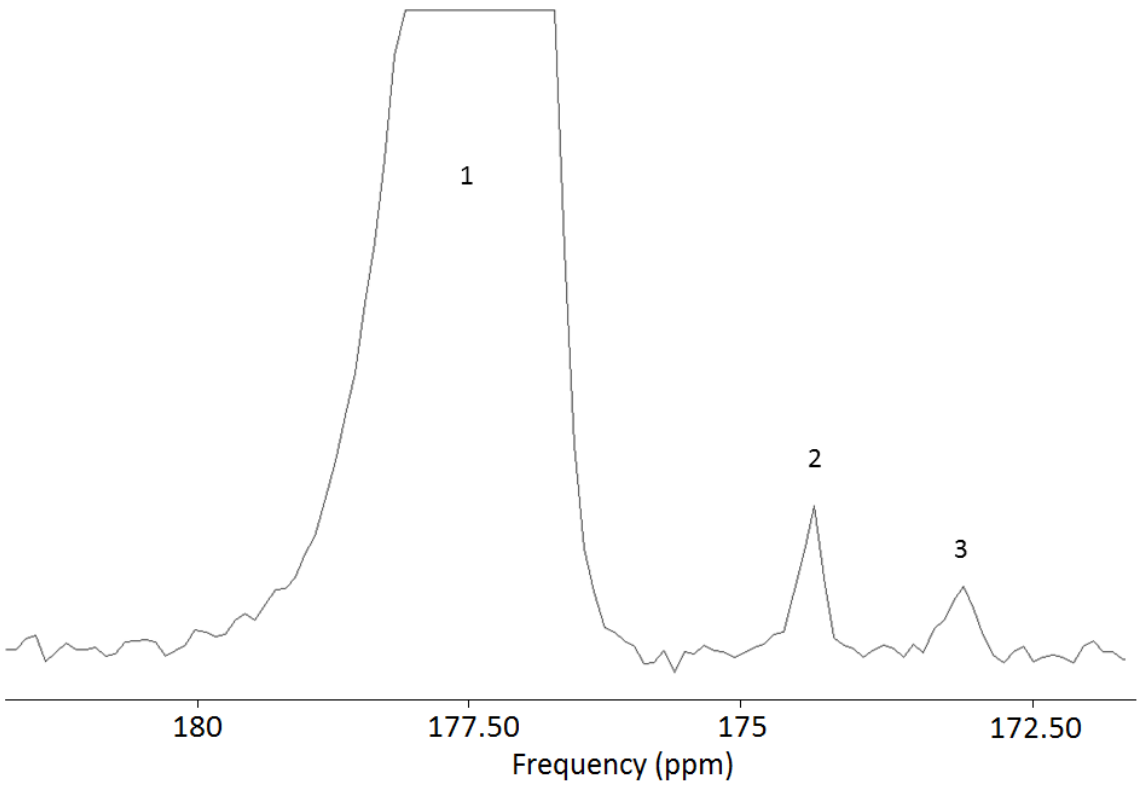


Figure 5.18: A representative spectrum from hyperpolarized [1-^{13}C]alanine in the isolated perfused rat heart. The peaks are (1) alanine 178.50 ppm, (2) impurity 173.50 ppm, (3) pyruvate 172.80 ppm. Lactate could not be seen above the noise.

5.5 Lactate

The formulation used for lactate was straightforward to prepare, and remains a non-viscous liquid upon formulation. ^{13}C lactate is commonly supplied as a mixture with water, likely due to its hygroscopic nature. Obtaining the labelled compound with less water present should improve polarization considerably. Its liquid state polarization was 6±2%, with a hyperpolarized T_1 of 32±9 seconds. An example microwave sweep is shown in Figure 5.19. It polarizes well, and good quality spectra were obtained,

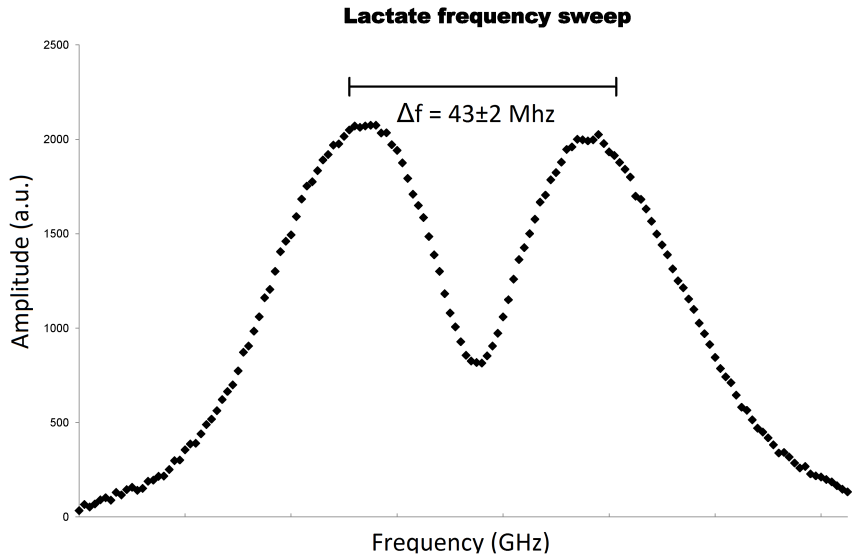


Figure 5.19: An example microwave sweep of hyperpolarized [1-^{13}C]lactate. Δf represents the difference in microwave frequency between the peak amplitude maxima.

an example of which is shown in Figure 5.20. Due to the successful polarization of lactate, with excellent signal to noise spectra and in sensible physiological concentrations (which can span anything from 1 mM to around 10 mM in excercise [163]), a concentration study was performed, to evaluate its use across a range of relevant physiological concentrations.

5.5.0.4 Methods

Perfusion protocol: For [1-^{13}C]lactate, male Wistar rat hearts (n = 6) were perfused as previously described in Chapter 4. The perfusion buffer was standard KH, with the addition of 0.1 mM sodium pyruvate, and either 2 mM, 4 mM or 8 mM sodium lactate. Following polarization of the frozen [1-^{13}C]lactic acid for an hour, the sample was dissolved with 6 ml of hot NaOH/EDTA/Tris buffer to neutralise the pH, and diluted into KH buffer. This solution was then delivered to the heart as a bolus over 120 seconds, with the hyerpolarized lactate concentration reaching the heart being equal to that in the original perfusion buffer.

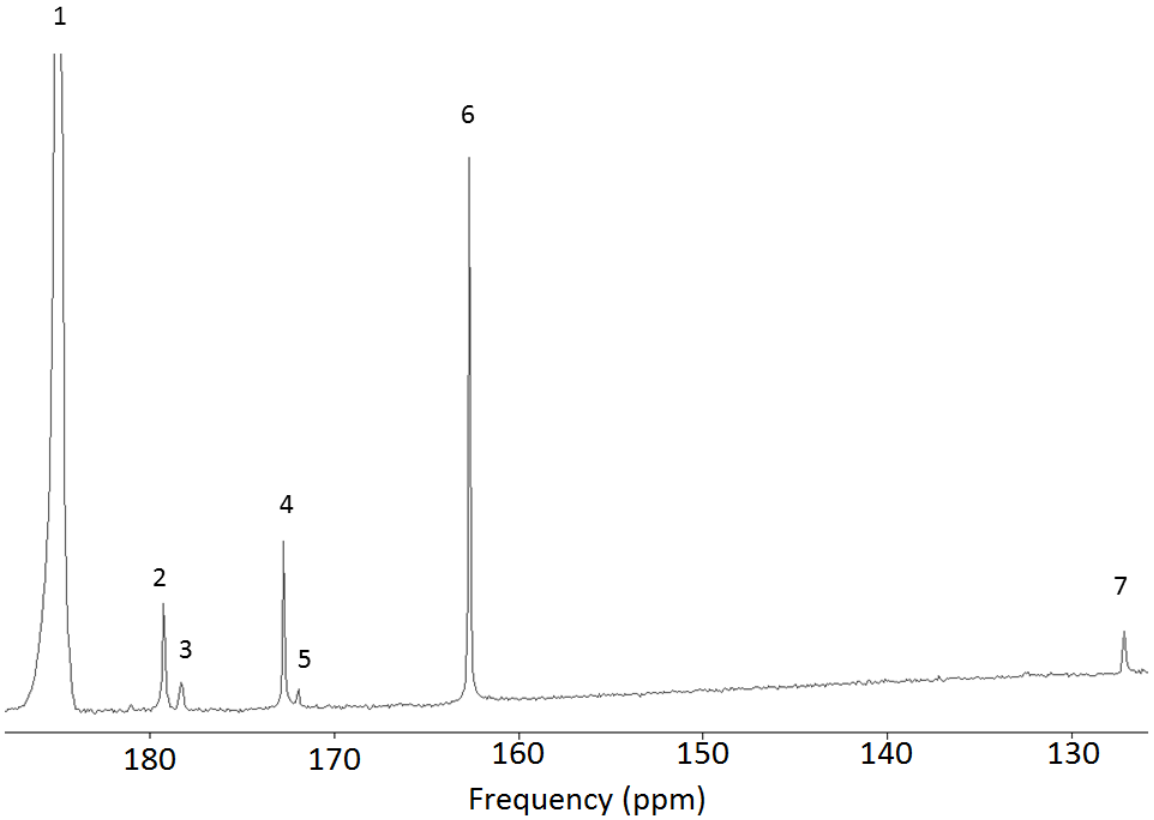


Figure 5.20: A representative spectrum from hyperpolarized [1-^{13}C]lactate in the isolated perfused rat heart. The peaks are (1) lactate 185.02 ppm (2) impurity 179.20 ppm (3) alanine 178.30 ppm (4) pyruvate 172.80 ppm (5) impurity 171.96 ppm (6) bicarbonate 162.69 ppm (7) CO_2 127.15 ppm.

Spectroscopy: A ^{13}C pulse-acquire experiment was then started (TR = 1 s, FA = 30^{o}, BW = 180 ppm, 4096 pts), and the sum of 60 spectra were taken beginning with the first appearance of hyperpolarized lactate. All metabolites were normalized to the hyperpolarized lactate signal. A 10 minute fully relaxed ^{31}P scan was performed, followed by a series of rapid 30 second ^{31}P scans using a dual tuned 20 mm ^{1}H / ^{31}P probe, over a period of 50 mins. Twenty minutes into the rapid ^{31}P scan, perfusion buffer in the hearts was changed from the initial KH with lactate, to KH with a different, randomized concentration of lactate. The hyperpolarized ^{13}C scan was then repeated. pH using ^{31}P data was calculated by using the change in chemical shifts between PCr and Pi automatically within the jMRUI processing software.

Data analysis: Comparison between two groups was carried out using a paired t-test. For multiple group comparisons, a 1-way ANOVA with a posthoc Bonferonni-Holm correction was applied. All tests were carried out at the $p<0.05$ significance level. Units are a.u., unless otherwise specified. Correlations between data sets were performed using a Pearson's correlation coefficient (CC) analysis. Data are expressed as mean±standard deviation. Spectra were processed and quantified using jMRUI, as was the signal to noise ratio (SNR). Following processing, all ^{13}C metabolite signal amplitudes were corrected for lactic acid sample size, receiver gain on the NMR system, and the polarizations achieved on the HyperSense.

5.5.0.5 Results

Cardiac energetics: The data for cardiac energetics are shown in Table 5.6, with respect to different sodium lactate concentrations.

Cardiac metabolism: Spectra had suitable spectral quality at all hyperpolarized [1-^{13}C]lactate concentrations (a sample spectrum is shown in Figure 5.20). As expected, [1-^{13}C]lactate signal increased linearly with concentration (R^2 = 0.91). There were significant increases in pyruvate (2 mM: 0.0006±0.00008, 4 mM: 0.0008±0.0002, 8

Sodium lactate concentration	Heart rate (BPM)	RPP (mmHg / min)	PCr / ATP (a.u.)	pH
2 mM	280±40	34000±8000	1.4±0.1	7.3±0.1
4 mM	270±20	25000±8000	1.5±0.01	7.3±0.1
8 mM	270±30	25000±8000	1.7±0.1	7.3±0.1

Table 5.6: Cardiac energetics with different concentrations of sodium lactate. There were no significant differences between any of the groups.

mM: 0.0019±0.0005) and PDH flux (2 mM: 0.002±0.0002, 4 mM: 0.002±0.0004, 8 mM: 0.004±0.0005), with no changes seen in alanine (2 mM: 0.0002±0.0001, 4 mM: 0.0002±0.0001, 8 mM: 0.0003±0.0003), as shown in Figure 5.21.

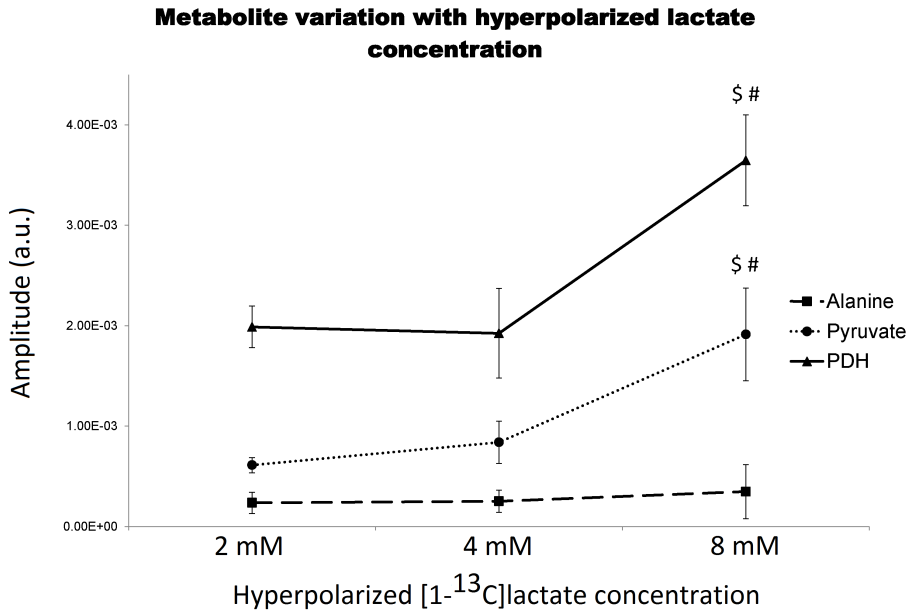


Figure 5.21: There were significant increases for both PDH (bicarbonate and CO_2 flux) and pyruvate amplitude when using a hyperpolarized [1-^{13}C]lactate concentration of 8 mM with respect to 4 mM ($, $p<0.05$) and 2 mM (#, $p<0.05$). No significant differences were seen with alanine.

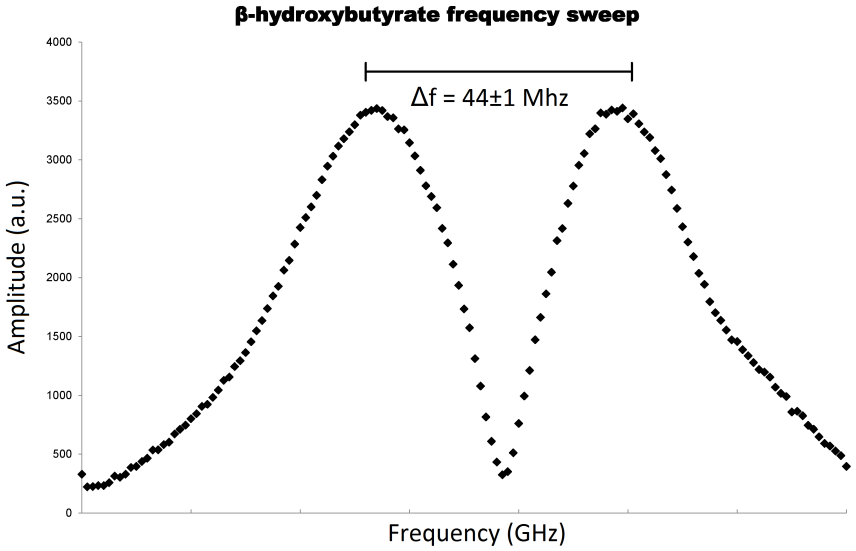
5.5.0.6 Discussion

There was no evidence of increasing lactate concentration detrimentally affecting the heart at any concentration used in this study. Lactate was particularly useful as a hyperpolarized probe, in that physiologically, it has such a wide concentration span

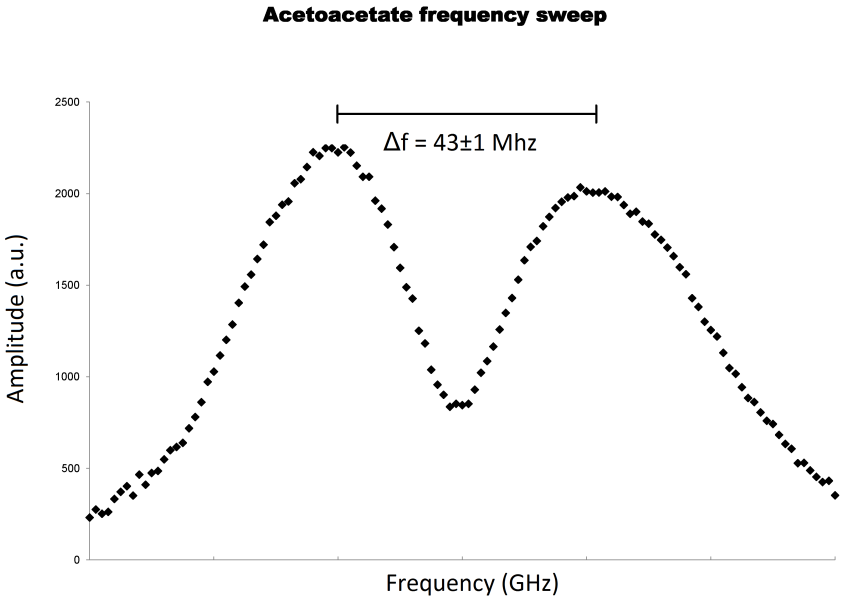
in blood, during both physiological and pathological conditions. This means that using high concentrations in order to obtain better signal to noise ratio could be justified, depending on the animal model used. In any case, this would not be needed as the lactate probe hyperpolarizes very well. From the data obtained, it is difficult to conclude that enzyme saturation is present. In the case of alanine production for example, whilst a consistent linear increase was seen with increasing hyperpolarized [1-^{13}C]pyruvate concentrations, the same was not seen in this study. There are only a few possibilities for the channeling of hyperpolarized lactate. Its uptake could simply be reduced (via the MCT1 transporters), and thus not metabolised, although this argument is not supported by the increased PDH flux, and that of pyruvate shown in the data. Or, it could be converted to pyruvate, after which it could proceed either to alanine or via the PDH enzyme. In any case, the data would suggest that much higher concentrations of lactate would be required to saturate PDH flux.

5.6 β-hydroxybutyrate and acetoacetate

Both preparations were extremely similar in their formulation, due to their structural similarities and therefore similar molecular masses and chemical properties. β-hydroxybutyrate was formulated by taking 280 mg β-hydroxybutyrate and mixing with 9.4 mg OX063, 50 μl DMSO and 150 μl H_2O. Each sample was made up from 32.94 μl of this sample, with 3.5 μl 10 mM Dotarem. Acetoacetate was formulated by taking 277 mg sodium acetoacetate and mixing with 9.4 mg OX063, 50 μl DMSO and 150 μl H_2O. Each sample was made up from 32.94 μl of this solution, with 3.5 μl 10 mM Dotarem. The liquid state polarizations obtained for β-hydroxybutyrate and acetoacetate respectively were 3±1% and 8±2%. The hyperpolarized T_1's for both compounds were 20±1 and 28±3 seconds respectively. Microwave sweeps for the compounds are shown in Figure 5.22. Good results were observed in the isolated perfused



(a)



(b)

Figure 5.22: Figures (a) and (b) show the microwave sweeps for β-hydroxybutyrate and acetoacetate respectively. Δf represents the difference in microwave frequency between the peak amplitude maxima. Microwave irradiation was carried out for 300 seconds per 1 MHz step.

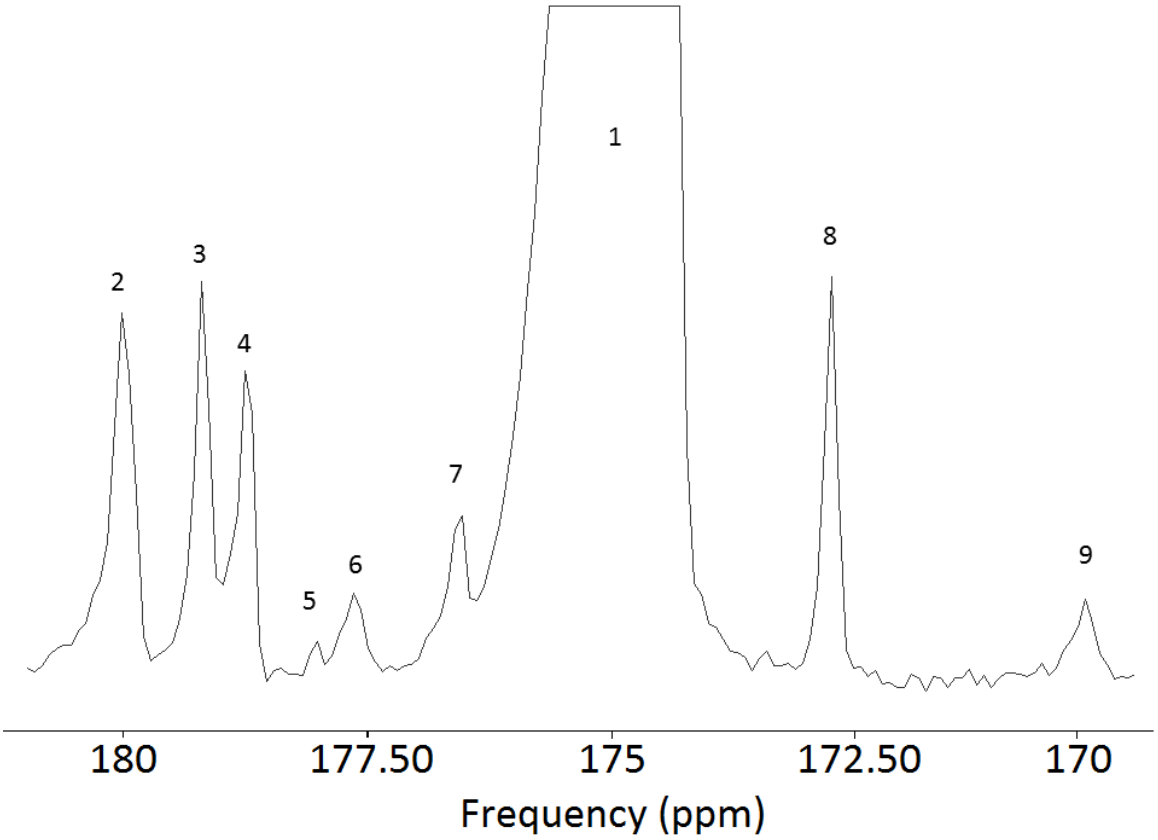


Figure 5.23: A representative spectrum from hyperpolarized [1-^{13}C]acetoacetate in the isolated perfused rat heart. The peaks are (1) acetoacetate 174.6 ppm, (2) C5 glutamate 181.08 ppm (3) β-hydroxybutyrate 180.11 ppm (4) unknown 179.58 ppm (5) unknown 178.78 ppm (6) citrate 178.25 ppm (7) unknown 177.02 ppm (8) acetyl carnitine 172.52 ppm (9) ethyl acetoacetate (impurity) 169.34 ppm.

heart (Figure 5.23) particularly with acetoacetate as compared to β-hydroxybutyrate (Figure 5.24) , which would make these probes interesting compounds to follow up. The use of ketone bodies have so far not been seen in published literature concerning hyperpolarization experiments, although it has been suggested that these experiments have already been attempted, but have failed. This is perhaps explained by the fact that such experiments would likely have been attempted *in vivo*, and comment cannot be made as to whether these compounds would successfully work as formulated. Attempts to improve the formulation of these ketone bodies, as a result of failure

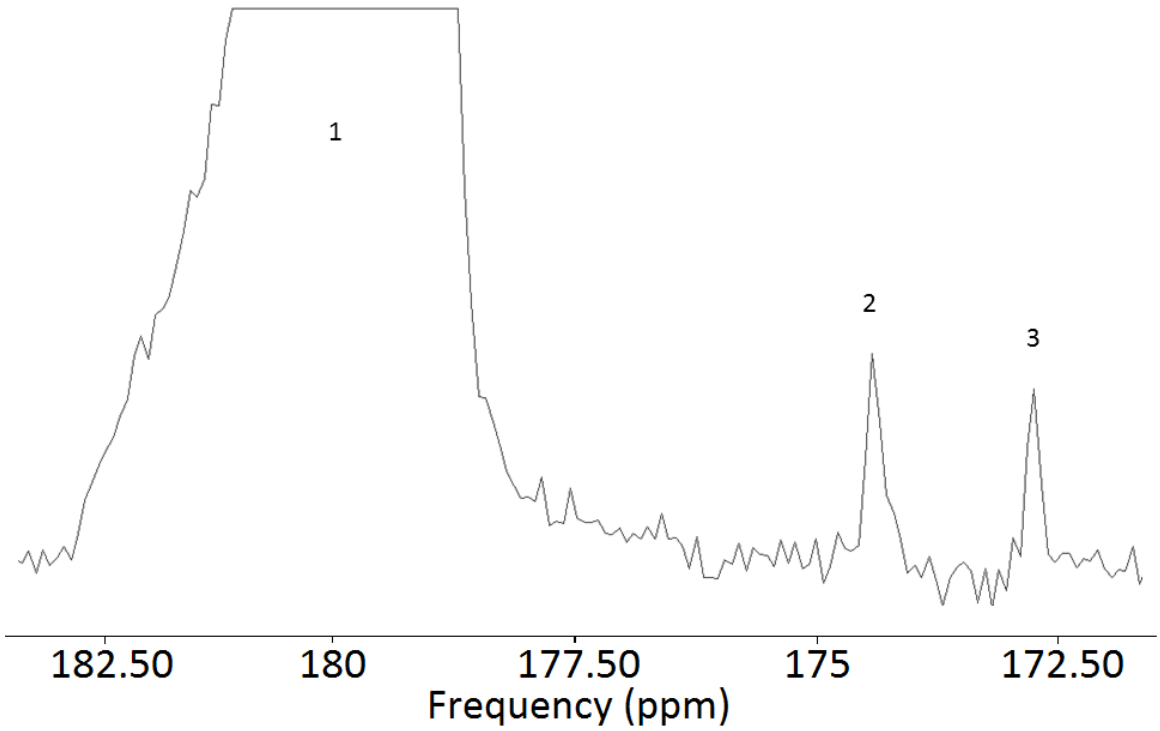


Figure 5.24: A representative spectrum from hyperpolarized [1-^{13}C]β-hydroxybutyrate in the isolated perfused rat heart. The peaks are (1) β-hydroxybutyrate 180.11 ppm (2) acetoacetate 174.6 ppm (3) acetyl carnitine 172.52 ppm.

to see any metabolites upon testing are being actively developed. It is extremely promising that hyperpolarized ketone bodies could be explored as one of the major fuel substrates in the human body. Ketone bodies have so far been widely used in steady state ^{13}C and ^{14}C experiments [164, 165], as well as real time ^{12}C PET experiments [166–168], and have provided a great deal of information on ketone body metabolism. In addition, the metabolites of both β-hydroxybutyrate and acetoacetate were visible with good spectral quality at a concentration of 4 mM representative of a mild disease state, such as that induced by the type II diabetic study performed earlier in Section 5.3.7. However, this concentration is toward the lower limit in order to obtain spectra with good signal quality, and thus a concentration study was not possible, nor necessary. The next step for these compounds should be evaluation *in vivo*, as was previously described using the hyperpolarized butyrate probe. The use of the fed / fasted study, followed by the diabetic study would be ideal models, given the wealth of information concerning ketone body metabolism in these states [169].

5.7 Discussion

In summary, a variety of metabolically relevant compound for the rat heart have been formulated and evaluated for their potential use. These results are summarized in Tables 5.7 and 5.8, with the inclusion of the widely used [1-^{13}C]pyruvate used as a comparison for the different physical property values stated.

It can now be seen why [1-^{13}C]pyruvate has become so widespread in its use. With its long T_1, good polarization and simple formulation, it was the ideal metabolite with which to lead research into DNP hyperpolarization. A vast amount is now known about compound formulation, and using standard techniques with a systematic approach, it is possible to attempt the polarization of any small metabolite with a long T_1. The biggest challenge that currently exists will be the synthesis of interesting

DNP probe	Compound formulation	Concentration of neat sample (M)	Concentration of sample in 6 ml dissolution buffer (mM)	Radical (OX063) concentration (mM)	Gadolinium (Dotarem) concentration (mM)
Pyruvate (C1)	Each sample consisted of 15 µl of [1-^{13}C]pyruvic acid, with 15 mM OX063, and 1.5 µl 10 mM Dotarem.	13.3	35	15	0.9
Alanine (C1)	Each sample was made from 20 mg [1-^{13}C]alanine.HCl, with 5 µl of 60 mM OX063 dissolved in water, 15 µl DMSO and 2 µl 10 mM Dotarem.	6.4	27	11.9	0.8
Lactate (C1)	Each sample consisted of 25.4 µl lactate solution with 25.4 µl DMSO, 0.581 mg OX063 and 3 µl Dotarem.	4.1	37.7	7.6	0.6
Butyrate (C1)	Each sample was made up from 20.74 µl butyric acid, 0.54 mg OX063, 5.18 µl DMSO and 3.4 µl 10 mM Dotarem.	7.7	37.6	12.9	1.2
β-hydroxybutyrate (C1)	280 mg β-hydroxybutyrate was mixed with 9.4 mg OX063, 50 µl DMSO and 150 µl H_2O. Each sample was made up from 32.94 µl of this solution, with 3.5 µl 10 mM Dotarem.	6.1	21	18	1
Acetoacetate (C1)	277 mg sodium acetoacetate was mixed with 9.4 mg OX063, 50 µl DMSO and 150 µl H_2O. Each sample was made up from 32.94 µl of this solution, with 3.5 µl 10 mM Dotarem.	6.1	21	18	1

Table 5.7: Compound formulations. All compounds were polarized at the 1-^{13}C position.

DNP probe	Hyperpolarized T_1 (s)	Polarization (%)	Buildup amplitude (a.u.)	Buildup time constant (s)	MW sweep peak to peak separation (MHz)
Pyruvate	34±7	18±3	9000±900	1500±180	61±11
Alanine	22±1	3±1	10000±1000	3100±170	38±1
Lactate	32±9	6±2	10000±400	2500±100	43±2
Butyrate	20±1	7±4	16000±300	1700±300	36±10
β-hydroxybutyrate	16±1	3±1	18000±2500	2000±300	44±1
Acetoacetate	28±3	8±2	11000±3000	3000±600	43±1

Table 5.8: Compound characterization

metabolic targets with a labelled ^{13}C nucleus placed as required. Solving this problem will require better collaborations with academic chemistry facilities, or, as the technique of DNP hyperpolarization becomes more widespread, the largest chemical suppliers will begin to, and indeed have already started, to work with research groups to fulfil demands in this respect.

Chapter 6

Assessment of Alternative Organs

6.1 Introduction

The aim of the work described in this chapter was to develop a new perfusion system that would allow the use of DNP in combination with the isolated perfused mouse heart and liver. Ample work exists on the use of DNP with *in vivo* mouse models, particularly for the study of cancer [98, 113, 145, 170, 171]. The advantages of using isolated perfused organ models have been discussed throughout this thesis, and whilst some preliminary work has been performed on the use of the isolated perfused mouse liver with DNP [172], it is not routinely used in research. As a crucial organ in metabolic homeostasis in the body, the ability to probe murine hepatic metabolism, along with the isolated perfused mouse heart using DNP, on which no literature currently exists, would allow for a broader understanding of metabolic dysfunction in diseased models.

The mouse is an ideal model system in which to incorporate DNP studies, due to the extremely wide range of transgenetic models available for study [173]. Genetic models of rats have only existed in the last ten years [174], using somatic cell manipulation for example [175], but this appears to be particularly difficult in the rat as

compared to the mouse. Attempts at characterising and generating new models using arbitrary chemical mutations have also been slow to develop [176], and provide a questionable method of genetically diversifying a species. It is only very recently that rat models [177] have shown considerable expansion potential by using a zinc finger based technique [178], although even this, whilst promising, is currently very limited in terms of available models [179]. In addition, these new models and their breeding licenses are very expensive. In terms of study design, the mouse has a shorter gestation period, with more rapid growth rates than the rat, and is therefore better suited for studies requiring several generations of mice for model generation (eg [180]).

In terms of experimental design, the use of the small isolated perfused mouse heart opens up the potential use of smaller RF coils with higher homogeneity and sensitivity, providing spectra with increased signal to noise ratios. Narrower linewidths should also be possible, to allow for better separation of metabolite peaks. Exploration of the isolated mouse liver may allow for the visualization of hyperpolarized [1-^{13}C]pyruvate metabolite peaks not previously seen *in vivo* [181], offering an insight into its anaplerotic nature.

This chapter discusses the complete design and implementation of a system capable of perfusing the isolated mouse heart and liver. To demonstrate the stability of the developed system, and the ability to visualize useful metabolic information via DNP, an ischemia reperfusion study was performed on both the isolated mouse heart and liver. This provided a simple, reliable and robust demonstration of the developed techniques to visualize changes in metabolism that are known to occur following periods of ischemia [182, 183]. Further, it allowed for demonstration of the ability to combine these novel DNP studies with more traditional assessments, such as ^{31}P MR spectroscopy to probe high energy phosphate levels.

6.2 Rig design

6.2.1 Methods of perfusion

Before proceeding to modifying the existing perfusion system, we first sought to address the question of how isolated organ preparations should ideally be carried out when combined with DNP experiments, and whether it was possible to have a system that could easily accomodate different approaches.

6.2.1.1 Cardiac perfusion

Cardiac perfusion techniques can be split into two major types of perfusion, the Langendorff mode (retrograde perfusion) [90] or the working heart preparation [184]. Langendorff heart perfusion involves cannulation of the aorta, and subsequent perfusion with KH buffer. The retrograde perfusion of buffer via the aorta closes the semilunar aortic valve (by design to prevent oxygenated blood from re-entering the left ventricle), which forces buffer flow to proceed via the left and right coronary arteries, thus perfusing the myocardium itself. The buffer then flows via the coronary sinus, and Thebesian veins, predominantly into the right atrium, and to a small extent into the ventricles themselves. For this reason, to allow buffer to escape the various chambers of the heart upon perfusion, the pulmonary artery is cut, and a small drain is placed inside the left ventricle (depending on the size of the heart). The problem with the Langendorff method, as described so far, is the lack of a workload for the heart to contract against. The use of the isolated heart without workload (unless by design, such as simulating the unloaded condition as in a left ventricular assist device (LVAD) for example) is metabolically and physiologically unsound as a model [185,186]. This problem is normally solved by inserting a polyethylene balloon connected to a pressure transducer, into the left ventricle, and inflating it so that an end diastolic pressure of around 4 mmHg is reached. This is a good alternative to the

working heart model described below in providing the heart with a workload, and is essential for the study of metabolism in the Langendorff perfused heart.

The second perfusion method is the working heart (Neely's model), where the heart is initially perfused in the Langendorff mode. During this time, the pulmonary vein is also cannulated. Buffer flow is then directed as it would be *in vivo*; i.e. the buffer proceeds through the left atrium at an adjustable pressure (preload) into the left ventricle before being ejected via the cannulated aorta, where the height of the column against which the heart contracts can be adjusted to set the desired workload (afterload). The preload and afterload can both be monitored using pressure transducers, and it is possible to acquire pressure volume loop data from inside the left ventricle using this model. It is the ideal perfusion model for metabolic and physiologic studies, as it best reflects the *in vivo* situation. A summary of both perfusion modes is shown in Figure 6.1.

However, this preference for the working heart model changes in experiments where the perfusion equipment needs to be mobile, e.g. to allow placement of the perfused organ into the bore of a superconducting magnet for NMR data acquisition. The technical challenges of using the working mode in this situation become very time consuming. The constaints of the magnet are such that it must be possible to freely move the organ and the tubing connected to it (the umbilical) in and out of the magnet, without too much disruption in cardiac function. In addition, there is a space constraint within the RF coils used to acquire the NMR data. The RF coils are generally either 10 mm or 20 mm wide and the perfused heart must fit within this space, in its own sealed container, to prevent fluid leaking into the magnet which could damage it and the RF and gradient coils inside (Figure 6.2). Given the Langendorff model allows the myocardium to be provided with a workload to contract against using an intraventricular balloon, and thus provides a physiological assessment of metabolism, this was chosen as the perfusion method used in the work described

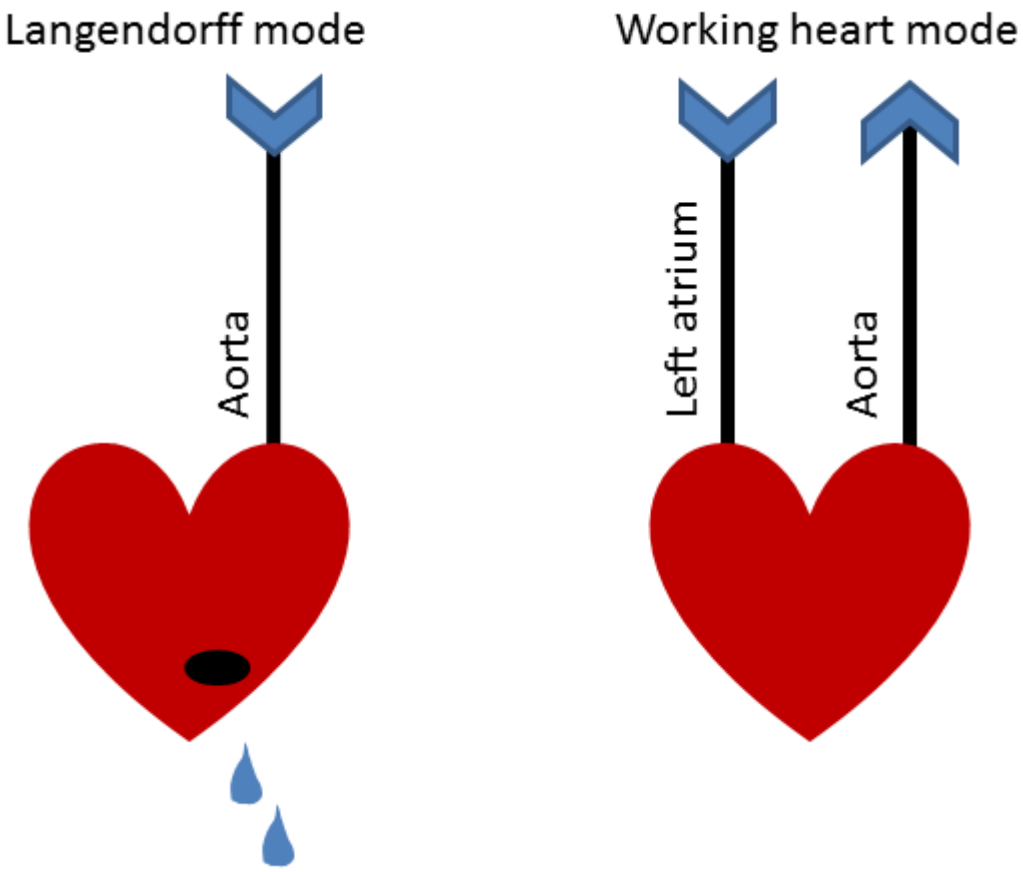


Figure 6.1: A diagram showing the two perfusion modes. Langendorff, where perfusion is done in a retrograde fashion, via the aorta. The buffer typically leaves the coronary circulation via the right atrium, the right ventricle and then the pulmonary artery. Some buffer builds up in the left ventricle, which is removed by an inserted drain. In the working heart mode, buffer is perfused via the left atrium, left ventricle, and out of the aorta against a set pressure column.

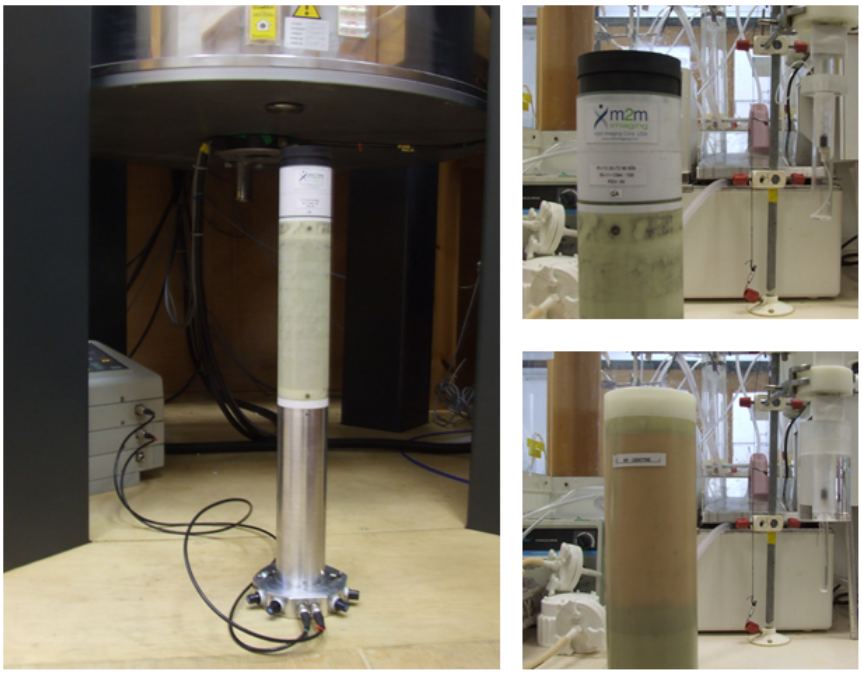


Figure 6.2: This figure shows a typical RF coil (20 mm), in the leftmost pane. This coil would be inserted underneath the magnet, and the umbilical, supporting the organ is inserted from the top of the magnet, such that the organ is positioned within the top 6 cm of the coil. On the right panes, are the NMR tubes attached to the umbilical, which would contain a rat heart / mouse liver (top right) or mouse heart (bottom right), shown next to the RF coils used with them. These tubes would be inserted approximately 2 - 6 cm into the top of each of the coils.

here.

6.2.1.2 Hepatic perfusion

The available choices for perfusion are easier for the liver. First implemented in the rat model around thirty years ago [187], liver perfusion is a widely used model for studying hepatic metabolism and function [188]. The liver is most commonly cannulated via the portal vein, which *in vivo* is responsible for the majority of the blood flow to the liver [189]. The function of the portal vein has been previously described in Chapter 2, but needs to be supplemented *in vivo* by the hepatic artery to provide adequate oxygen supply. *Ex vivo*, perfusion via the portal vein is preferred and was therefore chosen as the approach in this work. For more intricate studies of liver function, the hepatic vein and the bile duct may also be cannulated, and the output analysed to provide a measure of liver performance.

6.2.1.3 General perfusion requirements

Before detailing perfusion techniques in further detail, a broad overview of the standard perfusion machinery is provided (Figure 6.3). It consists of a heated reservoir containing KH buffer which is then pumped to a heated lung, via a filter, where a mixture of 95% O_2 and 5% CO_2 is passed across the buffer over a very large surface area, in order to oxygenate the buffer. The carbon dioxide is required to maintain normal pH within the perfusion buffer, and is in equilibrium with the bicarbonate present in the KH buffer. The lung is very efficient, and can saturate the buffer with an oxygen tension of around 600 mmHg. Other methods exist for oxygenating the buffer, including the use of gas permeable silastic tubing or a simple glass diffuser in the buffer resevoir. All these oxygenation methods have their uses depending on the particular experiment being performed. The oxygenation level is especially important for both the liver, which has a very high O_2 demand, and for the mouse heart, whose

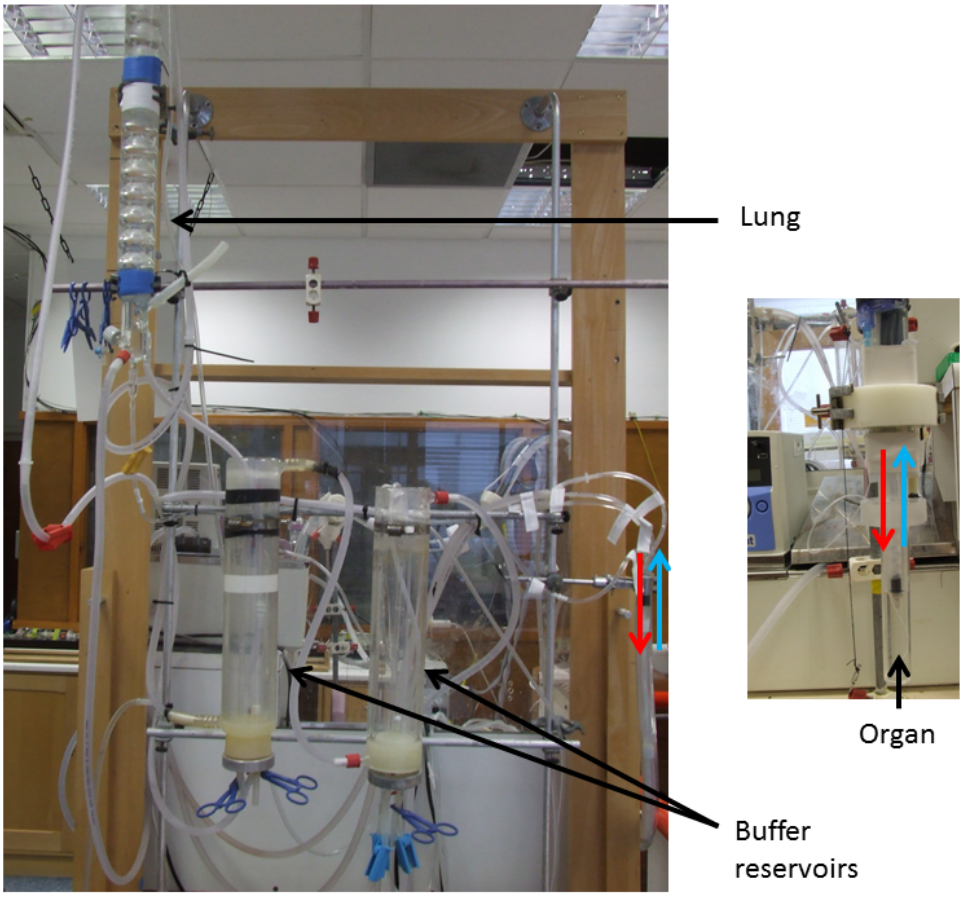


Figure 6.3: This figure shows the back of the perfusion rig. On the left pane, the two buffer resevoirs are shown, whose buffer proceeds up to the lung, and back to both the buffer reservoir (thereby oxygenating the buffer in the resevoir), and to the umbilical (red oxygenated buffer arrow), where it arrives at the end of the umbilical, where the organ is perfused (right pane). It is then returned deoxygenated (blue arrow) back to either the buffer reservoir, or to a waste container.

perfusion buffer loses oxygen rapidly, due to the low coronary flow rate of the mouse heart (around 2 mls / min [190]). In the heart, a lack of adequate oxygenation is observed as a gradual increase in end diastolic pressure (EDP). In the liver, other than through the use of continuous flow oxygen probes, a suitable alternative is to take samples of buffer immediately before and after the liver, to ensure the oxygen gradient is sufficiently high. From the lung, the buffer can then take two paths; it can either return back to the resevoir, or can proceed to the perfused organ, after which it is returned via a separate line back to the buffer resevoir (in cases where the buffer is to be recirculated), or to a waste container.

With the decision to choose the Langendorff mode as the perfusion method, there is a need to choose between using either the constant flow method, where a fixed flow rate of buffer is delivered to the organ irrespective of vascular resistance, or a constant pressure method, where a fixed pressure head is established but the flow through the organ depends on the resistance offered. Constant flow perfusions override the physiological mechanisms in place in both the heart and liver to regulate flow. In the heart, the majority of coronary flow occurs during diastole, due to the contraction of the heart occluding a portion of the coronary arteries. A constant flow would then impose a large pressure on the aortic valves and coronary arteries. In the liver, this is perhaps more important, due to the particularly large degree of vasculature present, which is carefully regulated by vasodilating and vasoconstricting agents. In studies involving ischemia for example, the liver has been shown to use these mechanisms to protect itself against ischemia-reperfusion injury [191]. Changes in coronary flow, for example in ischemia studies, would be expected to change in the presence of infarcted, or otherwise metabolically compromised tissue [192, 193]. The constant flow system therefore masks the true physiological changes effected by the target organ system. However, it is technically easier to implement and when combined with pressure transducers to measure changes in coronary or hepatic pressure, can provide

useful data. It also makes the task of integrating DNP perfused organ preparations considerably easier. The challenge with DNP integration is that the hyperpolarized probe is always decaying rapidly, and thus must be delivered to the organ as quickly as possible. Using a constant flow system, with small diameter tubing (reducing the dead volume), the time to delivery can be shortened considerably and standardized across experiments. In the heart, a suitable compromise can be to initially perfuse under constant pressure, measure the coronary flow, and then set the constant flow pump to match it.

However, a constant pressure setup provides a more physiological way of perfusing isolated organs, without significantly overriding vascular regulation. The heart will typically rely on large pressure heads (80 – 100 mmHg [190]) for optimal perfusion and function, whilst the liver uses a lower perfusion pressure of around 20 mmHg. It is sometimes necessary, particularly with the liver, to force supra-physiological flow rates to ensure adequate oxygen delivery to the organ in preparations that use colloidal buffers (as opposed to buffers mixed with erythrocytes, or even blood [188]). An interesting side-effect of the low oxygen carrying capacity of colloidal buffers in the heart is a reported doubling in ventricular wall thickness during perfusion, not seen when oxygen carrying substrates are added (such as perfluorocarbons) [194].

The constant pressure setup is more difficult to achieve in combination with DNP. The requirement for larger bore tubing than would be needed with constant flow systems (to ensure adequate flow rates) means an increase in dead space within the tubing, and thus a longer period of time before the hyperpolarized probe reaches the organ. Nevertheless, given the physiological advantages, a constant pressure system was chosen for the final design. A constant flow system could however easily be added without modification, should the need arise.

In terms of isolated perfused organs exclusively used with DNP, the literature reveals published material from only two other laboratories. For the mouse liver, the protocol

previously used involved constant, weight independant flow [172], and with the rat heart, perfusion was carried out using a constant pressure preparation at 100 mmHg [19].

6.2.1.4 Rig specifications

Table 6.1 summarizes the ideal specifications that the perfusion setup should have, given the above considerations.

Organ manipulation	1. A simple, universal luer lock attachment for cannulated organs. 2. A sturdy, NMR safe container to hold the organ should be provided, and suitable for both 10 mm and 20 mm diameter coils.
Organ monitoring	1. Easy placement of a polyethylene balloon for functional measurements (heart). 2. Inflow buffer temperature monitoring to organ. 3. Ability to sample buffer inputs and organ effluent.
Flow rates	1. Must be able to deliver a flow rate of at least 25 mls / min, at 80 mmHg, in the presence of an isolated rat heart and at least 10 mls / min for the isolated mouse heart [190]. 2. Must be able to deliver up to 15 mls / min for the mouse liver.
Oxygenation	1. The lung must oxygenate the buffer to a partial pressure of at least 550 mmHg. 2. The buffer, at the input to the organ must be at 37 °C and must have an O_2 tension of around 500 mmHg at the lowest flow rate of 2 ml / min for the mouse heart.
Durability and maintenance	1. The tubing and material used must be resistant to strong acids and bases (used for cleaning), as well as high temperatures. It should have a non-stick internal wall. 2. The umbilical should be easy to clean. For this reason, the requirements in (1), concerning high temperature and acid stability are important for the use of boiling water and acid washing. 3. The buffer lines must be water tight, so as not to allow water jacketing fluid to mix with buffer. 4. The umbilical in particular should be easy to dissasemble and maintain. Ideally, this would involve adhesive free compression fittings where possible.
Buffer quality	1. A mechanism should be in place to filter buffer being delivered to the organ. 2. Air bubbles that may block vascular flow should be trapped before entering the organ. 3. The last remaining portion of apparatus (umbilical head) delivering buffer to the organ should be transparent, for visual confirmation that no air bubbles are present.

DNP substrate delivery	1. The hyperpolarized substrate should be delivered quickly to the target organ, without disruption to its function, using a reliable switching mechanism. 2. It should reach the organ within a time frame that would provide adequate signal to noise ratio for the acquisition of metabolic NMR data.
Additional protocols	1. A line to supply drugs or other compounds to the organ should be in place.
Magnet safety and data quality	1. Whilst metal is acceptable in the umbilical, it must be non magnetic. 2. For any metal present, it should be kept far from the organ, or the sensitive region of the coil, in order to avoid disruption to the magnetic field homogeneity. 3. The organ should have sufficient space in its enclosure, in order to avoid artefacts from turbulent fluid motion, which disrupts NMR signal quality. 4. The sensitive central area of the coil must be accessible to the organ.
Target organ	1. The rat and mouse heart must be perfused within the sytem. 2. The rat and mouse liver should be perfused within the system. 3. Perfusion of other organs should be possible with no additional effort (i.e. the kidney).
Type of perfusion	1. This perfusion setup must be capable of constant pressure perfusion. 2. Ideally, it should integrate the ability to use constant flow in combination with an additional pressure transducer when using this method.

Table 6.1: Specifications for the design of a perfusion rig.

In developing the perfusion apparatus for perfused mouse heart and liver studies, the following steps were taken in order to meet these specifications:

Organ manipulation: a male to male luer lock adapter was used for universal attachment of readily available cannulae. This allows perfusion of organs either where cannulation is done *ex vivo* (the heart) or *in vivo* (the liver). The container for the organ in NMR experiments is typically NMR quality borosilicate material. However, it is fragile, expensive, and unnecessary in a hyperpolarized experiment involving the perfused organ, where SNR levels are relatively high. For this reason, a 20 mm Perspex tube was used for the rat heart and mouse liver experiments. It was necessary to

maintain a 10 mm NMR glass tube for the mouse heart, as it was not easily possible to create a magnet safe tube with the thin wall thickness required.

Organ monitoring: a groove was etched into the umbilical head to allow a balloon line to run uninterrupted, and without risk of compression, from a secured pressure transducer to the heart. The balloon line was kept as short as reasonably possible to ensure accurate measurements. The use of a long balloon line can induce standing waves causing artificially high contractile functions. Balloon line selection was important – stiff tubing caused extreme sensitivity of the balloon to EDP, giving inaccurate readings. A small bore, flexible tubing was used, which provided the correct balance for transmitting hydrostatic pressure to the pressure transducer. The balloon line was connected to a blunted needle, attached to a disposable blood pressure transducer.

Flow rates: Given the disparity between the potential flow rates of the mouse heart and liver, and those of the rat heart, two switchable buffer transmission lines were used, with different bore sizes. This was done to minimize the dead volume for hyperpolarized applications in each situation, and to ensure rapid substrate delivery. The small bore buffer line is used for mouse heart and liver applications, whereas the much larger flow capacity line is used for the rat heart.

Oxygenation: A glass lung was used (instead of other methods previously discussed), due to its efficiency at oxygenating buffer, where space is not a concern. In order to maintain oxygen tension as far as possible to the organ, gas impermeable buffer lines were used. In addition, careful temperature regulation can have a large impact on buffer oxygenation. Temperature should be increased gradually across the perfusion apparatus to reach 37 °C at the organ, so as to ensure the buffer is as saturated as possible with oxygen, which decreases as temperature increases. For this reason, the main buffer resevoirs were heated to 38 °C, and the umbilical was then heated as appropriate given the flow rate to achieve the desired temperature.

Durability and maintenance: To provide the chemical and thermal resistance needed

for this system, as well as tubing which is designed to be smooth (in that it does not accumulate deposits easily), medical grade Tygon S-50-HL tubing was used exclusively in the umbilical except for the buffer lines. This Tygon tubing was temperature resistant to beyond 74 °C (though may suffer from discoloration above this value), did not readily absorb fluid and had a large bend radius (the minimum radius that the tubing can be bent before it folds and halts flow). The buffer lines used flexible NORPRENE tubing, which shares many of the properties of the S-50-HL tubing used, however, it was considerably more flexible, and had a smaller bend radius. Its disadvantage however was that it is opaque. Transparency should be used wherever possible in a perfusion system, to aid with problem solving. In order to maintain watertightness between the buffer lines, and the external waterjacketing, cyanoacrylate glue was used for all connections. All other connections with no surrounding fluid were compression fitted. Connections between metal and non-tubing components were made using two part epoxy adhesive with a 24 hour curing time.

Buffer quality: All buffer was filtered on initial preparation with a 0.45 µm filter, but further filtered on the rig with a 5 µm filter (between the buffer reservoir and the lung, and between the organ, and the return buffer line). This was to avoid any large deposits blocking the microvasculature within the organs. To avoid air bubbles in the buffer, the umbilical head was fitted with a wide bore buffer delivery path, which acts as a large bubble trap, and does not disrupt flow signicantly when air is present. Polymethylmethacrylate (Perspex) was chosen as the material for the umbilical head. It was transparent, a desirable quality when monitoring the buffer for air bubbles upon organ perfusion.

DNP substrate delivery: The most reliable way to deliver DNP substrate to the heart was to use a simple three way tap system for both lines (Figure 6.4), which allows buffer from the lung to pass through to the organ, or can be switched to allow buffer from a heated buffer reservoir (into which the hyperpolarized substrate is mixed) at

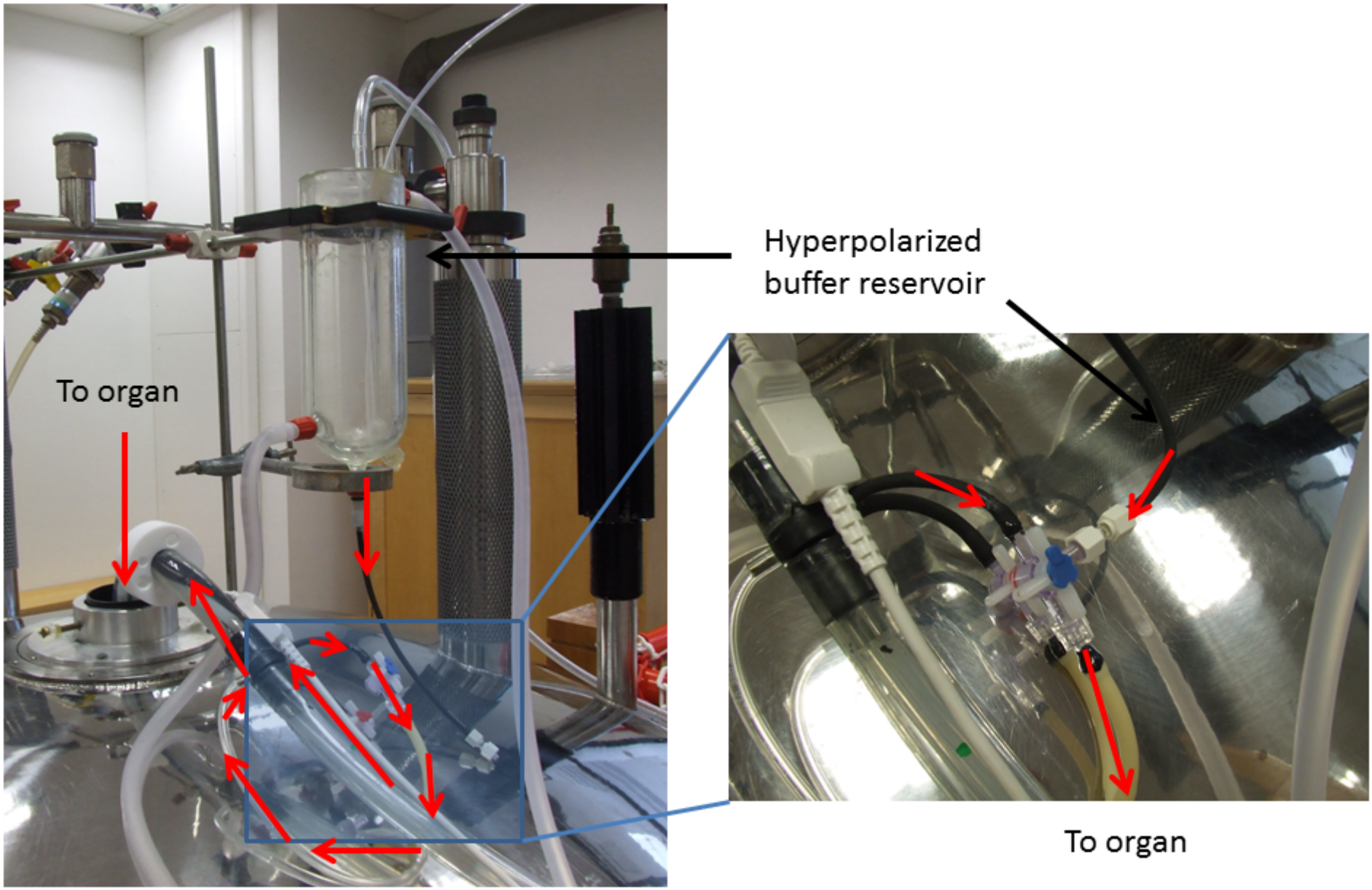


Figure 6.4: An image showing the delivery of KH buffer from both non-hyperpolarized buffer reservoirs (represented by incoming red oxygenated buffer arrows on the left pane), or hyperpolarized buffer reservoirs. A simple three way tap (right pane) allows switching of buffer between the two different reservoirs.

the same height as the lung to proceed to the organ. This creates the shortest path for the hyperpolarized solution to the organ, whilst keeping the pressure head constant. Once the hyperpolarized experiment has finished, the tap can be switched back to the buffer flow from the lung. The tubing bore size for the small flow (mouse heart and liver) and large flow (rat heart) lines were chosen on a trial and error basis. The time for the hyperpolarized substrate to reach the organs was assessed (described later in this chapter).

Additional protocols: a multiway port was added to the umbilical head, which supports an in-line thermocouple to monitor buffer temperature, as well as a drug injection port, for experiments such as late gadolinium contrast (as used in Chapter 3) or other drug delivery. This port can also be attached to a pressure transducer for constant flow experiments.

Magnet safety and data quality: all tubing connectors used within the umbilical were stainless steel, and were kept well outside of the sensitive coil region, to avoid magnetic field disturbances. The tubes used to contain the organ were large enough to accomodate the organ, with enough space below the organ effluent area to allow circulation without signicant flow artefacts.

Target organ: Other than factors already mentioned, including oxygenation, and adequate buffer line bore size, no further actions were needed to allow the perfusion of rat or mouse hearts within the system, nor for the mouse liver. The rat liver, however, warrants comment. It was not possible to perfuse the rat liver within this system, due to the large size of the rat liver following perfusion. The problem arises in particular when the organ is perfused with colloidal buffer, which increases the size of the liver beyond the maximum size that can be accomodated in a 20 mm tube. Other methods were tried, including attempts to perfuse isolated lobes following the surgical anatomy of the liver [195], but ultimately, the lobes could not be sufficiently isolated, and separating the lobes caused severe trauma. The only other possibility

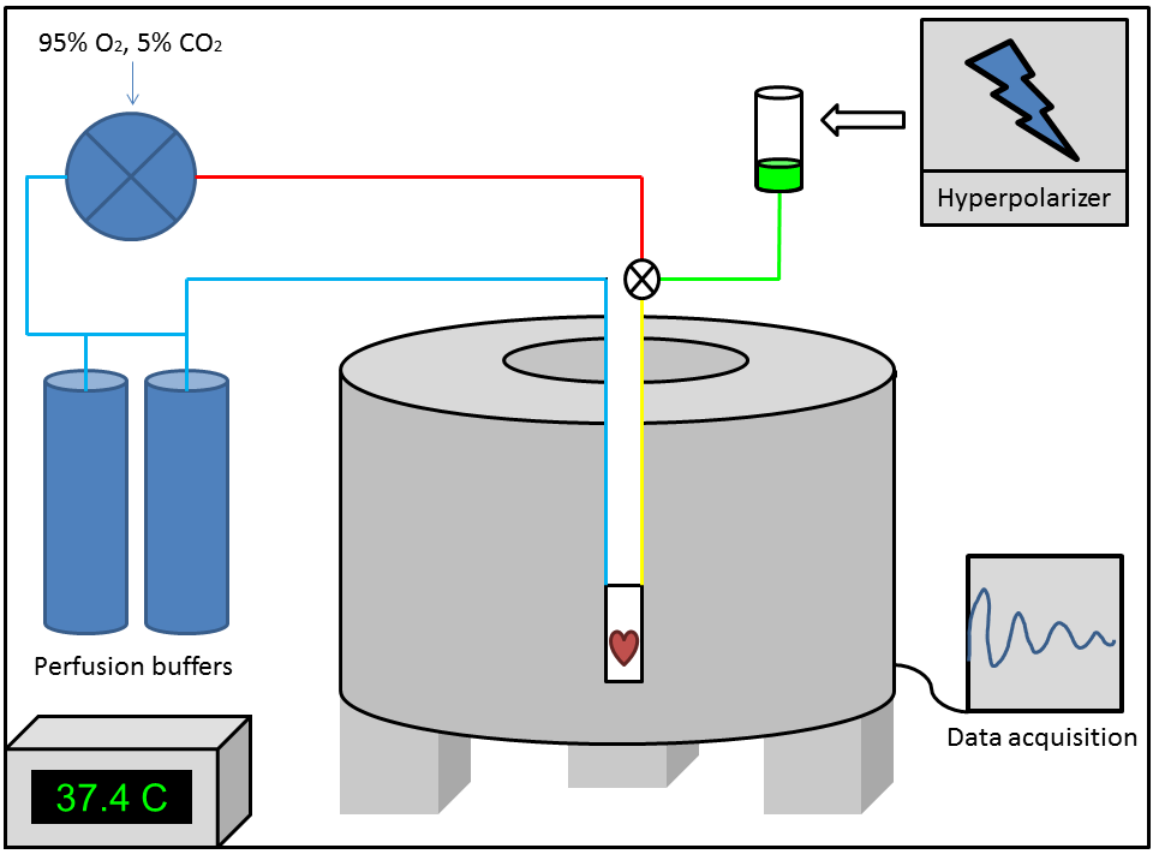


Figure 6.5: A schematic of the perfusion apparatus used. Perfusion buffers (KH) can be drawn from either cylinder, and proceed to be oxygenated with a mixture of oxygen and carbon dioxide. This gassed buffer proceeds to a tap, above the magnet, which can either allow the buffer through uninterrupted, or, can be switched to let through KH buffer containing a hyperpolarized probe. In both cases, the buffer proceeds to supply the isolated perfused organ inside the magnet, where spectral data is then acquired. The buffer is then returned back to the storage cylinders. The buffer in this system is delivered to the organ at 37°C.

may be to use juvenile rats, as this could be achived on the current perfusion setup, but did not offer a feasible method for long term experimental work.

Types of perfusion: The system is capable of perfusing at constant pressure, from 80 mmHg to 120 mmHg. A constant flow system can easily be integrated using the existing umbilical tubing.

An overview of the perfusion setup used is shown as a diagram in Figure 6.5.

6.3 Perfusion setup testing

In order to evaluate and test the performance of this new perfusion design, an ischemia reperfusion protocol was chosen for both the mouse heart and liver.

6.3.1 Mouse heart

6.3.1.1 Materials and methods

Perfusion: Hearts from 6 male C57/BL6 mice (Harlan, UK) (body weight: 36±5 g, heart weight: 250±10 mg) were perfused in the Langendorff mode as follows. A 3 ml / kg injection of sodium pentobarbitone was administered via the intraperitoneal route using a 27 Gauge needle. After loss of pedal reflexes and those of the tail, an upper midline incision was made, a thoracotamy performed, and the heart removed by clamping the attached lungs, and carefully excising the bundle of tissue. The lungs and thymus were removed, and the aorta cannulated using a 16 Gauge cannula and 5/0 suture.

Spectroscopy: The hearts were initially perfused with modified KH buffer containing 11 mM glucose, 1.9 mM $CaCl_2$, 0.5 mM Na_2EDTA and 1.25 mM pyruvate at 100 mmHg pressure. A small polyethylene balloon was inserted into the left ventricle and the EDP adjusted to achieve a pressure of approximately 4 – 5 mmHg once in the magnet. This balloon was set to continually monitor heart rate and developed pressure throughout experiments as a measure of cardiac function. The hearts were allowed to equilibrate for 15 minutes, during which time they were centered in the sensitive region of a 20 mm dual tuned ^{1}H / ^{13}C coil, and shimming was performed to reduce the proton linewidth to around 40 Hz. A hyperpolarized pyruvate study was performed as previously described in Section 3.2. Briefly, a 1.25 mM hyperpolarized [1-^{13}C]pyruvate solution was delivered to the heart as a bolus over 150 seconds, and a ^{13}C pulse-acquire experiment commenced (TR = 1 s, FA = 30^{o}, BW = 180 ppm,

4096 pts). Following acquisition, the sum of 60 spectra were taken, beginning with the first spectrum showing the appearance of hyperpolarized pyruvate, and the ratio of the bicarbonate and CO_2 signals to the pyruvate signal was used as a measure of flux through the pyruvate dehydrogenase (PDH) enzyme. All other metabolites were similarly normalized. pH was assessed using the ratio of bicarbonate and CO_2 in the Henderson-Hasselbalch equation, with pKa = 6.15, as previously reported [116].

A fully relaxed 10 minute ^{31}P acquisition was performed using a dual tuned 10 mm ^{1}H / ^{31}P probe (TR = 15s, NS = 40, SW = 49.391 ppm, TD = 2048, FA = 90^{o}) , followed by a series of rapid 30 second ^{31}P scans for 30 minutes (NS = 120, SW = 49.391 ppm, TD = 2048, FA = 60^{o}). The period up until this point will be referred to as "pre-ischemia". Ten minutes into these scans, the buffer flow was stopped, to begin a period of global ischemia (referred to as "ischemia"). Following the end of the rapid ^{31}P scan, ischemia was maintained for an additional 5 minutes, during which time the 20 mm ^{13}C coil was re-inserted. Immediately upon reperfusion (referred to as "reperfusion"), another 1.25 mM hyperpolarized [1-^{13}C]pyruvate acquisition was carried out, marking the end of the ischemic period after a total of 25 minutes. The period following this will be referred to as "post-ischemia". A further series of rapid ^{31}P scans were carried out for 20 minutes, followed by a fully relaxed 10 minute ^{31}P scan. The rapid ^{31}P scans were analyzed by normalizing the data against the fully relaxed ^{31}P initially acquired to account for partial saturation effects. Following normalization, the middle ten minute segments during the pre-ischemic, ischemic and post ischemic periods for PCr, ATP, Pi levels were taken and averaged. Each of these segments were normalized to pre-ischemia. Flow rates were measured at the beginning, and end of perfusion. Figure 6.6 summarizes this protocol diagrammatically.

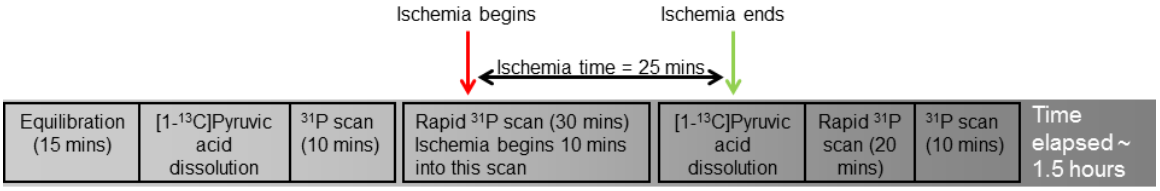


Figure 6.6: A diagrammatical representation of the protocol carried out in the isolated perfused mouse heart. Ten minute ^{31}P scans are fully relaxed, whilst the rapid ^{31}P scans are partially saturated.

Data analysis: Comparison between two measurements was carried out using a paired t-test. For temporal data with more than two measurements, a 1 way ANOVA with a posthoc Bonferonni-Holm correction was applied. Data were analyzed in a paired fashion, by normalization. All tests were carried out at the $p<0.05$ significance level. Correlations between data sets were performed using a Pearson's correlation coefficient (CC) analysis. Units are a.u., unless otherwise specified. Data are expressed as mean±standard deviation. Spectra were processed and quantified using jMRUI as previously descibed in Chapter 4.

6.3.1.2 Results

Cardiac function: A trace of RPP over time is shown in Figure 6.7.

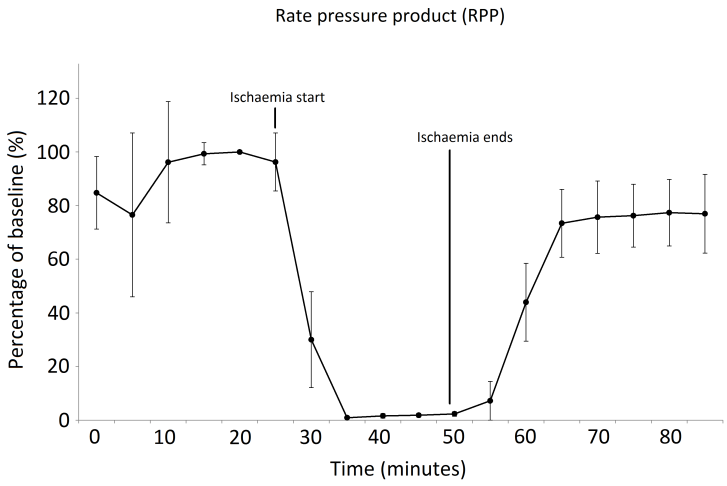


Figure 6.7: Cardiac function (shown as RPP) over the duration of the experiment, averaged across all hearts. RPP can be seen to decrease quickly upon ischemia, and gradually return upon reperfusion. n = 6

In terms of heart function, no significant differences were seen in heart rate 15 minutes immediately pre or post ischemia (330±50 vs 340±20 BPM), nor for EDP (5±1 vs 6±1 mmHg). Significant differences were seen in both developed pressure (80±10 vs 60±20 mmHg), and RPP (heart rate x developed pressure) (27,000±7000 vs 20,000±6000 mmHg / min, equivalent to a recovery to 75±17% of pre-ischemic RPP), as shown in Figure 6.8. Cardiac function was not assessed during ischemia, due to the lack of any detectable heart rate, or developed pressure.

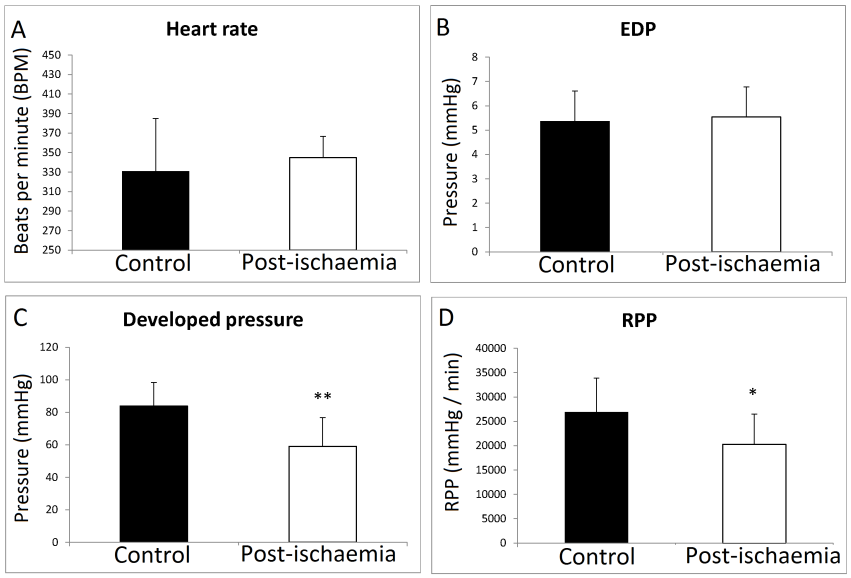


Figure 6.8: Summary of the cardiac functional data. Significant changes between pre-ischemic and post-ischemic periods were present only with developed pressure and RPP (rate pressure product). *p<0.05, **p<0.01, n = 6

Cardiac energetics: ^{31}P data revealed no significant change in PCr / ATP as judged from the fully relaxed scans taken during pre-ischemic and post-ischemic periods of the experiment (1.9±0.3 to 2.8±0.7, p = 0.09, Figure 6.9), but did reveal a significant increase in PCr post-ischemia when compared to pre-ischemia (14±9% increase), with no significant change in ATP.

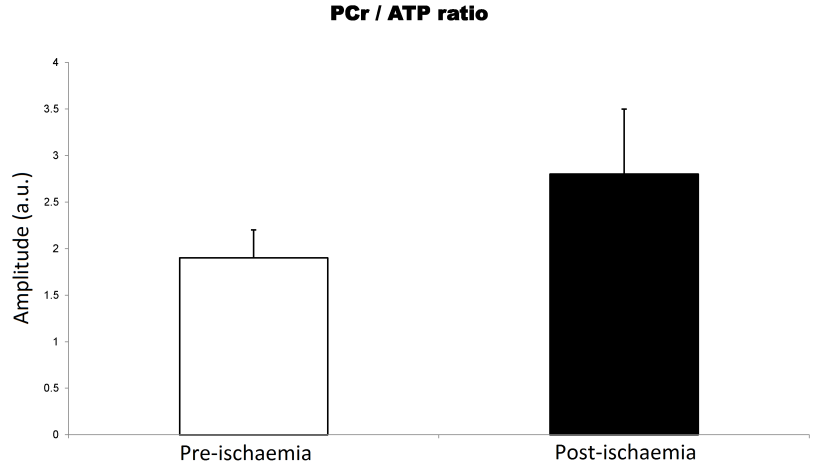


Figure 6.9: This figure shows the PCr / ATP ratio pre and post-ischemia, which was not significant. n = 6

This is reflected in the temporal ^{31}P data as shown in Figure 6.10. There were significant differences in PCr levels between pre-ischemic, ischemic and post-ischemic time periods (ischemia: 27±5%, post-ischemia: 112±12% of pre-ischemic PCr values). Significant changes in Pi were seen only between pre-ischemia and ischemia, and between ischemia and post-ischemia (ischemia: 950±30%, post-ischemia: 170±180% of pre-ischemic Pi values). No differences were seen between any of the periods for ATP levels.

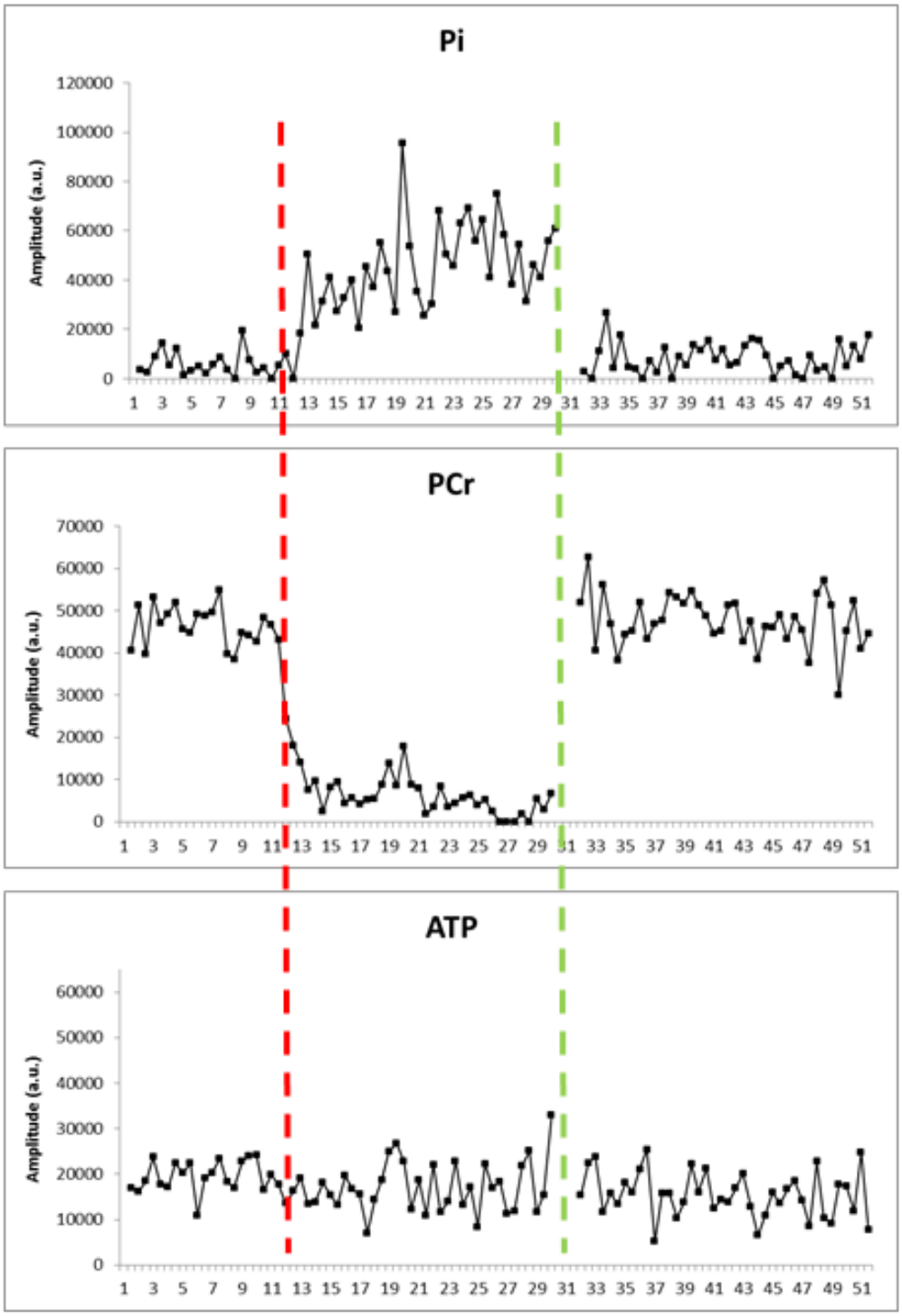
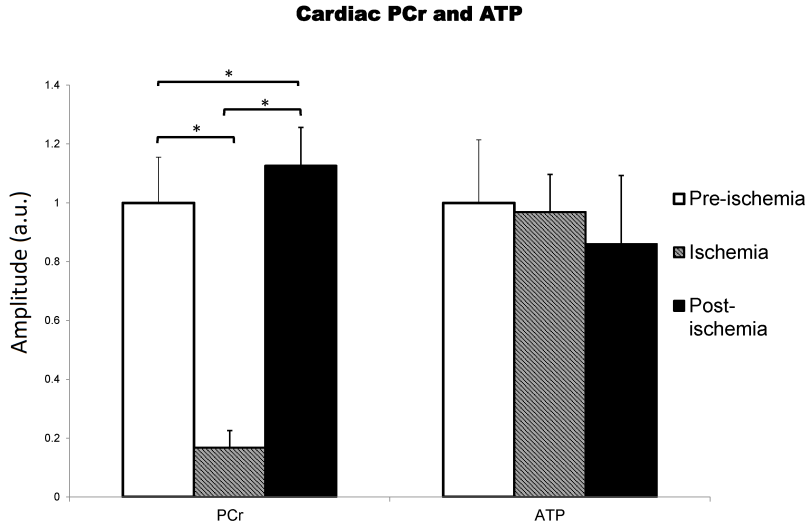
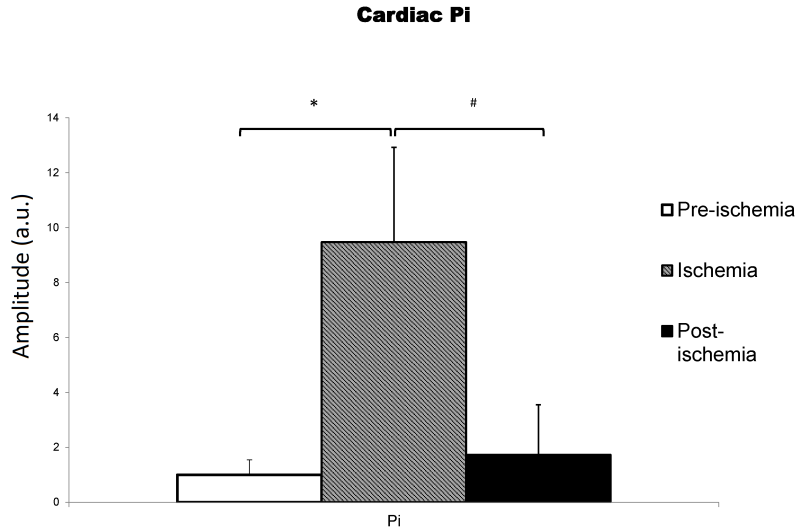


Figure 6.10: A representative overview of the temporal changes (in minutes) that occur with PCr, ATP and Pi during the course of the experiment. The red dashed line represents the induction of ischemia, and the green dashed line represents reperfusion, which occurs during the break in ^{31}P acquisition, when hyperpolarized [1-^{13}C] pyruvate data is being acquired. n = 6

These results are summarized in Figure 6.11, depicting the averages taken over 10 minutes, during each of pre-ischemia, ischemia and post-ischemia. pH could not be determined in the pre-ischemic period, due to very low levels of Pi.



(a)



(b)

Figure 6.11: The graphs show the changes in PCr, ATP and Pi over the course of the experiment during pre-ischemia, ischemia and post-ischemia. Signicant differences between all groups exist for PCr. No significant changes were present between any groups for ATP. Pi shows significant differences only between pre-ischemia and ischemia, as well as ischemia and post-ischemia. n = 6

Signal timings: In order to assess how quickly the hyperpolarized substrate was

reaching the mouse heart, timings were calculated from the point of switching to the hyperpolarized pyruvate buffer to the instant that the hyperpolarized pyruvate signal was seen on the spectrometer. During the pre-ischemic period, the minimum time was 31 seconds, and the maximum was 140 seconds (mean was 80±40 seconds), with the time being inversely proportional to coronary flow rate (R^2 = 0.779, linear fit, Figure 6.12).

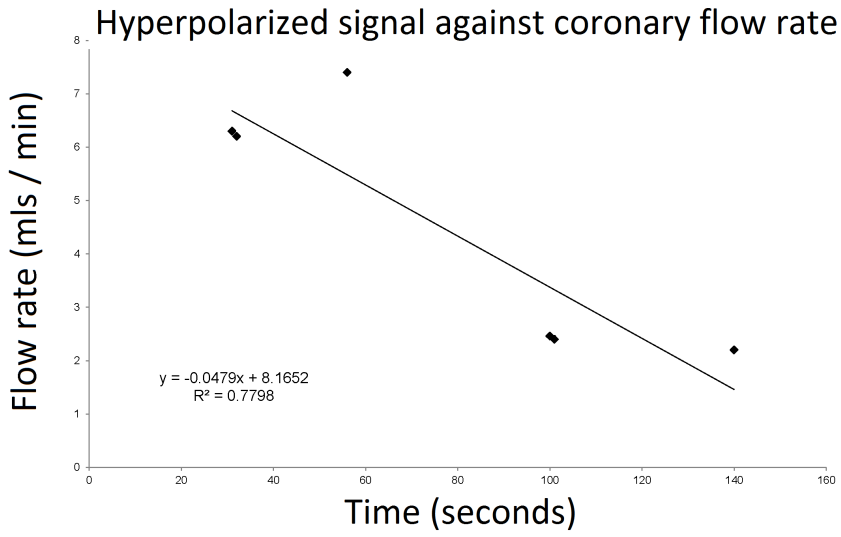


Figure 6.12: A plot of coronary flow rate against the arrival time of the hyperpolarized pyruvate signal. n = 6

Flow rates were significantly higher during reperfusion (202±92% increase compared to control flow, n = 3). This was reflected in the hyperpolarized signal times seen upon reperfusion when compared to pre-ischemic values (80±40 vs 40±10 seconds, p = 0.06). In addition, the pre-ischemic and reperfusion hyperpolarized [1-^{13}C]pyruvate scan revealed a significant increase in signal to noise ratio (50±40 to 90±20 a.u.), reflecting the increased flow rate to the heart and therefore the reduced time for hyperpolarized signal decay. Post-ischemic when compared to pre-ischemic coronary flow rates were each different, but showed no trend for either net increase or decrease (4.5±2.4 vs 4.2±2.7 ml / min, p = 0.17). This serves to validate the use of a perfusion system capable of variable flow rates.

Cardiac metabolism: Figure 6.13 shows sample hyperpolarized [1-^{13}C]pyruvate spectra obtained from the mouse heart, pre-ischemia and during reperfusion.

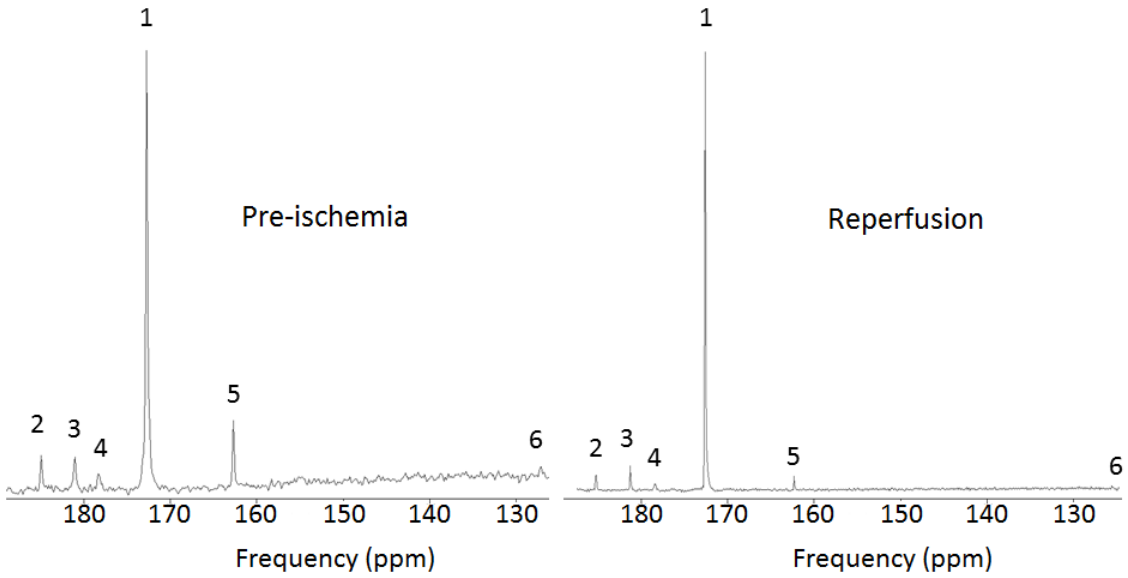


Figure 6.13: Sample spectra in the isolated perfused mouse heart of hyperpolarized [1-^{13}C]pyruvate (1) and its metabolites, lactate (2), pyruvate hydrate (3), alanine (4), bicarbonate (5) and CO_2 (6). PDH flux was seen to be higher pre-ischemia. Note also the higher signal to noise ratio seen upon reperfusion, due to the increase in flow rate to the isolated heart, and therefore increase in hyperpolarized signal.

Comparing pre-ischemic and reperfusion periods, hyperpolarized [1-^{13}C]pyruvate scans revealed significant decreases in alanine from (0.07±0.03 to 0.031±0.007), and PDH flux (0.120±0.05 to 0.026±0.007). No significant changes were seen for lactate (0.08±0.04 to 0.04±0.01, p = 0.06) (Figure 6.14).

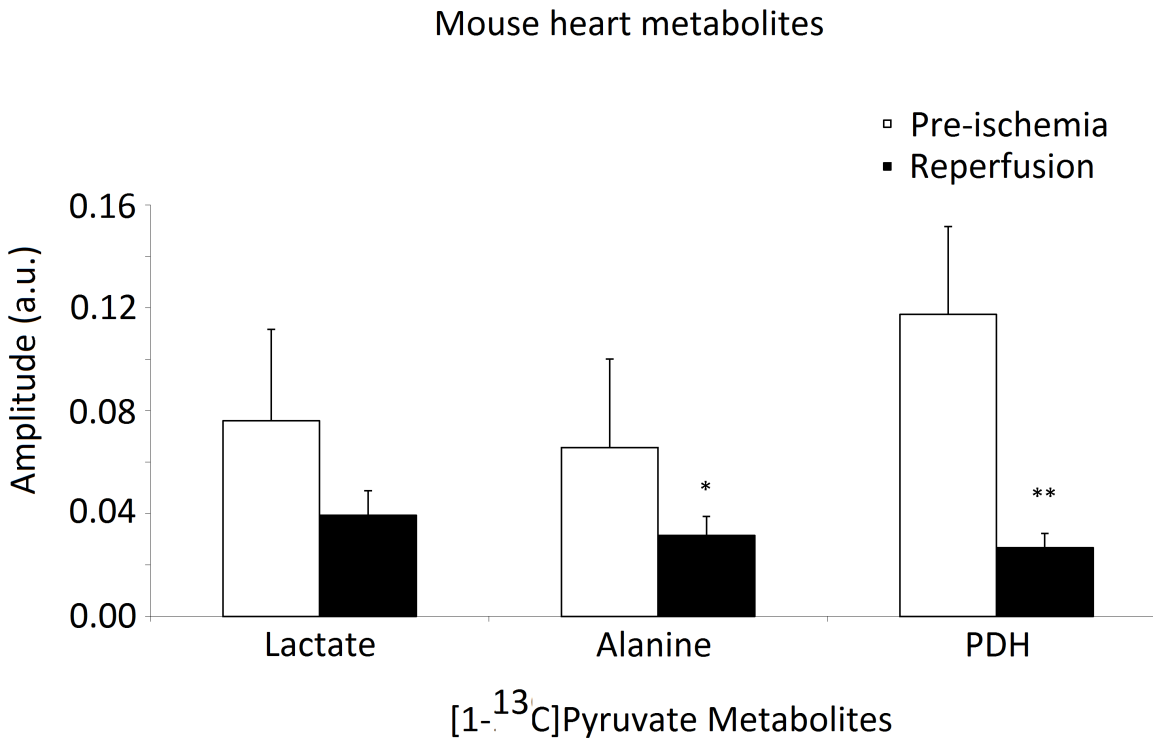


Figure 6.14: Quantification of the main metabolites seen in the isolated perfused mouse heart. PDH, the sum of bicaronate and CO_2 fluxes, was significantly decreased upon reperfusion. *p<0.05, **p<0.01, n = 6

pH, as determined using the ratio between bicarbonate and CO_2 from the hyperpolarized pyruvate dissolution, showed no significant differences between the pre-ischemic and reperfusion period (6.9±0.3 to 6.8±0.2, n = 5). PDH flux as measured by hyperpolarized [1-^{13}C]pyruvate and cardiac contractile function (RPP) were plotted against each other during both hyperpolarized dissolutions (pre-ischemia, and reperfusion), however, no strong correlations were found (CC = 0.40 and 0.25 respectively).

6.3.1.3 Discussion

This study has successfully demonstrated that DNP hyperpolarization can be used in combination with the isolated perfused mouse heart. In all but one of the hearts studied, the signal to noise ratio seen was very good, although where coronary flow rates were very low, spectra were considerably noisier, but still analysable. It was

necessary to sum spectra to quantify the hyperpolarized data, which is not normally necessary in the rat heart when using a hyperpolarized pyruvate concentration of 0.625 mM. This is due to the increased coronary flow rates in the rat heart, providing greater signal. In terms of metabolism, PDH flux was greatly reduced during reperfusion following ischemia. This may be expected since the heart has been under anaerobic metabolism conditions for around 25 minutes, and thus would be producing and exporting lactate via the same monocarboxylate transporter (MCT) used to import hyperpolarized pyruvate. This would imply that all metabolism of pyruvate, not simply PDH flux should be decreased, which was the case. In addition, it is possible that pyruvate was being diverted from PDH, to replenish TCA cycle intermediates depleted during ischemia [196], although this was not reflected in the spectra seen, where metabolites such as aspartate or malate should be present if there was a high level of anaplerosis. Surprising however was the decrease seen in lactate levels. Following such an experiment, high lactate levels would be expected due to the need to produce ATP anaerobically [197], as previously shown in the isolated perfused rat heart [77]. It has further been shown that the ability of the heart to recover its contractile function is inversely proportional to lactate levels and other anaerobic metabolites causing disruption to the ETC enzymes [198], even when, as in this study, no significant changes are seen in the adenosine nucleotide levels [199]. One possible explanation for the absence of an observed large lactate pool via hyperpolarized [1-^{13}C]pyruvate is that the dead volume of the mouse heart perfusion line was too large and thus by the time the hyperpolarized substrate had reached the myocardium, the accumulated lactate pool had been washed away. It was a shortfall of this study that a further hyperpolarized [1-^{13}C]pyruvate dissolution was not carried out upon stable recovery of the hearts following ischemia, to see the extent to which metabolic fluxes had recovered, and whether that was linked to the recovery of the contractile function. It is particularly interesting to note in light of the work

performed in Chapter 4, that even less PDH flux would be seen if fatty acids had been supplied [118], and the way in which this may have affected post-ischemic PDH recovery.

Given the flow rates seen from this study, and the relatively high signal to noise from the hyperpolarized data, it would seem feasible to make use of fatty acids bound to BSA, as proposed in Chapter 4, in studies involving the perfused mouse heart in future, especially given that from a metabolic point of view, fatty acid oxidation has been shown to be inhibited during ischemia [200, 201] and to predominate oxidative metabolism upon reperfusion, even if cardiac recovery is impared [202–204]. Intralipid in large concentrations, or combined with heparin [118] could be used with no hyperpolarized signal loss, if the maintenance of a higher hyperpolarized pyruvate signal level were needed. Concerning flow rates, it is also believed that lower concentrations of pyruvate (< 1.25 mM) could be used but this should however be evaluated properly to ensure that enzyme saturation is not occurring as demonstrated in Chapter 4.

Cardiac energetics, as measured by ^{31}P, revealed a sharp decrease in PCr during ischemia, in order to maintain the ATP pool via the creatine kinase shuttle [205], with a corresponding increase in inorganic phosphate (Pi), occuring as ATP and ADP are hydrolyzed, providing energy for the myocardium. That the ATP levels did not decrease significantly pre and post-ischemia implies that this model of ischemia reperfusion was not so severe as to cause complete myocardial failure [206], as further demonstrated by the stability, and lack of significant change pre and post-ischemia in EDP and heart rate [207], as well as by the contractile recovery of all hearts to $75\pm17\%$ of preischemic RPP. This was in surprising contrast to a similar protocol carried out in the perfused rat heart, where hearts were maintained in global ischemia for only 10 minutes, yet saw a steady drop in ATP levels of around 25%, and contractile recovery to only around 56% of pre-ischemic levels [109], findings also reflected in other animal studies [208, 209]. This is perhaps best explained, at least in one of the

studies carried out, by a difference in myocardial temperature. Greve et al used a system whereby the NMR probe itself was heated to 37 °C, which meant the heart would remain at a physiological temperature irrespective of whether or not any buffer flow was present. However, the protocol as carried out in this study required a buffer flow to maintain physiological temperature. Thus the model of ischemia reperfusion used here can be considered mild, as a result of the drop in myocardial temperature, having a preservative effect. Also demonstrated was the increase in post-ischemic PCr over pre-ischemic values seen in this study, with a concomitant decrease in the forward creatine kinase reaction (PCr –> ATP). Although not reflected elsewhere, the measured reverse creatine kinase reaction was increased post-ischemia (i.e. ATP –> PCr) [205]. This may suggest a compensatory mechanism, to protect the heart in the event of further ischemic insults.

6.3.2 Liver perfusion

6.3.2.1 Materials and methods

Perfusion*:* Livers from 4 male C57/BL6 mice (Harlan, UK) (body weight: 23±4 g) were all perfused in the fed state before 11:00 AM as follows. A 3 ml / kg injection of sodium pentobarbitone was administered via the intraperitoneal route using a 27 Gauge needle. After loss of pedal reflexes, and those of the tail, a lower midline incision was made, and the abdominal epidermal layer removed. The abdominal viscera were pushed aside, to expose the inferior vena cava (IVC), the right kidney, the portal vein, and the lower portion of the liver. A loose suture (3/0, used throughout) was placed around the inferior vena cava, distal to the right renal vein junction, and another around the portal vein, 1 cm from the junction to the liver, taking care to avoid the thin, yellow bile duct running parallel. The portal vein was then cannulated with a 24 Gauge cannula, taking care not to insert the cannula too far into the portal vein junction. Success was denoted by the inflow of blood into the cannula. The

suture to the portal vein was tied, the hepatic vein cut, and the suture around the IVC tied. Approximately 10 mls of cold KH solution was perfused through the liver. If the perfusion had been successfully performed, all the lobes showed a distinct colour change, to a lighter shade; failure of any of the lobes to do so typically indicated a cannula that has been inserted too far forward into the portal vein. This was corrected by withdrawing the cannula slightly and reperfusing with KH solution. The liver was now carefully [183] removed, starting from the diaphragm, and cutting the ligaments attaching the stomach to the left lobes of the liver, working down toward the dorsal connecting tissue until the liver was free. Cyanoacrylate adhesive compound was then applied at the portal vein – cannula junction, to provide additional support due to the large weight of the liver (around 2 g).

Spectroscopy: The livers were initially perfused with KH buffer containing only 11 mM glucose and 0.625 mM pyruvate at 80 mmHg pressure. A 20 mm Perspex tube was inserted around the liver, and the organ allowed to equilibrate for 15 minutes, during which time it was centered in the sensitive region of a 20 mm dual tuned ^{1}H / ^{13}C coil, and shimming performed to reduce the proton linewidth to around 50 Hz. A hyperpolarized pyruvate study was then performed as previously described in Section 3.2. Briefly, a 0.625 mM hyperpolarized [1-^{13}C]pyruvate solution was delivered to the liver as a bolus over 120 seconds, and a ^{13}C pulse-acquire experiment commenced (TR = 1 s, FA = 30^{o}, BW = 180 ppm, 4096 pts). Following acquisition, 60 spectra were summed, beginning with the first spectrum in which hyperpolarized [1-^{13}C]pyruvate signal could be seen, and the ratio of the bicarbonate and CO_2 signals to the pyruvate signal was used as a measure of flux through the pyruvate dehydrogenase (PDH) enzyme. Other metabolites were analyzed in the same way. A fully relaxed 10 minute ^{31}P acquisition was then performed using a dual tuned 20 mm ^{1}H / ^{31}P probe (TR = 15 s, NS = 40, SW = 49.391 ppm, TD = 2048, FA = 90^{o}), followed by the acquisition of a series of rapid 30 second ^{31}P spectra over a period of 30 minutes (NS = 120,

SW = 49.391 ppm, TD = 2048, FA = 60°). This period of time will subsequently be referred to as "pre-ischemia". Ten minutes into this ^{31}P acquisition, the buffer flow was stopped, to begin a period of global ischemia (referred to as "ischemia"). Twenty minutes into the ischemic challenge, at the end of the ^{31}P scan, ischemia was maintained for an additional 5 minutes, during which time the ^{13}C coil was re-inserted, and immediately upon reperfusion, another 0.625 mM hyperpolarized [1-^{13}C]pyruvate dissolution was carried out (referred to as reperfusion), marking the end of the ischemic period after a total of 25 minutes. The period following this point will be referred to as "post-ischemia". A further rapid ^{31}P scan was carried out for 20 minutes, followed by a fully relaxed 10 minute ^{31}P scan. The rapid ^{31}P scans were analyzed by normalizing the data against the fully relaxed ^{31}P scan initially acquired to correct for partial saturation effects. Following normalization, the middle ten minute segments during the pre-ischemic, ischemic and post ischemic periods for ATP and Pi levels were taken and averaged. Each of these segments were normalized to pre-ischemia. pH, as derived from ^{31}P data was calculated by measuring the relative chemical shift change between Pi and ATP. Flow rates were measured during pre-ischemia, upon reperfusion and post-ischemia. Figure 6.15 summarizes the protocol diagrammatically.

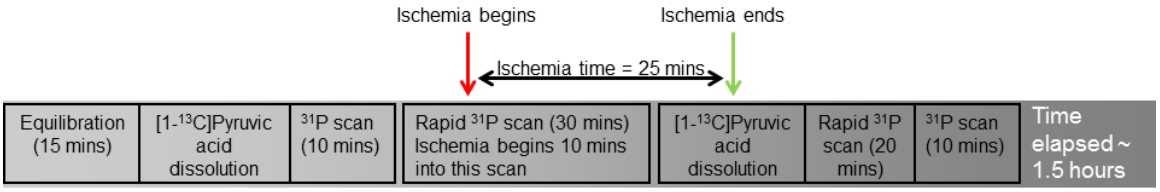


Figure 6.15: A schematic representation of the ischemia reperfusion protocol carried out in the liver.

Data analysis: Comparisons between two measurements were carried out using a paired t-test. For temporal data with more than two measurements, a 1 way ANOVA

with a posthoc Bonferonni-Holm correction was applied. Data were analyzed in a paired fashion, by normalization. All tests were carried out at the $p<0.05$ significance level. Correlations between data sets were performed using a Pearson's correlation coefficient (CC) analysis. Units are a.u., unless otherwise specified. Data are expressed as mean±standard deviation. Spectra were normally analyzed using jMRUI as previously described, however, it was not possible to analyze small metabolites (the anaplerotic pathway products - malate C1 and C4, and aspartate C1 and C4) using jMRUI due to their close proximity to larger metabolites. For these resonances, ACD/NMR 12 was used (Ontario, Canada).

6.3.2.2 Results

Hepatic energetics: ^{31}P data revealed a significant change in ATP / Pi as judged from the fully relaxed scans taken during the pre-ischemic and post-ischemic periods of the experiment (4.2±1.6 to 2.5±1.6), as well as a significant increase in Pi (17,800±8,000 to 20,600±10,600 a.u.) and a significant decrease in ATP levels (33,500±10,300 to 21,000±5,600 a.u.), but no significant change in pH (7.3±0.1 to 7.2±0.1), as shown in Figure 6.16. Representative temporal ^{31}P data is shown in Figure 6.17.

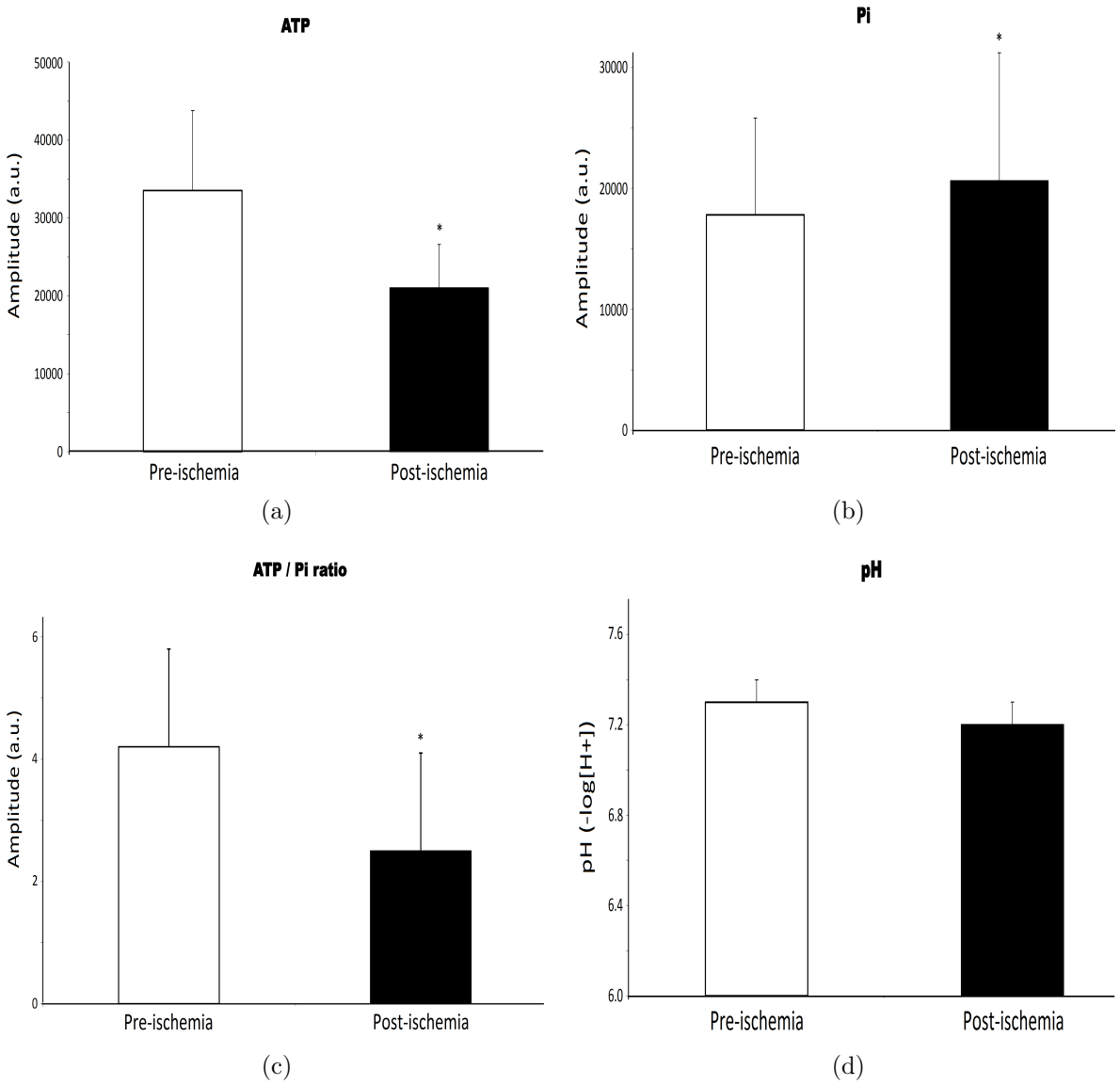


Figure 6.16: The diagrams above show the changes in ATP, Pi, ATP/Pi ratio and pH as derived from the fully relaxed ^{31}P data. n = 4, *p<0.05

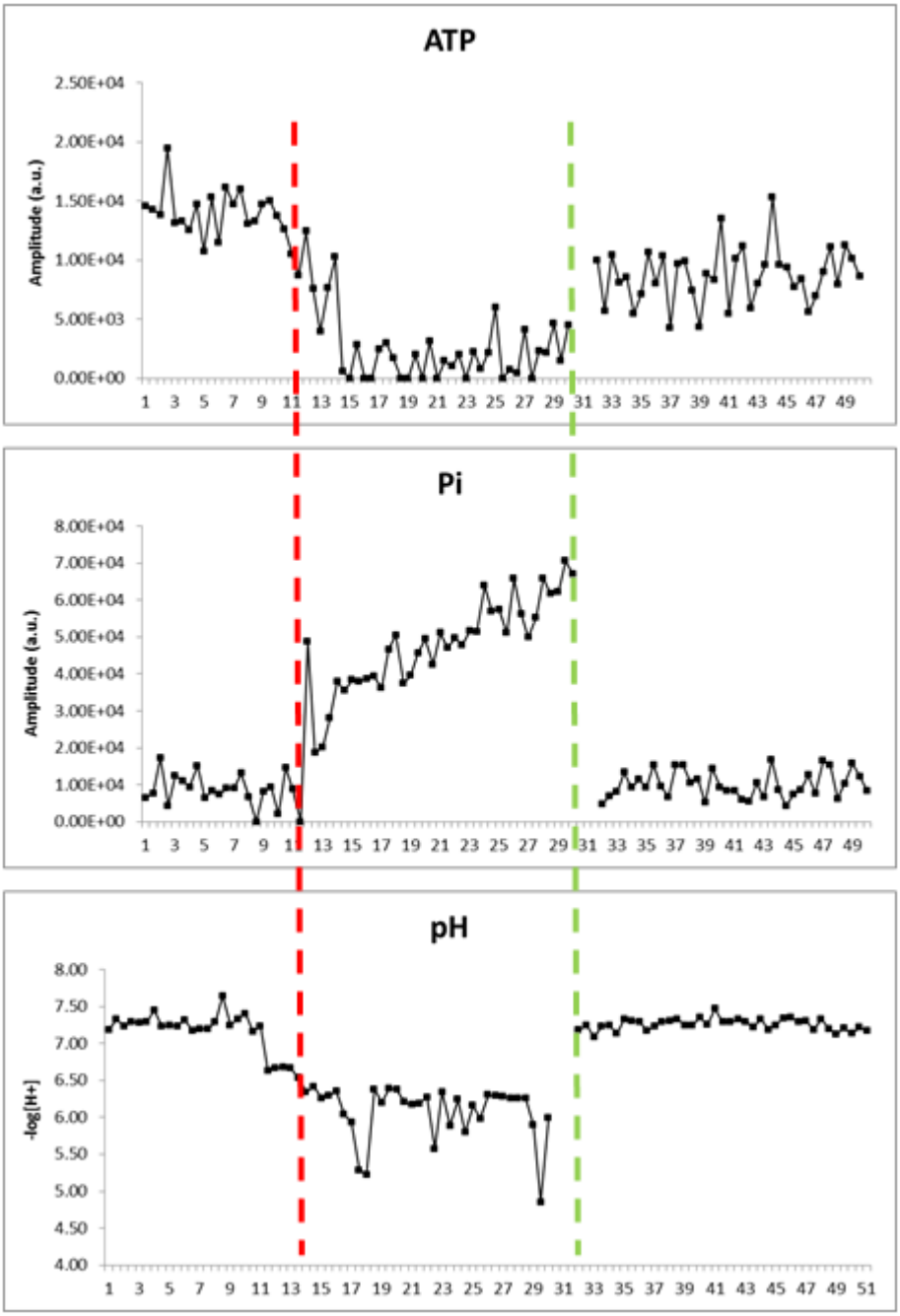
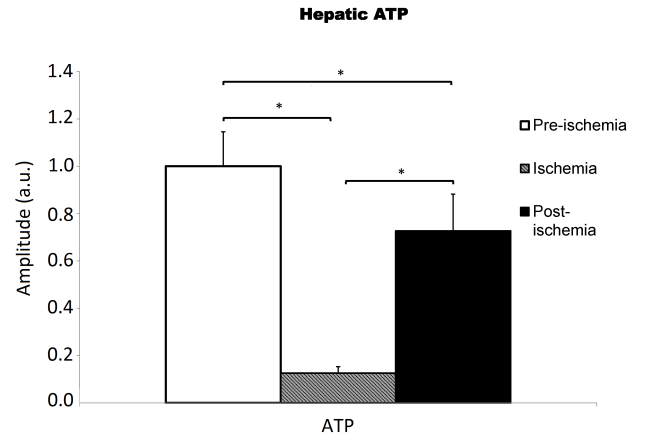


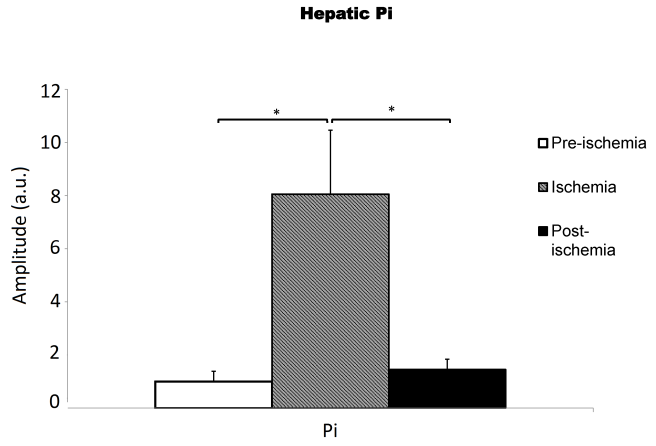
Figure 6.17: A representative overview of the temporal changes (in minutes) that occur with ATP, Pi and pH during the course of the experiment. The red dashed line represents the induction of ischemia, and the green dashed line represents reperfusion, which occurs during the break in ^{31}P acquisition, when hyperpolarized [1-^{13}C] pyruvate data is being acquired. PCr is not typically seen in the liver.

Using the averages derived from the temporal ^{31}P data, there were significant differences in ATP levels between pre-ischemic, ischemic and post-ischemic time periods

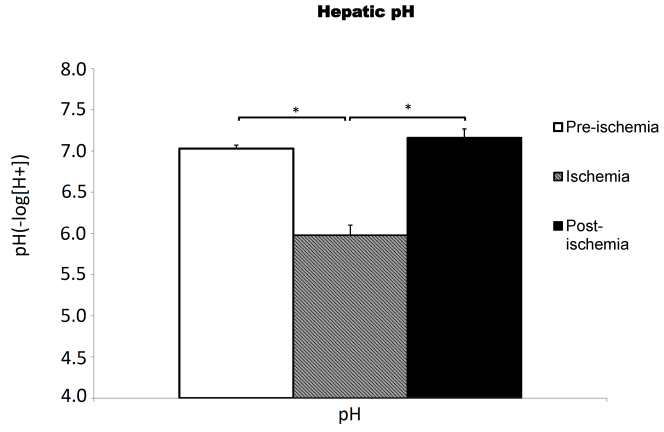
(ischemia: 12±2%, post-ischemia: 72±15% of pre-ischemic ATP values). Significant changes in Pi and pH (as measured by relative chemical shift change between Pi and α-ATP) were seen only between pre-ischemia and ischemia, as well as between ischemia and post-ischemia (ischemia: 805±24%, post-ischemia: 145±38% of pre-ischemic Pi values), and for pH (pre-ischemia: 7.0±0.3, ischemia: 5.9±0.1, post-ischemia: 7.1±0.1) (Figure 6.18).



(a)



(b)



(c)

Figure 6.18: Bar graphs showing the relative changes in ATP and Pi, and the absolute pH values. The ATP chart has significant differences between all groups. Pi and pH values during ischemia and post-ischemia are both significantly different relative to pre-ischemia. The white bar represents pre-ischemia, the grey ischemia and black post-ischemia. n = 4

Signal timings: In order to assess how quickly the hyperpolarized substrate was reaching the mouse liver, the timings were calculated from the point of switching to the buffer containing hyperpolarized pyruvate, to the instant that a hyperpolarized pyruvate signal was seen on the spectrometer. During the pre-ischemic period, the minimum time was 8 seconds, and the maximum was 16 seconds (mean was 11±3 seconds), with the time being inversely proportional to hepatic flow rate (CC = -0.97, Figure 6.19).

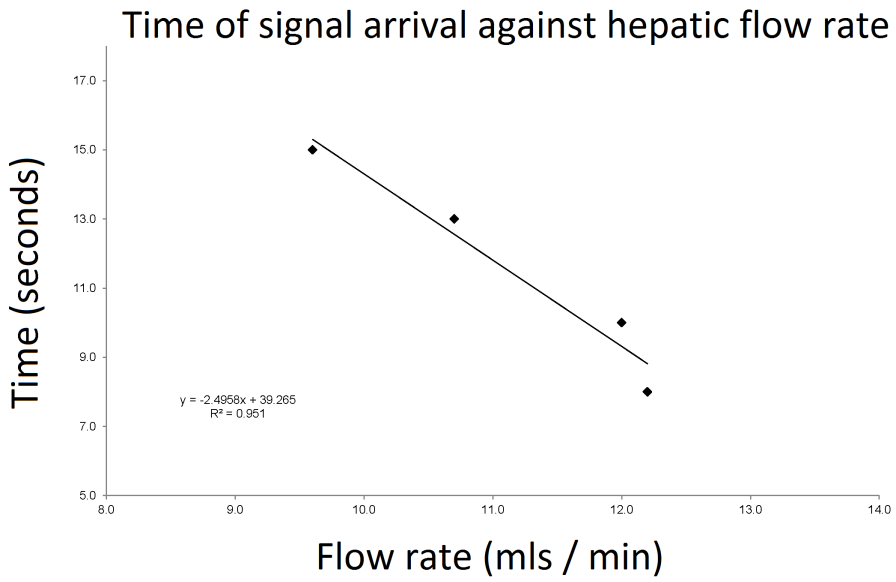
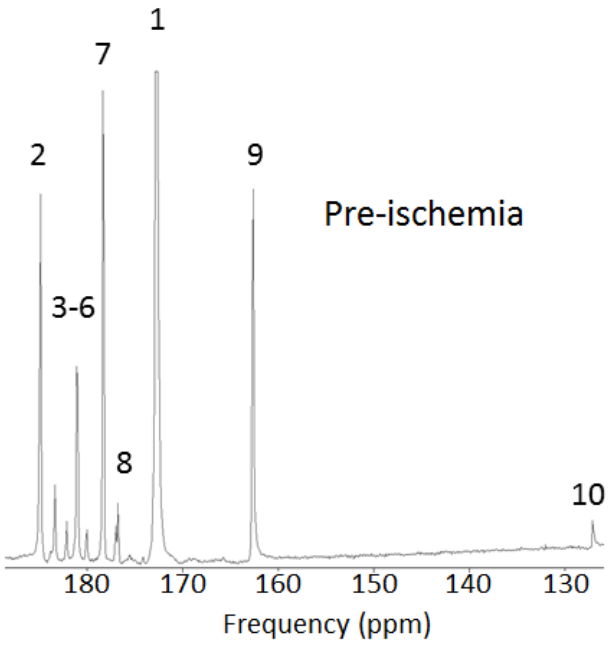


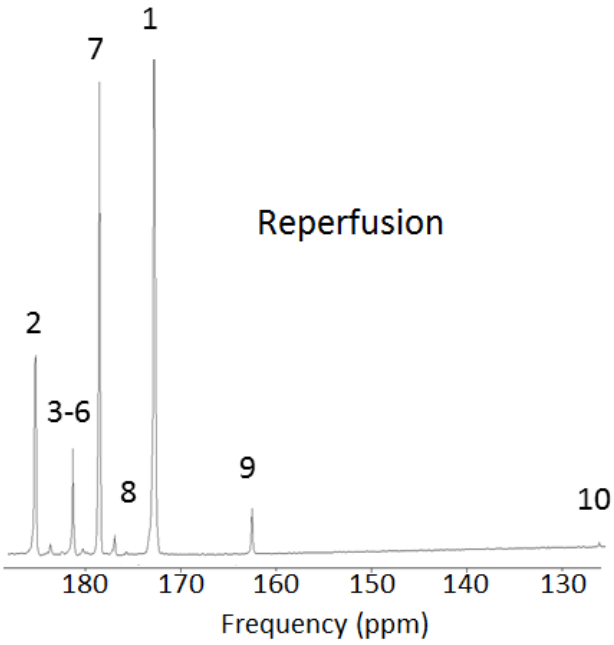
Figure 6.19: A plot depicting the arrival time of the hyperpolarized [1-^{13}C]pyruvate signal against hepatic flow rate. n = 4

The time taken for the hyperpolarized signal to reach the perfused liver upon reperfusion when compared to pre-ischemia did not vary (11±1 vs 11±3 seconds respectively). Flow rates showed individual variations 30 minutes post-ischemia relative to pre-ischemia for all livers but this was not significant (11±1 to 10±2 mls / mins, p = 0.16).

Hepatic metabolism: Example spectra are shown in Figure 6.20.



(a)



(b)

Figure 6.20: Shown are example hyperpolarized [1-^{13}C]pyruvate spectra acquired during the pre-ischemic and reperfusion periods in the liver. The peaks correspond to pyruvate (1), lactate (2), 1-malate (3), 4-malate (4), pyruvate hydrate (5), 4-aspartate (6), alanine (7), 1-aspartate (8), bicarbonate (9) and CO_2 (10).

Spectra acquired both during pre-ischemia and reperfusion were of good spectral

quality, with well defined anaplerotic metabolite peaks seen. Comparing pre-ischemic and reperfusion hyperpolarized [1-^{13}C]pyruvate scans, revealed a significant increase in alanine (0.18±0.06 to 0.6±0.2), and a significant decrease in PDH (0.27±0.13 to 0.05±0.02). Whilst not significant at the $p<0.05$ level, an increase was seen for lactate (0.22±0.03 to 0.39±0.14, $p = 0.09$) (Figure 6.21).

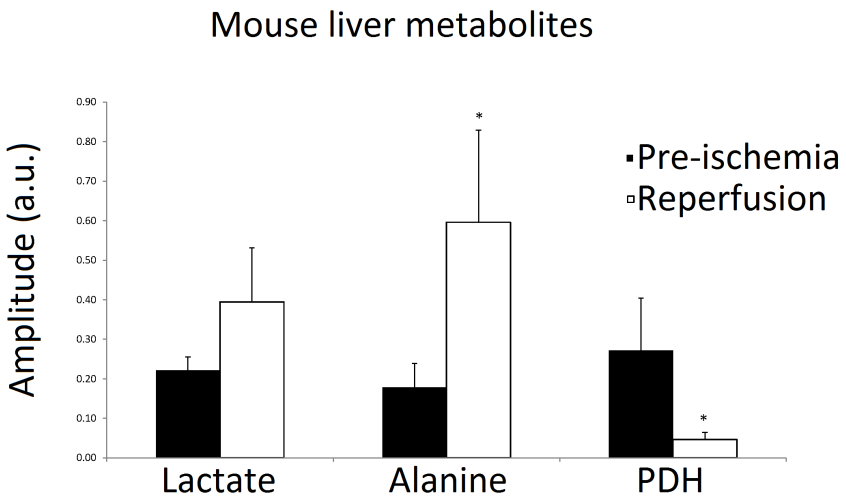


Figure 6.21: The metabolites lactate, alanine and PDH (the sum of bicarbonate and CO_2). Significant differences were seen for alanine and PDH. n = 4

It was not possible to determine pH using the bicarbonate and CO_2 ratio (as described in Section 6.3.1.1), due to the very low production of CO_2 upon reperfusion following ischemia, as shown in Figure 6.20. Concerning the anaplerotic metabolites, a significant decrease was seen in 1-aspartate (0.017±0.009 to 0.001±0.0003). Whilst not significant, decreases in 4-aspartate (0.029±0.018 to 0.005±0.001, $p = 0.073$) and 4-malate (0.013±0.010 to 0.005±0.005, $p = 0.054$) were seen. 1-malate showed no apparent change (0.026±0.026 to 0.017±0.014, $p = 0.34$) (Figure 6.22). This data is shown in diagrammatic form in Table 6.2.

Metabolite	Pre-ischaemia	Reperfusion
Alanine	0.18±0.06	0.6±0.2*
PDH	0.27±0.13	0.05±0.02*
Lactate	0.22±0.03	0.39±0.14
1-aspartate	0.017±0.009	0.001±0.0003*
4-aspartate	0.029±0.018	0.005±0.001
1-malate	0.026±0.026	0.017±0.014
4-malate	0.013±0.010	0.005±0.005

Table 6.2: Hepatic metabolites. * denotes p<0.05

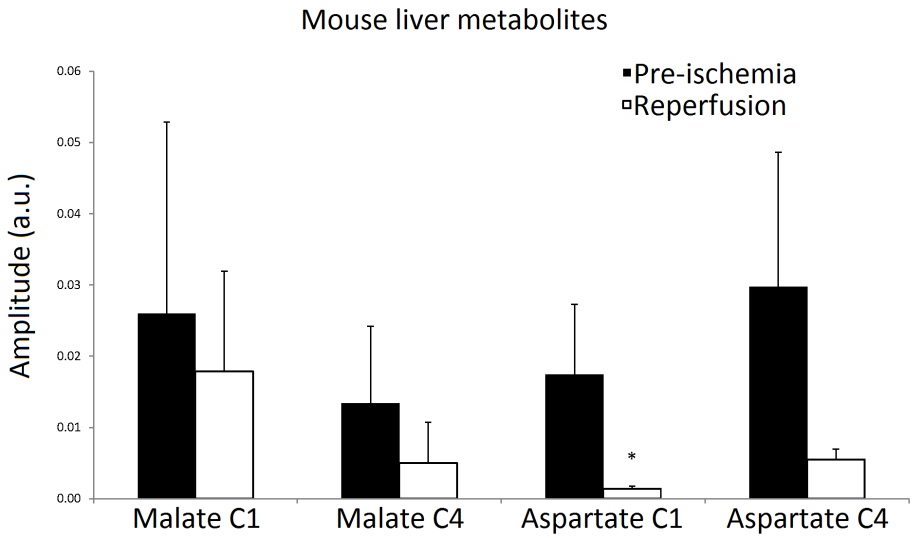


Figure 6.22: The anaplerotic hepatic metabolites during pre-ischemia and during reperfusion. A general trend for their decrease is seen, although only 1-aspartate revealed a significant difference. n = 4

6.3.2.3 Discussion

This study has demonstrated that DNP hyperpolarization can successfully be combined with the isolated perfusion of mouse livers and can provide spectra of excellent quality (Figure 6.20). Before proceeding to their analysis, some comments should be made concerning the perfusion methods used. Given the recommended perfusion pressure of 20 mmHg or less via the portal vein, explanation is warranted as to why this perfusion was done at 80 mmHg. Magnet based liver perfusion studies predominantly use constant flow systems, either with a flow rate of around 3 mls /

gram wet weight / min of liver tissue [188] or a mass independant constant flow rate ranging from 8 mls / min [172] to 20 mls / min [210] for reasons previously stated concerning adequate hepatic oxygenation. As a perfusion using 20 mmHg was not technically possible within the vertical bore magnet without additional equipment, which could potentially be implemented within a new rig system, and a constant flow system was not desireable, a cannula specifically selected to have a maximum flow rate of 14.5 mls / min was selected in order to protect the liver from an overload of buffer. Firstly, the liver is able to control its vascular resistance according to oxygen demands [211–214], and thus to a limited extent, determine its own flow rate. A small sample of buffer, immediately pre and post the liver revealed oxygen removal from the liver of around 200 mmHg, equivalent to approximately 1.5 µmol O_2 / gram wet weight / min extraction rate, which is comparable to previous work, when taking flow rate into account [172, 210].

Flow rates in the liver were more than rapid enough to provide all hyperpolarized spectra with high signal to noise ratios. Liver metabolism has a large anaplerotic component [215], to support its role in controlling glucose homeostasis within the body, which it performs via glycogenolysis, gluconeogenesis and ketone body production. This was reflected in the hyperpolarized [1-^{13}C]pyruvate spectra (Figure 6.20), where the anaplerotic TCA cycle intermediates malate (labelled at C1 and C4) and aspartate (labelled at C1 and C4) were seen. PDH flux was reduced in the liver following ischemia, (it is naturally low as a result of anaplerotic flux via pyruvate carboxylase, with pyruvate distributed in a 1:1 ratio for both routes in the fed state, or 1:7 in the fasted state (PDH:pyvuate carboxylase respectively) [216]). This may suggest diversion of pyruvate away from PDH upon reperfusion. The significant increase in alanine, and substancial increase in lactate therefore warrants further comment. Lactate is typically expected to be increased during conditions of anaerobic metabolism, as would be present in ischemia, and there is a protective role

for the associated acidosis in ischemic injury [217]. In addition, during hypoxia, a decrease in the alanine pool (despite an increase in production [218]) via glutamate metabolism has been suggested, for anaerobic metabolism to produce energy, with the end product succinate. Upon reperfusion, the priority for energy generation is the use of pyruvate to supply anaplerotic components, in particular malate and oxaloacetate to allow continuation of the TCA cycle, following their depletion [196]. The rise in alanine upon reperfusion however, is particularly interesting in this case. The activity of the enzyme ALT (catalysing the conversion of alanine to pyruvate) may rise for several reasons. During periods of fasting, cold [219] or with the use of steroids known to promote gluconeogenesis, the activity of ALT (sometimes referred to as GPT, glutamic pyruvic transaminase) rises several fold above control levels, with a concomitant increase in protein derived nitrogen utilization [220]. In the case of a stressor, such as ischemia or fasting [221], it would therefore be expected that increases in alanine (and lactate) production would be seen in order to produce glucose [216, 222–224] upon reperfusion. This is partially validated in a ^{13}C steady state metabolism study, demonstrating an increase in label to the gluconeogenic precursors lactate and alanine [225]. The gluconeogenic pathway has however been shown to be downregulated during ischemia and following reperfusion [225]. More recent work however demonstrates a reversible decrease in glycolytic enzyme activity, with a maintenance of the gluconeogenic pathway [226]. The information combined would suggest a role for the increased levels of alanine to be diverted into gluconeogenesis. In addition, given the suggested maintenance of the gluconeogenic pathway, it would seem that given the decrease in PDH flux (and thus a decrease in acetyl CoA production), that the anaplerotic pools of aspartate are being depleted, and shuttled into gluconeogenesis. Finally, it is simply possible that as PDH flux is downregulated during and immediately following ischemia, that the hyperpolarized pyruvate taken up by the liver cannot proceed via the anaplerotic pathway quickly enough,

and therefore has no other choice but to accumulate as alanine and lactate.

Looking at the ^{31}P data, the ATP levels were shown to decrease substantially upon ischemia, without complete recovery, and have been demonstrated to be good markers for liver energetics and disease [227, 228]. Ideally, a further hyperpolarized [1-^{13}C]pyruvate scan should have been performed during the post-ischemic recovery period, in order to determine whether any changes in carbohydrate metabolism accompany the partial ATP recovery post-ischemia.

It has also been shown that the fed state of the animal is key to the impact of ischemia, sub-sequential ATP depletion and its ability to recover [229–231] (although there is some disagreement [232]). This is due to the low critical ATP levels in the fasted liver [233], presumably as a result of gluconeogenic processes. Indeed, it is likely that as a result of this ATP depletion, a proportion of cells underwent apoptosis [234]. The ATP levels recovered to 72±15% of the pre-ischemic values, and remained stable, perhaps indicating a chronic decrease in ATP synthesis [235]. Preconditioning may improve this recovery, by reducing lactate accumulation and ATP usage via AMPK [236]. The Pi levels increased significantly during ischemia and have been shown to be deleterious to the hepatocytes [237]. The ATP / Pi ratio [238,239], used as a marker of liver energetics, reflects the drop in ATP and was significantly decreased. This data is in keeping with previous ischemia reperfusion work carried out, using both pseudo *in vivo* [240,241] or traditional isolated perfused liver models [242]. It should be noted that no PCr was present in the liver, due to the very low expression of the CK enzyme.

6.3.2.4 Conclusion

In conclusion, the work in this chapter has demonstrated the possibility of using both the perfused mouse heart and liver with hyperpolarized DNP. Despite being unable to see all the acute metabolic changes that would have been expected in the mouse heart,

hyperpolarized DNP in combination with the isolated perfused mouse heart should have no problems looking at genetic models of disease, nor drug treatments, where the effect is not transient (less than a couple of minutes). The isolated perfused liver proved to be an excellent demonstration of the ability to look at changes in both transient and long term metabolism, given its higher flow rate. There was no evidence that the methods of perfusion used were deliterious, as the liver provided stable energetic parameters throughout the experiment.

Chapter 7

General Discussion and Future Directions

It has taken more than 40 years for the DNP technique to expand from its initial applications in physics [26] and biophysics [243], to its use today in the study of the biology of living systems, as a means of looking at the real-time changes that occur in metabolism. Developing the creativity and envisaged use for any technique often relies on developments in other areas of science, even if seemingly unrelated at the time. The development of techniques for isolated perfused organs and extensive *in vivo* testing alongside the progression of theoretical physics are what have allowed the concept of DNP to exist as widely as it does today. This thesis has explored the combination of DNP with isolated perfused organ systems, and has found new ways in which to optimize and further develop hyperpolarized DNP experiments, which will improve the available methods to study biological systems.

The ability to acquire high quality metabolic images using CSI will allow for the localization and visualization of metabolic dysfunction in any region of the myocardium, in addition to the global information previously obtained using a variety of different hyperpolarized probes. Such a technique may be useful in various cardiac models of

disease, where inhomogenous damage across the myocardium is observed (e.g. myocardial infarction), or where the location of biochemical disturbances are simply unknown in a given disease model. Further developments to the use of DNP and CSI would involve a shorter protocol, as is currently possible *in vivo* [85]. This should allow acquisitions of higher spatial and temporal resolution images of the isolated perfused heart, and should also permit probes other than pyruvate, which tend to have lower polarizations, to be imaged. Improved spatial resolution of the CSI protocol should also allow the possibility of imaging in the isolated perfused mouse heart, which at present would be difficult due to its small size. In addition, imaging the metabolism of the isolated perfused liver should form part of future work performed, as a way of assessing liver viability, as real-time techniques allowing assessment of hepatic performance are lacking. This may prove to be particularly useful in measuring the extent of disease induced hepatic damage.

The work carried out in this thesis exploring the effects of deviating too far from the physiological conditions that organs are subjected to *in vivo* should provide a framework under which more physiologically relevant experiments can be performed. Deviations from normal *in vivo* conditions not only affect the physiological data acquired, but also the quality of the hyperpolarized signal, and therefore solutions to this needed to be devised with regards to careful probe concentration selection and the use of fatty acids. Keeping these considerations in mind should avoid inaccurate conclusions being drawn from DNP metabolic data.

Concerning the probes developed in this thesis, the basic principles for compound development have been detailed, and allow for initial trials of probes of interest to be carried out rapidly, before deciding upon whether or not they are suitable for extended study in altered metabolic models, both *ex vivo* and *in vivo*. Improvements in this area will come from research into better electron sources (the radical used), as well as ingenious new ways of using the higher polarizations of nuclei such as protons

to augment those of carbon, the most relevant nucleus metabolically.

With regard to the work performed on isolated perfused mouse organs, all genetic models available in the mouse have now been unlocked for use with the combination of DNP and perfused organs. Such experiments will make it possible to study a large variety of disease models, obtaining data from both the mouse heart and the mouse liver, thus providing insight on the wider metabolic picture of disease. Future work in this area should involve experimental work with murine disease models, characterizing the changes seen with different hyperpolarized probes, in tandem with a validation of the technique and data interpretation using established methods involving destructive tissue analysis. Only in this way can DNP be accepted not only in the field of magnetic resonance, but also in dedicated metabolic laboratories. Performing hyperpolarized work in the isolated perfused mouse organ is particularly relevant where *in vivo* technology is let down by inadequate performance of the magnetic resonance imaging system, unable to adequately localize metabolism from myocardial or hepatic tissue. This results in contamination from muscle, blood, as well as from other organs. This problem is made worse by the small size of the mouse, and the large slice thicknesses typically used in imaging.

Beyond the scope of the work performed in this thesis, there is the potential for more global changes to improve all aspects of DNP experimentation. The most important change would be to find a way to increase the polarizations produced across all probes. This intrinsically depends on two factors, firstly, maintaining a low sample temperature, and, secondly, using higher magnetic fields in the polarizer (and therefore higher microwave frequencies). Cooling systems and materials that are capable of very low temperatures ($<<$ 1 K) are available, but large cooling power is required to dissipate the heat generated from the insertion of the initial room temperature sample, the microwave source and the dissolution process, which presents a complex engineering problem. Further, with the increasing availability of commercial high

frequency, high power microwave sources, enhanced polarizations are also possible by increasing the magnetic field of the polarizer system. Such improvements have recently been demonstrated with the development of a commercially available system [244], although there is still much progress that could be made in this area. Such increases in polarization would help counteract the issues seen when using albumin bound fatty acid preparations, thus improving the signal seen from hyperpolarized probes under physiological conditions. Also, in organ systems with low flow rates, such as the isolated perfused mouse heart demonstrated in this thesis, increased hyperpolarized signal would ensure that good quality spectra were obtainable across a wide range of coronary flow rates. Further, increased polarizations would allow for a wider array of novel probes to be used, some of which have already been developed, but cannot be used at present due to the constraints of low sensitivity.

In summary, throughout this thesis, many developments have been made to allow routine use of DNP hyperpolarization in *ex vivo* isolated perfused organ models. It has been demonstrated to work reliably, and in conditions that are closer to accurately reflecting the desired variables present *in vivo*, whilst offering all the advantages of a controlled and reproducible method of assessing metabolism in real-time.

References

[1] J. G. Salway. *Metabolism at a Glance*. Wiley-Blackwell, 3rd edition edition, November 2003.

[2] G Perriello, R Jorde, N Nurjhan, M Stumvoll, G Dailey, T Jenssen, D M Bier, and J E Gerich. Estimation of glucose-alanine-lactate-glutamine cycles in postabsorptive humans: role of skeletal muscle. *The American Journal of Physiology*, 269(3 Pt 1):E443–450, September 1995. PMID: 7573421.

[3] Knuuti. PET metabolic imaging.

[4] E L Coe. Inhibition of glycolysis in ascites tumor cells preincubated with 2 -deoxy- 2-fluoro- d -glucose. *Biochimica Et Biophysica Acta*, 264(2):319–327, April 1972. PMID: 4260430.

[5] P Som, H L Atkins, D Bandoypadhyay, J S Fowler, R R MacGregor, K Matsui, Z H Oster, D F Sacker, C Y Shiue, H Turner, C N Wan, A P Wolf, and S V Zabinski. A fluorinated glucose analog, 2-fluoro-2-deoxy-d-glucose (F-18): nontoxic tracer for rapid tumor detection. *Journal of Nuclear Medicine: Official Publication, Society of Nuclear Medicine*, 21(7):670–675, July 1980. PMID: 7391842.

[6] *Molecular Imaging and Contrast Agent Database (MICAD)*. National Center for Biotechnology Information (US), Bethesda (MD), 2004. PMID: 22624173.

[7] U Tateishi, T Oka, and T Inoue. Radiolabeled RGD peptides as integrin alpha(v)beta3-targeted PET tracers. *Current medicinal chemistry*, 19(20):3301–3309, July 2012. PMID: 22664242.

[8] Daniel Kaemmerer, Vikas Prasad, Wolfgang Daffner, Sven-Petter Haugvik, Stefan Senftleben, Richard P Baum, and Merten Hommann. Radioguided surgery in neuroendocrine tumors using ga-68-labeled somatostatin analogs: a pilot study. *Clinical nuclear medicine*, 37(2):142–147, February 2012. PMID: 22228336.

[9] Katja Dettmer, Pavel A Aronov, and Bruce D Hammock. Mass spectrometry-based metabolomics. *Mass Spectrometry Reviews*, 26(1):51–78, February 2007. PMID: 16921475.

[10] Cameron J Holloway, Joseph Suttie, Sairia Dass, and Stefan Neubauer. Clinical cardiac magnetic resonance spectroscopy. *Progress in cardiovascular diseases*, 54(3):320–327, December 2011. PMID: 22014498.

[11] Cameron Holloway, Michiel ten Hove, Kieran Clarke, and Stefan Neubauer. MR spectroscopy in heart failure. *Frontiers in bioscience (Scholar edition)*, 3:331–340, 2011. PMID: 21196379.

[12] Cameron Holloway, Lowri Cochlin, Ion Codreanu, Edward Bloch, Marzieh Fatemian, Cezary Szmigielski, Helen Atherton, Lisa Heather, Jane Francis, Stefan Neubauer, Peter Robbins, Hugh Montgomery, and Kieran Clarke. Normobaric hypoxia impairs human cardiac energetics. *FASEB journal: official publication of the Federation of American Societies for Experimental Biology*, 25(9):3130–3135, September 2011. PMID: 21646398.

[13] A. Consoli, N. Nurjhan, J. J Reilly, D. M Bier, and J. E Gerich. Contribution of liver and skeletal muscle to alanine and lactate metabolism in humans. *American Journal of Physiology - Endocrinology And Metabolism*, 259(5):E677–E684, November 1990.

[14] P J Pacy, P A Bannister, and D Halliday. Influence of insulin on leucine kinetics in the whole body and across the forearm in post-absorptive insulin dependent diabetic (type 1) patients. *Diabetes Research (Edinburgh, Scotland)*, 18(4):155–162, December 1991. PMID: 1842750.

[15] Markus Himmelsbach. 10 years of MS instrumental developments–impact on LC-MS/MS in clinical chemistry. *Journal of Chromatography. B, Analytical Technologies in the Biomedical and Life Sciences*, 883-884:3–17, February 2012. PMID: 22177236.

[16] S W Provencher. Estimation of metabolite concentrations from localized in vivo proton NMR spectra. *Magnetic Resonance in Medicine: Official Journal of the Society of Magnetic Resonance in Medicine / Society of Magnetic Resonance in Medicine*, 30(6):672–679, December 1993. PMID: 8139448.

[17] Lars Stegger, Anne-Nadine Hoffmeier, Klaus P Schäfers, Sven Hermann, Otmar Schober, Michael A Schäfers, and Gregor Theilmeier. Accurate noninvasive measurement of infarct size in mice with high-resolution PET. *Journal of nuclear medicine: official publication, Society of Nuclear Medicine*, 47(11):1837–1844, November 2006. PMID: 17079817.

[18] R J BING, A SIEGEL, I UNGAR, and M GILBERT. Metabolism of the human heart. II. studies on fat, ketone and amino acid metabolism. *The American Journal of Medicine*, 16(4):504–515, April 1954. PMID: 13148192.

[19] Karlos X. Moreno, Scott M. Sabelhaus, Matthew E. Merritt, A. Dean Sherry, and Craig R. Malloy. Competition of pyruvate with physiological substrates

for oxidation by the heart: implications for studies with hyperpolarized [1-13C]pyruvate. *American Journal of Physiology - Heart and Circulatory Physiology*, 298(5):H1556 –H1564, May 2010.

[20] The influence of a magnetic field on radiation frequency. *Proceedings of the Royal Society of London*, 60(359-367):514–515, January 1896.

[21] M. Borghini. Dynamic polarization of nuclei by electron-nucleus dipolar coupling ("Effet solide"). *Physical Review Letters*, 16(24):1135, June 1966.

[22] M. Borghini. Spin-temperature model of nuclear dynamic polarization using free radicals. *Physical Review Letters*, 20(9):419, February 1968.

[23] A. Abragam. Overhauser effect in nonmetals. *Physical Review*, 98(6):1729–1735, June 1955.

[24] C. D. Jeffries. Polarization of nuclei by resonance saturation in paramagnetic crystals. *Physical Review*, 106(1):164–165, April 1957.

[25] M. Borghini and K. Scheffler. Experimental evidence for dynamic nuclear polarization by cooling of electron spin-spin interactions. *Physical Review Letters*, 26(22):1362–1365, May 1971.

[26] Albert W. Overhauser. Polarization of nuclei in metals. *Physical Review*, 92(2):411–415, October 1953.

[27] H. G. Dehmelt. Paramagnetic resonance reorientation of atoms and ions aligned by electron impact. *Physical Review*, 103(4):1125–1126, 1956.

[28] J. P. Wittke and R. H. Dicke. Redetermination of the hyperfine splitting in the ground state of atomic hydrogen. *Physical Review*, 103(3):620–631, 1956.

[29] H. G. Dehmelt. Slow spin relaxation of optically polarized sodium atoms. *Physical Review*, 105(5):1487–1489, March 1957.

[30] O. S. Leifson and C. D. Jeffries. Dynamic polarization of nuclei by electron-nuclear dipolar coupling in crystals. *Physical Review*, 122(6):1781–1795, June 1961.

[31] J. F. Jacquinot, W. Th. Wenckebach, M. Goldman, and A. Abragam. Polarization and NMR observation of ˆ43ca nuclei in CaF_2. *Physical Review Letters*, 32(20):1096–1097, May 1974.

[32] T. R. Carver and C. P. Slichter. Polarization of nuclear spins in metals. *Physical Review*, 92(1):212–213, October 1953.

[33] Thomas R. Carver and Charles P. Slichter. Experimental verification of the overhauser nuclear polarization effect. *Physical Review*, 102(4):975–980, May 1956.

[34] Johannes Natterer and Joachim Bargon. Parahydrogen induced polarization. *Progress in Nuclear Magnetic Resonance Spectroscopy*, 31(4):293–315, November 1997.

[35] Gareth A. Morris and Ray Freeman. Enhancement of nuclear magnetic resonance signals by polarization transfer. *Journal of the American Chemical Society*, 101(3):760–762, 1979.

[36] Ralph W Adams, Juan A Aguilar, Kevin D Atkinson, Michael J Cowley, Paul I. P Elliott, Simon B Duckett, Gary G. R Green, Iman G Khazal, Joaquín López-Serrano, and David C Williamson. Reversible interactions with para-hydrogen enhance NMR sensitivity by polarization transfer. *Science*, 323(5922):1708–1711, March 2009.

[37] Hunter Middleton, Robert D. Black, Brian Saam, Gordon D. Cates, Gary P. Cofer, Robert Guenther, William Happer, Lawrence W. Hedlund, G. Alan Johnson, Kim Juvan, and John Swartz. MR imaging with Hyperpolarized3He gas. *Magnetic Resonance in Medicine*, 33(2):271–275, February 1995.

[38] Eduard E de Lange, Talissa A Altes, James T Patrie, John D Gaare, Jeffrey J Knake, 3rd Mugler, John P, and Thomas A Platts-Mills. Evaluation of asthma with hyperpolarized helium-3 MRI: correlation with clinical severity and spirometry. *Chest*, 130(4):1055–1062, October 2006. PMID: 17035438.

[39] Neil Woodhouse, Jim M Wild, Edwin J. R van Beek, Nigel Hoggard, Nicki Barker, and Christopher J Taylor. Assessment of hyperpolarized 3He lung MRI for regional evaluation of interventional therapy: A pilot study in pediatric cystic fibrosis. *Journal of Magnetic Resonance Imaging*, 30(5):981–988, November 2009.

[40] Lindsay Mathew, Miranda Kirby, Roya Etemad-Rezai, Andrew Wheatley, David G McCormack, and Grace Parraga. Hyperpolarized ^{3}He magnetic resonance imaging: preliminary evaluation of phenotyping potential in chronic obstructive pulmonary disease. *European Journal of Radiology*, 79(1):140–146, July 2011. PMID: 19932577.

[41] Leif Schröder, Thomas J Lowery, Christian Hilty, David E Wemmer, and Alexander Pines. Molecular imaging using a targeted magnetic resonance hyperpolarized biosensor. *Science*, 314(5798):446–449, October 2006.

[42] Xin Zhou, Yanping Sun, Mary Mazzanti, Nils Henninger, Joey Mansour, Marc Fisher, and Mitchell Albert. MRI of stroke using hyperpolarized 129Xe. *NMR in Biomedicine*, 24(2):170–175, February 2011. PMID: 20821723.

[43] Physics projects deflate for lack of helium-3 - IEEE spectrum. http://spectrum.ieee.org/biomedical/diagnostics/physics-projects-deflate-for-lack-of-helium3.

[44] Chester F. Hwang and D. A. Hill. New effect in dynamic polarization. *Physical Review Letters*, 18(4):110–112, January 1967.

[45] Chester F. Hwang and Daniel A. Hill. Phenomenological model for the new effect in dynamic polarization. *Physical Review Letters*, 19(18):1011–1014, October 1967.

[46] A. Abragam. *The Principles of Nuclear Magnetism.* Clarendon Press, reprint edition, April 1994.

[47] Jan H. Ardenkjær-Larsen, Björn Fridlund, Andreas Gram, Georg Hansson, Lennart Hansson, Mathilde H. Lerche, Rolf Servin, Mikkel Thaning, and Klaes Golman. Increase in signal-to-noise ratio of > 10,000 times in liquid-state NMR. *Proceedings of the National Academy of Sciences of the United States of America*, 100(18):10158–10163, September 2003. PMID: 12930897 PMCID: 193532.

[48] Evan R. McCarney, Brandon D. Armstrong, Mark D. Lingwood, and Songi Han. Hyperpolarized water as an authentic magnetic resonance imaging contrast agent. *Proceedings of the National Academy of Sciences*, 104(6):1754 – 1759, February 2007.

[49] Ulrich L Günther. Dynamic nuclear hyperpolarization in liquids. *Topics in Current Chemistry*, October 2011. PMID: 22025060.

[50] A. Comment, B. van den Brandt, K. Uffmann, F. Kurdzesau, S. Jannin, J.A. Konter, P. Hautle, W.Th. Wenckebach, R. Gruetter, and J.J. van der Klink. Design and performance of a DNP prepolarizer coupled to a rodent MRI scanner. *Concepts in Magnetic Resonance Part B: Magnetic Resonance Engineering*, 31B(4):255–269, 2007.

[51] Marie A Schroeder, Lowri E Cochlin, Lisa C Heather, Kieran Clarke, George K Radda, and Damian J Tyler. In vivo assessment of pyruvate dehydrogenase flux in the heart using hyperpolarized carbon-13 magnetic resonance. *Proceedings of the National Academy of Sciences*, 105(33):12051–12056, August 2008.

[52] V.S. Bajaj, C.T. Farrar, M.K. Hornstein, I. Mastovsky, J. Vieregg, J. Bryant, B. Eléna, K.E. Kreischer, R.J. Temkin, and R.G. Griffin. Dynamic nuclear polarization at 9T using a novel 250GHz gyrotron microwave source. *Journal of magnetic resonance (San Diego, Calif. : 1997)*, 160(2):85–90, February 2003. PMID: 12615147 PMCID: 2914497.

[53] Vasyl Denysenkov, Mark J Prandolini, Marat Gafurov, Deniz Sezer, Burkhard Endeward, and Thomas F Prisner. Liquid state DNP using a 260 GHz high power gyrotron. *Physical Chemistry Chemical Physics: PCCP*, 12(22):5786–5790, June 2010. PMID: 20461255.

[54] Robert G Griffin. Dynamic nuclear polarization at 9T using a novel 250 gyrotron microwave source. *Journal of Magnetic Resonance (San Diego, Calif.: 1997)*, 213(2):410–412, December 2011. PMID: 22152359.

[55] Colin D Joye, Robert G Griffin, Melissa K Hornstein, Kan-Nian Hu, Kenneth E Kreischer, Melanie Rosay, Michael A Shapiro, Jagadishwar R Sirigiri, Richard J Temkin, and Paul P Woskov. Operational characteristics of a 14-w 140-GHz gyrotron for dynamic nuclear polarization. *IEEE Transactions on Plasma Science. IEEE Nuclear and Plasma Sciences Society*, 34(3):518–523, June 2006. PMID: 17431442.

[56] Vikram S Bajaj, Melissa K Hornstein, Kenneth E Kreischer, Jagadishwar R Sirigiri, Paul P Woskov, Melody L Mak-Jurkauskas, Judith Herzfeld, Richard J Temkin, and Robert G Griffin. 250GHz CW gyrotron oscillator for dynamic nuclear polarization in biological solid state NMR. *Journal of Magnetic Resonance (San Diego, Calif.: 1997)*, 189(2):251–279, December 2007. PMID: 17942352.

[57] H. Van Dijk and D. Shoenberg. Tables of vapour pressure of liquid helium, 1949.

[58] Daniel Ball. *Optimizing of Hyperpolarization of Novel Substrates Using Dynamic Nuclear Polarization*. PhD thesis, University of Oxford, Department of Physiology, Anatomy and Genetics, 2008.

[59] D G Bruce, L H Storlien, S M Furler, and D J Chisholm. Cephalic phase metabolic responses in normal weight adults. *Metabolism: Clinical and Experimental*, 36(8):721–725, August 1987. PMID: 3298939.

[60] E S Hwang, B A Hirayama, and E M Wright. Distribution of the SGLT1 na+/glucose cotransporter and mRNA along the crypt-villus axis of rabbit small intestine. *Biochemical and biophysical research communications*, 181(3):1208–1217, December 1991. PMID: 1764071.

[61] S A Adibi and D W Mercer. Protein digestion in human intestine as reflected in luminal, mucosal, and plasma amino acid concentrations after meals. *The Journal of Clinical Investigation*, 52(7):1586–1594, July 1973. PMID: 4718954.

[62] M Chen, Y Yang, E Braunstein, K E Georgeson, and C M Harmon. Gut expression and regulation of FAT/CD36: possible role in fatty acid transport in rat enterocytes. *American Journal of Physiology. Endocrinology and Metabolism*, 281(5):E916–923, November 2001. PMID: 11595646.

[63] N Abumrad, C Harmon, and A Ibrahimi. Membrane transport of long-chain fatty acids: evidence for a facilitated process. *Journal of Lipid Research*, 39(12):2309–2318, December 1998. PMID: 9831619.

[64] James A Hamilton. Fatty acid transport: Difficult or easy? *Journal of Lipid Research*, 39(3):467–481, March 1998.

[65] N Loirdighi, D Ménard, E Delvin, and E Levy. Ontogeny and location of HMG-CoA reductase, ACAT, and MGAT in human small intestine. *The American Journal of Physiology*, 273(1 Pt 1):G62–67, July 1997. PMID: 9252510.

[66] J H Cummings. Short chain fatty acids in the human colon. *Gut*, 22(9):763–779, 1981.

[67] W E Roediger. The colonic epithelium in ulcerative colitis: an energy-deficiency disease? *Lancet*, 2(8197):712–715, October 1980. PMID: 6106826.

[68] Knud Erik Bach Knudsen, Anja Serena, Nuria Canibe, and Katri S Juntunen. New insight into butyrate metabolism. *Proceedings of the Nutrition Society*, 62(01):81–86, 2003.

[69] H Ruppin, S Bar-Meir, K H Soergel, C M Wood, and M G Schmitt. Absorption of short-chain fatty acids by the colon. *Gastroenterology*, 78(6):1500–1507, June 1980. PMID: 6768637.

[70] S G Peters, E W Pomare, and C A Fisher. Portal and peripheral blood short chain fatty acid concentrations after caecal lactulose instillation at surgery. *Gut*, 33(9):1249–1252, September 1992. PMID: 1427380.

[71] Victor Lorber and Margaret Cook. THE METABOLISM OF n-BUTYRATE-C14 BY MAMMALIAN HEART MUSCLE. *Journal of Biological Chemistry*, 215(2):823 –832, 1955.

[72] L E Mallet, J H Exton, and C R Park. Control of gluconeogenesis from amino acids in the perfused rat liver. *The Journal of Biological Chemistry*, 244(20):5713–5723, October 1969. PMID: 4310604.

[73] Rong-Ze Yang, Greorghe Blaileanu, Barbara C Hansen, Alan R Shuldiner, and Da-Wei Gong. cDNA cloning, genomic structure, chromosomal mapping, and functional expression of a novel human alanine aminotransferase. *Genomics*, 79(3):445–450, March 2002. PMID: 11863375.

[74] R Gudi, M M Bowker-Kinley, N Y Kedishvili, Y Zhao, and K M Popov. Diversity of the pyruvate dehydrogenase kinase gene family in humans. *The Journal of Biological Chemistry*, 270(48):28989–28994, December 1995. PMID: 7499431.

[75] J Rowles, S W Scherer, T Xi, M Majer, D C Nickle, J M Rommens, K M Popov, R A Harris, N L Riebow, J Xia, L C Tsui, C Bogardus, and M Prochazka. Cloning and characterization of PDK4 on 7q21.3 encoding a fourth pyruvate dehydrogenase kinase isoenzyme in human. *The Journal of Biological Chemistry*, 271(37):22376–22382, September 1996. PMID: 8798399.

[76] J. Denis McGarry and Daniel W. Foster. Ketogenesis and cholesterol synthesis in normal and neoplastic tissues of the rat. *Journal of Biological Chemistry*, 244(15):4251 –4256, 1969.

[77] Marie A Schroeder, Helen J Atherton, Daniel R Ball, Mark A Cole, Lisa C Heather, Julian L Griffin, Kieran Clarke, George K Radda, and Damian J Tyler. Real-time assessment of krebs cycle metabolism using hyperpolarized

13C magnetic resonance spectroscopy. *FASEB Journal: Official Publication of the Federation of American Societies for Experimental Biology*, 23(8):2529–2538, August 2009. PMID: 19329759.

[78] Helen J Atherton, Michael S Dodd, Lisa C Heather, Marie A Schroeder, Julian L Griffin, George K Radda, Kieran Clarke, and Damian J Tyler. Role of pyruvate dehydrogenase inhibition in the development of hypertrophy in the hyperthyroid rat heart: a combined magnetic resonance imaging and hyperpolarized magnetic resonance spectroscopy study. *Circulation*, 123(22):2552–2561, June 2011. PMID: 21606392.

[79] Matthew E Merritt, Crystal Harrison, Charles Storey, A Dean Sherry, and Craig R Malloy. Inhibition of carbohydrate oxidation during the first minute of reperfusion after brief ischemia: NMR detection of hyperpolarized 13CO2 and H13CO3-. *Magnetic Resonance in Medicine: Official Journal of the Society of Magnetic Resonance in Medicine / Society of Magnetic Resonance in Medicine*, 60(5):1029–1036, November 2008. PMID: 18956454.

[80] Dirk Mayer, Yi-Fen Yen, James Tropp, Adolf Pfefferbaum, Ralph E Hurd, and Daniel M Spielman. Application of subsecond spiral chemical shift imaging to real-time multislice metabolic imaging of the rat in vivo after injection of hyperpolarized 13C1-pyruvate. *Magnetic resonance in medicine: official journal of the Society of Magnetic Resonance in Medicine / Society of Magnetic Resonance in Medicine*, 62(3):557–564, September 2009. PMID: 19585607.

[81] Florian Wiesinger, Eliane Weidl, Marion I Menzel, Martin A Janich, Oleksandr Khegai, Steffen J Glaser, Axel Haase, Markus Schwaiger, and Rolf F Schulte. IDEAL spiral CSI for dynamic metabolic MR imaging of hyperpolarized [1-(13) c]pyruvate. *Magnetic resonance in medicine: official journal of the Society of Magnetic Resonance in Medicine / Society of Magnetic Resonance in Medicine*, 68(1):8–16, July 2012. PMID: 22127962.

[82] Angus Z Lau, Albert P Chen, Ralph E Hurd, and Charles H Cunningham. Spectral-spatial excitation for rapid imaging of DNP compounds. *NMR in Biomedicine*, 24(8):988–996, October 2011. PMID: 21751271.

[83] H F Brink, M D Buschmann, and B R Rosen. NMR chemical shift imaging. *Computerized Medical Imaging and Graphics: The Official Journal of the Computerized Medical Imaging Society*, 13(1):93–104, February 1989. PMID: 2538222.

[84] Luca Menichetti, Francesca Frijia, Alessandra Flori, Florian Wiesinger, Vincenzo Lionetti, Giulio Giovannetti, Giovanni Donato Aquaro, Fabio A. Recchia, Jan Henrik Ardenkjaer-Larsen, Maria Filomena Santarelli, and Massimo Lombardi. Assessment of real-time myocardial uptake and enzymatic conversion of hyperpolarized [1-13C]pyruvate in pigs using slice selective magnetic resonance spectroscopy. *Contrast Media & Molecular Imaging*, 7(1):85–94, 2012.

[85] Angus Z Lau, Albert P Chen, Nilesh R Ghugre, Venkat Ramanan, Wilfred W Lam, Kim A Connelly, Graham A Wright, and Charles H Cunningham. Rapid multislice imaging of hyperpolarized 13C pyruvate and bicarbonate in the heart. *Magnetic Resonance in Medicine: Official Journal of the Society of Magnetic Resonance in Medicine / Society of Magnetic Resonance in Medicine*, 64(5):1323–1331, November 2010. PMID: 20574989.

[86] Klaes Golman, J. Stefan Petersson, Peter Magnusson, Edvin Johansson, Per Åkeson, Chun-Ming Chai, Georg Hansson, and Sven Månsson. Cardiac metabolism measured noninvasively by hyperpolarized 13C MRI. *Magnetic Resonance in Medicine*, 59(5):1005–1013, 2008.

[87] Damian J Tyler, Craig A Lygate, Jürgen E Schneider, Paul J Cassidy, Stefan Neubauer, and Kieran Clarke. CINE-MR imaging of the normal and infarcted rat heart using an 11.7 t vertical bore MR system. *Journal of Cardiovascular Magnetic Resonance: Official Journal of the Society for Cardiovascular Magnetic Resonance*, 8(2):327–333, 2006. PMID: 16669175.

[88] Daniel J Stuckey, Carolyn A Carr, Stephanie J Meader, Damian J Tyler, Mark A Cole, and Kieran Clarke. First-pass perfusion CMR two days after infarction predicts severity of functional impairment six weeks later in the rat heart. *Journal of Cardiovascular Magnetic Resonance: Official Journal of the Society for Cardiovascular Magnetic Resonance*, 13:38, 2011. PMID: 21812990.

[89] L C Heather, A F Catchpole, D J Stuckey, M A Cole, C A Carr, and K Clarke. Isoproterenol induces in vivo functional and metabolic abnormalities: similar to those found in the infarcted rat heart. *Journal of physiology and pharmacology: an official journal of the Polish Physiological Society*, 60(3):31–39, September 2009. PMID: 19826179.

[90] O. Langendorff. Untersuchungen am überlebenden säugethierherzen. *Pflüger, Archiv für die Gesammte Physiologie des Menschen und der Thiere*, 61(6):291–332, 1895.

[91] Angus Z Lau, Albert P Chen, Jennifer Barry, John J Graham, William Dominguez-Viqueira, Nilesh R Ghugre, Graham A Wright, and Charles H Cunningham. Reproducibility study for free-breathing measurements of pyruvate metabolism using hyperpolarized (13) c in the heart. *Magnetic resonance in medicine: official journal of the Society of Magnetic Resonance in Medicine / Society of Magnetic Resonance in Medicine*, July 2012. PMID: 22760647.

[92] V S Constantine and R W Mowry. Selective staining of human dermal collagen. II. the use of picrosirius red F3BA with polarization microscopy. *The Journal of Investigative Dermatology*, 50(5):419–423, May 1968. PMID: 4172462.

[93] H M LYLE. An improved tissue technique with hematoxylin-eosin stain. *The American Journal of Medical Technology*, 13(4):178–181, July 1947. PMID: 20255364.

[94] Peder E Z Larson, Adam B Kerr, Albert P Chen, Michael S Lustig, Matthew L Zierhut, Simon Hu, Charles H Cunningham, John M Pauly, John Kurhanewicz, and Daniel B Vigneron. Multiband excitation pulses for hyperpolarized 13C dynamic chemical-shift imaging. *Journal of Magnetic Resonance (San Diego, Calif.: 1997)*, 194(1):121–127, September 2008. PMID: 18619875.

[95] Simon Hu, Michael Lustig, Albert P Chen, Jason Crane, Adam Kerr, Douglas A C Kelley, Ralph Hurd, John Kurhanewicz, Sarah J Nelson, John M Pauly, and Daniel B Vigneron. Compressed sensing for resolution enhancement of hyperpolarized 13C flyback 3D-MRSI. *Journal of Magnetic Resonance (San Diego, Calif.: 1997)*, 192(2):258–264, June 2008. PMID: 18367420.

[96] Simon Hu, Michael Lustig, Asha Balakrishnan, Peder E Z Larson, Robert Bok, John Kurhanewicz, Sarah J Nelson, Andrei Goga, John M Pauly, and Daniel B Vigneron. 3D compressed sensing for highly accelerated hyperpolarized (13)C MRSI with in vivo applications to transgenic mouse models of cancer. *Magnetic Resonance in Medicine: Official Journal of the Society of Magnetic Resonance in Medicine / Society of Magnetic Resonance in Medicine*, 63(2):312–321, February 2010. PMID: 20017160.

[97] Peder E Z Larson, Simon Hu, Michael Lustig, Adam B Kerr, Sarah J Nelson, John Kurhanewicz, John M Pauly, and Daniel B Vigneron. Fast dynamic 3D MR spectroscopic imaging with compressed sensing and multiband excitation pulses for hyperpolarized 13C studies. *Magnetic Resonance in Medicine: Official Journal of the Society of Magnetic Resonance in Medicine / Society of Magnetic Resonance in Medicine*, 65(3):610–619, March 2011. PMID: 20939089.

[98] Albert P Chen, Mark J Albers, Charles H Cunningham, Susan J Kohler, Yi-Fen Yen, Ralph E Hurd, James Tropp, Robert Bok, John M Pauly, Sarah J Nelson, John Kurhanewicz, and Daniel B Vigneron. Hyperpolarized c-13 spectroscopic imaging of the TRAMP mouse at 3T-initial experience. *Magnetic Resonance in Medicine: Official Journal of the Society of Magnetic Resonance in Medicine / Society of Magnetic Resonance in Medicine*, 58(6):1099–1106, December 2007. PMID: 17969006.

[99] Angus Z Lau, Albert P Chen, and Charles H Cunningham. Integrated bloch-siegert b_1 mapping and multislice imaging of hyperpolarized ^{13}C pyruvate and bicarbonate in the heart. *Magnetic Resonance in Medicine: Official Journal of the Society of Magnetic Resonance in Medicine / Society of Magnetic Resonance in Medicine*, 67(1):62–71, January 2012. PMID: 21656549.

[100] S Levitsky and H Feinberg. Biochemical changes of ischemia. *The Annals of Thoracic Surgery*, 20(1):21–29, July 1975. PMID: 803171.

[101] Sam E Day, Mikko I Kettunen, Ferdia A Gallagher, De-En Hu, Mathilde Lerche, Jan Wolber, Klaes Golman, Jan Henrik Ardenkjaer-Larsen, and Kevin M

Brindle. Detecting tumor response to treatment using hyperpolarized 13C magnetic resonance imaging and spectroscopy. *Nature Medicine*, 13(11):1382–1387, November 2007. PMID: 17965722.

[102] Klaes Golman, Jan H. Ardenkjær-Larsen, J. Stefan Petersson, Sven Månsson, and Ib Leunbach. Molecular imaging with endogenous substances. *Proceedings of the National Academy of Sciences of the United States of America*, 100(18):10435–10439, September 2003. PMID: 12930896 PMCID: 193579.

[103] J. H. Ardenkjaer-Larsen, S. Macholl, and H. Jóhannesson. Dynamic nuclear polarization with trityls at 1.2 k. *Applied Magnetic Resonance*, 34(3):509–522, August 2008.

[104] Peder E Z Larson, Galen Reed, Adam B Kerr, John M Pauly, Robert Bok, Marcus Ferrone, Andrea Harzstark, Sarah J Nelson, John Kurhanewicz, and Daniel Vigneron. Localized dynamics of hyperpolarized 13C pyruvate in prostate cancer patients. *ISMRM, Melbourne*, 2012.

[105] Simon Hu, Albert Chen, Matthew Zierhut, Robert Bok, Yi-Fen Yen, Marie Schroeder, Ralph Hurd, Sarah Nelson, John Kurhanewicz, and Daniel Vigneron. *In Vivo* carbon-13 dynamic MRS and MRSI of normal and fasted rat liver with hyperpolarized ^{13}c-pyruvate. *Molecular Imaging and Biology*, 11(6):399–407, November 2009.

[106] Marie A Schroeder, Helen J Atherton, Lisa C Heather, Julian L Griffin, Kieran Clarke, George K Radda, and Damian J Tyler. Determining the in vivo regulation of cardiac pyruvate dehydrogenase based on label flux from hyperpolarised [1-13C]pyruvate. *NMR in biomedicine*, 24(8):980–987, October 2011. PMID: 21387444.

[107] Ralph E Hurd, Yi-Fen Yen, Dirk Mayer, Albert Chen, David Wilson, Susan Kohler, Robert Bok, Daniel Vigneron, John Kurhanewicz, James Tropp, Daniel Spielman, and Adolf Pfefferbaum. Metabolic imaging in the anesthetized rat brain using hyperpolarized [1-13C] pyruvate and [1-13C] ethyl pyruvate. *Magnetic Resonance in Medicine: Official Journal of the Society of Magnetic Resonance in Medicine / Society of Magnetic Resonance in Medicine*, 63(5):1137–1143, May 2010. PMID: 20432284.

[108] In vivo13carbon metabolic imaging at 3T with hyperpolarized13C-1-pyruvate. *Magnetic Resonance in Medicine*, 58(1):65, 2007.

[109] Marie Schroeder. *Development of Novel Hyperpolarized Magnetic Resonance Techniques for Metabolic Imaging of the Heart*. Department of Physiology, Anatomy and Genetics, Oxford, 2008.

[110] Helen J Atherton, Marie A Schroeder, Michael S Dodd, Lisa C Heather, Emma E Carter, Lowri E Cochlin, Simon Nagel, Nicola R Sibson, George K

Radda, Kieran Clarke, and Damian J Tyler. Validation of the in vivo assessment of pyruvate dehydrogenase activity using hyperpolarised 13C MRS. *NMR in Biomedicine*, 24(2):201–208, February 2011. PMID: 20799252.

[111] Crystal Harrison, Chendong Yang, Ashish Jindal, Ralph J Deberardinis, M A Hooshyar, Matthew Merritt, A Dean Sherry, and Craig R Malloy. Comparison of kinetic models for analysis of pyruvate-to-lactate exchange by hyperpolarized (13) c NMR. *NMR in biomedicine*, March 2012. PMID: 22451442.

[112] Warren S Warren, Elizabeth Jenista, Rosa Tamara Branca, and Xin Chen. Increasing hyperpolarized spin lifetimes through true singlet eigenstates. *Science*, 323(5922):1711–1714, 2009.

[113] John Kurhanewicz, Daniel B Vigneron, Kevin Brindle, Eduard Y Chekmenev, Arnaud Comment, Charles H Cunningham, Ralph J DeBerardinis, Gary G Green, Martin O Leach, Sunder S Rajan, Rahim R Rizi, Brian D Ross, Warren S Warren, and Craig R Malloy. Analysis of cancer metabolism by imaging hyperpolarized nuclei: Prospects for translation to clinical research. *Neoplasia (New York, N.Y.)*, 13(2):81–97, February 2011. PMID: 21403835 PMCID: PMC3033588.

[114] A L Kerbey, P J Randle, R H Cooper, S Whitehouse, H T Pask, and R M Denton. Regulation of pyruvate dehydrogenase in rat heart. mechanism of regulation of proportions of dephosphorylated and phosphorylated enzyme by oxidation of fatty acids and ketone bodies and of effects of diabetes: role of coenzyme a, acetyl-coenzyme a and reduced and oxidized nicotinamide-adenine dinucleotide. *Biochemical Journal*, 154(2):327–348, February 1976. PMID: 180974 PMCID: PMC1172714.

[115] E Abemayor, G B Kovachich, and N Haugaard. Effects of dichloroacetate on brain pyruvate dehydrogenase. *Journal of Neurochemistry*, 42(1):38–42, January 1984. PMID: 6689696.

[116] Marie A Schroeder, Pawel Swietach, Helen J Atherton, Ferdia A Gallagher, Phillip Lee, George K Radda, Kieran Clarke, and Damian J Tyler. Measuring intracellular pH in the heart using hyperpolarized carbon dioxide and bicarbonate: a 13C and 31P magnetic resonance spectroscopy study. *Cardiovascular Research*, 86(1):82–91, April 2010. PMID: 20008827.

[117] Taegtmeyer H, Hems R, and Krebs H A. Utilization of energy-providing substrates in the isolated working rat heart. http://www.biochemj.org/bj/186/0701/bj1860701_browse.htm, March 1980.

[118] B Renstrom, A J Liedtke, and S H Nellis. Mechanisms of substrate preference for oxidative metabolism during early myocardial reperfusion. *The American journal of physiology*, 259(2 Pt 2):H317–323, August 1990. PMID: 2386216.

[119] J R Neely and H E Morgan. Relationship between carbohydrate and lipid metabolism and the energy balance of heart muscle. *Annual Review of Physiology*, 36:413–459, 1974. PMID: 19400669.

[120] Deborah Hill. Alginate encapsulated lactate dehydrogenase and hyperpolarized MR as a platform to characterize enzyme kinetics, May 2012.

[121] Jay M Mirtallo, Joseph F Dasta, Kurt C Kleinschmidt, and Joseph Varon. State of the art review: Intravenous fat emulsions: Current applications, safety profile, and clinical implications. *The Annals of pharmacotherapy*, 44(4):688–700, April 2010. PMID: 20332339.

[122] Wojciech Polenceusz, Jacek Kupisiak, Robert Goch, and Dariusz Paczkowski. [Intralipid for treatment of local anaesthetic-induced toxicity]. *Anestezjologia intensywna terapia*, 40(4):249–252, December 2008. PMID: 19517666.

[123] B L McNiff. Clinical use of 10% soybean oil emulsion. *American journal of hospital pharmacy*, 34(10):1080–1086, October 1977. PMID: 411372.

[124] INTRALIPID (SOYBEAN OIL) EMULSION [FRESENIUS KABI AB]. http://dailymed.nlm.nih.gov/dailymed/drugInfo.cfm?id=6275.

[125] Y. Cheng and D. Hauton. Cold acclimation induces physiological cardiac hypertrophy and increases assimilation of triacylglycerol metabolism through lipoprotein lipase. *Biochimica et Biophysica Acta*, 1781(10):618–626, October 2008. PMID: 18722549 PMCID: PMC2568868.

[126] W Stremmel, L Pohl, A Ring, and T Herrmann. A new concept of cellular uptake and intracellular trafficking of long-chain fatty acids. *Lipids*, 36(9):981–989, September 2001. PMID: 11724471.

[127] J F Glatz, J J Luiken, F A van Nieuwenhoven, and G J Van der Vusse. Molecular mechanism of cellular uptake and intracellular translocation of fatty acids. *Prostaglandins, leukotrienes, and essential fatty acids*, 57(1):3–9, July 1997. PMID: 9250601.

[128] L Giménez-Llort, J Vilanova, N Skottova, G Bengtsson-Olivecrona, M Llobera, and M Q Robert. Lipoprotein lipase enables triacylglycerol hydrolysis by perfused newborn rat liver. *The American journal of physiology*, 261(4 Pt 1):G641–647, October 1991. PMID: 1928350.

[129] S Vilaró, M Reina, I Ramírez, and M Llobera. Intralipid administration induces a lipoprotein lipase-like activity in the livers of starved adult rats. *The Biochemical journal*, 236(1):273–278, May 1986. PMID: 3790076.

[130] P P Forget, J Fernandes, and P H Begemann. Utilization of fat emulsion during total parenteral nutrition in children. *Acta paediatrica Scandinavica*, 64(3):377–384, May 1975. PMID: 808087.

[131] J Nordenström, G Neeser, T Olivecrona, and J Wahren. Effect of medium- and long-chain triglyceride infusion on lipoprotein and hepatic lipase in healthy subjects. *European journal of clinical investigation*, 21(6):580–585, December 1991. PMID: 1778219.

[132] Jae Mo Park, Sonal Josan, Taichang Jang, Milton Merchant, Yi-Fen Yen, Ralph E Hurd, Lawrence Recht, Daniel M Spielman, and Dirk Mayer. Metabolite kinetics in c6 rat glioma model using magnetic resonance spectroscopic imaging of hyperpolarized [1-(13) c]pyruvate. *Magnetic resonance in medicine: official journal of the Society of Magnetic Resonance in Medicine / Society of Magnetic Resonance in Medicine*, February 2012. PMID: 22334279.

[133] Timothy H Witney, Mikko I Kettunen, and Kevin M Brindle. Kinetic modeling of hyperpolarized 13C label exchange between pyruvate and lactate in tumor cells. *The Journal of biological chemistry*, 286(28):24572–24580, July 2011. PMID: 21596745.

[134] Tao Xu, Dirk Mayer, Meng Gu, Yi-Fen Yen, Sonal Josan, James Tropp, Adolf Pfefferbaum, Ralph Hurd, and Daniel Spielman. Quantification of in vivo metabolic kinetics of hyperpolarized pyruvate in rat kidneys using dynamic 13C MRSI. *NMR in biomedicine*, 24(8):997–1005, October 2011. PMID: 21538639.

[135] E A Boehm, B E Jones, G K Radda, R L Veech, and K Clarke. Increased uncoupling proteins and decreased efficiency in palmitate-perfused hyperthyroid rat heart. *American journal of physiology. Heart and circulatory physiology*, 280(3):H977–983, March 2001. PMID: 11179038.

[136] M C Sugden, D A Priestman, K A Orfali, and M J Holness. Hyperthyroidism facilitates cardiac fatty acid oxidation through altered regulation of cardiac carnitine palmitoyltransferase: studies in vivo and with cardiac myocytes. *Hormone and metabolic research = Hormon- und Stoffwechselforschung = Hormones et métabolisme*, 31(5):300–306, May 1999. PMID: 10422724.

[137] J. Douglas Ashbrook, Arthur A Spector, and John E Fletcher. Medium chain fatty acid binding to human plasma albumin. *Journal of Biological Chemistry*, 247(21):7038–7042, November 1972.

[138] A A Spector, K John, and J E Fletcher. Binding of long-chain fatty acids to bovine serum albumin. *Journal of Lipid Research*, 10(1):56–67, January 1969. PMID: 5773785.

[139] H Vorum, R Brodersen, U Kragh-Hansen, and A O Pedersen. Solubility of long-chain fatty acids in phosphate buffer at pH 7.4. *Biochimica Et Biophysica Acta*, 1126(2):135–142, June 1992. PMID: 1627615.

[140] M J Bennett, David Hauton, David G. Hole, and Rhys D. Evans. Preparation of radiolabelled very-low-density lipoprotein (VLDL) in high yield by extended rat liver perfusion. *Biotechnology Letters*, 22(4):301–306, 2000.

[141] R D Evans, M J Bennett, and D Hauton. Perfused heart studies to investigate lipid metabolism. *Biochemical Society transactions*, 28(2):113–120, February 2000. PMID: 10816111.

[142] L Zhu, E Kurian, F G Prendergast, and M D Kemple. Dynamics of palmitic acid complexed with rat intestinal fatty acid binding protein. *Biochemistry*, 38(5):1554–1561, February 1999. PMID: 9931022.

[143] Kellen Brunaldi, Nasi Huang, and James A Hamilton. Fatty acids are rapidly delivered to and extracted from membranes by methyl-beta-cyclodextrin. *Journal of lipid research*, 51(1):120–131, January 2010. PMID: 19625735.

[144] Biju K Pillai, Ravi Jasuja, Jeffrey R Simard, and James A Hamilton. Fast diffusion of very long chain saturated fatty acids across a bilayer membrane and their rapid extraction by cyclodextrins: implications for adrenoleukodystrophy. *The Journal of biological chemistry*, 284(48):33296–33304, November 2009. PMID: 19801636.

[145] Menna R Clatworthy, Mikko I Kettunen, De-En Hu, Rebeccah J Mathews, Timothy H Witney, Brett W C Kennedy, Sarah E Bohndiek, Ferdia A Gallagher, Lorna B Jarvis, Kenneth G C Smith, and Kevin M Brindle. Magnetic resonance imaging with hyperpolarized [1,4-13C2]fumarate allows detection of early renal acute tubular necrosis. *Proceedings of the National Academy of Sciences of the United States of America*, July 2012. PMID: 22837393.

[146] Kayvan R Keshari, John Kurhanewicz, Robert Bok, Peder E Z Larson, Daniel B Vigneron, and David M Wilson. Hyperpolarized 13C dehydroascorbate as an endogenous redox sensor for in vivo metabolic imaging. *Proceedings of the National Academy of Sciences of the United States of America*, 108(46):18606–18611, November 2011. PMID: 22042839.

[147] Simon Hu, Minhua Zhu, Hikari A I Yoshihara, David M Wilson, Kayvan R Keshari, Peter Shin, Galen Reed, Cornelius von Morze, Robert Bok, Peder E Z Larson, John Kurhanewicz, and Daniel B Vigneron. In vivo measurement of normal rat intracellular pyruvate and lactate levels after injection of hyperpolarized [1-(13)C]alanine. *Magnetic resonance imaging*, 29(8):1035–1040, October 2011. PMID: 21855243.

[148] Dirk Mayer, Yi-Fen Yen, Sonal Josan, Jae Mo Park, Adolf Pfefferbaum, Ralph E Hurd, and Daniel M Spielman. Application of hyperpolarized [1-(13) c]lactate for the in vivo investigation of cardiac metabolism. *NMR in biomedicine*, 25(10):1119–1124, October 2012. PMID: 22278751.

[149] Hyla Allouche-Arnon, Mathilde H Lerche, Magnus Karlsson, Robert E Lenkinski, and Rachel Katz-Brull. Deuteration of a molecular probe for DNP hyperpolarization–a new approach and validation for choline chloride. *Contrast media & molecular imaging*, 6(6):499–506, December 2011. PMID: 22144028.

[150] J.H. Ardenkjaer-Larsen. More than 50% 13C polarization in solution by the DNP-NMR method: 200,000-fold enhancement compared to 3 t and room temperature. *ISMRM*, 2009.

[151] Z W Yu and P J Quinn. Dimethyl sulphoxide: a review of its applications in cell biology. *Bioscience reports*, 14(6):259–281, December 1994. PMID: 7620078.

[152] Sven Macholl, Haukur Jóhannesson, and Jan Henrik Ardenkjaer-Larsen. Trityl biradicals and 13C dynamic nuclear polarization. *Physical Chemistry Chemical Physics*, 12(22):5804, 2010.

[153] Lloyd Lumata, Zoltan Kovacs, Craig Malloy, A Dean Sherry, and Matthew Merritt. The effect of 13C enrichment in the glassing matrix on dynamic nuclear polarization of [1-13C]pyruvate. *Physics in Medicine and Biology*, 56(5):N85–92, March 2011. PMID: 21285486.

[154] Johanne G. Bloemen, Koen Venema, Marcel C. van de Poll, Steven W. Olde Damink, Wim A. Buurman, and Cornelis H. Dejong. Short chain fatty acids exchange across the gut and liver in humans measured at surgery. *Clinical Nutrition*, 28(6):657–661, December 2009.

[155] Zhanguo Gao, Jun Yin, Jin Zhang, Robert E Ward, Roy J Martin, Michael Lefevre, William T Cefalu, and Jianping Ye. Butyrate improves insulin sensitivity and increases energy expenditure in mice. *Diabetes*, 58(7):1509–1517, 2009.

[156] Anne C Nilsson, Elin M Östman, Knud Erik Bach Knudsen, Jens J Holst, and Inger M. E Björck. A cereal-based evening meal rich in indigestible carbohydrates increases plasma butyrate the next morning. *The Journal of Nutrition*, 140(11):1932–1936, 2010.

[157] A Trenkle. Effects of short-chain fatty acids, feeding, fasting and type of diet on plasma insulin levels in sheep. *The Journal of nutrition*, 100(11):1323–1330, November 1970. PMID: 5476435.

[158] A Junod, A E Lambert, L Orci, R Pictet, A E Gonet, and A E Renold. Studies of the diabetogenic action of streptozotocin. *Proceedings of the Society for Experimental Biology and Medicine. Society for Experimental Biology and Medicine (New York, N.Y.)*, 126(1):201–205, October 1967. PMID: 4864021.

[159] K Srinivasan, B Viswanad, Lydia Asrat, C L Kaul, and P Ramarao. Combination of high-fat diet-fed and low-dose streptozotocin-treated rat: a model for type 2 diabetes and pharmacological screening. *Pharmacological research: the official journal of the Italian Pharmacological Society*, 52(4):313–320, October 2005. PMID: 15979893.

[160] A Ritzhaupt, I S Wood, A Ellis, K B Hosie, and S P Shirazi-Beechey. Identification and characterization of a monocarboxylate transporter (MCT1) in pig

and human colon: its potential to transport l-lactate as well as butyrate. *The Journal of physiology*, 513 (Pt 3):719–732, December 1998. PMID: 9824713.

[161] Christos Hadjiagapiou, Larry Schmidt, Pradeep K. Dudeja, Thomas J. Layden, and Krishnamurthy Ramaswamy. Mechanism(s) of butyrate transport in caco-2 cells: role of monocarboxylate transporter 1. *American Journal of Physiology - Gastrointestinal and Liver Physiology*, 279(4):G775 –G780, October 2000.

[162] Carsten Juel, Mads K Holten, and Flemming Dela. Effects of strength training on muscle lactate release and MCT1 and MCT4 content in healthy and type 2 diabetic humans. *The Journal of physiology*, 556(Pt 1):297–304, April 2004. PMID: 14724187.

[163] Keitaro Matsumoto, Takashige Koba, Koichiro Hamada, Hisaya Tsujimoto, and Ryoichi Mitsuzono. Branched-chain amino acid supplementation increases the lactate threshold during an incremental exercise test in trained individuals. *Journal of nutritional science and vitaminology*, 55(1):52–58, February 2009. PMID: 19352063.

[164] G Blomqvist, J O Thorell, M Ingvar, V Grill, L Widén, and S Stone-Elander. Use of r-beta-[1-11C]hydroxybutyrate in PET studies of regional cerebral uptake of ketone bodies in humans. *The American journal of physiology*, 269(5 Pt 1):E948–959, November 1995. PMID: 7491948.

[165] 3rd Russell, R R and H Taegtmeyer. Pyruvate carboxylation prevents the decline in contractile function of rat hearts oxidizing acetoacetate. *The American journal of physiology*, 261(6 Pt 2):H1756–1762, December 1991. PMID: 1750532.

[166] J L Vanoverschelde, W Wijns, J Kolanowski, A Bol, P M Decoster, C Michel, M Cogneau, G R Heyndrickx, B Essamri, and J A Melin. Competition between palmitate and ketone bodies as fuels for the heart: study with positron emission tomography. *The American journal of physiology*, 264(3 Pt 2):H701–707, March 1993. PMID: 8456973.

[167] Fabien Pifferi, Sébastien Tremblay, Etienne Croteau, Mélanie Fortier, Jennifer Tremblay-Mercier, Roger Lecomte, and Stephen C Cunnane. Mild experimental ketosis increases brain uptake of 11C-acetoacetate and 18F-fluorodeoxyglucose: a dual-tracer PET imaging study in rats. *Nutritional neuroscience*, 14(2):51–58, March 2011. PMID: 21605500.

[168] M'hamed Bentourkia, Sébastien Tremblay, Fabien Pifferi, Jacques Rousseau, Roger Lecomte, and Stephen Cunnane. PET study of 11C-acetoacetate kinetics in rat brain during dietary treatments affecting ketosis. *American journal of physiology. Endocrinology and metabolism*, 296(4):E796–801, April 2009. PMID: 19176356.

[169] E O Balasse and F Féry. Ketone body production and disposal: effects of fasting, diabetes, and exercise. *Diabetes/metabolism reviews*, 5(3):247–270, May 1989. PMID: 2656155.

[170] Ferdia A Gallagher, Mikko I Kettunen, and Kevin M Brindle. Imaging pH with hyperpolarized 13C. *NMR in biomedicine*, 24(8):1006–1015, October 2011. PMID: 21812047.

[171] David M Wilson, Kayvan R Keshari, Peder E Z Larson, Albert P Chen, Simon Hu, Mark Van Criekinge, Robert Bok, Sarah J Nelson, Jeffrey M Macdonald, Daniel B Vigneron, and John Kurhanewicz. Multi-compound polarization by DNP allows simultaneous assessment of multiple enzymatic activities in vivo. *Journal of magnetic resonance (San Diego, Calif.: 1997)*, 205(1):141–147, July 2010. PMID: 20478721.

[172] Matthew E Merritt, Crystal Harrison, A Dean Sherry, Craig R Malloy, and Shawn C Burgess. Flux through hepatic pyruvate carboxylase and phosphoenolpyruvate carboxykinase detected by hyperpolarized 13C magnetic resonance. *Proceedings of the National Academy of Sciences of the United States of America*, 108(47):19084–19089, November 2011. PMID: 22065779.

[173] International mouse strain resource. http://www.findmice.org/.

[174] Helen R. Pilcher. It's a knockout. *Nature News*, May 2003.

[175] Qi Zhou, Jean-Paul Renard, Gaëlle Le Friec, Vincent Brochard, Nathalie Beaujean, Yacine Cherifi, Alexandre Fraichard, and Jean Cozzi. Generation of fertile cloned rats by regulating oocyte activation. *Science (New York, N.Y.)*, 302(5648):1179, November 2003. PMID: 14512506.

[176] Sushuang Zheng, Kindiya Geghman, Sushila Shenoy, and Chenjian Li. Retake the center stage - new development of rat genetics. *Journal of genetics and genomics = Yi chuan xue bao*, 39(6):261–268, June 2012. PMID: 22749013.

[177] Amaya Aleixandre de Artiñano and Marta Miguel Castro. Experimental rat models to study the metabolic syndrome. *The British journal of nutrition*, 102(9):1246–1253, November 2009. PMID: 19631025.

[178] A. M. Geurts, G. J. Cost, Y. Freyvert, B. Zeitler, J. C. Miller, V. M. Choi, S. S. Jenkins, A. Wood, X. Cui, X. Meng, A. Vincent, S. Lam, M. Michalkiewicz, R. Schilling, J. Foeckler, S. Kalloway, H. Weiler, S. Menoret, I. Anegon, G. D. Davis, L. Zhang, E. J. Rebar, P. D. Gregory, F. D. Urnov, H. J. Jacob, and R. Buelow. Knockout rats via embryo microinjection of zinc-finger nucleases. *Science*, 325(5939):433–433, July 2009.

[179] Knockout rat and knockout mouse models. http://www.sageresearchmodels.com/research-models.

[180] Michele M. Hickey, Jennifer C. Lam, Natalie A. Bezman, W. Kimryn Rathmell, and M. Celeste Simon. von Hippel–Lindau mutation in mice recapitulates chuvash polycythemia via hypoxia-inducible factor-2? signaling and splenic erythropoiesis. *The Journal of Clinical Investigation*, 117(12):3879–3889, December 2007. PMID: 17992257 PMCID: PMC2066197.

[181] Daniel M Spielman, Dirk Mayer, Yi-Fen Yen, James Tropp, Ralph E Hurd, and Adolf Pfefferbaum. In vivo measurement of ethanol metabolism in the rat liver using magnetic resonance spectroscopy of hyperpolarized [1-13C]pyruvate. *Magnetic resonance in medicine: official journal of the Society of Magnetic Resonance in Medicine / Society of Magnetic Resonance in Medicine*, 62(2):307–313, August 2009. PMID: 19526498.

[182] J R Neely, M J Rovetto, J T Whitmer, and H E Morgan. Effects of ischemia on function and metabolism of the isolated working rat heart. *The American journal of physiology*, 225(3):651–658, September 1973. PMID: 4726499.

[183] P Schemmer, H D Connor, G E Arteel, J A Raleigh, H Bunzendahl, R P Mason, and R G Thurman. Reperfusion injury in livers due to gentle in situ organ manipulation during harvest involves hypoxia and free radicals. *The Journal of pharmacology and experimental therapeutics*, 290(1):235–240, July 1999. PMID: 10381781.

[184] J R Neely and M J Rovetto. Techniques for perfusing isolated rat hearts. *Methods in enzymology*, 39:43–60, 1975. PMID: 1171353.

[185] H Noda, T Nishimura, M Kinoshita, Y Taenaka, K Kihara, M Sago, M Hayashi, H Takano, and T Akutsu. Myocardial free fatty acid metabolism of the ischemic heart treated by left ventricular assist device. *ASAIO transactions / American Society for Artificial Internal Organs*, 34(3):294–296, September 1988. PMID: 3196523.

[186] C Depre, P J Davies, and H Taegtmeyer. Transcriptional adaptation of the heart to mechanical unloading. *The American journal of cardiology*, 83(12A):58H–63H, June 1999. PMID: 10750589.

[187] G J Gores, L J Kost, and N F LaRusso. The isolated perfused rat liver: conceptual and practical considerations. *Hepatology (Baltimore, Md.)*, 6(3):511–517, June 1986. PMID: 3519420.

[188] M Bessems, N A 't Hart, R Tolba, B M Doorschodt, H G D Leuvenink, R J Ploeg, T Minor, and T M van Gulik. The isolated perfused rat liver: standardization of a time-honoured model. *Laboratory Animals*, 40(3):236–246, July 2006. PMID: 16803641.

[189] Y Shibayama and K Nakata. Role of hepatic artery in haemodynamics in normal and cirrhotic livers. *J. Gastroenterol. Hepatol.*, 6:591 – 594, 1991.

[190] Fiona J Sutherland, Michael J Shattock, Kathryn E Baker, and David J Hearse. Mouse isolated perfused heart: Characteristics and cautions. *Clinical and Experimental Pharmacology and Physiology*, 30(11):867–878, 2003.

[191] Mahmoud Abu-Amara, Shi Yu Yang, Alexander Seifalian, Brian Davidson, and Barry Fuller. The nitric oxide pathway–evidence and mechanisms for protection against liver ischaemia reperfusion injury. *Liver international: official journal of the International Association for the Study of the Liver*, 32(4):531–543, April 2012. PMID: 22316165.

[192] H J Döring. The isolated perfused heart according to langendorff technique–function–application. *Physiologia Bohemoslovaca*, 39(6):481–504, 1990. PMID: 2103635.

[193] F J Sutherland and D J Hearse. The isolated blood and perfusion fluid perfused heart. *Pharmacological research: the official journal of the Italian Pharmacological Society*, 41(6):613–627, June 2000. PMID: 10816330.

[194] R Southworth, S C Blackburn, K A B Davey, G K Sharland, and P B Garlick. The low oxygen-carrying capacity of krebs buffer causes a doubling in ventricular wall thickness in the isolated heart. *Canadian journal of physiology and pharmacology*, 83(2):174–182, February 2005. PMID: 15791291.

[195] Paulo Ney Aguiar Martins, Peter Neuhaus, Paulo Ney Aguiar Martins, and Peter Neuhaus. Surgical anatomy of the liver, hepatic vasculature and bile ducts in the rat, surgical anatomy of the liver, hepatic vasculature and bile ducts in the rat. *Liver International, Liver International*, 27, 27(3, 3):384, 384–392, 392, April 2007.

[196] Metabolic support for the postischaemic heart. *Lancet*, 345(8964):1552–1555, June 1995. PMID: 7791443.

[197] H R Cross, K Clarke, L H Opie, and G K Radda. Is lactate-induced myocardial ischaemic injury mediated by decreased pH or increased intracellular lactate? *Journal of molecular and cellular cardiology*, 27(7):1369–1381, July 1995. PMID: 7473783.

[198] W Rouslin. Mitochondrial complexes i, II, III, IV, and v in myocardial ischemia and autolysis. *The American journal of physiology*, 244(6):H743–748, June 1983. PMID: 6305212.

[199] J R Neely and L W Grotyohann. Role of glycolytic products in damage to ischemic myocardium. dissociation of adenosine triphosphate levels and recovery of function of reperfused ischemic hearts. *Circulation research*, 55(6):816–824, December 1984. PMID: 6499136.

[200] J T Whitmer, J A Idell-Wenger, M J Rovetto, and J R Neely. Control of fatty acid metabolism in ischemic and hypoxic hearts. *The Journal of biological chemistry*, 253(12):4305–4309, June 1978. PMID: 659417.

[201] Steven G Lloyd, Peipei Wang, Huadong Zeng, and John C Chatham. Impact of low-flow ischemia on substrate oxidation and glycolysis in the isolated perfused rat heart. *American journal of physiology. Heart and circulatory physiology*, 287(1):H351–362, July 2004. PMID: 15001444.

[202] Clifford D L Folmes, Daniel Sowah, Alexander S Clanachan, and Gary D Lopaschuk. High rates of residual fatty acid oxidation during mild ischemia decrease cardiac work and efficiency. *Journal of molecular and cellular cardiology*, 47(1):142–148, July 2009. PMID: 19303418.

[203] M Saddik and G D Lopaschuk. Myocardial triglyceride turnover during reperfusion of isolated rat hearts subjected to a transient period of global ischemia. *The Journal of biological chemistry*, 267(6):3825–3831, February 1992. PMID: 1740430.

[204] O L Bricknell and L H Opie. Effects of substrates on tissue metabolic changes in the isolated rat heart during underperfusion and on release of lactate dehydrogenase and arrhythmias during reperfusion. *Circulation research*, 43(1):102–115, July 1978. PMID: 207459.

[205] R L Nunnally and D P Hollis. Adenosine triphosphate compartmentation in living hearts: a phosphorus nuclear magnetic resonance saturation transfer study. *Biochemistry*, 18(16):3642–3646, August 1979. PMID: 476074.

[206] T C Vary, E T Angelakos, and S W Schaffer. Relationship between adenine nucleotide metabolism and irreversible ischemic tissue damage in isolated perfused rat heart. *Circulation research*, 45(2):218–225, August 1979. PMID: 445706.

[207] L N Maslov, A S Gorbunov, T V Lasukova, and Yu B Lishmanov. Inotropic and chronotropic effects of ischemic postconditioning on the model of isolated heart. *Bulletin of experimental biology and medicine*, 152(6):688–691, April 2012. PMID: 22803165.

[208] G Greve, O E Bakøy, T Holten, P Jynge, and T Saetersdal. Reversibility of mild to moderate ischemic injuries in the isolated rat heart. a characterization by 31P-NMR and by physiological and ultrastructural indices. *The American journal of pathology*, 142(4):1279–1289, April 1993. PMID: 8475998.

[209] S Neubauer, B L Hamman, S B Perry, J A Bittl, and J S Ingwall. Velocity of the creatine kinase reaction decreases in postischemic myocardium: a 31P-NMR magnetization transfer study of the isolated ferret heart. *Circulation research*, 63(1):1–15, July 1988. PMID: 3383370.

[210] Benzene metabolism in the isolated perfused mouse liver. http://www.ingentaconnect.com/content/ap/to/1997/00000146/00000001/art08209, September 1997.

[211] B Gess, K Schricker, M Pfeifer, and A Kurtz. Acute hypoxia upregulates NOS gene expression in rats. *The American journal of physiology*, 273(3 Pt 2):R905–910, September 1997. PMID: 9321866.

[212] Michael J Nowicki, Dongping Shi, Zhengwei Cai, Phyllis R Bishop, and Warren L May. Developmental expression of endothelial nitric oxide synthase (eNOS) in the rat liver. *Pediatric research*, 54(5):732–738, November 2003. PMID: 12904594.

[213] Bryan L Copple, Robert A Roth, and Patricia E Ganey. Anticoagulation and inhibition of nitric oxide synthase influence hepatic hypoxia after monocrotaline exposure. *Toxicology*, 225(2-3):128–137, August 2006. PMID: 16828949.

[214] Pilar Cejudo-Martín, Manuel Morales-Ruiz, Josefa Ros, Miguel Navasa, Guillermo Fernández-Varo, Josep Fuster, Francisca Rivera, Vicente Arroyo, Juan Rodés, and Wladimiro Jiménez. Hypoxia is an inducer of vasodilator agents in peritoneal macrophages of cirrhotic patients. *Hepatology (Baltimore, Md.)*, 36(5):1172–1179, November 2002. PMID: 12395327.

[215] S Jitrapakdee, A Vidal-Puig, and J C Wallace. Anaplerotic roles of pyruvate carboxylase in mammalian tissues. *Cellular and molecular life sciences: CMLS*, 63(7-8):843–854, April 2006. PMID: 16505973.

[216] S M Cohen. 13C and 31P NMR study of gluconeogenesis: utilization of 13C-labeled substrates by perfused liver from streptozotocin-diabetic and untreated rats. *Biochemistry*, 26(2):563–572, January 1987. PMID: 3030411.

[217] T Qian, A L Nieminen, B Herman, and J J Lemasters. Mitochondrial permeability transition in pH-dependent reperfusion injury to rat hepatocytes. *The American journal of physiology*, 273(6 Pt 1):C1783–1792, December 1997. PMID: 9435481.

[218] H Taegtmeyer. Metabolic responses to cardiac hypoxia. increased production of succinate by rabbit papillary muscles. *Circulation research*, 43(5):808–815, November 1978. PMID: 709743.

[219] G J KLAIN, D A VAUGHAN, and L N VAUGHAN. Interrelationships of cold exposure and amino acid imbalances. *The Journal of nutrition*, 78:359–364, November 1962. PMID: 14033265.

[220] F ROSEN, N R ROBERTS, and C A NICHOL. Glucocorticosteroids and transaminase activity. i. increased activity of glutamicpyruvic transaminase in four conditions associated with gluconeogenesis. *The Journal of biological chemistry*, 234(3):476–480, March 1959. PMID: 13641244.

[221] M C Moore, A D Cherrington, G Cline, M J Pagliassotti, E M Jones, D W Neal, C Badet, and G I Shulman. Sources of carbon for hepatic glycogen synthesis in the conscious dog. *The Journal of clinical investigation*, 88(2):578–587, August 1991. PMID: 1864968.

[222] S M Bailey and L A Reinke. Effect of low flow ischemia-reperfusion injury on liver function. *Life sciences*, 66(11):1033–1044, 2000. PMID: 10724450.

[223] J L Dimicoli, J Patry, R Adam, A Dennison, J F Nedelec, and H Bismuth. A magnetic resonance study of the effect of nutritional status on cold-preserved murine liver. *Gastroenterology*, 107(6):1764–1773, December 1994. PMID: 7958690.

[224] R A Iles, P G Baron, and R D Cohen. The effect of reduction of perfusion rate on lactate and oxygen uptake, glucose output and energy supply in the isolated perfused liver of starved rats. *The Biochemical journal*, 184(3):635–642, December 1979. PMID: 44194.

[225] S Morikawa, T Inubushi, K Takahashi, S Shigemori, and H Ishii. Relationship between gluconeogenesis and phosphoenergetics in rat liver assessed by in vivo 13C and 31P NMR spectroscopy. *NMR in biomedicine*, 10(1):18–24, January 1997. PMID: 9251111.

[226] T Inomoto, A Tanaka, M Awane, M Kanai, H Shinohara, S Hatano, S Sato, T Gomi, K Masuda, Y Someya, K Honda, Y Seino, and Y Yamaoka. Changes in glucose transporter 2 and carbohydrate-metabolizing enzymes in the liver during cold preservation and warm ischemia. *Transplantation*, 61(6):869–874, March 1996. PMID: 8623151.

[227] R Oberhaensli, B Rajagopalan, G J Galloway, D J Taylor, and G K Radda. Study of human liver disease with p-31 magnetic resonance spectroscopy. *Gut*, 31(4):463–467, April 1990. PMID: 2338275.

[228] P J Harvey, J E Gready, H M Hickey, D G Le Couteur, and A J McLean. 31P and 1H NMR spectroscopic studies of liver extracts of carbon tetrachloride-treated rats. *NMR in biomedicine*, 12(6):395–401, October 1999. PMID: 10516622.

[229] M Domenicali, G Vendemiale, G Serviddio, I Grattagliano, A M Pertosa, B Nardo, A Principe, A Viola, F Trevisani, E Altomare, M Bernardi, and P Caraceni. Oxidative injury in rat fatty liver exposed to ischemia-reperfusion is modulated by nutritional status. *Digestive and liver disease: official journal of the Italian Society of Gastroenterology and the Italian Association for the Study of the Liver*, 37(9):689–697, September 2005. PMID: 15935746.

[230] R Cywes, P D Greig, J R Sanabria, P A Clavien, G A Levy, P R Harvey, and S M Strasberg. Effect of intraportal glucose infusion on hepatic glycogen content and degradation, and outcome of liver transplantation. *Annals of surgery*, 216(3):235–246; discussion 246–247, September 1992. PMID: 1417173.

[231] Michaela Stadler, Vincent Nuyens, Laurence Seidel, Adelin Albert, and Jean G Boogaerts. Effect of nutritional status on oxidative stress in an ex vivo perfused rat liver. *Anesthesiology*, 103(5):978–986, November 2005. PMID: 16249672.

[232] R Sumimoto, J H Southard, and F O Belzer. Livers from fasted rats acquire resistance to warm and cold ischemia injury. *Transplantation*, 55(4):728–732, April 1993. PMID: 8475543.

[233] F Desmoulin, P J Cozzone, and P Canioni. Phosphorus-31 nuclear-magnetic-resonance study of phosphorylated metabolites compartmentation, intracellular pH and phosphorylation state during normoxia, hypoxia and ethanol perfusion, in the perfused rat liver. *European journal of biochemistry / FEBS*, 162(1):151–159, January 1987. PMID: 3816778.

[234] B G Rosser and G J Gores. Liver cell necrosis: cellular mechanisms and clinical implications. *Gastroenterology*, 108(1):252–275, January 1995. PMID: 7806049.

[235] Wayel Jassem and Nigel D. Heaton. The role of mitochondria in ischemia/reperfusion injury in organ transplantation. *Kidney International*, 66(2):514–517, 2004.

[236] C Peralta, R Bartrons, A Serafin, C Blázquez, M Guzmán, N Prats, C Xaus, B Cutillas, E Gelpí, and J Roselló-Catafau. Adenosine monophosphate-activated protein kinase mediates the protective effects of ischemic preconditioning on hepatic ischemia-reperfusion injury in the rat. *Hepatology (Baltimore, Md.)*, 34(6):1164–1173, December 2001. PMID: 11732006.

[237] A J Kowaltowski, R F Castilho, M T Grijalba, E J Bechara, and A E Vercesi. Effect of inorganic phosphate concentration on the nature of inner mitochondrial membrane alterations mediated by ca2+ ions. a proposed model for phosphate-stimulated lipid peroxidation. *The Journal of biological chemistry*, 271(6):2929–2934, February 1996. PMID: 8621682.

[238] R L Veech, J W Lawson, N W Cornell, and H A Krebs. Cytosolic phosphorylation potential. *The Journal of biological chemistry*, 254(14):6538–6547, July 1979. PMID: 36399.

[239] A P Koretsky, S Wang, J Murphy-Boesch, M P Klein, T L James, and M W Weiner. 31P NMR spectroscopy of rat organs, in situ, using chronically implanted radiofrequency coils. *Proceedings of the National Academy of Sciences of the United States of America*, 80(24):7491–7495, December 1983. PMID: 6584867.

[240] C R Malloy, C C Cunningham, and G K Radda. The metabolic state of the rat liver in vivo measured by 31P-NMR spectroscopy. *Biochimica et biophysica acta*, 885(1):1–11, January 1986. PMID: 3942791.

[241] M E Clouse and R G Lee. Simple liver perfusion model for NMR spectroscopic analysis. *Investigative radiology*, 20(8):808–812, November 1985. PMID: 4077434.

[242] A C McLaughlin, H Takeda, and B Chance. Rapid ATP assays in perfused mouse liver by 31P NMR. *Proceedings of the National Academy of Sciences of the United States of America*, 76(11):5445–5449, November 1979. PMID: 293654.

[243] P J Cozzone, P Canioni, L Sarda, and R Kaptein. 360-MHz nuclear magnetic resonance and laser photochemically induced dynamic nuclear polarization studies of bile salt interaction with porcine colipase a. *European journal of biochemistry / FEBS*, 114(1):119–126, 1981. PMID: 7215346.

[244] Jan H Ardenkjaer-Larsen, Andrew M Leach, Neil Clarke, John Urbahn, Denise Anderson, and Timothy W Skloss. Dynamic nuclear polarization polarizer for sterile use intent. *NMR in biomedicine*, 24(8):927–932, October 2011. PMID: 21416540.